

School of Molecular and Life Sciences

Luminescent Metal-Based Markers for Bacterial Imaging

Anna Maria Ranieri

**This thesis is presented for the Degree of
Doctor of Philosophy
of
Curtin University**

May 2019

Declaration

To the best of my knowledge and belief this thesis contains no material previously published by any other person except where due acknowledgment has been made.

This thesis contains no material which has been accepted for the award of any other degree or diploma in any university.

Signature:

Date: 17/05/2019

Abstract

The aim of this research was to investigate a series of platinum(II) and iridium(III) complexes as bacterial imaging agents and explore their capability to readily penetrate the cell envelopes of bacteria and enable the visualisation of different sub-cellular structures.

A series of platinum(II) complexes was firstly investigated. A dicyclopentadienyl ($C^{\wedge}N^{\wedge}C$) scaffold has been exploited to synthesise a variety of neutral and anionic complexes, which have been structurally and photophysically characterised. The photophysical analyses were performed in organic solvents and aqueous media, as well as in the solid state and in frozen matrix in order to explore the aggregation properties of the platinum(II) complexes. The behaviour of the neutral platinum(II) complexes has been tested in live mammalian cells as well as live bacteria. All the complexes showed good cellular uptake and low cytotoxicity against mammalian cells. In regard to bacterial cells, two model strains were considered (*Bacillus cereus* and *Escherichia coli*), and antimicrobial activity was observed only for *B. cereus*. Imaging experiments revealed that one platinum(II) complex, [Pt(CNC)(Py-Napht)], was suitable to be explored as a cellular and bacterial label, showing fast uptake and easy detectability from lipid vacuoles within *B. cereus*. The study on this complex was therefore extended to super-resolution imaging on bacteria and correlative imaging with ion nanoscopy, both of which proved successful.

A family of neutral and cationic iridium(III) complexes was then explored as bacterial imaging agents. The neutral and cationic complexes showed opposite trends in toxicity against *B. cereus*, and imaging experiments proved that the different toxicity corresponded to different sub-cellular localisation. Indeed, while the neutral complexes accumulated in lipid compartments, the cationic species stained fine structures resembling membrane proteins.

Finally, this research has focused on live acidophilic bacteria, which thrive at pH less than 3 and are endowed with a reverse membrane potential. Prompted by the lack of probes capable of staining live acidophiles, a series of neutral and anionic platinum(II) and iridium(III) complexes have been tested in *Acidithiobacillus ferrooxidans*, revealing that anionic complexes are promising candidates to exploit the reverse membrane potential and cross the membrane of these acidophilic species.

Supporting publications include:

A. M. Ranieri, L. K. Burt, S. Stagni, S. Zacchini, B. W. Skelton, M. I. Ogden, A. C. Bissember and M. Massi, *Organometallics*, **2019**, *38*, 1108–1117.

V. Fiorini, I. Zanoni, S. Zacchini, A. L. Costa, A. Hochkoeppler, V. Zanotti, A. M. Ranieri, M. Massi, A. Stefan and S. Stagni, *Dalton Trans.*, **2017**, *46*, 12328–12338.

Conference presentations include:

A. M. Ranieri, S. Stagni, E. Watkin, M. I. Ogden and M. Massi, *Transition Metal Complexes for Bacterial Imaging*, **ASMI 2018**. Oral presentation. November 2018, Perth, Australia

A. M. Ranieri, S. Stagni, E. Watkin, M. I. Ogden and M. Massi, *Photophysical Trends On Platinum(II) Dicyclometalated Complexes*, **OZOM11**. Poster presentation. January 2018 Perth, Australia

A. M. Ranieri, S. Stagni, E. Watkin, M. I. Ogden and M. Massi, *One-photon and multi-photon bacterial imaging with red-emitting dicyclometalated platinum(II) aggregates*, **RACI100**. Oral presentation. July 2017, Melbourne, Australia

A. M. Ranieri, S. Stagni, E. Watkin, M. I. Ogden and M. Massi, *Enhanced Single- and Multi-Photon Bacterial Imaging with Red Emitting Platinum(II) Aggregates*, **ISPPCC17**. Poster presentation. July 2017, Oxford, UK

A. M. Ranieri, S. Stagni, E. Watkin, M. I. Ogden and M. Massi, *Imaging bacteria with luminescent platinum(II) aggregates*, **OZOM10**. Oral presentation. January 2017, Dunedin, New Zealand.

A. M. Ranieri, S. Stagni, M. I. Ogden and M. Massi, *Anionic Phosphorescent Platinum(II) Complexes*, **ICOMC 2016**. Poster presentation. July 2016, Melbourne, Australia.

Statement of Contribution by Others

The aim of this section is to identify and summarise the nature and extend of the input by the candidate and any co-author, to each of the journal articles reported as supporting publications to this work. Publications originating from the content of this thesis, but published after thesis submission, will also be included. In addition to this, a statement from each co-author is provided in Appendix F.

1. Publication title: “Methylation of Ir(III)-tetrazolato complexes: an effective route to modulate the emission outputs and to switch to antimicrobial properties”

Reference details: V. Fiorini, I. Zanoni, S. Zacchini, A. L. Costa, A. Hochkoepler, V. Zanotti, A. M. Ranieri, M. Massi, A. Stefan and S. Stagni, *Dalton Trans.*, **2017**, *46*, 12328–12338.

Author	Contribution
Valentina Fiorini	Synthesised the tetrazolato ligands, designed and synthesised the iridium complexes, characterised the iridium complexes and performed the photophysical measurement and contributed to paper writing
Ilaria Zanoni	Synthesised the tetrazolato ligands and the iridium complexes
Stefano Zacchini	Resolved the crystal structure of the iridium complexes
Anna Luisa Costa	Contributed to paper reviewing
Alejandro Hochkoepler	Contributed to paper reviewing
Valerio Zanotti	Contributed to paper reviewing
Anna Maria Ranieri	Contributed to the microbiological testing of the iridium tetrazolato complexes
Massimiliano Massi	Contributed to paper writing and reviewing
Alessandra Stefan	Performed the microbiological testing of the iridium tetrazolato complexes and contributed to paper writing and reviewing

Candidate

Supervisor




Anna Maria Ranieri

A/Prof Massimiliano Massi

2. Publication title: “Anionic Cyclometalated Platinum(II) Tetrazolato Complexes as Viable Photoredox Catalysts”

Reference details: A. M. Ranieri, L. K. Burt, S. Stagni, S. Zacchini, B. W. Skelton, M. I. Ogden, A. C. Bissember and M. Massi, *Organometallics*, **2019**, 38, 1108–1117.

Author	Contribution
Anna M. Ranieri	Synthesised the tetrazolato ligands, designed and synthesised the platinum complexes, characterised the platinum complexes and performed the photophysical measurement and contributed to paper writing
Liam K. Burt	Performed photoredox catalysis measurements and cyclic voltammetry measurements and contributed to paper writing
Stefano Stagni	Supervised the synthesis of the platinum dimer and platinum complexes
Stefano Zacchini	Resolved the crystal structure of the platinum complex
Brian W. Skelton	Resolved the crystal structure of the platinum dimer
Mark I. Ogden	Supervised the research (synthesis, characterisation and photophysics) and contributed to paper writing and reviewing
Alex C. Bissember	Supervised the research (photocatalysis and cyclic voltammetry) and contributed to paper writing and reviewing
Massimiliano Massi	Supervised the research (synthesis, characterisation and photophysics) and contributed to paper writing and reviewing

Candidate

Supervisor




Anna Maria Ranieri

A/Prof Massimiliano Massi

3. Publication title: “Complementary approaches to imaging sub-cellular lipid architectures in live bacteria using phosphorescent iridium complexes and Raman spectroscopy”

Reference details: A. M Ranieri, C. Caporale, V. Fiorini, A. Hubbard, P. Rigby, S. Stagni, E. Watkin, M. I. Ogden, M. J. Hackett, M. Massi, *Chem. Eur. J.*, **2019**, *25*, 10566-10570. Note: Article published after thesis submission.

Author	Contribution
Anna M. Ranieri	Cultured bacteria, performed the toxicity assays (growth curves), designed and performed the confocal imaging experiments, contributed to the Raman spectroscopy experiments, contributed to paper writing
Chiara Caporale	Synthesised the iridium complexes, contributed to paper reviewing
Valentina Fiorini	Synthesised the iridium complexes
Alysia Hubbard	Contributed to and supervised the confocal imaging experiments
Paul Rigby	Contributed to and supervised the confocal imaging experiments
Stefano Stagni	Supervised the research (Synthesis of complexes, photophysical measurements), , contributed to paper reviewing
Elizabeth Watkin	Supervised the research (Bacterial cultures, toxicity assays, bacterial imaging), contributed to paper reviewing
Mark I. Ogden	Supervised the research and contributed to paper writing and reviewing
Mark J. Hackett	Designed and performed the Raman spectroscopy experiments, contributed to paper writing and reviewing
Massimiliano Massi	Supervised the research and contributed to paper writing and reviewing

Candidate

Supervisor




Anna Maria Ranieri

A/Prof Massimiliano Massi


4. Publication title: “A platinum(II) based correlative probe for bacteria”

Reference details: Anna M. Ranieri, Kathryn G. Leslie, Song Huang, Stefano Stagni, Denis Jacquemin, Haibo Jiang, Alysia Hubbard, Elizabeth Watkin, Mark I. Ogden, Elizabeth J. New, Massimiliano Massi, *submitted for review*, **2019**. Note: Article submitted after thesis submission.

Author	Contribution
Anna M. Ranieri	Synthesised the platinum(II) complexes, characterised the complexes, performed the photophysical measurements, cultured the bacteria, performed the toxicity assays, performed the superresolution imaging experiments, contributed to paper writing
Kathryn G. Leslie	Synthesised and characterised the naphthalamide ligand
Song Huang	Performed the nanoSIMS experiments
Stefano Stagni	Supervised the research (Synthesis, photophysical analyses)
Denis Jacquemin	Performed the computational calculations and contributed to paper writing and reviewing
Haibo Jiang	Supervised the research (nanoSIMS) and contributed to paper writing and reviewing
Alysia Hubbard	Contributed to and supervised the superresolution imaging experiments
Elizabeth Watkin	Supervised the research (bacterial cultures, toxicity assays), contributed to paper reviewing
Mark I. Ogden	Supervised the research and contributed to paper writing and reviewing
Elizabeth J. New	Supervised the research and contributed to paper writing and reviewing
Massimiliano Massi	Supervised the research and contributed to paper writing and reviewing

Candidate

Supervisor




Anna Maria Ranieri

A/Prof Massimiliano Massi

Acknowledgments

It's funny how I thought about this moment so many times, and now I can't seem to find good enough words to wrap up these three and a half years of life. It has been an absolute rollercoaster of an experience, and I am so grateful for everyone I've had by my side along the way.

The first big round of thank you goes to my supervisors, A/ Prof. Max Massi, Prof Mark Ogden and Prof. Elizabeth Watkin. I must thank you for your immense knowledge and your support.

To Max, thank you for this incredible opportunity, for believing in me and pushing me to do more than I thought I could. For trusting me. Also, thank you for SO much laughter and the undecipherable gossips in "Romagnolo".

Mark, I can't find the words to say how important it was for me to know that you were always there. No matter how busy, you always go out of your way for your students. Your time, advice and enthusiasm have been invaluable for me.

To Liz, thank you for welcoming me to the world of microbiology, and most of all thank you because you have been a constant inspiration. For your ethic and courage, for your strength and your being so caring. Also, I can't count the times I have sat in your office winging about life! Thank you for putting up with that too!

My endless gratitude goes to A/ Prof. Stefano Stagni. There is no one else like you Stefano. I have done everything with the motivation, passion and ethics that I have found in your office from day one. Thank you.

Thank you to A/Prof Elizabeth New. You are not my supervisor on paper, but your contribution to my work and my growth has been immense.

I am so grateful for the amazing opportunity to work with A/Prof Paul Rigby and Mrs Alysia Hubbard. Paul, your passion for microscopy is contagious! Thank you for sharing it with me together with your knowledge. Lysh, thank you for investing so much of your time in helping me and for being so sweet and supportive.

Thank you to Dr. Mark (MAD) Hackett, for introducing me to Raman TV, for frying bacteria with me and for suggesting the best paper titles ever.

To all of the crazy people on level 2 – Lee, Cathy, Caitlyn, Andrew, Rob. You're a great bunch and you definitely make Curtin a better place.

Ben, I don't think I will ever meet anyone quite like you again. Thank you for your intelligence and for sharing it with me (Also, thank you for telling me when your birthday is!).

Thanks to Kofi, I knew you were special the moment I walked into Lab 10 for the first time. You once told me "you don't do science alone" and indeed- you went out of your way to help me so many times.

To Marcus, thank you for your help with all the bio-work and for the brainstorming on the floor, you quickly became so much more than a collaborator. Thank you also for the amazing time we had in Sydney and in Perth.

Thank you to Kate. No matter if in Perth, Sydney or Oxford. I could always find unconditioned support in you, both for science and life-related dilemmas.

Thank you to Lari, who has been a flatmate and then became a sister. Sydney will always be home until you are there.

To Marta. You taught me and supported me more than you know.

Thanks to Isabel, who despite moving around the UK has always found time to put up with me.

Thank you to my sweet, crazy Shifaza. For always reassuring me and giving me endless supply of positivity.

To Giulia, most of all because you actually kept your promise and came all the way down here to prove that Australia actually exists!.

Thank you to Elly, my costume-buddy, gin-buddy and intellectual conversations-buddy. Thank you for the quality time we share.

Thank you to Chiara, who came and pick me up from the airport and has been with me ever since. Not only this thesis would have not been possible (and edited, and submitted) without you, but I would probably be lost somewhere looking for my car keys if I haven't had you coming to the rescue so many times!

Himel, I owe you endless thanks for sticking by my side no matter what. Your couch will always be my favourite nap spot and my very safe place.

Thank you, Vasco. We have always been the best team and distance didn't change it.

To Nico. Could we laugh more than we do when we are together? Having you here makes me so happy. Thank you, Nani.

Thank you Fede (Fred). I truly think we were "separate alla nascita!"

To Vale. We share stubbornness, commitment and fast pace. Thank you Zia, for the constant encouragement and your patience.

Thanks to Ceci. It doesn't matter if half an hour, a day, a week. Time spent with you has always been therapeutic.

Fede, there hasn't been a thought or a feeling that I haven't shared with you in the past six years. Thank you.

I want to thank my Mum and Dad. It hasn't been easy for you in these years, but regardless you have supported any choice I have made, and you have believed in me. I hope that the woman I am today makes you proud.

Finally, to Max. You had such a great impact in my life in such a short time. Meeting you was the best thing that could have happened to me. Thank you.

Dedication

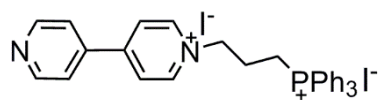
To Lorenzo.

Commonly used abbreviation and symbols

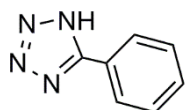
τ	Excited state lifetime
ϕ	Quantum yield
ϕ_r	Quantum yield of reference
λ_{abs}	Absorption wavelength
λ_{em}	Emission wavelength
λ_{ex}	Excitation wavelength
δ	Nuclear magnetic resonance chemical shift
ϵ	Molar absorptivity
AIE	Aggregation-induced emission
app	Apparent
BODIPY	4,4-difluoro-4-bora-3a,4a-diaza-s-indacene
bpy	2,2'-bipyridine
br	Broad (NMR)
BTB	doubly deprotonated form of the 1,2 bis-(1-H-tetrazol-5-yl)-benzene ligand
CNC	doubly deprotonated form of the 2,4,6-triphenylpyridine ligand
<i>ca.</i>	Circa/Approximately
d	Doublet (NMR)
DCM	Dichloromethane
DMEM	Dulbecco's modified eagle medium
DMF	Dimethylformamide
DMSO	Dimethylsulphoxide
F₂ppy	2-(2,4-difluorophenyl)pyridine
GS	Ground state
HOMO	Highest occupied molecular orbital
IC	Internal conversion
IC ₅₀	Half maximal inhibitory concentration
ICP-MS	Inductively coupled plasma mass spectrometry
IL	Intra-ligand
ILCT	Intra-ligand charge transfer

ISC	Intersystem crossing
J	Coupling constant (NMR)
k_{ISC}	Intersystem crossing rate constant
k_{nr}	Non-radiative decay rate constant
k_r	Radiative decay rate constant
LC	Ligand-centred
LLCT	Ligand-to-ligand charge transfer
LUMO	Lowest unoccupied molecular orbital
m	Multiplet (NMR)
MC	Metal-centred
MLCT	Metal-to-ligand charge transfer
MMLCT	Metal-metal-to-ligand charge transfer
Naph	1,8-Naphthalimide
NMR	Nuclear magnetic resonance
OLEDs	Organic light-emitting devices
Ph	Phenyl
ppy	2-phenylpyridine
Py	Pyridyl
s	Singlet (NMR)
S	Spin multiplicity
t	Triplet (NMR)
TEA⁺	Triethylammonium ion
TBA⁺	Tetrabutylammonium ion
Tz	Deprotonated form of the 1-H-tetrazol-5-yl ligand
UV	Ultraviolet
Vis	Visible
VR	Vibrational relaxation

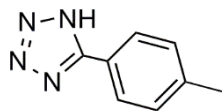
Commonly used abbreviations of compounds



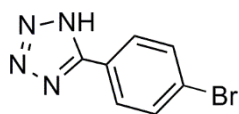
(bpy-PPH₃)²⁺ 2I⁻



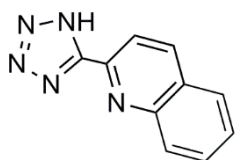
HTzH



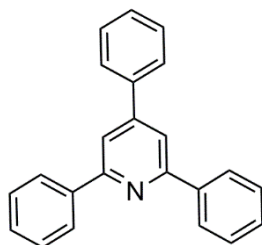
HTzMe



HTzBr



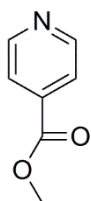
HTzQn



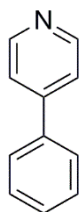
H₂CNC



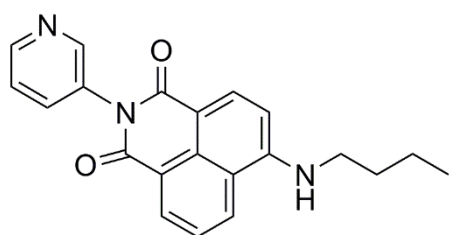
Py-H



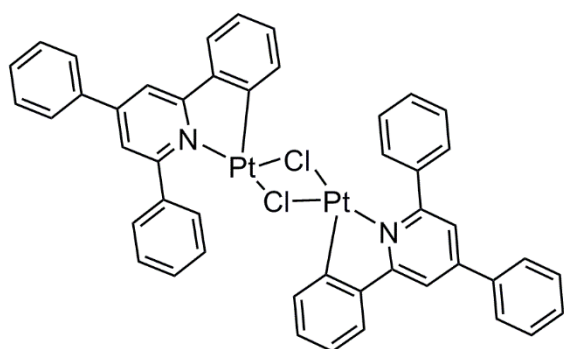
Py-CO₂Me



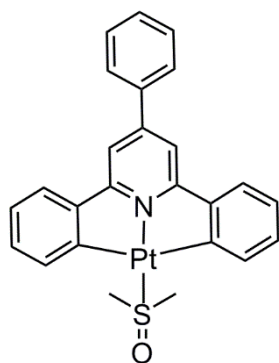
Py-Ph



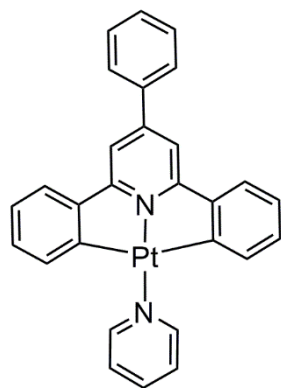
Py-Napht



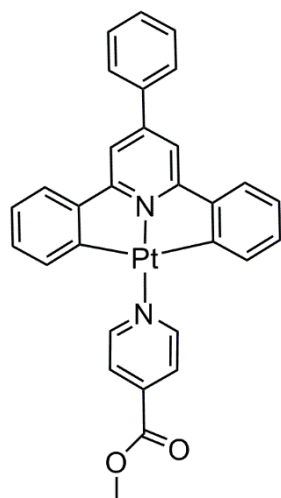
[Pt(CNC)(μ-Cl)]₂



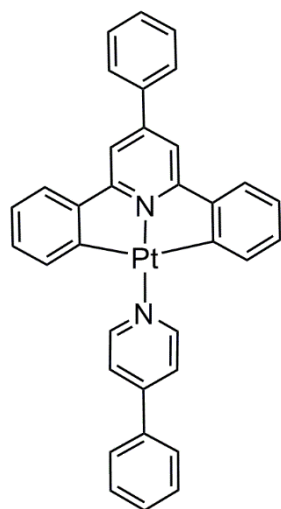
[Pt(CNC)(DMSO)]



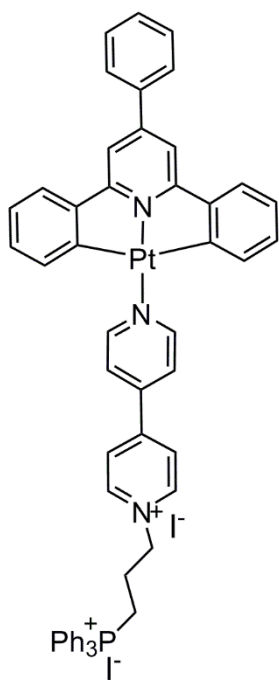
[Pt(CNC)(Py-H)]



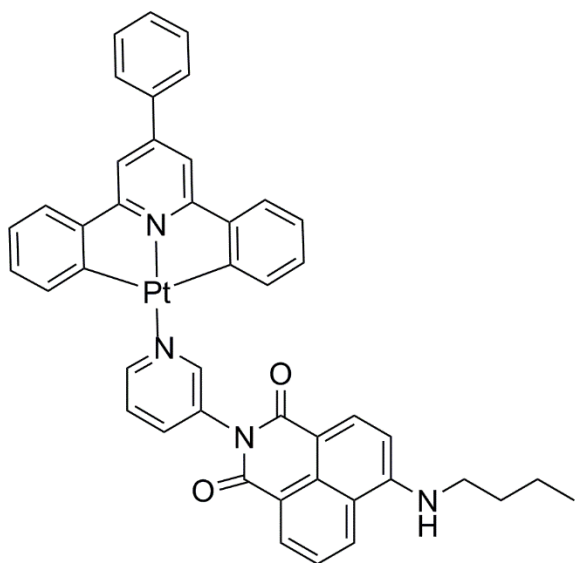
[Pt(CNC)(Py-CO₂Me)]



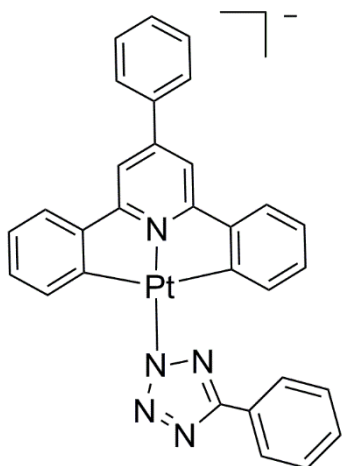
[Pt(CNC)(Py-Ph)]



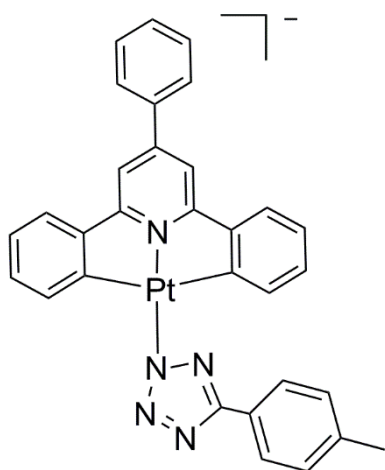
[Pt(CNC)(bpy-PPh₃)²⁺ 2I⁻]



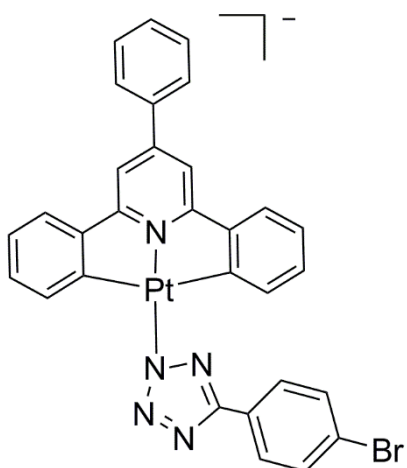
[Pt(CNC)(Py-Napht)]



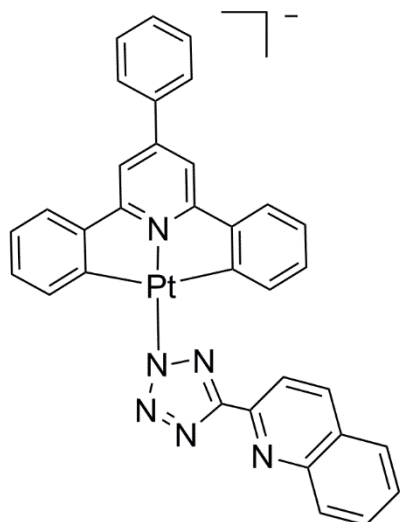
[Pt(CNC)(TzH)]⁻



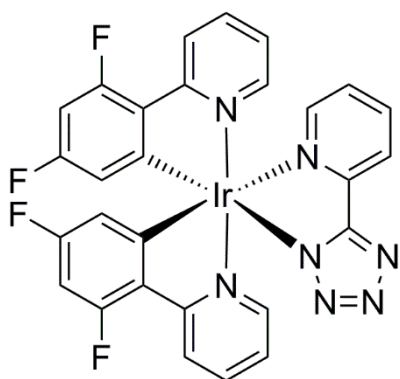
[Pt(CNC)(TzMe)]⁻



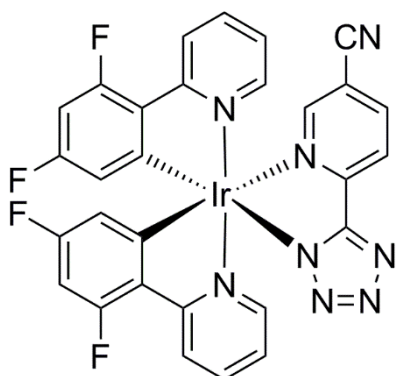
[Pt(CNC)(TzBr)]⁻



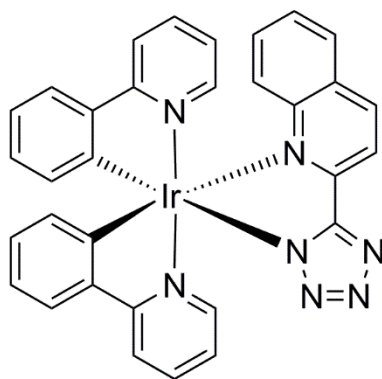
$[\text{Pt}(\text{CNC})(\text{TzQn})]^-$



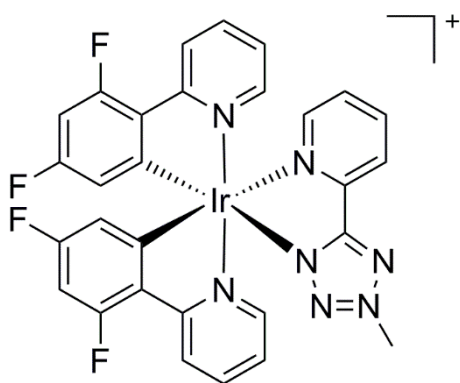
$[\text{Ir}(\text{F}_2\text{ppy})_2(\text{TzPy})]$



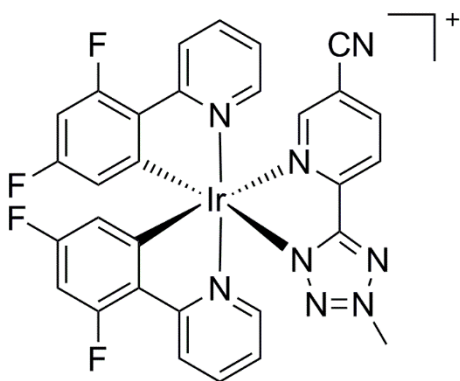
$[\text{Ir}(\text{F}_2\text{ppy})_2(\text{TzPyCN})]$



$[\text{Ir}(\text{ppy})_2(\text{TzQn})]$



$[\text{Ir}(\text{F}_2\text{ppy})_2(\text{TzPy-Me})]^+$



$[\text{Ir}(\text{F}_2\text{ppy})_2(\text{TzPyCN-Me})]^+$

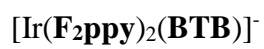
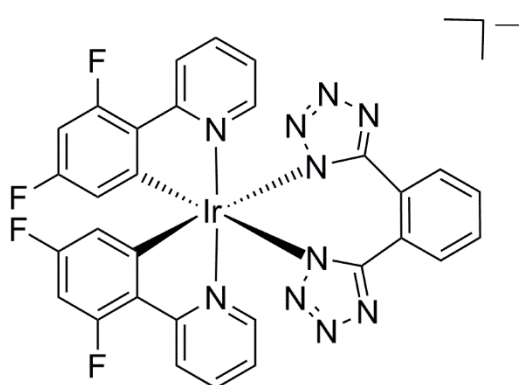
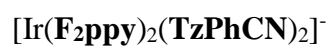
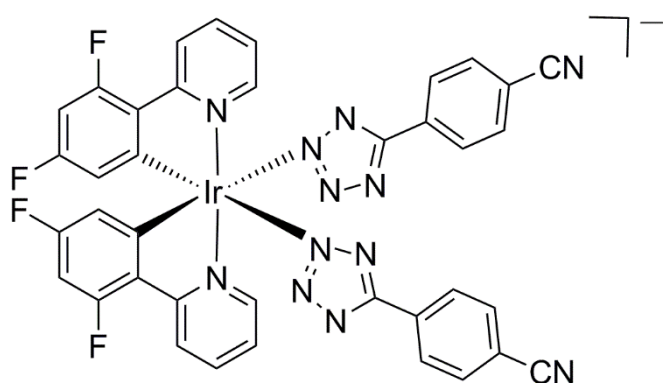
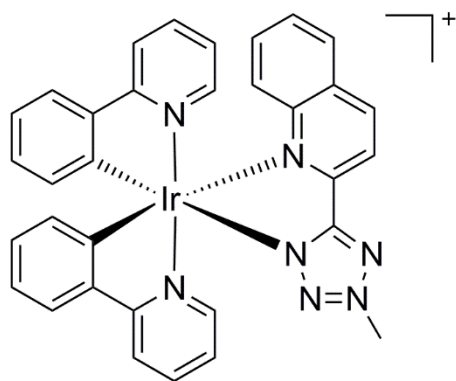


Table of contents

Declaration	i
Abstract	ii
Acknowledgments.....	ix
Dedication	xii
Commonly used abbreviation and symbols	xiii
Commonly used abbreviations of compounds	xv
Table of contents.....	xxiii
Chapter 1	1
1.1 Brief overview of the bacterial cell biology	1
1.1.1 Bacterial cell envelope and extracellular structures.....	1
1.1.2 Intracellular structures	3
1.1.3 Metabolic strategies.....	3
1.2 Acidophilic organisms	5
1.3 Future challenges in prokaryotic cell biology.....	8
1.4 Bacterial imaging.....	10
1.4.1 Fluorescence microscopy.....	10
1.4.2 Challenges in bacterial imaging.....	12
1.4.3 Genetically modified tags	14
1.4.4 Synthetic tags.....	15
1.5 Photophysical properties of d^6 and d^8 transition metal complexes	18
1.5.1 Fundamental concepts.....	18
1.5.2 Selection rules.....	21
1.5.3 Electronic structure and transitions for a d^6 configuration.....	22
1.5.4 Electronic structure and transitions for a d^8 configuration.....	25

1.6	Transition metal complexes in bioimaging	30
1.6.1	Transition metal complexes in cellular and tissue imaging	30
1.6.2	Interaction of transition metal complexes with bacterial species	32
1.7	This investigation and scope	36
Chapter 2	39
2.1	Introduction	39
2.2	Synthesis of the 2,4,6-triphenylpyridine ligand	41
2.3	Synthesis and characterisation of the Pt(II) dichloro-bridged dimer.....	42
2.4	Synthesis and characterisation of the neutral dicyclopalladium(II) platinum(II) complexes	44
2.4.1	Synthesis and characterisation of [Pt(CNC)(DMSO)]	44
2.4.2	Synthesis of neutral Pt(II) complexes with N-donor ligands	46
2.4.3	X-ray crystallography of the neutral Pt(II) complexes.....	48
2.5	Photophysical investigation and aggregation studies	52
2.5.1	Photophysical properties in dimethylsulfoxide	52
2.5.2	Photophysical properties in H ₂ O (0.1% DMSO).....	54
2.5.3	Photophysical properties in the solid state and frozen matrix	59
2.6	Biological investigation of the neutral dicyclopalladium(II) platinum(II) complexes.....	65
2.6.1	Cellular uptake and cytotoxicity studies in eukaryotic cells	65
2.6.2	Cytotoxicity studies on bacterial cells.....	67
2.6.3	Bio-imaging studies	70
2.7	Conclusions	72
2.8	Experimental	74
2.8.1	General synthetic procedures	74
2.8.2	Synthesis	74
2.8.3	Photophysical measurements	81
2.8.4	Cell culture	81

2.8.5	Uptake studies.....	82
2.8.6	Cell viability	82
2.8.7	Confocal microscopy on eukaryotic cells.....	83
2.8.8	Bacterial strains and growth conditions.....	83
2.8.9	Growth curves determination.....	84
2.8.10	Confocal microscopy on bacterial cells	84
Chapter 3	85
3.1	Introduction.....	85
3.2	Synthesis and characterisation	87
3.2.1	Synthesis of N-pyridil-4-butylamino -1,8-naphthalimide.....	87
3.2.2	Synthesis of the platinum(II)-naphthalimide complex [Pt(CNC)(Py-Napht)].....	88
3.3	Photophysical investigation	89
3.3.1	Absorption properties	89
3.3.2	Emission properties in solution and in the solid state.....	90
3.4	Computational investigation.....	94
3.5	Biological investigation	97
3.5.1	Cellular uptake and cytotoxicity studies in eukaryotic cells.....	97
3.5.2	Cellular staining.....	99
3.5.3	Cytotoxicity studies on bacterial cells	101
3.5.4	Bacterial staining and super-resolution Imaging	103
3.5.5	Bacterial imaging with NanoSIMS.....	106
3.6	Conclusion	108
3.7	Experimental.....	110
3.7.1	General synthetic procedures.....	110
3.7.2	Synthesis	110
3.7.3	Photophysical measurements	112
3.7.4	Theoretical calculations	112

3.7.5	Cell Culture	113
3.7.6	Uptake studies	113
3.7.7	Cell viability	114
3.7.8	Confocal microscopy on eukaryotic cells	114
3.7.9	Bacterial strains and growth conditions	114
3.7.10	Growth curves determination	114
3.7.11	Confocal microscopy on bacterial cells	114
3.7.12	NanoSIMS	115
Chapter 4	116
4.1	Introduction	116
4.2	Synthesis and characterization of the anionic platinum complexes. ...	118
4.3	Photophysical properties	122
4.3.1	Absorption properties	122
4.3.2	Emission properties in solution	124
4.3.3	Emission properties in solid state and frozen matrix	126
4.4	Electrochemical measurements	129
4.5	Photoredox catalysis	131
4.6	Conclusions	135
4.7	Experimental	136
4.7.1	General synthetic procedures	136
4.7.2	Photophysical measurements	139
4.7.3	Photoredox-catalyzed reactions	140
Chapter 5	143
5.1	Introduction	143
5.2	Interaction of live <i>Bacillus cereus</i> with neutral iridium(III) tetrazolato complexes.....	145
5.2.1	Photophysical properties and toxicity	145
5.2.2	Confocal imaging	147

5.3	Confocal Raman imaging of lipid inclusions in live <i>Bacillus cereus</i> .	150
5.4	Interaction of live <i>Bacillus cereus</i> with cationic iridium(III) tetrazolato complexes	152
5.4.1	Photophysical properties and toxicity	152
5.4.2	Confocal imaging.....	154
5.5	Conclusion	157
5.6	Experimental.....	158
5.6.1	Photophysical measurements	158
5.6.2	Bacterial strains and growth conditions	158
5.6.3	Growth curves determination.....	158
5.6.4	Confocal microscopy	158
5.6.5	Raman imaging	159
Chapter 6	160
6.1	Introduction.....	160
6.2	Photophysical properties at low pH.....	165
6.3	Imaging of <i>At. ferrooxidans</i> with MitoTracker Red and SYTO 9	168
6.3.1	Incubation test with MitoTracker Red	168
6.3.2	Incubation tests with SYTO 9.....	169
6.4	Imaging of <i>At. ferrooxidans</i> with transition metal complexes.....	171
6.5	Conclusion	173
6.6	Experimental.....	175
6.6.1	Photophysical properties.....	175
6.6.2	Bacterial strain and growth conditions	175
6.6.3	Confocal microscopy	175

Chapter 7	177
References	186
Appendix A	206
Appendix B	220
Appendix C	224
Appendix D	233
Appendix E	234
Appendix F	237

Chapter 1

Introduction

1.1 Brief overview of bacterial cell biology

1.1.1 Bacterial cell envelope and extracellular structures

Bacteria were amongst the first life forms to appear on earth, and they thrive in different habitats. Indeed, they are present in water, soil, in the deep portion of the earth's crust as well as in radioactive waste.^{1,2} Bacteria can be found in plants and animals, as naturally occurring species or as parasites. Bacteria are prokaryotic microorganisms. Prokaryotes are unicellular organisms that lack a membrane-bound nucleus as well as any other membrane-bound organelle, such as mitochondria. Bacteria are differentiated in terms of cell morphology, ranging from rods (bacilli), spheres (cocci), spiral shape or filamentous, and they are typically 0.5-5 μm in length. The bacterial cell envelope is constituted by the inner cell membrane, primarily made of phospholipids, and the bacterial cell wall, whose main constituent is peptidoglycan (**Figure 1.1**).^{3,4} In general, there are two different kinds of cell wall, which define the division of bacteria in two major groups: gram-positive bacteria and gram-negative bacteria. Gram-positive bacteria (i.e. *Bacillus cereus*, *Clostridium botulinum*), possess a thick cell wall consisting of many layers of peptidoglycan and teichoic acids. On the other side, gram-negative bacteria (i.e. *Escherichia coli*, *Pseudomonas aeruginosa*) have a relatively thin cell wall, with few layers of peptidoglycan, that is surrounded by a second lipid membrane, consisting of lipopolysaccharides and lipoproteins.³ This complex and sophisticated multilayered system protects bacteria from an often hostile environment, while allowing passage of nutrients and waste products through the membrane. The structural differences between gram-positive and gram-negative bacteria is often responsible for different protective and adaptive strategies that the two groups adopt in different environments.

For example, it is generally true that gram-negative bacteria are more resistant to antibiotics than gram-positive bacteria, and this improved resistance is often ascribed to the presence of an extra lipid membrane surrounding the peptidoglycan layer.^{3,4}

The external side of the bacterial cell envelope extends to different extracellular structures, such as fimbriae, pili and flagella. These appendages protrude from the bacterial cell wall and are responsible for bacterial motility, gripping and attachment to surfaces as well as acting as sensory organelles towards chemicals and temperature outside the cell.¹

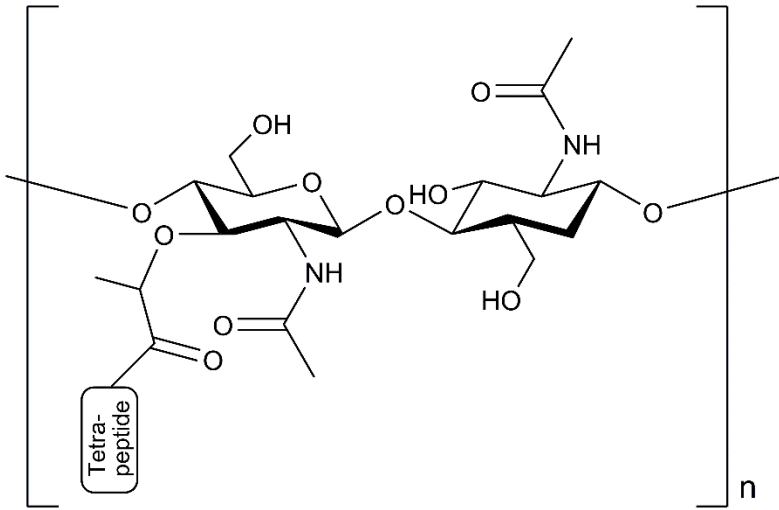


Figure 1.1 Structure of peptidoglycan

1.1.2 Intracellular structures

The inner cell membrane contains the bacterial cytoplasm. Despite not possessing the cellular compartmentalisation of eukaryotic species, bacterial cells are endowed with a rich sub-cellular architecture. The bacterial DNA is located in the cytoplasmic region. An irregularly shaped body, named nucleoid, contains the bacterial single chromosome together with RNA and its associated proteins. Bacteria also contain DNA plasmids and ribosomes.¹ Besides these essential components, bacteria possess a wide range of nutrient storage structures, to compensate the lack of nutrients that the cell can be exposed to under stress conditions. For example, soluble nitrates are commonly stored in vacuoles, whereas excess carbon is stored in polyhydroxyalkanoates or glycogen inclusions. Gas vacuoles and other microcompartments, mainly rich in proteins, are found in different bacterial species and they play different roles in regulatory mechanisms.^{1,5} A complex system of structural filaments is also present in prokaryotes, constituting the bacterial cytoskeleton. Cytoskeletal elements regulate different processes including cell division and shape determination.^{1,6}

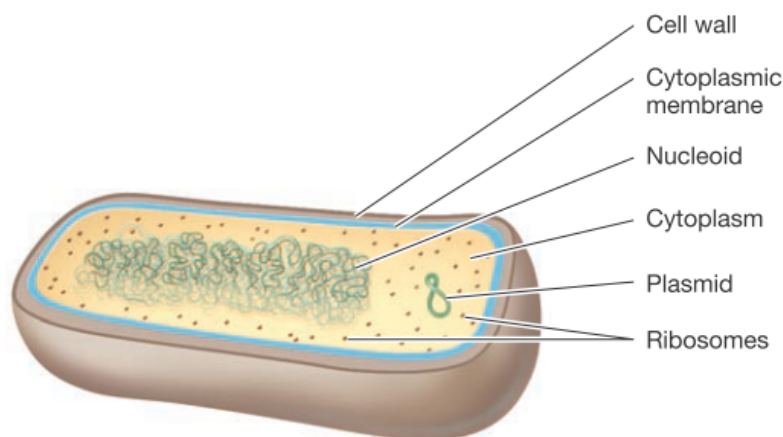


Figure 1.2 Diagram of prokaryotic cell. Image reproduced with permission from ref¹

1.1.3 Metabolic strategies

Bacterial metabolism can be classified based on how the organism obtains carbon, energy and reducing equivalents for energy preservation.¹ Bacteria can obtain carbon, which is then used for cell mass synthesis, from CO₂ fixation (autotrophic organisms), from organic compounds (heterotrophic organisms), or from both sources

(mixotrophic organisms). The energy that is necessary for living and growing can be obtained from external chemical compounds (chemotrophic organisms) or from light (phototrophic organisms). Moreover, reducing equivalents can be obtained from inorganic compounds (lithotrophic organisms) or organic compounds (organotrophic organisms).¹ Importantly, most bacteria thrive in moderate environments in terms of external temperature and pH. As such, they are classified as mesophiles and neutrophiles.¹ The term mesophile defines organisms that grow best in moderate temperatures, ranging from 20°C to 45°C. The term neutrophile refers instead to organisms that require a neutral pH, ranging between 5.5 and 7.9. On the other hand, organisms that thrive in extreme conditions and environments are known as extremophiles.¹

1.2 Acidophilic organisms

Acidophilic organisms are extremophilic organisms that have a pH optimum for growth lower than pH 3.^{1,7} Acidophilic bacteria are found in natural and anthropogenic systems, such as deep-sea hydrothermal vents or extremely acidic sites linked to mining of metals and coal. One of the archetypal acidophile species, *Acidihalobacter prosperus*, (**Figure 1.3**) was firstly isolated from a marine geothermal field at the beach of Porto di Levante (Vulcano, Italy),^{8,9} whereas other species such as *Acidithiobacillus ferrooxidans* and *Leptospirillum ferriphilum* are abundant in natural environments associated with pyritic ore bodies, coal deposits and their acidified drainages.¹⁰ In general, acidophiles are mixotrophic, chemotrophic and lithotrophic organisms (Section 1.1.3). Importantly, they are iron and/or sulfur oxidising bacteria and as such, they can accelerate the oxidative dissolution of sulfide minerals. This process, known as bioleaching, has been harnessed in the biomining industry to promote the extraction of metals from sulfur or iron containing ores, and acidophilic bacteria currently find application in the recovery of copper, gold and uranium from low-grade ores.¹⁰ Besides their important bio-technological application acidophiles may have an important evolutionary role, as they may be representative of archaic life forms in the early life of our planet, where extreme environments were far more widespread.^{7,11}

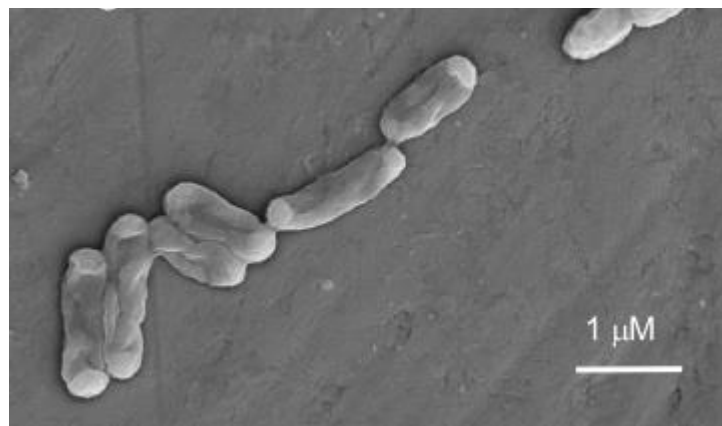


Figure 1.3 TEM image of *Acidihalobacter prosperus*. Image courtesy of Kieran Mulronev.

While growing at pH 1-2, acidophiles maintain a circumneutral intracellular pH that is necessary for the normal cellular function of protein, enzymes and nucleic acids. Hence, these species have to tolerate a pH gradient of around 6 order of magnitude across the membrane and oppose the otherwise natural influx of protons from the outer side to the inner side of the membrane. pH homeostasis in acidophiles remains poorly understood. Baker-Austin and Dopson (2007) described in detail the most recent insights regarding pH homeostatic mechanisms in acidophiles, describing the different mechanisms that these bacteria seem to adopt to cope in such extreme environments (**Figure 1.4**).⁷ Besides having a thick and highly impermeable cell membrane to restrict the inward flow of protons, the membrane channels have an extremely reduced pore size and are endowed with proton export systems such as efflux pumps and secondary transporters, that can efficiently pump excess protons outside the cell. An essential homeostatic mechanism in acidophiles is the generation of a positive membrane potential. This is opposite to what is observed in neutrophilic species, and acidophiles generate and maintain an overall positive charge along the inner side of the membrane, and a negative charge on the outer side. This generates a chemiosmotic barrier that inhibits the influx of protons.⁷

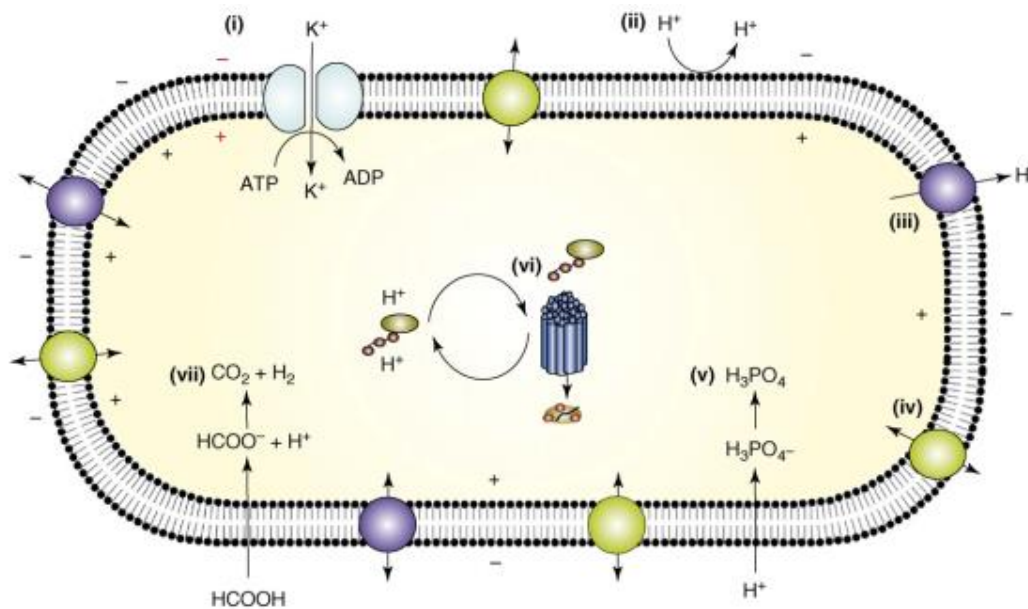


Figure 1.4 Schematic representation of pH homeostasis in acidophiles and different strategies to oppose to the influx of protons. (i) Reverse membrane potential (ii) Highly impermeable cell membrane. (iii) Proton efflux pumps. (iv) Secondary transporters. (v) and (vii) Buffering systems and organic acid degradation systems. (vi) DNA and protein repair systems. Image reproduced with permission from ref ⁷.

Moreover, a range of intracellular buffering systems, proton uncoupling and organic acid degradation mechanisms are present to maintain a neutral intracellular pH, in case protons manage to cross the cytoplasmatic membrane.⁷ Biomolecules that are damaged due to low pH, such as proteinaceous substrates or nucleic acids undergo prompt repairation *via* DNA and protein repair systems (**Figure 1.4**).

1.3 Future challenges in prokaryotic cell biology

The past decades have witnessed a considerable advance in our understanding of prokaryotic cell biology. Technical advances in genomics and proteomics, together with the advent of more sophisticated imaging techniques allowed microbiologists, biologists, pathologists and doctors to characterise the bacterial cell, uncovering new sub-cellular structures and investigating their specific functions.^{1,12} Despite this progress and the apparent simplicity of prokaryotic organisms, the mechanisms underpinning many microbiological processes are yet to be delineated. Bacterial infections remain one of the pressing concerns for the wellbeing of our society,^{13,14} and a deeper understanding of the pathogen biology as well as the complex host-pathogen interaction are required to provide improved antibacterial treatments. Besides the medical context, the bio-technological application of bacterial species in different industrial settings is attracting increasing research and commercial interest. For example, bacteria are emerging as alternative sources for lipids that can be used for food, fuel and chemical production^{15–20} and for biopolymers such as polylactic acids and polyhydroxyalkanoates.^{5,21,22}

In this context, increasing research on new cultivation systems and innovative strategies to improve the productivity has prompted the need to shed light on the molecular mechanisms involved in bacterial production, trafficking and storage of nutrients and lipids. In the field of biomining, the bacterial metabolic activity of acidophilic species is utilised for the mobilisation and recovery of metals from low-grade ores.^{10,23} A better understanding of the complex microbiology of acidophilic organisms, especially related to pH homeostasis is essential to control the growth and leaching capability of these organisms. Considering the different scenarios described in this section, a common, major challenge in prokaryotic cell biology will be to further define the genotype-phenotype relationship. This will allow to unravel the key function of many proteins and enzymes, to understand how the complex membrane systems are assembled and regulated, and how different species respond to stress and interact with the external environment. Yao and Carballido-López state in their review¹² that to do this, “*it is imperative to characterize where, when, and how molecular events take place in the cell*”, to complement the information obtained with genetic studies. Light and electronic microscopies allow the study of single cells with high spatial and

temporal resolution. For these reasons, a wide range of imaging platforms including Transmission Electron Microscopy (TEM), Scanning Electron Microscopy (SEM) and different Light Microscopy (LM) techniques have been exploited in the past decade to image bacteria *in vivo* and *in vitro*. In this chapter, the application of optical imaging on bacteria will be discussed, with emphasis on fluorescence imaging and the different approaches that have been developed to exploit this technique in the study of prokaryotic microorganisms.

1.4 Bacterial imaging

1.4.1 Fluorescence microscopy

Fluorescent optical imaging is based on the detection of emitted light, in the form of bioluminescence or fluorescence coming from a tag. The signal detected is then used to create a contrast image that enables the visualisation of a target molecule or cell at resolution that depends on the instrument used for the experiment. In this section, a brief overview of the microscopy techniques used to image bacteria, their main advantages and limitation will be discussed.

Wide-field epifluorescence microscopy

Conventional wide-field epifluorescence microscopy is the most commonly used technique to image bacteria.^{12,24} The term “epifluorescence” finds its roots in the ancient Greek language, where “epi” (επι) means “upon”. With an epifluorescence microscope, the light source excites the entire sample present in the optical path of the incident light and the emission (fluorescence) is detected throughout the sample in an unfocused manner. The light sources commonly used are normally xenon or mercury lamps, that are able to provide high-intensity illumination covering the entire visible spectrum. The different excitation and emission wavelength are then selected with the use of appropriate filters. Epifluorescence systems are relatively inexpensive and easy to use, therefore this technique is routinely used in many laboratories, despite providing poor contrast due to the fact that fluorescence is also detected from above and below the focal plane, hence increasing the signal to noise ratio.¹²

Laser scanning confocal microscopy

With confocal laser scanning microscopy, only the in-focus signal is collected. When scanning across the sample, a laser beam passes through a small aperture and is then focused into a small focal volume by an objective lens. Importantly, a pinhole is placed in front of the detector to keep only the in-focus signal and lowering the signal to noise ratio. While providing improved contrast and the possibility to perform optical sectioning of the sample, the main limitation of confocal microscope is that most of the light is blocked by the pinhole, resulting in weaker signals. Importantly, compared to epifluorescence microscopy, the equipment is generally more expensive and the scanning process is significantly slower. Moreover, improved resolution can be

obtained for samples that are thicker than the focal plane (around 0.5 μM).^{12,24} For both epifluorescence microscopy and confocal microscopy, the signal-to-noise ratio can be significantly improved using deconvolution, which removes the blurring originated from out-of-focus signal with mathematical methods.^{12,24}

Superresolution microscopies

Spatial resolution in optical microscopes is limited by the wavelength of light. According to the Abbe diffraction limit the lateral resolution (i.e. along the x,y axis) and the axial resolution (i.e. along the z axis) can be estimated considering the wavelength of the incident light, λ , and the numerical aperture of the objective, NA. The lateral resolution of conventional microscopes is estimated to be around 200-300 nm (λ/NA), whereas the axial resolution is in the 500-700 nm range ($2\lambda/\text{NA}^2$).¹² This is due to the fact that every point source of light emits a 3-D diffraction pattern, that is technically named point-spread function and that can be explained via complex mathematical functions.¹² The practical result of this phenomenon is that any object whose size is below the resolution limit of the instrument, will show up as blurred and two separate objects that are within a distance that is smaller than the resolution limit will not show up as separated.¹² Superresolution techniques are able to break the diffraction limit, pushing the resolution down to 10-50 nm. In the past decades, a variety of superresolution techniques have been developed, based on different approaches.^{24,25}

The most used setups to date are Structured Illumination Microscopy (SIM – lateral resolution 45-62 nm), Stimulated Emission Depletion (STED – lateral resolution around 50 nm), Photo-Activated Localization Microscopy (PALM – lateral resolution around 20 nm) or Stochastic Optical Reconstruction Microscopy (STORM – lateral resolution around 20 nm).

All these techniques present advantages and limitations in terms of setup complexity, acquisition time and data processing, as well as capability of performing imaging in live or fixed samples. Importantly, the different techniques have different fluorophore requirements. In brief, PALM and STORM are based on the phenomena of photoactivation and photoswitching, therefore their use is limited to fluorophores that possess appropriate photophysical properties. STED microscopy excites the fluorophore in use with a laser, to then selectively switch off a portion of the signal with another, independent laser (depletion). Hence, only fluorophores that can be

excited and depleted by separate lasers can be used. On the other hand, the achievement of improved resolution with SIM is achieved with illumination patterns and image processing, hence it is independent of the fluorophore, allowing more flexibility.

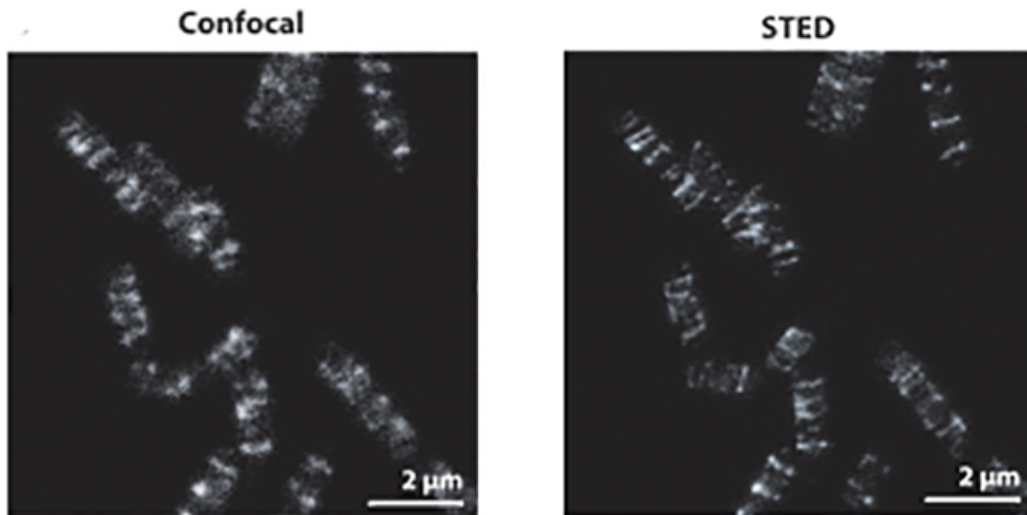


Figure 1.5 Comparison of confocal (left) and STED (right) of the same *Bacillus subtilis* samples expressing a GFP-tagged protein. Reproduced with permission from ref.¹²

1.4.2 Challenges in bacterial imaging

Performing imaging on bacterial cells does present additional challenges in comparison to eukaryotic systems. First, live bacteria are motile and about one-tenth in size in comparison to common mammalian cells (**Figure 1.6**). Indeed, averaging 1-5 µm in length and around 0.5 µm, bacterial cells have a size that is close or inferior to the resolution limit of traditional microscopes (Section 1.4.1). It is possible to image a bacterial cell with epifluorescence and confocal laser scanning microscopy, to a satisfactory level of contrast and resolution that often even enables the visualisation of sub-structures within the cytoplasmic region. However, it is necessary to resort to superresolution techniques to clearly resolve cellular substructures such as proteins or nucleic acids with nanometer precision and in the past decade, superresolution microscopy has been extensively applied to image bacterial specimen.^{12,24-26} The vast majority of fluorescence imaging on bacteria is based on the detection of non-

12

endogenous fluorescence, hence relying on the use of fluorescent tags. Most of the imaging studies on bacteria have used genetically encoded proteins. An alternative approach relies on the use of synthetic small-molecule probes. Both these approaches will be discussed in the next sections. Moreover, it is important to discuss how the main challenge in bacterial imaging is the extremely robust cell envelope of these microorganisms. Indeed, the thick and resistant cell wall that bacteria are endowed with, inhibits the uptake of the vast majority of the reported small-molecule probes.²⁶ Due to this, a large number of synthetic tags that have been reported to label live bacteria have been mainly used to stain the cell surface or extracellular components.

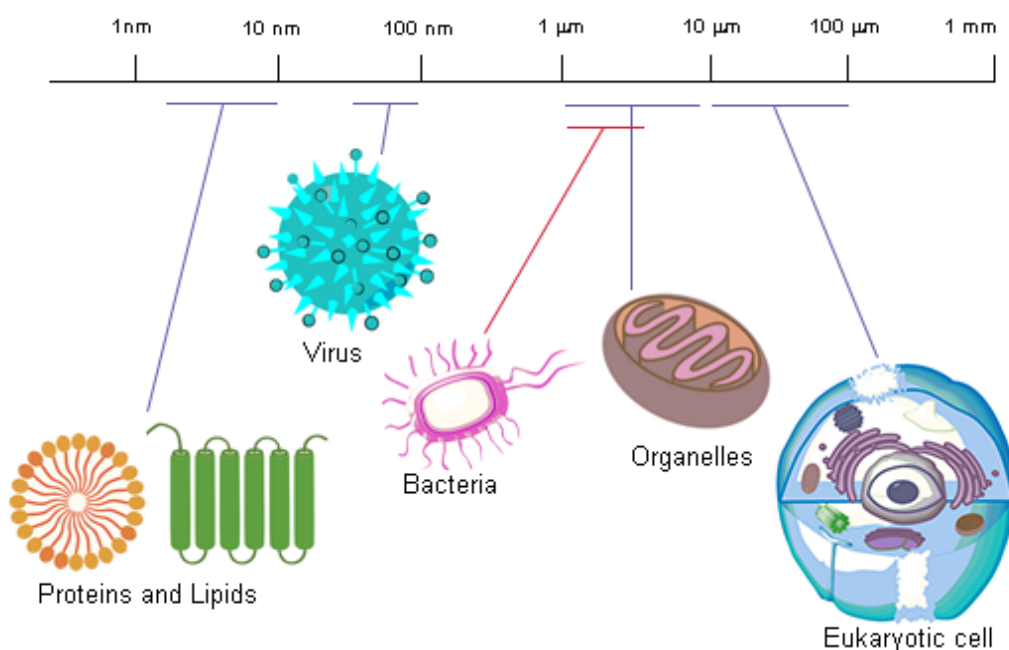


Figure 1.6 Schematic size comparison between bacteria, eukaryotic cells and subcellular components such as proteins and lipids.

1.4.3 Genetically modified tags

Bacteria can be engineered to express fluorescent proteins. In this technique, a fluorescent protein is designed and then fused with a protein of interest. The genetically modified bacteria will then express the fluorescent protein, enabling the visualisation of its localisation and dynamics (**Figure 1.7**).^{12,26,27} The use of this kind of genetically encoded tags in bioimaging is based on a naturally chemiluminescent protein, the green fluorescent protein (GFP)²⁸, that was firstly discovered and isolated by the organic chemist and marine biologist Osamu Shimomura, in 1962.²⁹ This relatively small protein exhibits green fluorescence if excited with UV or blue wavelengths. Since its isolation and purification, a broad variety of GFP analogues have been developed, with emission wavelengths that cover the entire visible spectrum.³⁰ While representing the most commonly used approach in bacterial imaging, fluorescent proteins present several disadvantages. First, they are not suitable to image non proteinaceous substrates such as peptidoglycan, lipids, nucleic acids and other metabolites. Moreover, it has been proven that the use of this genetically encoded tags can alter the function of the targeted protein, besides affecting its localisation, hence leading to mislocalizations and artefacts in the imaging experiments.

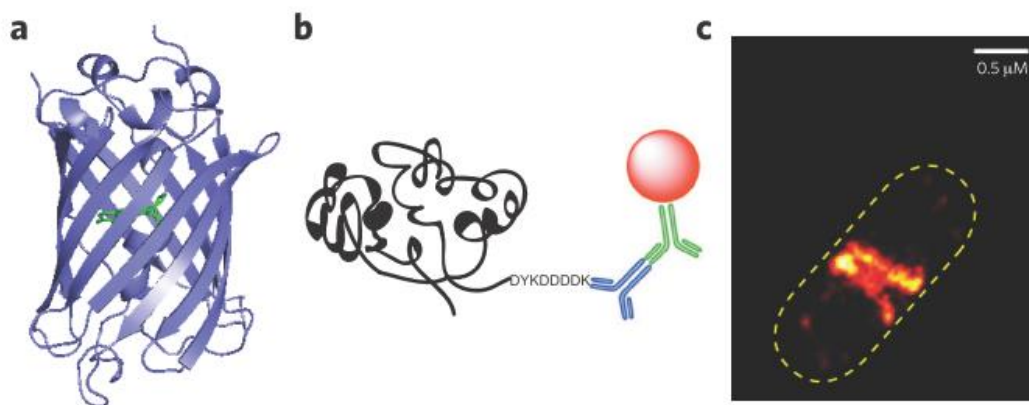


Figure 1.7 a. Sample structure of GFP. b. Schematic representation of the tagging process. c. *E. coli* expressing a fluorescent protein imaged with PALM. Image reproduced with permission of ref.²⁶

1.4.4 Synthetic tags

Commercial dyes such as SYTO 9™ and Propidium Iodide (PI) are routinely used to stain bacteria. Commonly commercialised in LIVE/DEAD kits, they are used to discriminate live and dead populations of bacterial cells with fluorescence microscopy and more importantly with Flow Cytometry. While being able to stain DNA, PI is not able to cross the cell membrane of live bacteria, therefore it can only be used to stain non-viable bacterial samples. The structure of SYTO 9™ has not been yet disclosed, however it is known to be a rhodamine derivative with high affinity for DNA and RNA.³¹ Due to its remarkable permeability properties, this green fluorescent dye can cross the membrane of live species and hence it is used as a nucleic acid stain for live bacterial cultures. In the past decades, an increasing research effort has focused on the synthesis of new dyes to label bacteria and a wide range of fluorophores has been reported. Amongst the different design strategies that have been extensively reviewed by Kocaoglu and Carlson²⁶, one straightforward approach to stain bacteria is to functionalise known antibiotic scaffolds that are able to target the cell wall. An example of fluorescent BODIPY-conjugated penicillin is depicted in **Figure 1.8**, top^{26,32,33}. In this system, while the BODIPY unit provides bright fluorescence, the penicillin scaffold binds to membrane proteins called penicillin binding proteins, hence targeting the cell membrane. Similarly, clinically used antibiotics such as oxazolidinone derivatives can be functionalised with a fluorophore and used to target live bacterial cells (**Figure 1.8**, bottom).³⁴ Following this approach, a wide range of peptidoglycan-inspired chemical probes have been reported,³⁵⁻³⁷ together with carbohydrate derivatives to stain extracellular components.³⁸⁻⁴⁰ Smith *et al* have expanded the library of bacterial imaging agents based on BODIPY scaffolds, reporting BODIPY conjugates appended with Zn(II)-dipicolylamine ligands.^{41,42} This ligand has shown good suitability to target the bacterial cell surface, and it has been exploited by the same group to functionalise different fluorophores used to target and monitor bacterial infections in living mice.^{43,44} Recently, an aggregation induced emission fluorophore, 4,4'-(1,2-diphenylethene-1,2-diyl)bis(4,1-phenylene)diboronic acid as well as its functionalised versions have been reported for bacterial imaging as well as for bacterial viability determination and bacterial killing⁴⁵⁻⁴⁷ (**Figure 1.9**).

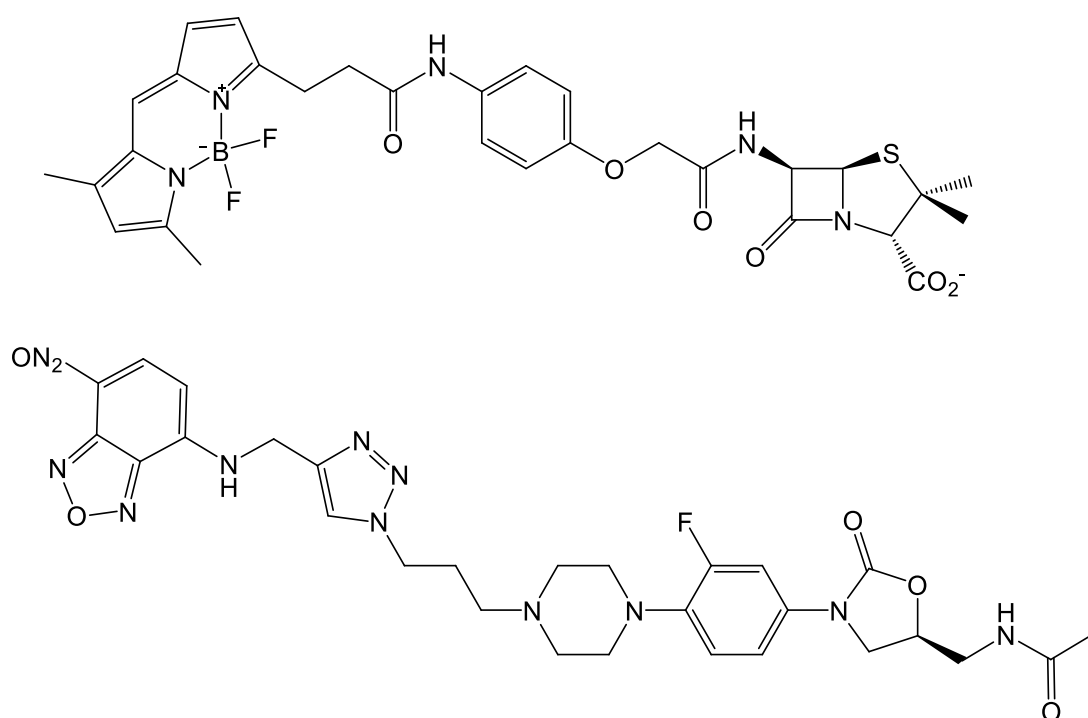


Figure 1.8 Top: BODIPY-conjugated penicillin probe. Bottom: oxazolidinone antibiotic fluorescent derivative.

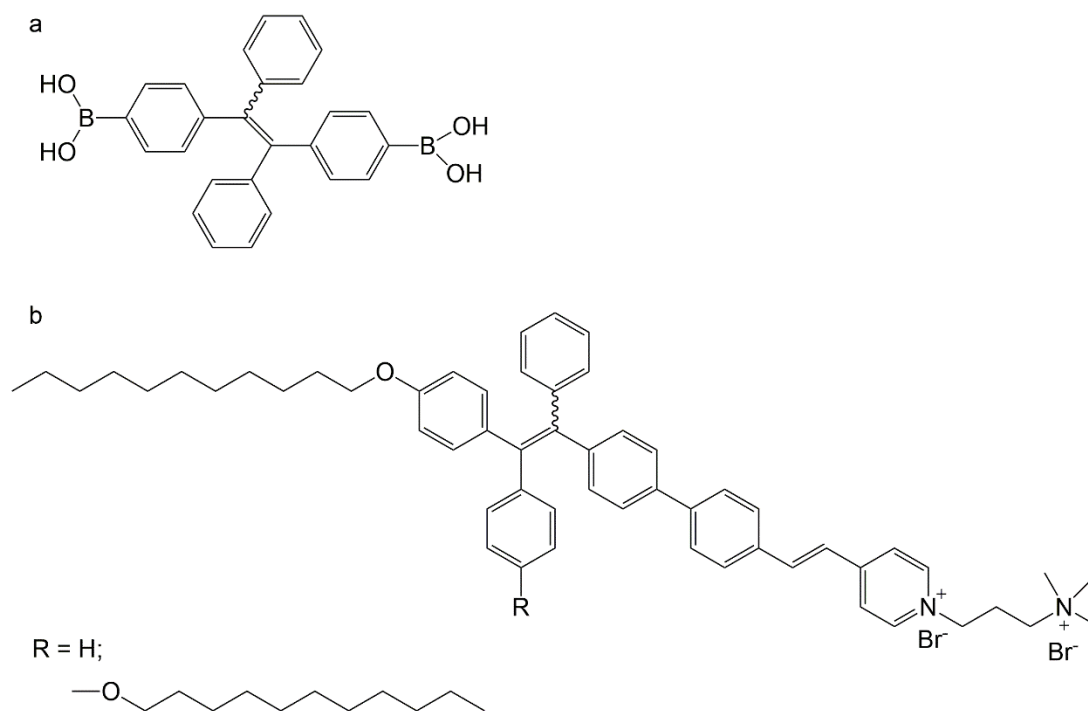


Figure 1.9 a: chemical formula of the 4,4'-(1,2-diphenylethene-1,2-diyl)bis(4,1-phenylene)diboric acid reported in ref⁴⁵. b: functionalised derivatives from ref^{46,47}.

Different bacteria-tracking systems have been designed functionalising a wide range of nanoparticles or composite materials with surface-targeting units. These bio-

functionalised nanoparticles have been exploited to target, label and in some cases kill antibiotic-resistant bacteria, however similarly to the most of the dyes previously discussed, they did not show ability to cross the bacterial cell wall.^{14,48,49}

1.5 Photophysical properties of d⁶ and d⁸ transition metal complexes

1.5.1 Fundamental concepts

Photophysical processes arise from the interaction of a molecule with light. The absorption of light by a molecule in a dilute solution is described by the Beer–Lambert–Bouguer law (Equation 1.1)

$$I = I_0 \times 10^{\varepsilon bc} \quad (1.1)$$

where I is the intensity of the transmitted light at a given wavelength, I_0 is the intensity of the incident radiation at the same given wavelength), ε is the molar absorptivity coefficient, b is the optical path, and c is the concentration of the solution. The molar absorptivity coefficient, ε , is an indication of the capability of a compound to absorb a given wavelength of light. The absorption of light at an appropriate wavelength promotes the compound to an electronically excited state, which can then undergo chemical reaction or return to the ground state via radiative and non-radiative decay pathways. Absorption (excitation), radiative and non-radiative decay mechanisms are illustrated in a simplified version of the Jablonski diagram depicted in **Figure 1.10**.

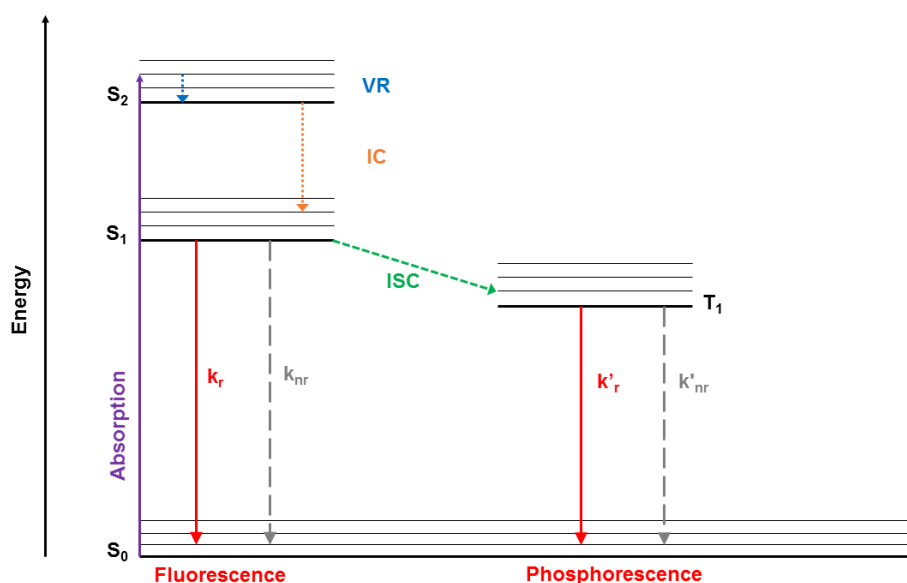


Figure 1.10 Simplified Jablonski diagram illustrating Absorption, radiative and non-radiative pathways.

In the diagram, the singlet ground state is labelled as S_0 , whereas the first two singlet electronically excited states are S_1 and S_2 . The first triplet excited state is named as T_1 . When populating each of these electronic states, a molecule can exist in many vibrational levels. Upon excitation (i.e. photon absorption), a molecule is likely to be in an upper vibrational level of a given electronically excited state, as described by the Franck-Condon principle. In this scenario, the most favoured process is vibrational relaxation (VR).⁵⁰ During vibrational relaxation, the vibrational energy gained during the transition to the excited state is redistributed, and the molecule moves down to the lowest vibrational level of that excited state. Besides this intra-state vibrational decay process, non-radiative decays can occur between two different electronically excited states. A transition that involves two excited states of the same spin multiplicity (i.e. S_1 and S_0) is defined as internal conversion (IC).^{50,51} On the other hand, a transition between two excited states of different spin multiplicity (i.e. T_1 and S_0) is known as inter-system crossing (ISC). ISC is considered a spin-forbidden transition, as it violates the spin selection rule.^{50,51} In the presence of heavy atoms however, spin-orbit coupling is promoted with a consequent relaxation of the spin selection rule, hence the transition becomes partially allowed.

The non-radiative decay between the excited state and the ground state is regulated by the overlapping of the lowest vibrational level of the excited state with the vibrational levels of the ground state. The overlapping of these levels depends on the energy gap between the ground state and excited state. The energy gap law, shown in **Equation 1.2**, describes the relationship between the rate of the non-radiative decay (k_{nr}) and the energy gap between the two states (ΔE).

$$k_{nr} = A e^{-\alpha \Delta E} \quad (1.2)$$

In this equation, A is a pre-exponent coefficient, whereas α is a proportionality constant. According to the energy gap law, the larger the energy gap between two states, the slower the non-radiative decay rate.⁵²

Besides non-radiative decay pathways, an excited state can also return to the ground state by the spontaneous emission of a photon. This process is named radiative decay, and the spontaneous emission of a photon is commonly defined as luminescence. Transitions occurring between two states of the same multiplicity are termed *fluorescence*. If a change of multiplicity takes place, the transition is defined as *phosphorescence*.^{50,51}

The rate of the radiative decay process is commonly defined by the radiative decay constants k_r . Overall, the decay rate of an excited state takes into account both k_r and k_{nr} , and the excited state lifetime (τ) is defined as the inverse of their sum (**Equation 1.3**)

$$\tau = \frac{1}{k_{nr} + k_r} \quad (1.3)$$

A proportion of the radiative decay to the overall decay from an excited state is instead given by the quantum yield (Φ), as per **Equation 1.4**.

$$\phi = \frac{k_r}{k_{nr} + k_r} \quad (1.4)$$

From a conceptual point of view, the quantum yield defines the ratio of emitted photons to absorbed photons. Together with the excited state lifetime, the quantum yield is exploited to describe k_{nr} and k_r . Indeed, rearranging the equations illustrated above, **Equation 1.5** and **Equation 1.6** can be obtained to define k_{nr} and k_r , respectively.

$$k_r = \frac{\phi}{\tau} \quad (1.5) \quad k_{nr} = \frac{1-\phi}{\tau} \quad (1.6)$$

1.5.2 Selection rules

An electronic transition is considered allowed or forbidden based on selection rules. These rules define the probability of a transition to occur based on overlap, multiplicity of ground and excited state, as well as electronic wavefunction symmetry. In this paragraph, the Laporte selection rule and the spin conservation rule are defined.

Laporte selection rule

In centrosymmetric molecules, a transition is forbidden if it occurs between states with the same parity (gerade, *g* or ungerade, *u*). A relaxation to this rule is allowed by a process named *vibronic coupling*, due to which the centre of inversion of the molecule is removed thanks to asymmetric vibrations of the latter. Due to this, forbidden transition can be observed, as in the case of d-d transitions in octahedral metal complexes.

Spin conservation rule

According to the spin conservation rule, an electronic transition is forbidden if it occurs between states of different spin multiplicity (*S*). Hence, considering the overall spin variation ΔS , if $\Delta S = 0$ the transition is allowed, and if $\Delta S \neq 0$ the transition is forbidden. Therefore, singlet ($S = 0$) to singlet transitions will be allowed, whereas triplet ($S = 1$) to singlet transition are spin-forbidden. The presence of heavy atoms such as transition metal ions, however, increases the probability of spin-forbidden transitions by mixing the two states with different multiplicity, due to spin-orbit coupling.

1.5.3 Electronic structure and transitions for a d^6 configuration

To better understand the photophysical properties of transition metal complexes, it is necessary to describe the nature of the electronic transitions that can take place upon their interaction with light. This can be done by examining the electronic structure of the complex. A low spin d^6 transition metal complex will typically adopt the electronic configuration illustrated in the molecular orbital diagram shown in **Figure 1.11**.

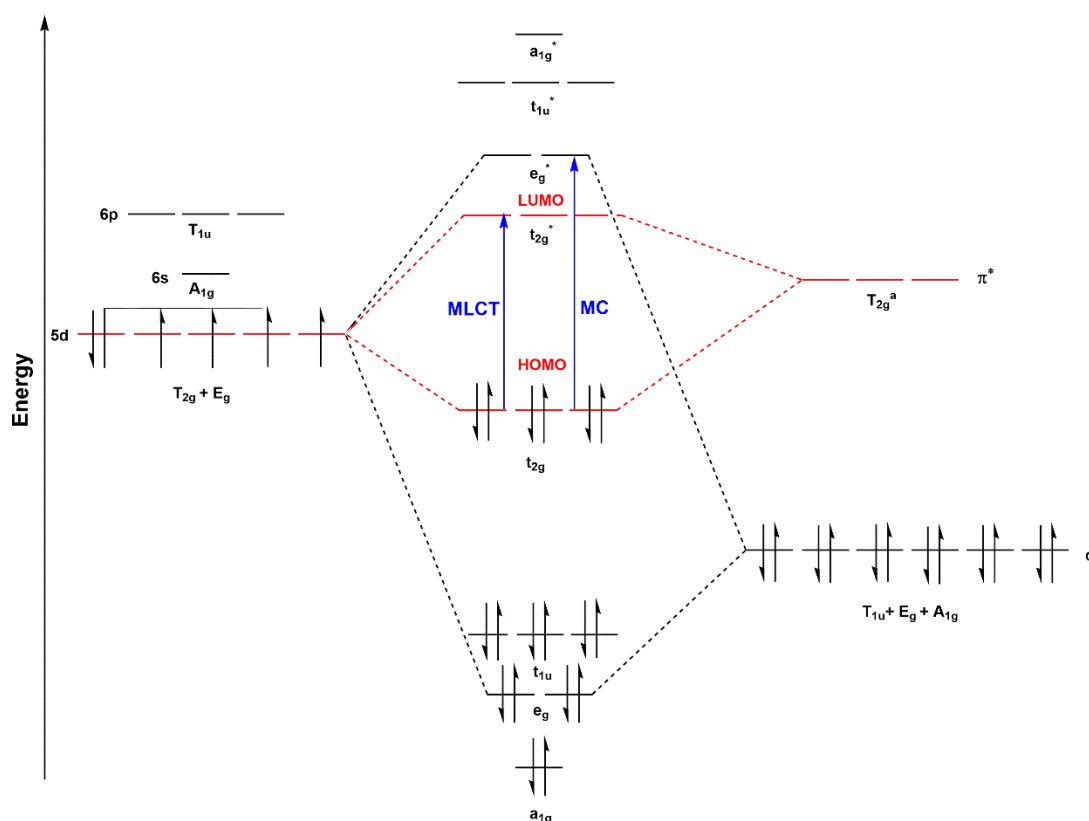


Figure 1.11 Simplified MO diagram for a low spin d^6 transition metal complex, coordinated to 6 equivalent π accepting ligands. The formation of the relevant molecular orbitals has been indicated with dashed lines. The HOMO and LUMO orbitals are highlighted in red, whereas MC and MLCT transitions are highlighted in blue. a: only the T_{2g} combination is considered for simplicity.

This diagram ideally describes second or third row transition metal complexes surrounded by π -accepting ligands, arranged in an octahedral geometry. For simplicity in the construction of the diagram, the ligands in the coordination sphere of the metal

ion are considered to be all equivalent. In this configuration, the metal ion can be considered to form bonds with the 5d, 6s and 6p orbitals.

The orbitals depicted in the diagram are classified and labelled according to their symmetry in the octahedral point group, as shown in **Figure 1.11**. The 5d orbitals are represented by symmetry labels T_{2g} and E_g , the 6s orbitals is represented as A_{1g} , and the 6p is labelled as T_{1u} . Low spin d^6 transition metal complexes are typically stable. Indeed, as shown in **Figure 1.11**, the bonding orbitals (a_{1g} , e_g , t_{1u} and t_{2g}) are filled, whereas the anti-bonding orbitals (a_{1g}^* , e_g^* , t_{1u}^* and t_{2g}^*) are empty. Due to the presence of π -accepting ligands, which produce a strong crystal field, the e_g^* orbitals are considered higher in energy than the t_{2g}^* . The t_{2g} and t_{2g}^* represent the highest occupied molecular orbital (HOMO) and lowest unoccupied molecular orbital (LUMO), respectively. The relative position of the t_{2g} orbital in the diagram can vary depending on the specific energies of the π^* orbitals of the ligand.^{50,53}

The electronic transitions of an octahedral transition metal complex can be of different natures. The most common ones are depicted in a simplified Jablonski diagram, shown in **Figure 1.12**. The orbital t_{2g} (HOMO) is predominantly metal-based, whereas the t_{2g}^* (LUMO) is predominantly ligand based. Hence, the transition from the HOMO orbital to the LUMO is typically defined as metal-to-ligand-charge-transfer. The transition that occurs from the t_{2g} orbitals to the empty e_g^* orbitals is known as a metal-centred (MC) transition. MC transition are commonly defined as “dark” states (i.e. non-emissive), as the population of anti-bonding orbitals leads to significant distortion and favours the decay via non-radiative pathways. For this reason, the population of MC states must be minimised in order to optimise the emission intensity of a metal complex. Hence, it is important that the difference in energy between the MLCT and the MC state is large enough that competition between the two states can be avoided. In second and third row transition metal complexes, the ligand-field strength increases, hence MC states are raised to high energy.^{50,53}

Electronic transitions can take place on the ligand themselves, with an electron being transferred from an occupied π orbital to an empty π^* on the same ligand. These transitions are known as ligand-centred (LC), intra-ligand (IL) or π - π^* transitions. Moreover, if the ligands in the coordination sphere are not equivalent, a transition can take place between the π orbital of one ligand and the π^* orbital of another ligand. These transitions are defined as ligand-to-ligand-charge-transfer (LLCT). Together

with vibrational relaxation (VR) processes, these transitions are not considered in the Jablonski diagram (shown in **Figure 1.12**). In this simplified representation, upon absorption of a photon the metal complex can be excited to the $^1\text{MLCT}$, ^1LC or ^1MC state, depending on the photon energy.^{50,53} The complex will then undergo vibrational relaxation (VR) and internal conversion (IC) to the lowest $^1\text{MLCT}$, in accordance with Kasha's rule.^{50,53} The presence of the heavy metal can then promote inter-system crossing (ISC) to $^3\text{MLCT}$. The complex can then decay to the ground state (GS) via non-radiative (k_{nr}) and radiative (k_{r}) pathways.

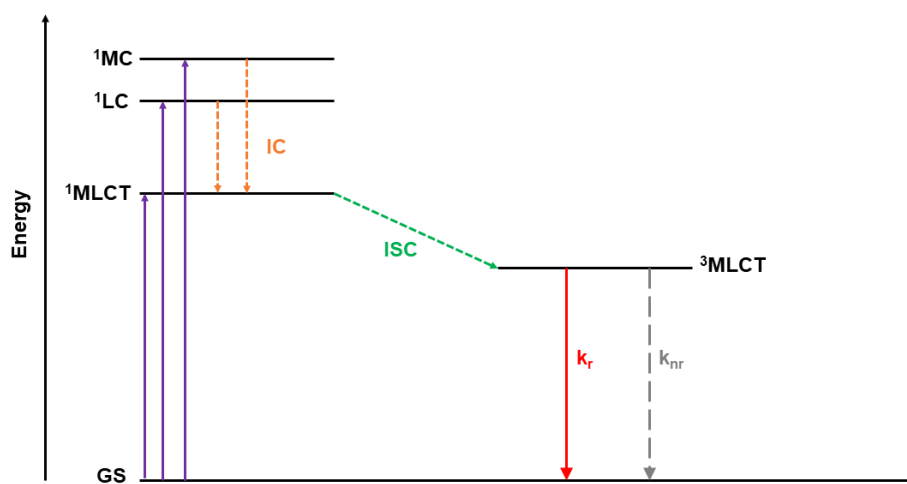


Figure 1.12 Simplified Jablonski diagram for an octahedral d^6 metal complex. In this representation, the lowest excited state is the MLCT state. VR transition and the LLCT excited states are omitted for simplicity.

1.5.4 Electronic structure and transitions for a d^8 configuration

Platinum(II) complexes are endowed with unique chemical and photophysical properties, due to their d^8 electronic configuration and the 4-coordinate square-planar geometry that can lead, through different mechanisms, to the formation of aggregates. Once formed, the aggregate can be considered as new chemical species with new chemical-physical and photophysical properties. In this section, the design principles for luminescent platinum(II) complexes bearing terdentate ligands will be overviewed, together with a brief discussion of platinum(II) self-assembled systems and some of the factors affecting their aggregation mechanisms.

1.5.4.1 Design principles for luminescent platinum(II) metal complexes

Both stability and emission properties of platinum(II) complexes are dramatically affected by their $5d^8$ electronic configuration and 4-coordinate square-planar geometry. A simple ligand field-splitting diagram (**Figure 1.13**) of d^8 metal ion shows how this configuration has a thermodynamic preference to form square planar complexes when coordinating strong-field ligands. Indeed, with this geometry, the ligand field is high and three of the occupied orbitals are stabilised, whereas the unoccupied orbital is pushed to higher energies. When populated through the absorption of light, the dx^2-y^2 orbital allows the molecule to undergo significant distortion once the excited state is formed, leading to non-radiative decays.⁵⁴⁻⁵⁷ Hence, platinum(II) complexes with simple inorganic ligands (i.e. $\text{Pt}(\text{NH}_3)_4^{2+}$) are not emissive in solution at room temperature.⁵⁵ Introducing conjugate aromatic ligands leads to MLCT and LC states, although the distorted MC excited state is often thermally accessible and promotes thermal deactivation.^{55,57} One common strategy to enhance the emission of transition metal complexes is to use multidentate ligands, such as terpyridyl ligands ($\text{N}^{\wedge}\text{N}^{\wedge}\text{N}$), to obtain a rigidified system which allows less distortion upon the formation of the excited state. Although this consideration is generally valid, a remarkable number of platinum(II) $\text{N}^{\wedge}\text{N}^{\wedge}\text{N}$ complexes are still not emissive at room temperature, as for example complex **6**⁵⁸ (**Figure 1.14**).^{55,57} This is due to the fact that platinum(II) does not ideally fit in the bite of the terpyridine and, as a consequence, the overall structure of the complex is distorted when the metal ion

is bound to the ligand. Thus, the ligand field is reduced, and non-radiative decays pathways are promoted. A common strategy to obtain platinum(II) complexes showing emission at room temperature is to modify the terdentate ligand, increasing the conjugation and introducing cyclometalating sites (**Figure 1.14**).^{55,57}

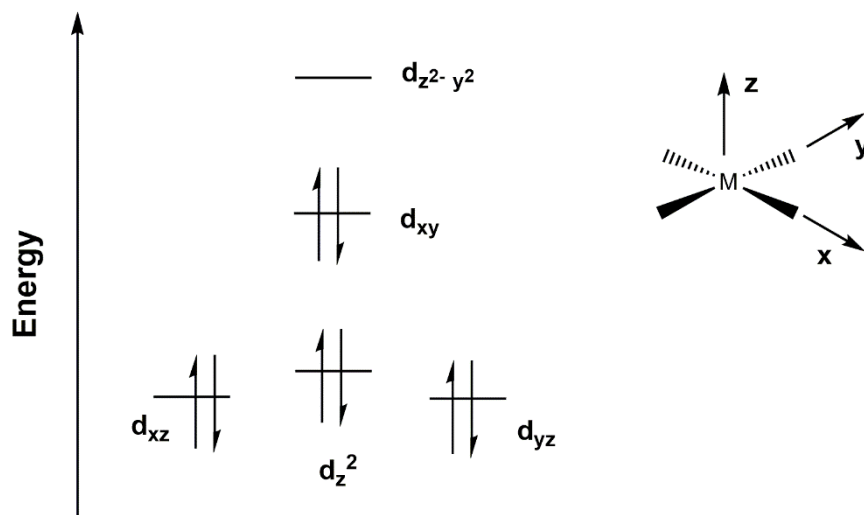


Figure 1.13 Simple ligand field-splitting diagram for metal d orbitals in a square planar complex. By convention, the z axis is set perpendicular to the plane of the complex and the bonds between M and the ligand lie along the x and y axis. While the $d_{x^2-y^2}$ orbital is always the highest in energy, the relative positions of the lower energy levels depend on the ligands set.

Indeed, C-deprotonated cyclometalated ligands ($N^{\wedge}C^{\wedge}N$ or $C^{\wedge}N^{\wedge}N$) are strong σ -donors, hence they push the MC state to higher energies.⁵⁷ Complex **7**⁵⁹ and complex **8**⁶⁰ are shown in **Figure 1.14** as an example. However, despite the presence of two covalent Pt-C bonds, introducing a second cyclometalating site does not lead to emission enhancement. Because of the double cyclometallation, platinum complexes supported by a doubly deprotonated, cyclometalating ligand ($C^{\wedge}N^{\wedge}C$) undergo strong distortion upon shifting to the excited state. Hence, many platinum $C^{\wedge}N^{\wedge}C$ complexes are not emissive in solution at room temperature. Che and co-workers reported the first family of platinum(II) dicyclic complexes that are emissive at room temperature. In these species, the cyclometalating ligands are highly-conjugated and incorporate carbazole, fluorene and thiophene heterocyclic units (complex **9**⁶¹).

Combining variations both in the ancillary ligand and in the chelating one provides a broad variety of strongly emissive complex, with high photoluminescence quantum yields and long excited state lifetimes.

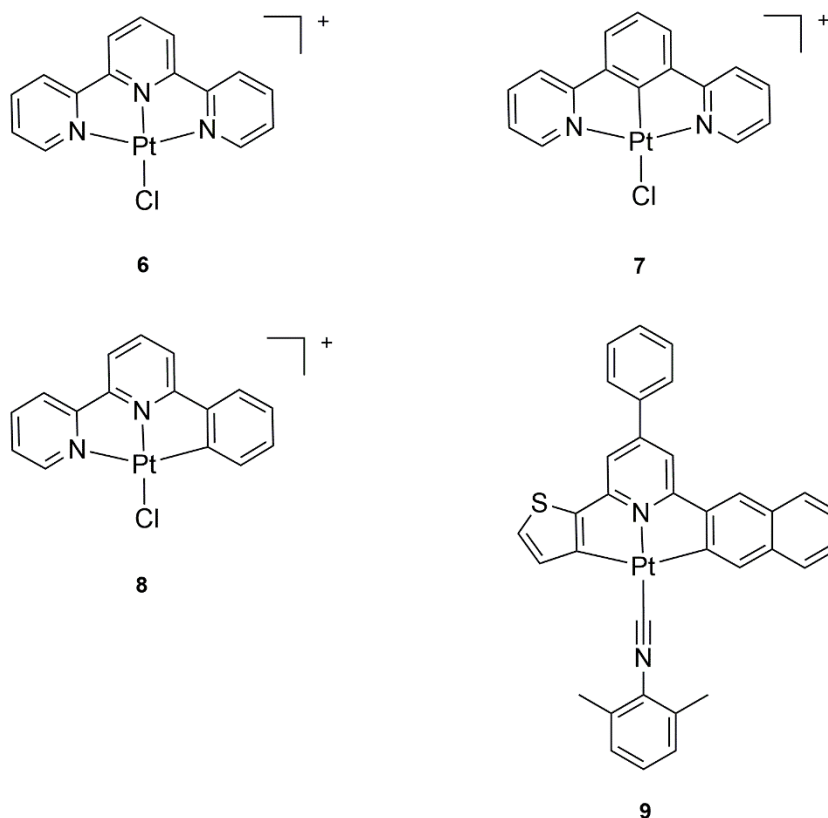


Figure 1.14 Chemical structure of platinum complexes **6-9**. Complex **6** is not emissive in solution at room temperature, whereas in complex **7-9** emission is enhanced via modifications of the terdentate ligand.

1.5.4.2 Self-assembled platinum(II) systems and aggregation induced emission (AIE)

Aggregation has been considered for a long time an unfavourable phenomenon for luminescent transition metal complexes. Indeed, upon the formation of aggregates, complexes may be susceptible to a phenomenon called aggregation caused quenching (ACQ), that causes a dramatic decrease in luminescence properties such as emission intensity, photoluminescence quantum yields and colour purity. Moreover, the aggregate is less soluble and can give rise to the formation of undesired precipitates. On the other hand, however, aggregates can give rise to enhanced luminescence

properties, due to opposite phenomena such as aggregation induced emission (AIE) or aggregation induced emission enhancement (AIEE).^{54,55,62} Therefore, species that are not emissive in their monomeric form, may show emission upon aggregation in solution. Moreover, the packing resulting from aggregation has a shielding effect from the environment and therefore from quenching species, while affording a rigidochromic effect that decreases the non-radiative processes.⁵⁴ As for platinum(II) complexes, their square planar coordination geometry makes them essentially flat and this characteristic enables them to form macrostructures which originate from the stacking of the single monomers. The d_{z^2} orbital is perpendicular to the plane of the molecule and when the intermolecular distance is appropriate (3-3.5 Å) it can interact with the d_{z^2} orbital of an adjacent molecule. As a result, weak bonding and antibonding $d\sigma$ and $d\sigma^*$ orbitals are formed via metal-metal interaction.^{54,63} In **Figure 1.15**, a simplified molecular orbital diagram is shown to illustrate this interaction.

In terms of optical properties, the main consequence of this metal-metal interaction is that a new excited state ($d\sigma^*-\pi^*$) is formed, which lies at lower energy in comparison to the $\pi-\pi^*$ lowest excited state of the monomer. This state defines a new set of HOMO-LUMO orbitals and it is usually described as metal-metal to ligand charge transfer (MMLCT) excited state. In **Figure 1.15**, the electronic transitions occurring within a monomer molecule (MLCT/LC) are highlighted together with the new formed transition resulting from the interaction of two complexes (MMLCT).⁵⁴ Importantly, the presence of planar, conjugated aromatic ligands can promote $\pi-\pi$ interaction between the ligands, giving rise to similar aggregation effects.⁵⁵

As aggregation induced emission takes place, a switch-on in the emission or the appearance of a new emission feature can be observed. The peculiar structure of a given complex has a key role in the formation of aggregates, in terms of ligand system as well as counterions in charged species. However, there are several additional factors that affect the aggregation process. First, it is clear how aggregation is a concentration-dependent phenomenon. Moreover, this process is strongly affected by temperature, as the aggregation constant is expected to increase at low temperatures. The presence of a polar solvent with a good solvation capacity usually overcomes the tendency to form aggregates, whereas by using a solvent/anti-solvent mixture the opposite effect can be obtained.^{64,65} With specific chemical structures and functionalities, aggregation can also depend on the pH of the solution.⁶⁶ In the past decade, platinum(II) aggregates

have been investigated for a number of applications, ranging from bio-imaging and bio-sensing^{67,68} to the fabrication of WOLED.^{69,70}

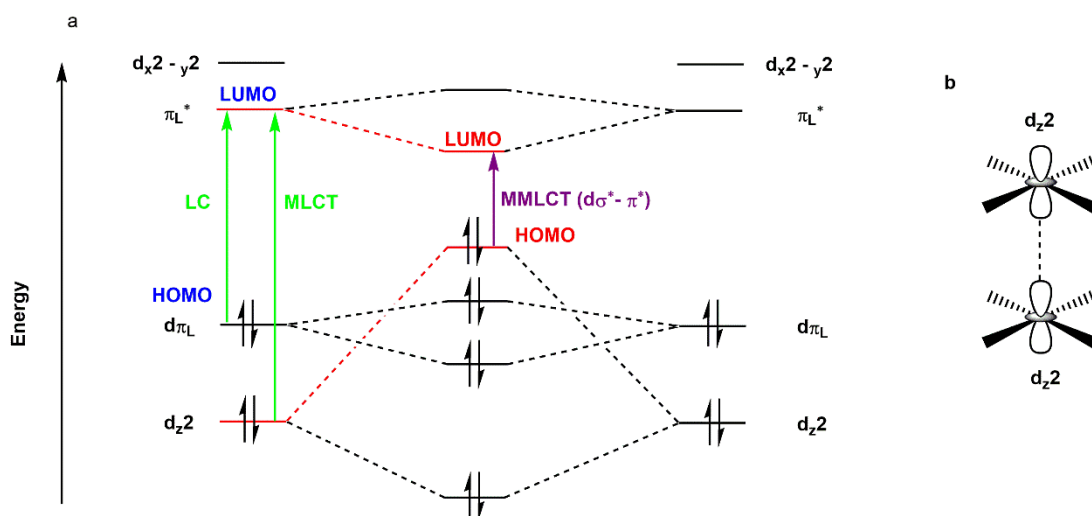


Figure 1.15 a: Molecular orbital diagram for two interacting square-planar platinum(II) complexes. The MLCT/LC transitions within the monomers are highlighted in green, whereas the MMLCT transition is highlighted in purple. The formation of the new HOMO-LUMO set is highlighted in red, whereas the typical HOMO-LUMO when just the monomer is present are labelled in blue. b: schematic representation of the interaction between two adjacent d_{z^2} orbitals.

1.6 Transition metal complexes in bioimaging

1.6.1 Transition metal complexes in cellular and tissue imaging

Transition metal complexes possess richer photophysical and photochemical properties than most common organic fluorophores, offering good emission tunability, large Stoke shifts and improved photostability.^{54,71} For these reasons, transition metal complexes of ruthenium(II), rhenium(I), iridium(III) platinum(II) and gold(I) have been extensively studied in the past decade as alternative imaging tools to most traditionally used organic dyes. Furthermore, due to the presence of the heavy metal ion, these complexes have the great advantage to be detectable with other imaging techniques, such as electron microscopy. Hence, they have recently found a new potential application in the emerging field of correlative imaging,^{72,73} where the same probe is used to perform imaging with two independent techniques. In the field of optical imaging, a number of transition metal complexes have been designed to target cells and tissue with sub-cellular specificity. Indeed, complexes have been designed to modulate their target affinity towards a wide range of organelles^{54,71,74–80} from cellular DNA⁸¹ and mitochondria^{82,83} to endoplasmic reticulum⁸⁴, lysosomes⁸⁵ or lipid droplets⁸⁶. Selected examples of Ru(II)⁸⁷ (**10**), Re(I)⁷⁷ (**11**), Ir(III)⁷⁷ (**12**), Pt(II)⁸⁸ (**13**), and Au(I)⁸⁹ (**14**), complexes investigated as cellular imaging tools are depicted in **Figure 1.16**.

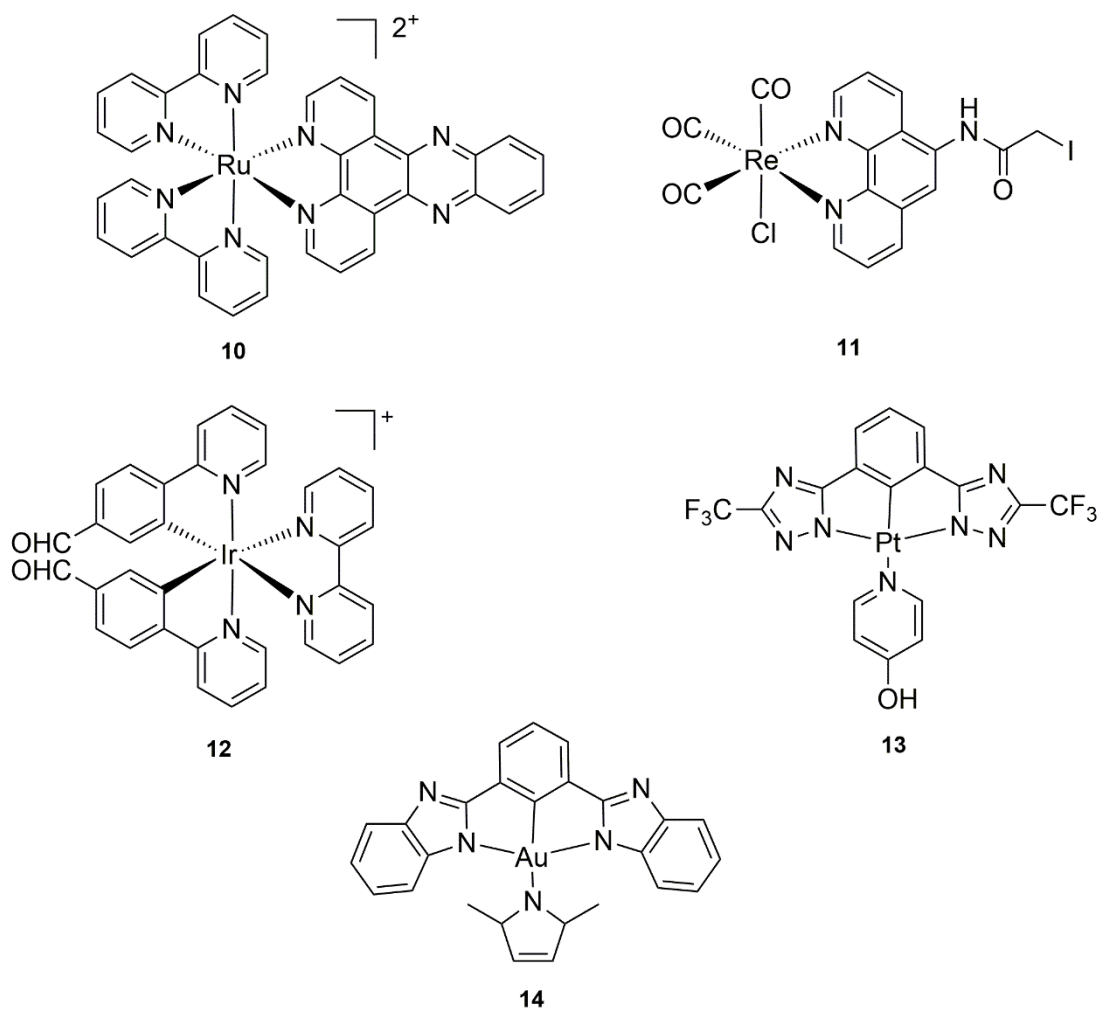


Figure 1.16 Examples of transition metal complexes investigated as imaging probes.

1.6.2 Interaction of transition metal complexes with bacterial species

Besides being extensively investigated as imaging probes, transition metal complexes have been also studied as antimicrobial agents.⁹⁰⁻⁹⁸ Keene and co-workers have reported a broad variety of Ru(II) mononuclear and polynuclear complexes that exhibited good antibacterial activity against different gram-positive and gram-negative bacterial strains⁹⁹⁻¹⁰⁷. As an example, complexes **15**, **16**, **17** and **18** (**Figure 1.17**) showed remarkable MIC levels against the gram-positive pathogens *Staphylococcus aureus* (*S. aureus*) and methicillin-resistant *Staphylococcus aureus* (MRSA), comparable to the MIC observed for the antibiotic ampicillin and gentamicin. Moreover, they showed activity against the gram-negative *E. coli* and *P. aeruginosa*.¹⁰³ Within some of the reported works, the luminescent properties of the Ru(II) complexes were exploited to verify cellular uptake and gain a better understanding of the antimicrobial activity.¹⁰³⁻¹⁰⁵ Even though the mode of action of these ruthenium(II) based systems is not well defined yet, important trends emerged highlighting how different factors including lipophilicity, presence of more than one metal centre, and overall charge of the system played a key role in the enhancement of the antimicrobial activity.

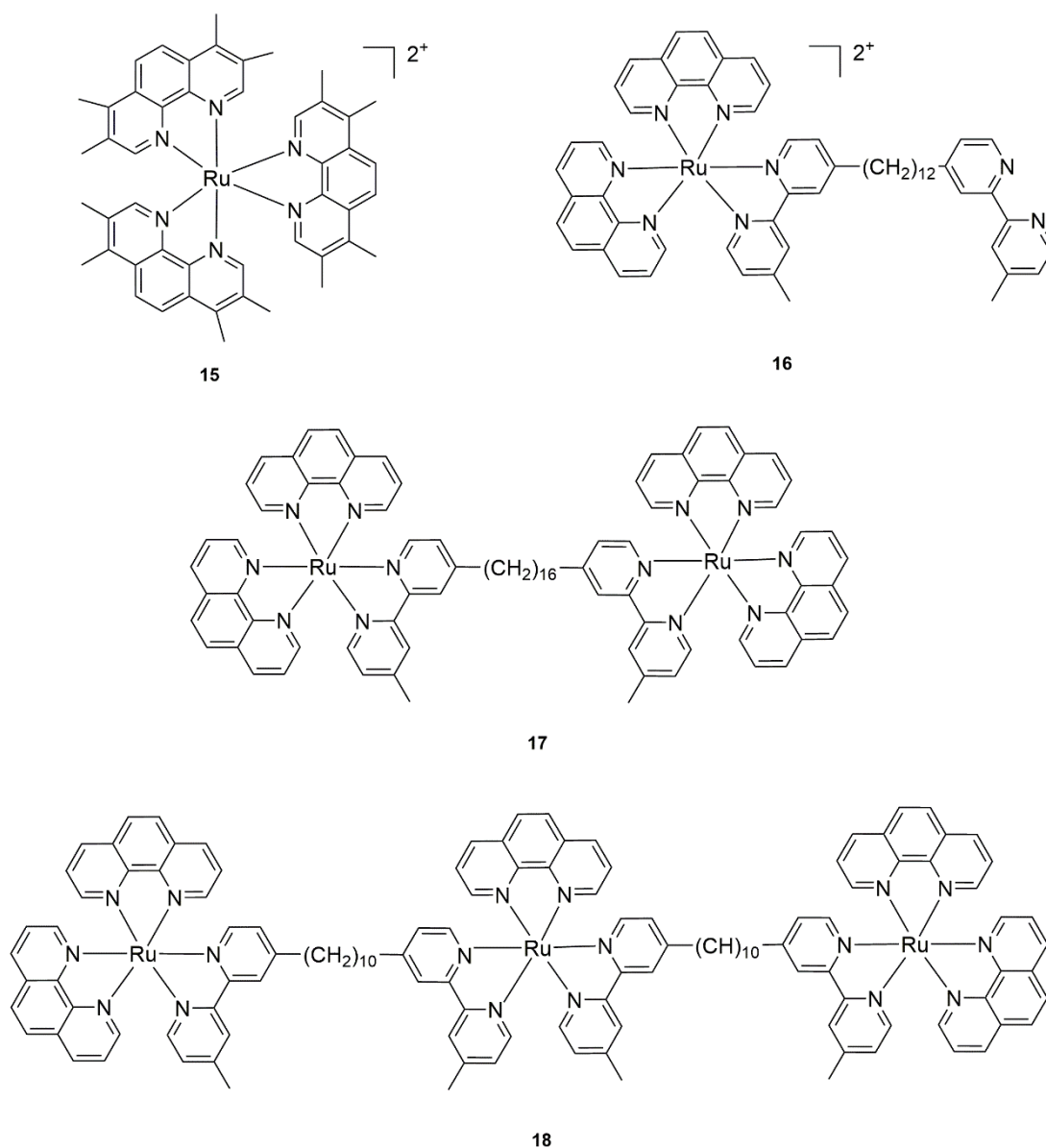


Figure 1.17 Chemical structure of mononuclear (**15**, **16**), dinuclear (**17**) and trinuclear (**18**) Ru(II) antibacterial complexes.

Crowley and his research group reported a new family of mononuclear and polynuclear Re(I) and Ru(II) complexes bearing 2-Pyridyl-1,2,3-triazole “click” ligands (**Figure 1.18**). Mononuclear Ru(II) complexes supported by diversely functionalised pyridyl-triazole ligands, as for example complex **19**, were tested against pathogenic strains such as *S. aureus*, MRSA and *E. coli*, showing good antimicrobial activity, with MIC values sometimes better than the values observed for the gentamicin control.¹⁰⁸ TEM analyses of *S. aureus* were also presented, showing how the antimicrobial activity of

these systems is strictly related to cell wall or membrane disruption. Ruthenium(II) dinuclear helicates developed from a bidentate 2-pyridyl-1,2,3-triazole ligand, as for example complex **20**, were also investigated¹⁰⁹. Importantly, Crowley and co-workers also expanded the study towards analogous Re(I) mononuclear and polynuclear complexes, in which the pyridyl-triazole building block has been exploited to build a variety of ligand scaffolds^{110,111}. Complex **21**, **22**, and **23** are shown in **Figure 1.18** as an example. These outcomes indicate the great potential of further expanding the breadth of metal-based antibacterial agents, focusing the design strategy on different metal centres as well as diversely functionalised ligand systems. Significantly, the reports on transition metal complexes as bacterial imaging agents have demonstrated the capability of these systems to interact with bacterial species. Surprisingly however, transition metal complexes have been scarcely investigated as luminescent probes for optical imaging in bacteria.

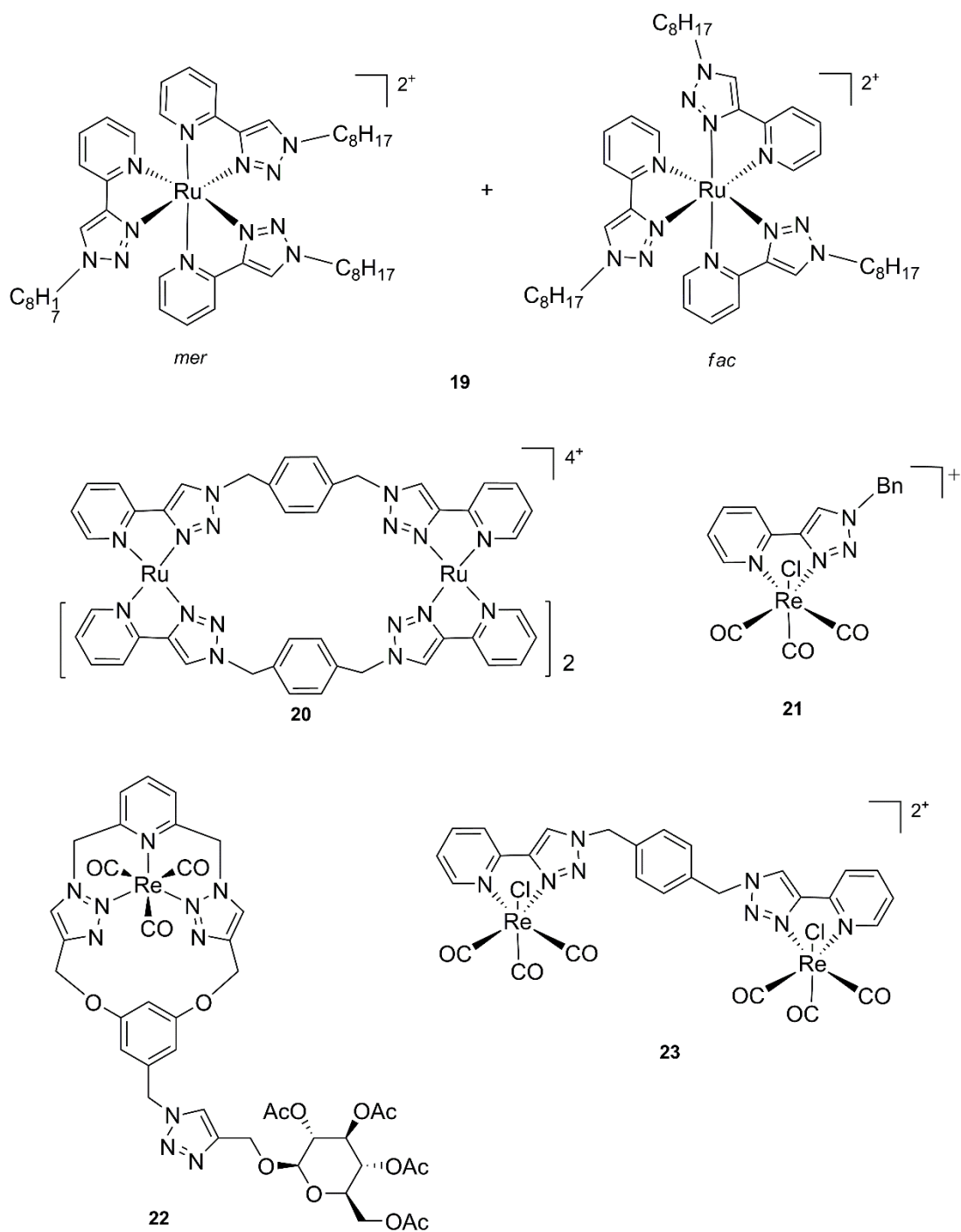


Figure 1.18 Chemical structures of mononuclear and polynuclear Ru(II) (**19**, **20**) and Re(I) (**21**, **22**, **23**) complexes.

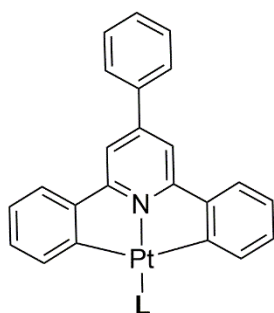
1.7 This investigation and scope

In the past decades, increasing research interest has focused on ruthenium(II), rhenium(I), iridium(III) platinum(II) and gold(I) complexes as luminescent probes. While their application in this field has been limited to their application in cellular and tissue imaging, their potential application as new antibacterial agents has been investigated. Although the mechanisms underpinning their antimicrobial activity have not yet been fully delineated, nonetheless these studies proved unequivocally that transition metal complexes are able to interact with bacterial cells. In this context, there is a surprising lack of reports about transition metal complexes investigated as luminescent probes for bacterial imaging. To further expand the knowledge in this field, this study aims to investigate different platinum(II) and iridium(III) metal complexes, assessing their potential to be exploited as bacterial imaging probes. Chapter 2 focuses on a new family of neutral platinum(II) dicyclometalated ($C^{\wedge}N^{\wedge}C$) complexes (**Figure 1.19**). Their photophysical properties have been studied, and their behaviour against bacterial cells has been assessed. Because the biological properties of platinum(II) $C^{\wedge}N^{\wedge}C$ complexes have been scarcely investigated, the new family of neutral platinum(II) $C^{\wedge}N^{\wedge}C$ complexes has also been tested against eukaryotic cells. Expanding from the family of platinum(II) complexes developed in Chapter 2, Chapter 3 is centred on a new platinum(II)-naphthalimide complex (**Figure 1.19**), that has been investigated as correlative probe for super-resolution microscopy and ion-nanoscopy of bacteria. The doubly deprotonated $C^{\wedge}N^{\wedge}C$ ligand calls for the synthesis of anionic platinum(II) species, which have been rarely reported in the literature: Chapter 4 focuses on the synthesis, photophysical characterisation and photocatalytic properties of a new family of anionic platinum(II) complexes (**Figure 1.19**). In Chapter 5, a series of neutral and cationic iridium(III) tetrazolato complexes previously reported by our group have been tested as bacterial imaging tools (**Figure 1.20**). Their capability to stain different sub-cellular compartments has been assessed, comparing their cellular localisation and toxicity to delineate a structure-activity relationship trend. While throughout the previous chapters the neutrophilic bacteria *B. cereus* and *E. coli* have been used as model species, Chapter 6 expands the study on bacterial imaging towards a fundamentally and industrially relevant class of extremophilic bacteria: acidophiles.

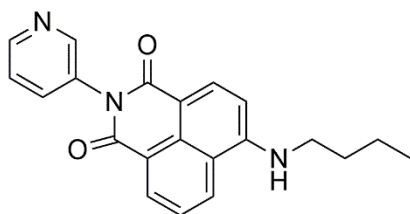
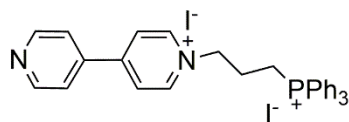
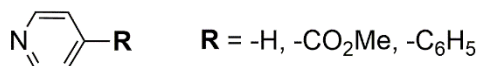
Different staining conditions have been tested with commercially available dyes and selected transition metal complexes against the model specie *At. ferrooxidans*, to delineate the first steps towards the first protocol to stain live acidophilic bacteria.

Pt(II) C^NC complexes

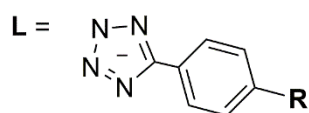
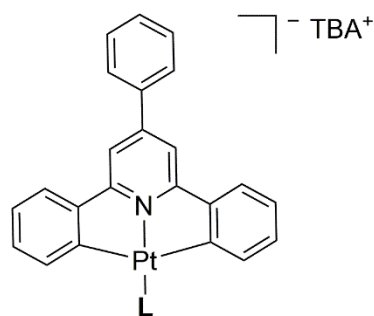
Neutral complexes



L = DMSO



Anionic complexes



R = -H, -CH₃, -Br

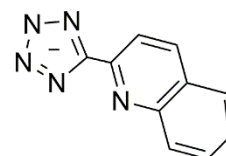
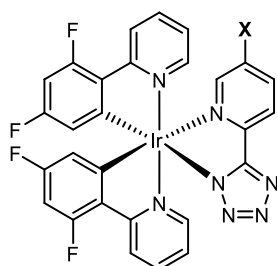


Figure 1.19 Left: Structure of target neutral platinum(II) complexes reported in Chapter 2 and Chapter 3. Right: Structure of the anionic platinum(II) complexes reported in Chapter 4.

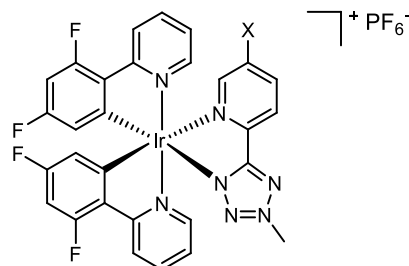
Ir(III) complexes

Neutral complexes



X = -H, -CN

Cationic complexes



X = -H, -CN

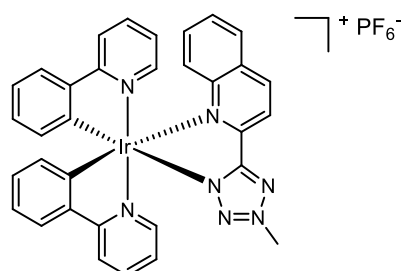
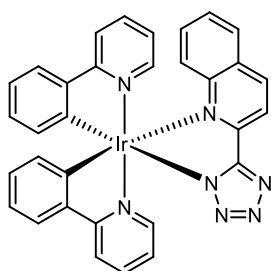


Figure 1.20 Structure of target neutral (left) and cationic (right) iridium(III) complexes discussed in Chapter 5.

Chapter 2

Synthesis, photophysical and biological investigation of a family of neutral dicyclometalated platinum complexes

2.1 Introduction

Transition metal complexes have been widely investigated in the past decade, due to their potential and real-market application in photo-catalysis, light-emitting devices, bio-sensing and bio-imaging.^{71,75,112–114} The interest in exploiting metal-based dyes for optical imaging has been driven by their advantageous photophysical properties, which offer the potential to overcome many of the drawbacks associated with the most commonly studied organic dyes, such as self-quenching and poor photostability. Amongst the second and third row transition metal complexes, Pt(II) has gained increasing attention due to its intriguing photochemical and photophysical properties.^{54,55,57} In fact, the free coordination sites due to the d^8 electronic configuration and square-planar geometry, allow the formation of assemblies *via* intramolecular interactions. It has been reported in the past few years how the dynamic process known as aggregation induced emission (AIE) can be tuned and exploited for the preparation of optical devices, hybrid materials and bio-sensors.^{62,69,70,115–118} In the field of optical imaging, a large number of platinum complexes have been reported, bearing bidentate $N^{\wedge}N$,^{119–121} $C^{\wedge}N$ ^{122–124} ligands as well as tridentate $N^{\wedge}N^{\wedge}N$,^{66,125–129} $N^{\wedge}C^{\wedge}N$ ^{59,69,70,130–134} and $C^{\wedge}N^{\wedge}N$ ^{135–138} ligands. The biological properties of these type of complexes as non-assembled systems have been widely studied, whereas more recently De Cola *et al* have expanded the application of platinum complexes in bio-imaging by exploiting Pt assemblies as cellular labels.^{54,88} Despite being investigated as cellular markers for eukaryotic cells, the biological properties of platinum(II) complexes towards bacterial cells have never been explored.

In this chapter, a new family of platinum(II) complexes bearing a doubly deprotonated $C^{\wedge}N^{\wedge}C$ ligand has been synthesised with the aim of investigating the photophysical and aggregation properties, and to assess their biological properties. Despite platinum

complexes bearing mono-deprotonated N[^]C[^]N and C[^]N[^]N chelating ligands have been widely investigated as cellular labels, there is a lack of reports on platinum(II) C[^]N[^]C complexes for biological application. Hence, before testing the synthesised platinum(II) complexes on bacteria, their properties towards eukaryotic cells have also been assessed.

Target compounds:

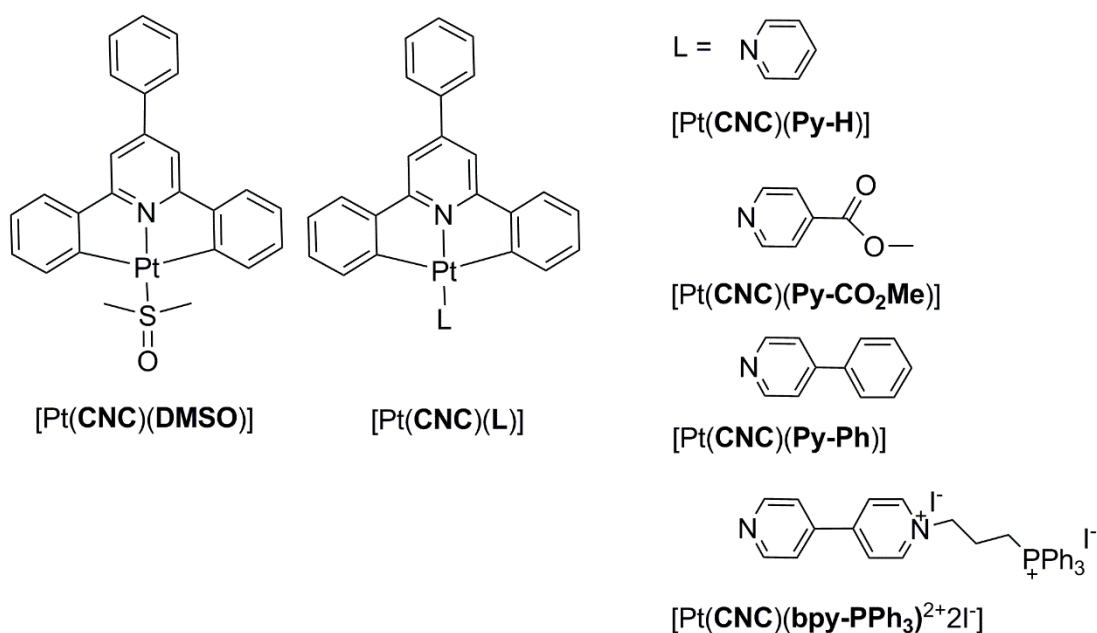


Figure 2.1 Chemical structure of the target platinum(II) dicyclopentadienyl complexes.

2.2 Synthesis of the 2,4,6-triphenylpyridine ligand (CNCH₂)

The cyclometalating ligand 2,4,6-triphenylpyridine ligand (CNCH₂) was synthesised following a two-step literature procedure,¹³⁹ shown in **Figure 2.2**. Benzaldehyde was combined with two equivalents of acetophenone and sodium hydroxide under solvent free conditions, to yield the diketone intermediate via aldol condensation, followed by Michael addition. The diketone was then converted to a pyridine via a double condensation in acetic acid, in the presence of an excess of ammonium acetate.

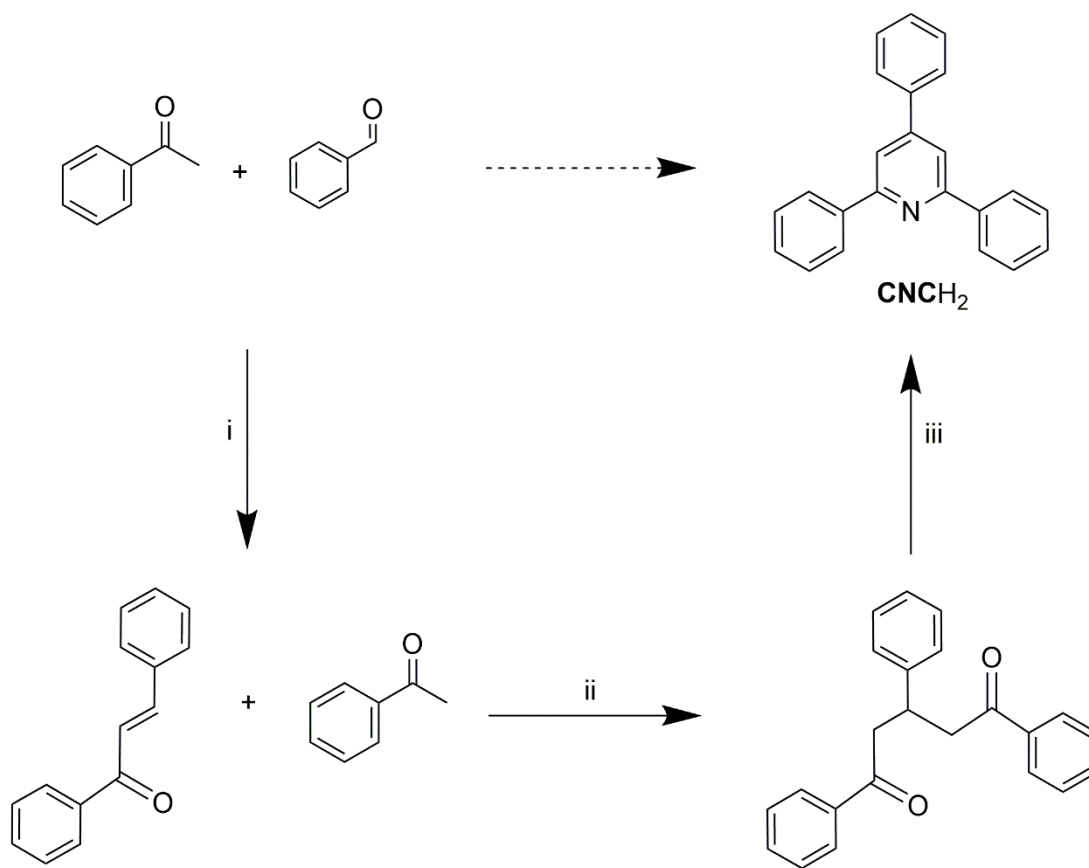


Figure 2.2. Scheme of the synthetic procedure for CNCH₂. Reagents and conditions: i) and ii) NaOH, grind, iii) NH₄OAc, CH₃COOH, reflux, 2 hours.

The synthesised product was characterised by ¹H-NMR and ¹³C-NMR spectroscopy. The ¹H-NMR and ¹³C-NMR spectra in CDCl₃ were consistent with previous reports of this compound.¹³⁹

2.3 Synthesis and characterisation of the Pt(II) dichloro-bridged dimer

The platinum(II) dichloro-bridged dimer $[\text{Pt}(\text{CNC})(\mu\text{-Cl})_2]$ was prepared following a methodology developed by Rourke *et al.*^{140,141} where the starting platinum(II) salt K_2PtCl_4 , together with a slight excess of the tridentate ligand are refluxed for three days in glacial acetic acid under inert conditions (**Figure 2.3**). At the end of the reaction time, some of the unreacted platinum(II) salt was recovered from the reaction mixture via decantation, and the desired product was filtered and washed with water, acetone and diethyl ether.

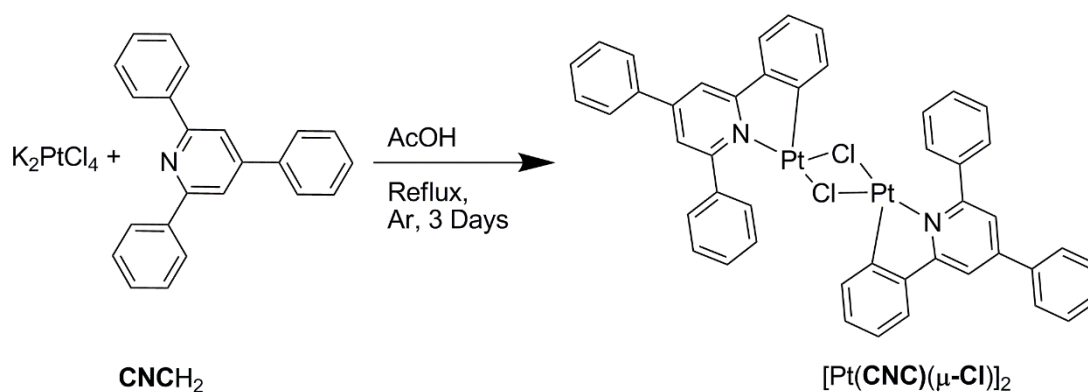


Figure 2.3. Scheme of the synthetic procedure for the platinum(II) dimer.

Alternative microwave assisted synthetic routes were attempted in order to reduce the reaction time. However, even though the desired product could be obtained, a considerable amount of solid degradation products (platinum blacks) was also obtained, even when the reaction vessel was kept under inert atmosphere, limiting the recovery of the unreacted K_2PtCl_4 . $[\text{Pt}(\text{CNC})(\mu\text{-Cl})_2]$ was obtained as a crystalline powder which was characterised by $^1\text{H-NMR}$ spectroscopy, whereas a $^{13}\text{C-NMR}$ could not be recorded due to the extremely low solubility of the compound. Single crystals suitable for X-ray diffraction were obtained for the platinum(II) dimer (**Figure 2.4**).

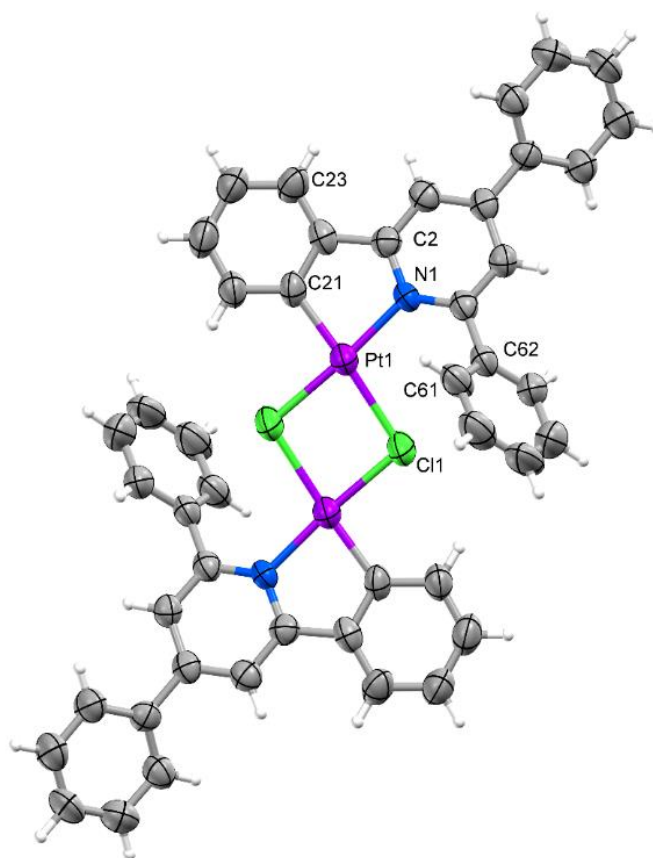


Figure 2.4 X-ray crystal structure of $[\text{Pt}(\text{CNC})(\mu\text{-Cl})_2]_2$, with thermal ellipsoids drawn at the 50% probability level. Pt(1)-C(21): 1.986 Å; Pt(1)-N(1): 2.057 Å

The dimer crystallises in the orthorhombic $Pbcn$ space group. Each of the platinum centres is tetracoordinated with a distorted square-planar geometry and bound to the N and C atoms of the monocyclometalated triphenylpyridine ligand as well as two *cis* chloro ligands that are bridging the two platinum centres. The remaining two unmetalated phenyl rings lie twisted with respect to the plane of the pyridine ring. The crystallographic data can be found in Appendix A, Table A.1- Table A.2.

2.4 Synthesis and characterisation of the neutral dicyclobmetalated platinum(II) complexes

2.4.1 Synthesis and characterisation of [Pt(CNC)(DMSO)]

The platinum(II) dimer was split by treatment with hot DMSO (150 °C), and the second cyclometalation afforded by addition of water and Na₂CO₃ (**Figure 2.5**).

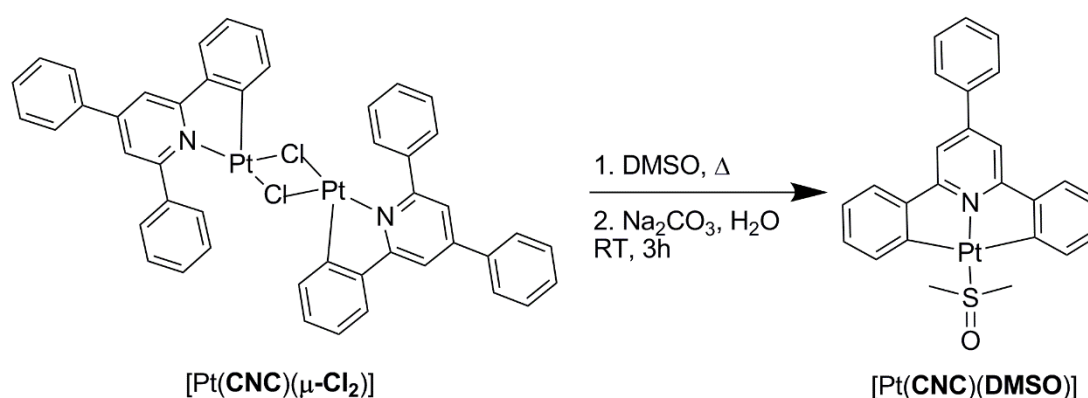


Figure 2.5 Scheme of the synthetic procedure for the neutral complex [Pt(CNC)(DMSO)].

In this way, the neutral dicyclobmetalated platinum(II) complex bearing DMSO as ancillary ligand was obtained and precipitated out of solution. The complex was fully characterised via ¹H-NMR and ¹³C-NMR spectroscopy. The ¹H-NMR spectrum of [Pt(CNC)(DMSO)] in Acetone-d₆ matches the expected structure of a mononuclear complex, where both the phenyl rings have been cyclometalated *ortho* to the linking pyridine C atom. A singlet corresponding to the two –CH₃ groups of the DMSO ligand is present at 3.69 ppm, showing the presence of the solvent molecule bound as ancillary ligand. Analysis of the crystal structure obtained for the complex confirmed the presence of the DMSO molecule, sulfur-bound to the Pt(II) centre (**Figure 2.6**), with a Pt-S distance of 2.195(3), which is consistent with related [(R-CNC)Pt-DMSO] complexes.^{142–145} The S atom is arranged with a pseudo tetrahedral geometry with the

S=O bond oriented on the plane of the square planar coordination of platinum, and the two methyl group above and below this plane.

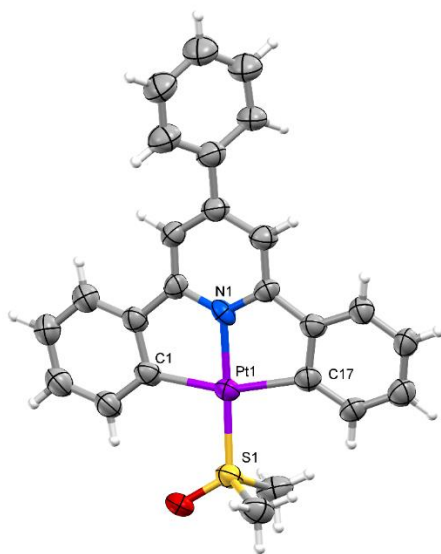


Figure 2.6 X-ray crystal structure of [Pt(CNC)(DMSO)] with displacement ellipsoids drawn at the 50% probability level. Lattice solvent molecules are removed for clarity. Pt(1)-N(1): 2.018 Å; Pt(1)-C(1): 2.074 Å; Pt(1)-S(1): 2.195 Å.

2.4.2 Synthesis of neutral Pt(II) complexes with N-donor ligands

The neutral complexes [Pt(CNC)(Py-H)], [Pt(CNC)(Py-CO₂Me)], [Pt(CNC)(Py-Ph)], and [Pt(CNC)(bpy-PPh₃)²⁺ 2I⁻] were synthesised via a ligand substitution reaction, where the DMSO molecule was displaced by the appropriate N-donor ligand. The reaction was carried out in dichloromethane at room temperature (**Figure 2.7**).

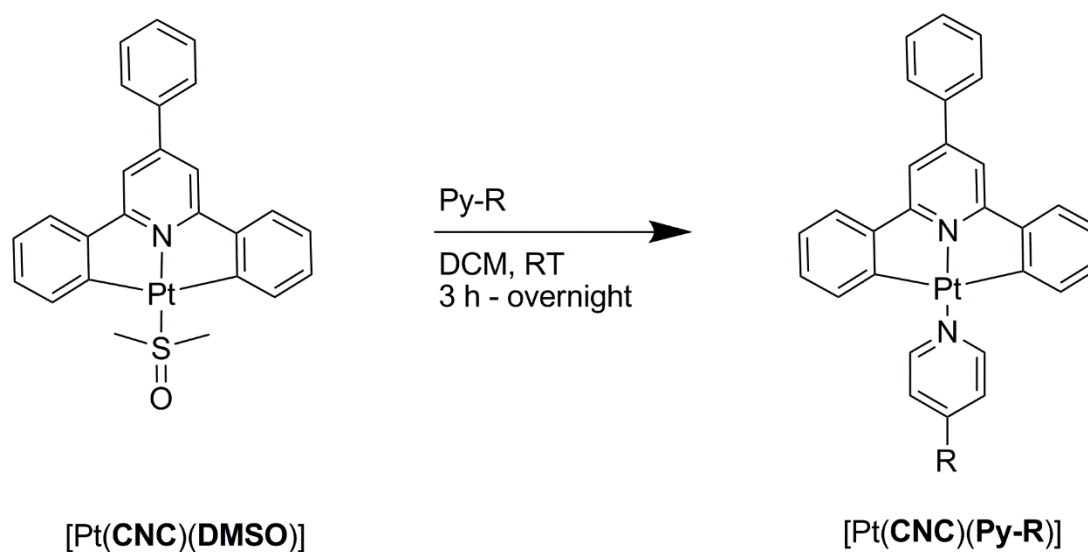


Figure 2.7 Scheme of the synthetic procedure for the neutral complexes of the general structure [Pt(CNC)(Py-R)]. R= 1) -H, [Pt(CNC)(Py-H)]; 2) -CO₂Me, [Pt(CNC)(Py-CO₂Me)]; 3) -PyPh, [Pt(CNC)(Py-Ph)]; 4) -bpyPPh₃²⁺ 2I⁻, [Pt(CNC)(bpy-PPh₃)²⁺ 2I⁻].

All the complexes were isolated in moderate to good yields (30-78%) by drying of the reaction mixture and addition of diethyl ether. Generally no further purification was required, with the exception of [Pt(CNC)(bpy-PPh₃)²⁺ 2I⁻] that was separated from residual [Pt(CNC)(DMSO)] by reprecipitation with dichloromethane and excess diethyl ether. The success of the reactions was confirmed by ¹H-NMR spectroscopy. Indeed, in the ¹H-NMR spectra of the target products, the signals of the corresponding N-bound ligand could be observed, at the expense of the singlet at 3.69 ppm, diagnostic of the presence of a Pt(II)-bound DMSO molecule, which was absent after isolation of the target products (**Figure 2.8**).

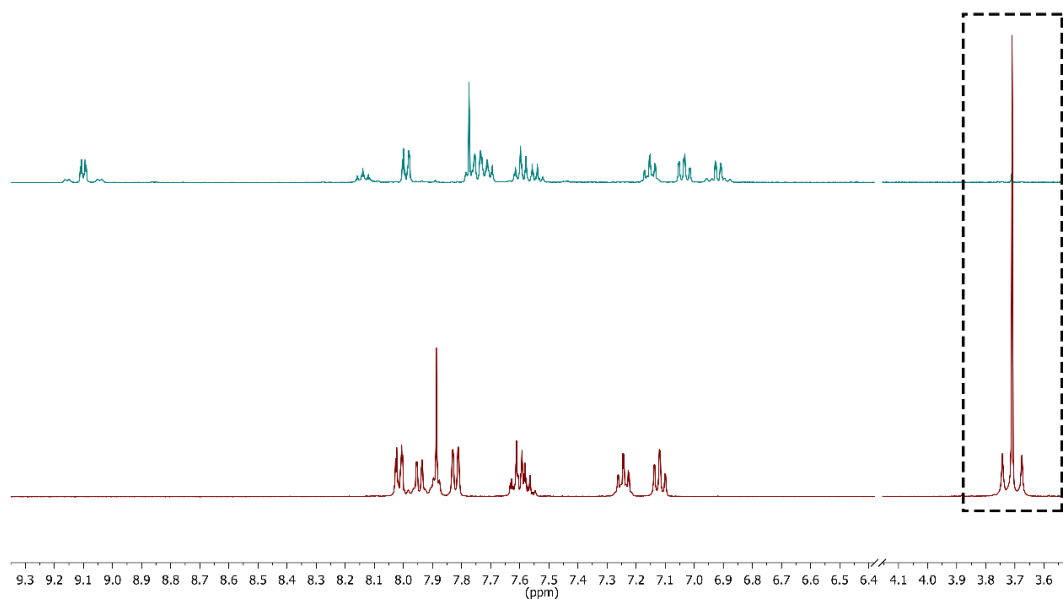


Figure 2.8. ¹H-NMR in acetone-*d*₆ for [Pt(CNC)(Py-H)] (top) and [Pt(CNC)(DMSO)] (bottom). In the spectrum for [Pt(CNC)(DMSO)], the characteristic singlet corresponding to the bound DMSO molecule is highlighted in the box.

2.4.3 X-ray crystallography of the neutral Pt(II) complexes

Single crystals suitable for X-ray diffraction were also obtained for [Pt(CNC)(Py-H)], [Pt(CNC)(Py-CO₂Me)] and [Pt(CNC)(Py-Ph)] via slow evaporation of a dichloromethane solution (**Figure 2.9**).

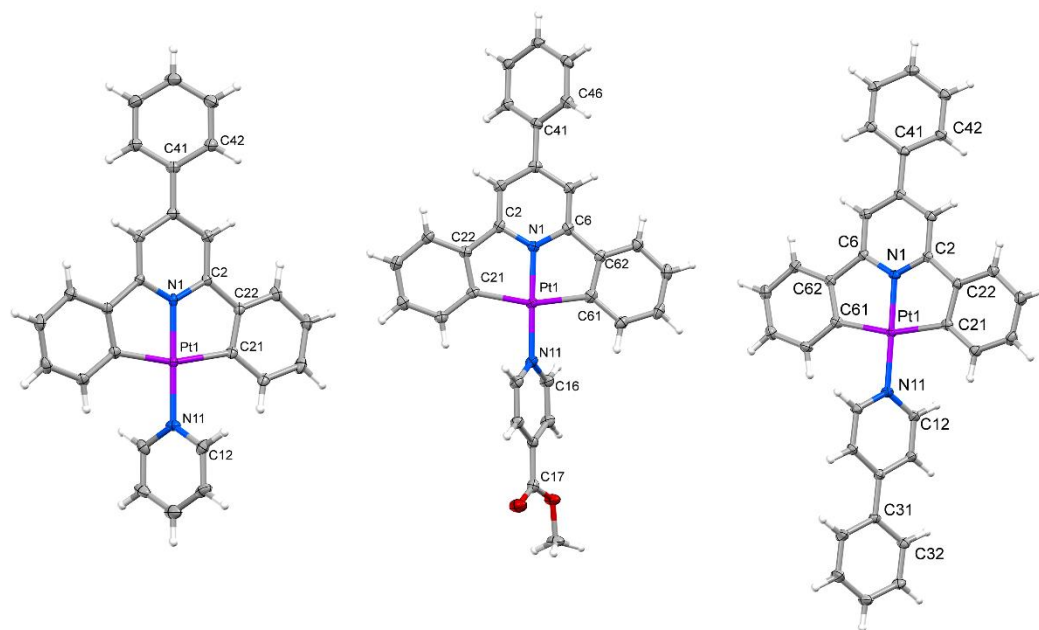


Figure 2.9 X-ray crystal structure of [Pt(CNC)(Py-H)] (left), [Pt(CNC)(Py-CO₂Me)] (middle) and [Pt(CNC)(Py-Ph)] (right) with displacement ellipsoids drawn at the 50% probability level. Lattice solvent molecules are removed for clarity.

Single crystal X-ray diffraction studies were carried out to investigate the structure and packing of the complexes in the solid state. Crystallographic data for the mononuclear complexes are summarised in Appendix A, Table A.3- Table A.10. The mononuclear complexes crystallise adopting a distorted square-planar geometry, where the bite angles of the trans aryl carbon atoms deviate from linearity, with values in the range of 161.5(5)-162.68(19)°, similarly to related platinum C^NC complexes.^{61,142,143,145} In [Pt(CNC)(Py-H)], [Pt(CNC)(Py-CO₂Me)] and [Pt(CNC)(Py-Ph)], instead of DMSO, a pyridine ligand is coordinated to the platinum ion, with the pyridine ring twisted from the plane of the Pt-CNC moiety and a Pt-N distance of 2.013-2.029 Å. These values are not significantly affected by the *para* substituent in the pyridine ring

and are comparable to those observed in literature. The crystal packing of the complexes shows the presence of relatively short interactions between neighbouring cyclometallating ligands ($d(\text{C}-\text{H}) = 2.760 - 2.892 \text{ \AA}$), whereas the shortest Pt-Pt distance observed is 6.016 \AA ($[\text{Pt}(\text{CNC})(\text{DMSO})]$), suggesting the absence of metal-metal interactions in the solid state for all of these materials.¹⁴³ The ancillary ligand in the fourth coordination site affects the packing of the complexes in the solid state. In the crystal packing of $[\text{Pt}(\text{CNC})(\text{DMSO})]$, the molecules are arranged in pairs and in a head-to-tail fashion along the a axis (**Figure 2.10**). Likewise, in the crystal structure of $[\text{Pt}(\text{CNC})(\text{Py}-\text{CO}_2\text{Me})]$, molecules adopt a head-to-tail arrangement, and they are stacked in a zig-zag network. (**Figure 2.11**). Monomers of $[\text{Pt}(\text{CNC})(\text{Py}-\text{H})]$ instead are arranged instead in triangles (**Figure 2.12**), while inspection of the packing of $[\text{Pt}(\text{CNC})(\text{Py}-\text{Ph})]$ (**Figure 2.13**) shows instead a more complex structural arrangement.

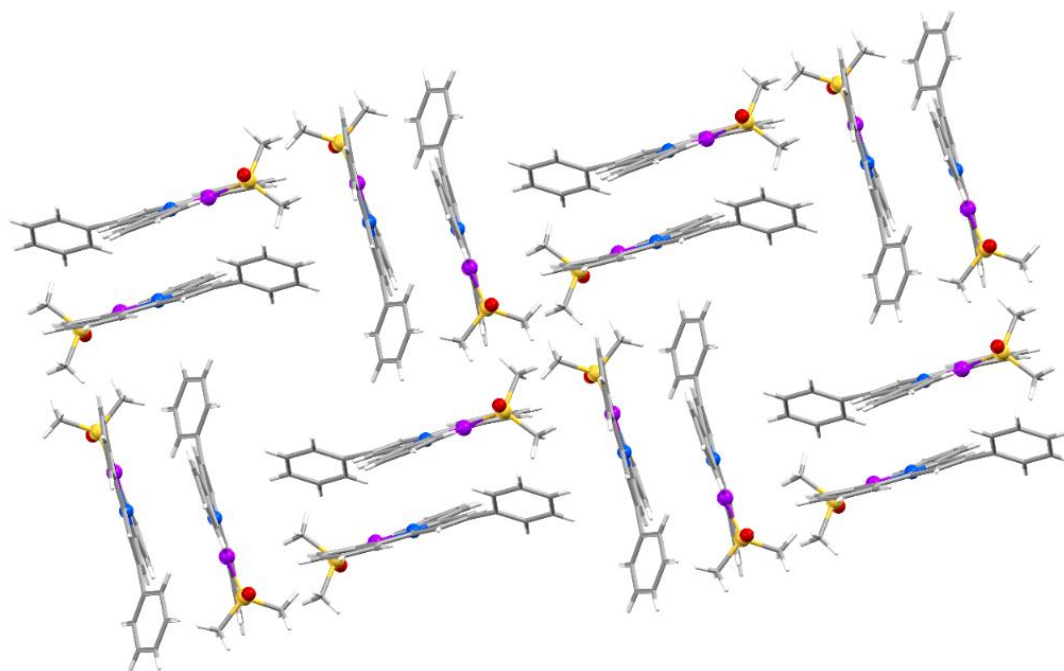


Figure 2.10 Diagrams showing the crystal packing of $[\text{Pt}(\text{CNC})(\text{DMSO})]$ showing the pairs of molecules in a head-to-tail arrangement along the a axis.

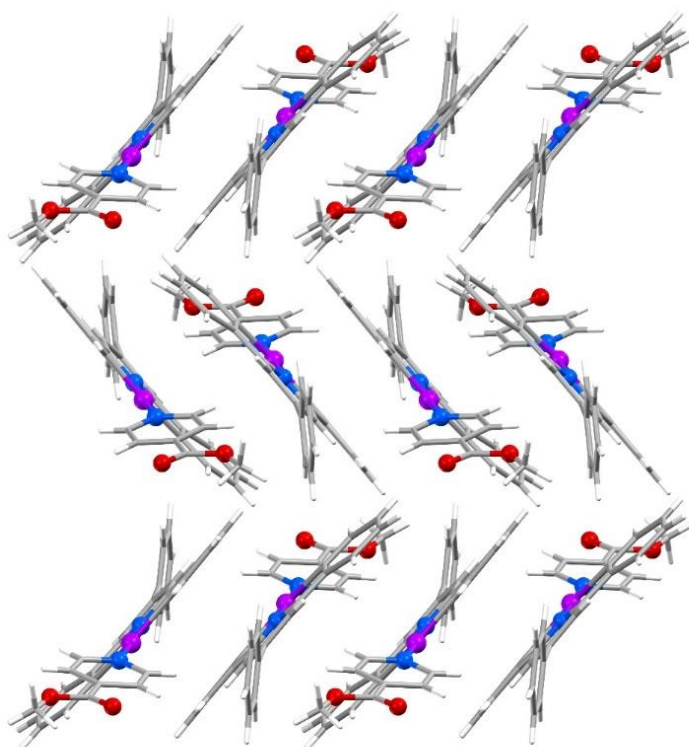


Figure 2.11 Crystal packing of [Pt(CNC)(Py-CO₂Me)]. View along the *a* axis.

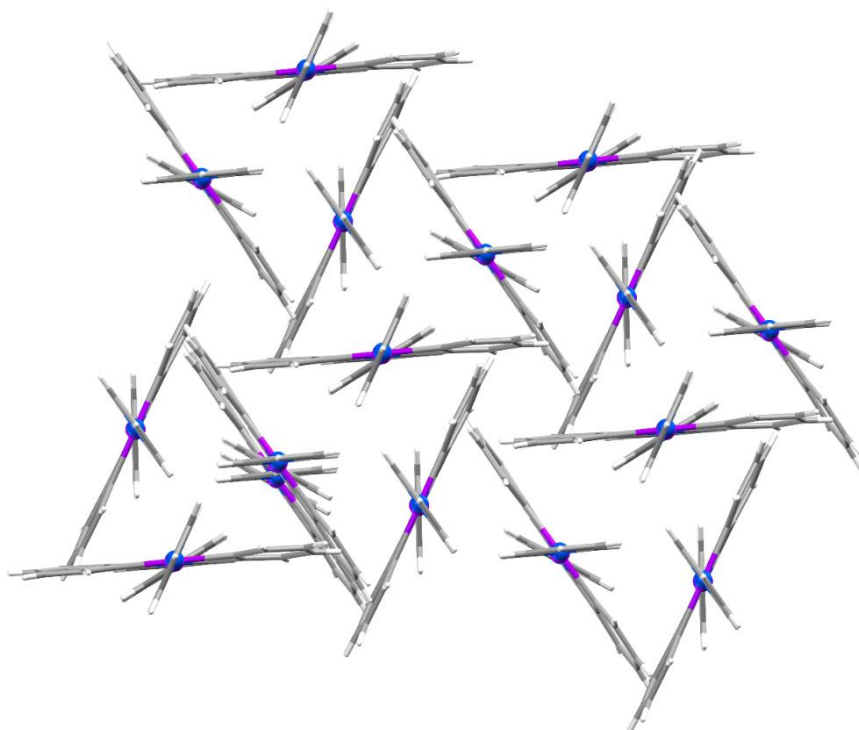


Figure 2.12 View along the *c* axis showing the arrangement in triangles of [Pt(CNC)(Py-H)].

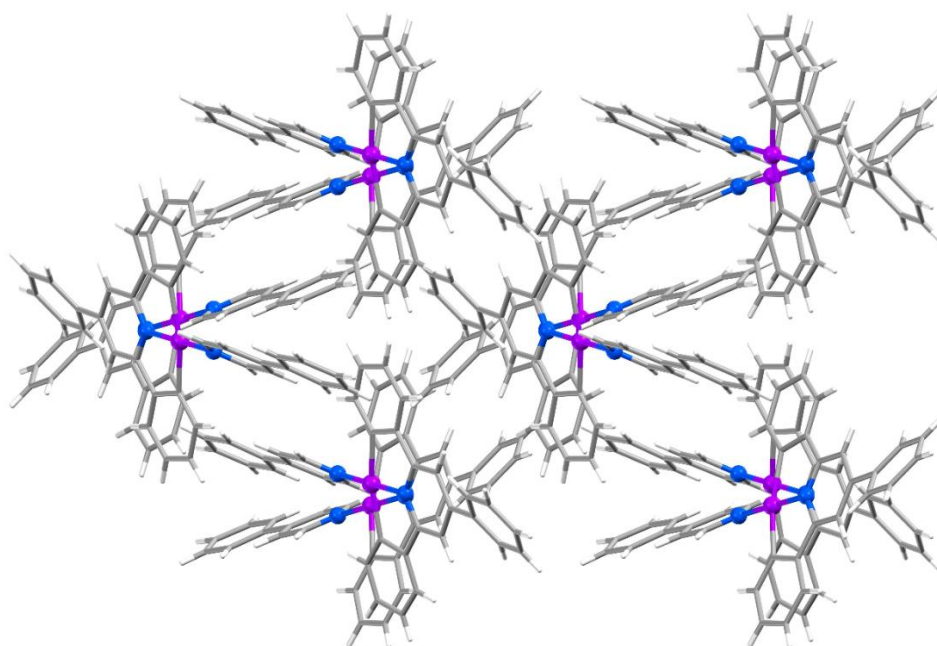


Figure 2.13 View along the *c* axis of the crystal packing of [Pt(CNC)(Py-Ph)].

2.5 Photophysical investigation and aggregation studies

2.5.1 Photophysical properties in dimethylsulfoxide

A summary of the absorption properties of the platinum(II) complexes in dilute DMSO solutions is listed in **Table 2.1**. The absorption spectra of dilute solutions of the complexes in DMSO are shown in **Figure 2.14**. The absorption profiles display two intense absorption bands with maxima at around 280 ($\epsilon = 6-9 \times 10^4 \text{ M}^{-1} \text{ cm}^{-1}$) and 350 nm ($\epsilon = 2-3 \times 10^4 \text{ M}^{-1} \text{ cm}^{-1}$), respectively.

Table 2.1 Absorption data of diluted (10^{-5} M) DMSO solutions of the platinum(II) complexes.

Complex	$\lambda_{\text{abs}} / \text{nm}$ ($10^4 \epsilon [\text{M}^{-1} \text{ cm}^{-1}]$)
[Pt(CNC)(DMSO)]	285 (9.31), 348 (3.61), 441 (0.09), 473 (sh, 0.04), 516 (0.004)
[Pt(CNC)(Py-H)]	286 (6.14), 346 (2.38), 439 (0.08), 477 (sh, 0.03), 515 (0.005)
[Pt(CNC)(Py-CO ₂ Me)]	285 (7.78), 347 (2.96), 441 (0.10), 470 (0.05), 515 (0.008)
[Pt(CNC)(Py-Ph)]	283 (9.69), 348 (3.61), 438 (0.11), 472 (0.05), 514 (0.006)
[Pt(CNC)(bpy-PPh ₃) ²⁺ 2I ⁻]	282 (9.81), 355 (2.04), 512 (0.02)

With reference to previously reported platinum(II) cyclometalated complexes, these high energy bands are assigned to metal-perturbed ligand-centred transitions (¹LC $\pi \rightarrow \pi^*$).^{61,143,145} Tailing from these to lower energies, a less intense band is observed with maximum at around 440 nm and molar absorptivity values of around $0.1 \times 10^4 \text{ M}^{-1} \text{ cm}^{-1}$, characteristic of a metal-to-ligand charge transfer transition (¹MLCT $5d \rightarrow \pi^*$). Furthermore, there are two very weak absorption bands with maxima at around 470 nm ($\epsilon = 0.03-0.05 \times 10^4 \text{ M}^{-1} \text{ cm}^{-1}$) and 515 nm ($\epsilon = 0.004-0.08 \times 10^4 \text{ M}^{-1} \text{ cm}^{-1}$) that are ascribed to spin-forbidden singlet-to-triplet transitions of ³LC and ³MLCT nature.¹⁴²⁻

¹⁴⁴ All the complexes were found to be non-emissive in DMSO solution at room temperature. Similarly, no emission was observed in different organic solvents such as dichloromethane or acetonitrile at room temperature.

This lack of emission is ascribed to the significant distortion experienced by the triplet excited state, in agreement with previous investigations of platinum complexes bound to this type of dicyclometalating ligand.^{55,57}

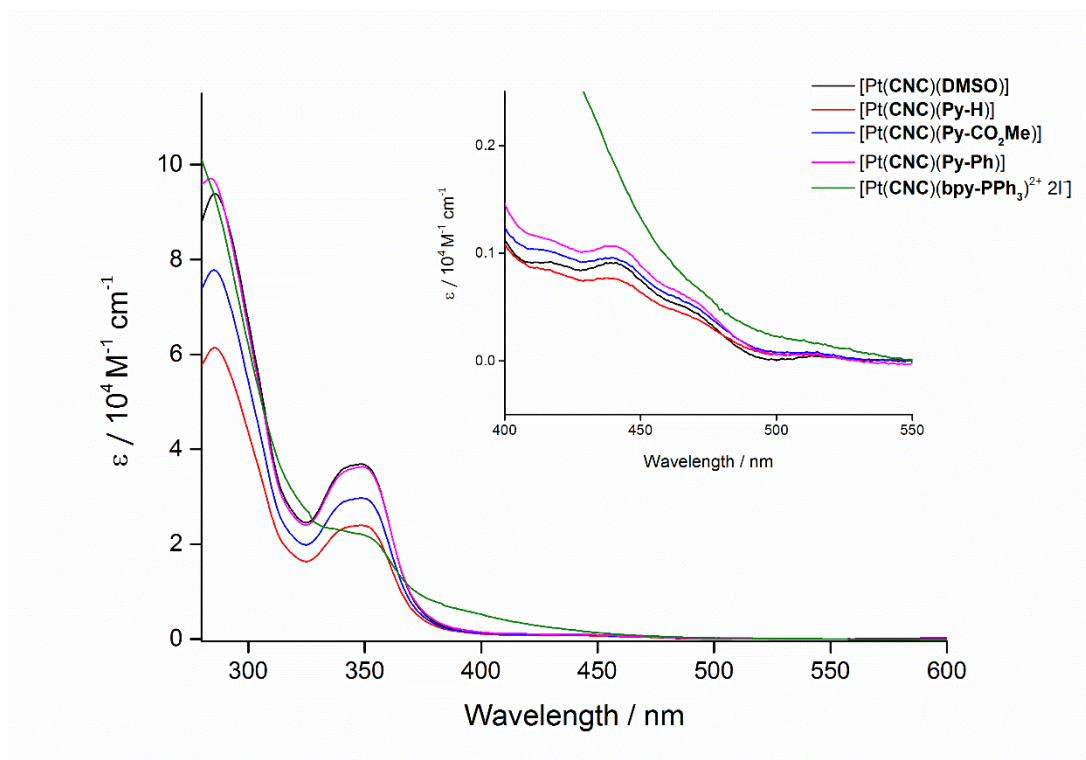


Figure 2.14 Absorption profiles of the neutral platinum complexes in DMSO.

2.5.2 Photophysical properties in H₂O (0.1% DMSO)

Cellular and bacterial staining are usually performed in aqueous media, therefore it was necessary to study the Pt compounds under these conditions. The final aqueous mixture used for the photophysical investigation in this section contained a 0.1% of DMSO.

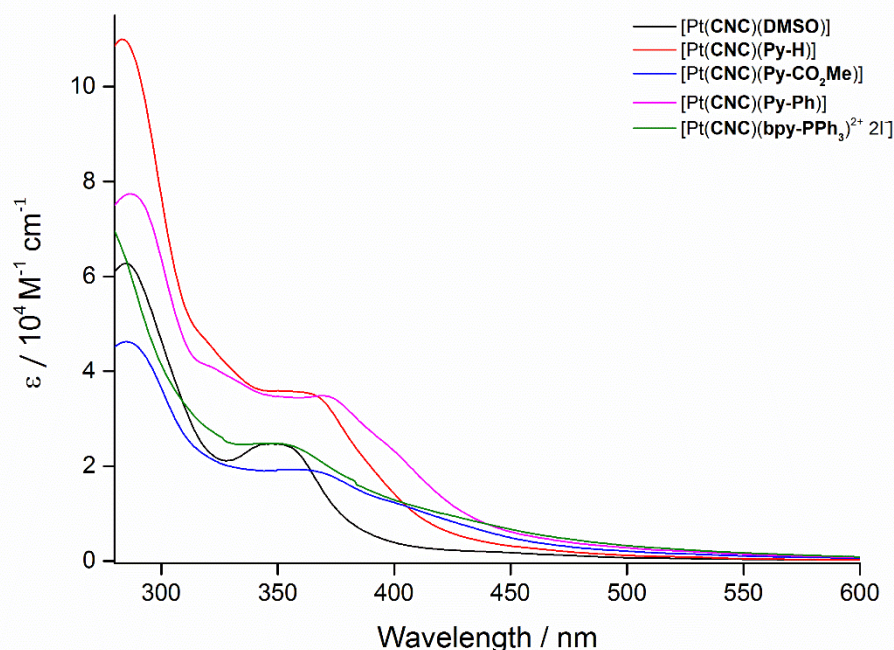


Figure 2.15 Absorption profiles of the neutral platinum complexes in H₂O (0.1% DMSO).

The absorption profiles of the complexes in aqueous solvent (**Figure 2.15**) follow the same trend as described in section 2.5.1 for DMSO solutions. However, a general broadening of the bands centred at around 350 nm towards the visible region of the spectrum is observed. A summary of the absorption properties of the platinum(II) complexes in aqueous solutions is listed in **Table 2.2**. Notably, all the complexes except for [Pt(CNC)(bpy-PPh₃)²⁺ 2I⁻] experience an emission switch-on in the aqueous environment, with the appearance of a broad band with maxima at 650-700 nm (**Table 2.3**). A comparison of the emission spectra in pure DMSO and in H₂O (0.1% DMSO) is shown in **Figure 2.16** and **Figure 2.17**, for [Pt(CNC)(DMSO)] and

[Pt(CNC)(Py-Ph)] as examples. The same comparisons for [Pt(CNC)(Py-H)] and [Pt(CNC)(Py-CO₂Me)] can be found in Appendix A, figures A1– A2.

Table 2.2 Absorption data of diluted (10⁻⁵ M) H₂O (0.1% DMSO) solutions of the platinum(II) complexes.

Complex	$\lambda_{\text{abs}} / \text{nm}$ ($10^4 \epsilon [\text{M}^{-1} \text{cm}^{-1}]$)
[Pt(CNC)(DMSO)]	285 (6.27), 352 (2.45), 442 (0.19), 474 (0.12), 516 (0.06)
[Pt(CNC)(Py-H)]	284 (10.99), 365 (3.46), 466 (0.24), 525 (0.09)
[Pt(CNC)(Py-CO ₂ Me)]	286 (4.62), 373 (1.79), 528 (0.15)
[Pt(CNC)(Py-Ph)]	288 (7.73), 375 (3.39), 528 (0.20)
[Pt(CNC)(bpy-PPh ₃) ²⁺ 2I ⁻]	283 (6.59), 359 (2.38), 440 (sh, 0.78)

The emission profiles for all the emissive complexes are reported in **Figure 2.18**. The featureless bands are attributed to aggregation induced emission, favoured by the presence of water acting as an anti-solvent.^{88,115,128,146} This also suggests that in the case of pure DMSO solutions, the solvation capacity of the solvent overcomes the tendency to form aggregates.¹⁴⁷ Only in the case of [Pt(CNC)(DMSO)], a hint of vibronic progression is visible in the 500-600 nm region, with spacing estimated around 1300 cm⁻¹, which is characteristic of the vibrational frequencies of the aromatic skeleton of the CNC ligand. The structured contribution to the emission band is likely to be originating from residual ³LC excited states. The low quantum yields and the relatively short excited state lifetimes are in agreement with the values measured in aqueous solutions for related platinum N[^]N[^]N and C[^]N[^]N complexes.^{66,148,149} The broadening of the absorption bands observed for the complexes in the aqueous environment is likely to be due to the formation of aggregates. It has been previously reported that upon ground state aggregation, the lower energy bands of the absorption spectra may not obey Beer's Law, provided that the association constants of the complexes are big enough to be observable in the UV-Vis absorption spectra.⁶⁷

Unfortunately, however, concentration-dependence studies could not be performed in these conditions, as the addition of water reduced the solubility of the complexes causing turbidity of the solution. For the same reasons, the quantum yields could only be estimated by using an integrating sphere.

On the other hand, the fact that [Pt(CNC)(bpy-PPh₃)²⁺ 2I⁻] does not show any emission in the aqueous mixture is likely to be due to the bulkiness of the alkylated bipyridine.⁶⁷ Furthermore, the charges of this ancillary ligand increase the overall solubility of the complex and this may disfavour the aggregation process, and therefore the emission enhancement.

Table 2.3 Photophysical properties of the platinum complexes from 10⁻⁵ M aqueous solutions (0.1% DMSO)

Complex	λ_{em} [nm]	τ_{aer} [ns] ^a	Φ_{aer} %
[Pt(CNC)(DMSO)]	650	52 (83), 20 (17)	0.80
[Pt(CNC)(Py-H)]	705	22 (85), 9 (15)	0.54
[Pt(CNC)(Py-CO ₂ Me)]	700	42 (85), 12 (15)	0.43
[Pt(CNC)(Py-Ph)]	690	25 (86), 10 (14)	0.49
[Pt(CNC)(bpy-PPh ₃) ²⁺ 2I ⁻]	_b	_b	_b

^aFor the biexponential excited state lifetime (τ), the relative weights of the exponential curves are reported in parentheses. ^bNot emissive.

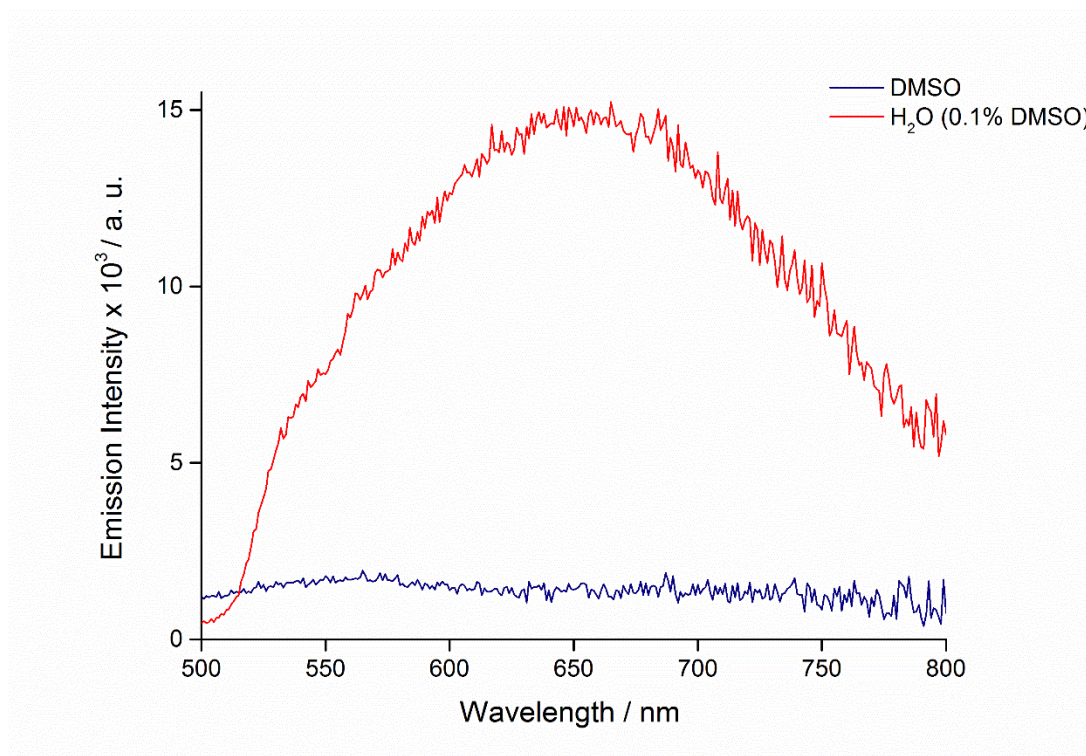


Figure 2.16 Emission profiles of [Pt(CNC)(DMSO)] from a diluted (10^{-5} M) DMSO (blue trace) and H₂O (0.1% DMSO, red trace) solution.

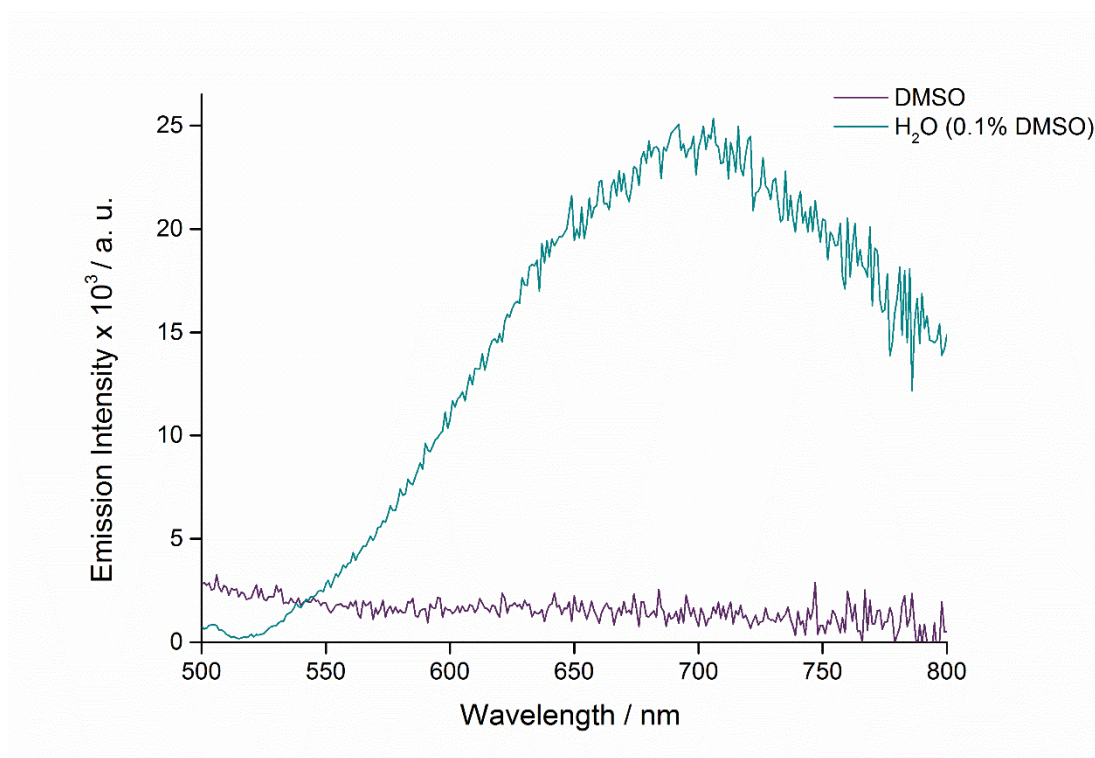


Figure 2.17 Emission profiles of [Pt(CNC)(Py-Ph)] from a diluted (10^{-5} M) DMSO (purple trace) and H₂O (0.1% DMSO, cyan trace) solution.

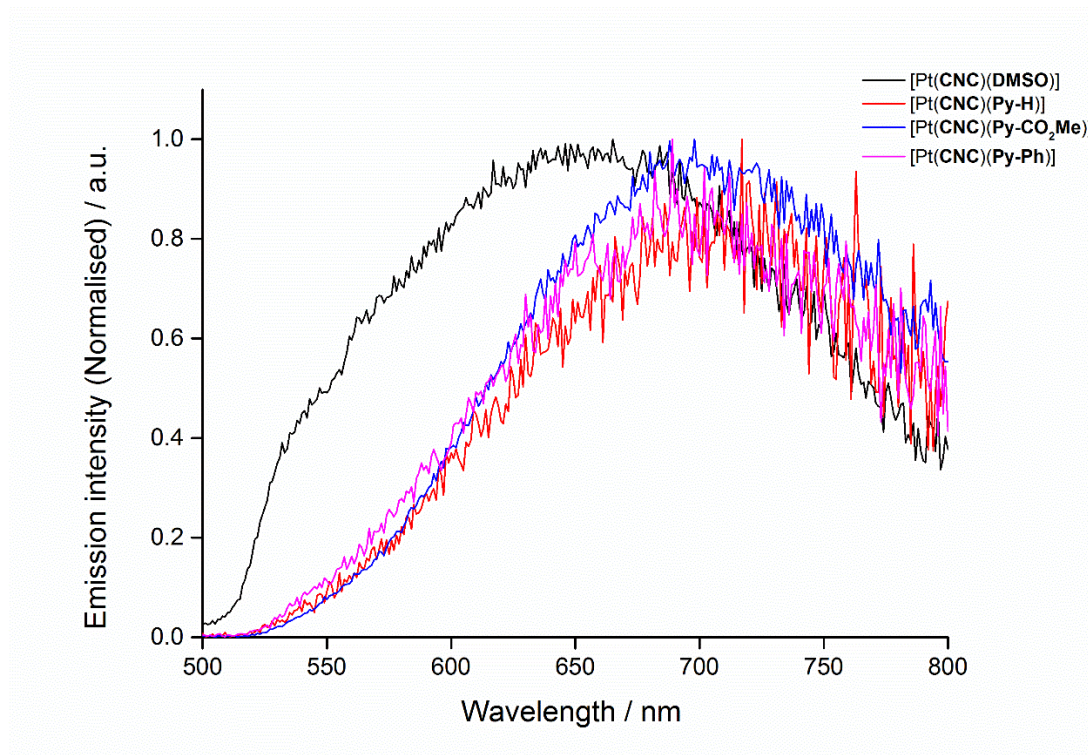


Figure 2.18 Emission profiles of the emissive platinum complexes from a diluted (10^{-5} M) H_2O (0.1% DMSO) solution. (Note: $[\text{Pt}(\text{CNC})(\text{bpy-PPH}_3)^{2+} 2\text{I}^-]$ is not emissive in these conditions).

2.5.3 Photophysical properties in the solid state and frozen matrix

To further investigate the aggregation properties of the platinum complexes in different environments, the photophysical characterisation of the complexes has been carried out in the solid state as well as in frozen glass at 77 K (**Table 2.4**). Consistently with what observed in aqueous solution all the complexes excluding [Pt(CNC)(bpy-PPh₃)²⁺ 2I⁻] exhibit enhanced emission properties in the solid state (**Figure 2.19**). [Pt(CNC)(DMSO)] shows a broad yet relatively structured emission, with spacing of 1209 and 1275 cm⁻¹, again diagnostic for the vibrations of the aromatic skeleton of the tridentate ligand.^{6,8,10} On the other hand, the rest of the emissive complexes display a very broad and unstructured band at around 700 nm. These emission energies are comparable to the ones observed in solution, therefore the emission in the solid state is assigned to the formation of aggregates arising from the close intermolecular contacts between the aromatic ligands, which are observed in the crystal lattice.⁶⁷

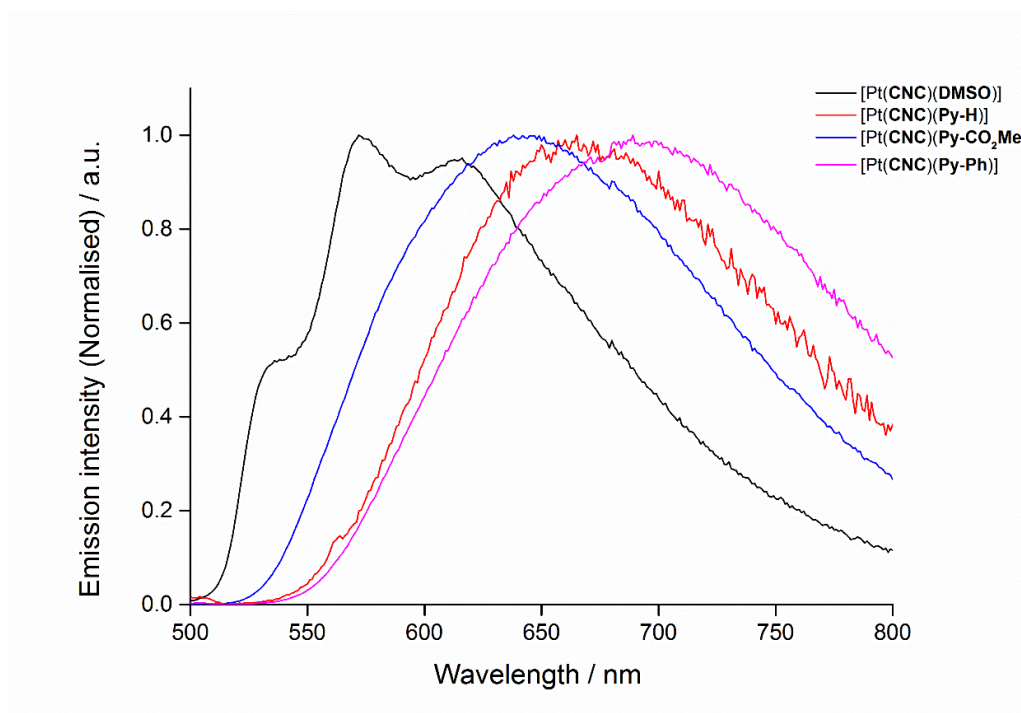


Figure 2.19 Emission profiles of the emissive platinum complexes from a solid thin film. (Note: [Pt(CNC)(bpy-PPh₃)²⁺ 2I⁻] is not emissive in these conditions).

The emission of [Pt(CNC)(DMSO)] as monomeric species can be easily detected at 77 K in a 10^{-5} M butyronitrile glass (**Figure 2.20**, black line). Indeed, the complex exhibits a highly structured green emission with vibronic spacing of about 1300 cm^{-1} , typical of the skeletal vibrational frequency of the C^NC ligand, and lifetimes up to 12 μs . These bands are in agreement with the emission profiles reported for related DMSO-bound Pt complexes of the general formula [Pt(R-CNC)(DMSO)] and are assigned to the phosphorescence of metal-perturbed $^3\pi\text{-}\pi^*$ states.^{61,129,145,151} The shoulder centred at 600 nm might suggest a hint of aggregation. This is supported by the slightly biexponential lifetime, which contains a shorter-lived component with a relative weight of 14%. [Pt(CNC)(Py-H)], [Pt(CNC)(Py-CO₂Me)] and [Pt(CNC)(Py-Ph)] show instead a red shifted, broad and unstructured band centred at around 650-660 nm (**Figure 2.20**). It is noteworthy that these bands remain dominant even at lower concentrations of 10^{-6} or 10^{-7} M, depending on the ancillary ligand (**Figures 2.21-2.23**). A significant contribution of the structured high energy bands is visible for [Pt(CNC)(Py-H)] and [Pt(CNC)(Py-CO₂Me)]. For these complexes, the excitation spectrum monitored at the low-energy band is different to the ones monitored at the high energy bands and the lifetime significantly shorter. The excitation spectra for [Pt(CNC)(Py-H)] are reported, as example, in **Figure 2.24**. The excitation spectra for the complexes in butyronitrile are reported in Appendix A, Figures A3 – A6. As reported for related platinum(II) complexes,^{142,145} the difference in excitation spectra and the shorter lifetimes suggest that the low energy emission bands are likely to originate from emissive states resulting from aggregation or oligomerisation of the complexes in the glassy matrix, due to Pt-Pt or $\pi\text{-}\pi$ interaction.^{67,152} This is further supported by the fact that [Pt(CNC)(bpy-PPh₃)²⁺ 2I⁻], bearing a bulky and charged ancillary ligand, shows an emission profile that is very similar to the one observed for [Pt(CNC)(DMSO)]. Indeed, the emission profile for [Pt(CNC)(bpy-PPh₃)²⁺ 2I⁻] is dominated by high energy bands in the range of 490-550 nm, typical of excited states arising from non-aggregate species, whereas the contribution of the shorter-lived, low-energy band is less obvious.

Table 2.4 Summary of the photophysical properties of the platinum complexes in the solid state and glassy matrix.

Complex	Medium (T [K])	λ_{em} [nm]	τ_{aer} [ns] ^a	Φ_{aer} %
[Pt(CNC)(DMSO)]	Solid film (298)	553sh, 572, 617	200	1.16
	Butyronitrile glass (77)	513 553 600sh	12006 11263 2261 (14), 9764 (86)	
[Pt(CNC)(Py-H)]	Solid film (298)	665	148	0.82
	Butyronitrile glass (77)	494 530 660	7121 7897 1852	
[Pt(CNC)(Py-CO ₂ Me)]	Solid film (298)	645	262	0.75
	Butyronitrile glass (77)	492 527 648	7248 7153 2723	
[Pt(CNC)(Py-Ph)]	Solid film (298)	695	323 (84), 43 (16)	0.78
	Butyronitrile glass (77)	657	1925	
[Pt(CNC)(bpy-PPh ₃) ²⁺ 2I ⁻]	Solid film (298)	-	-	-
	Butyronitrile glass (77)	490 522 559 627	5828 6381 6916 1392	

^aFor the biexponential excited state lifetime (τ), the relative weights of the exponential curves are reported in parentheses. ^bNot emissive.

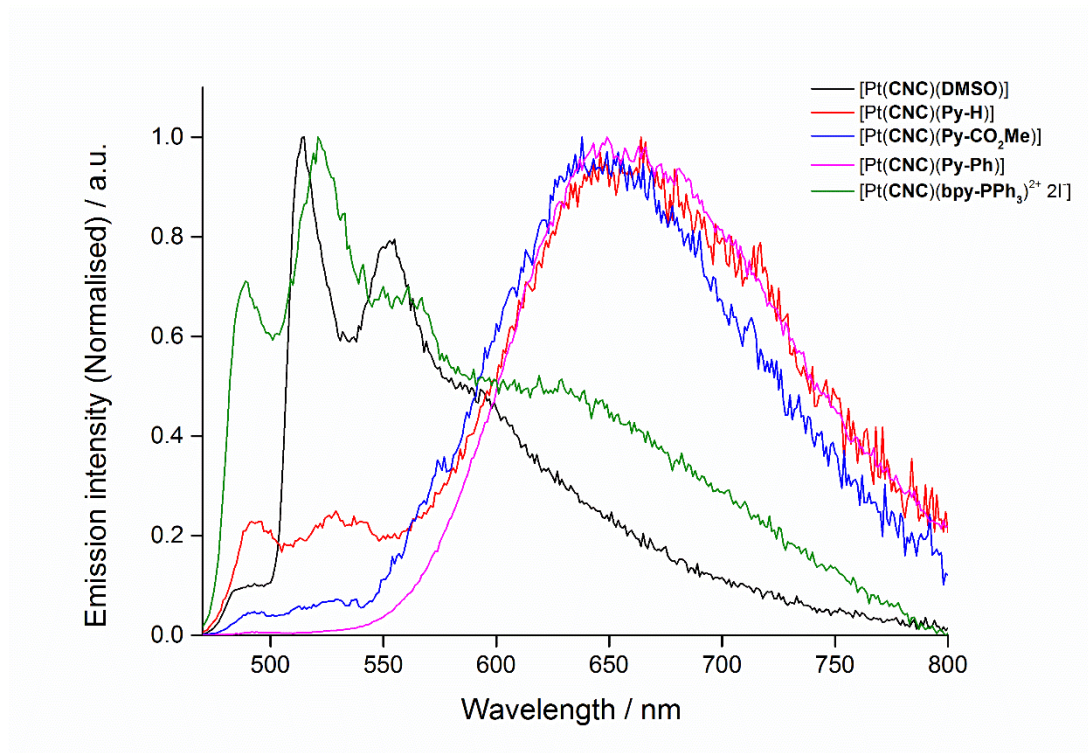


Figure 2.20 Emission profiles of the platinum complexes from a 10^{-5} M Butyronitrile glass (77K).

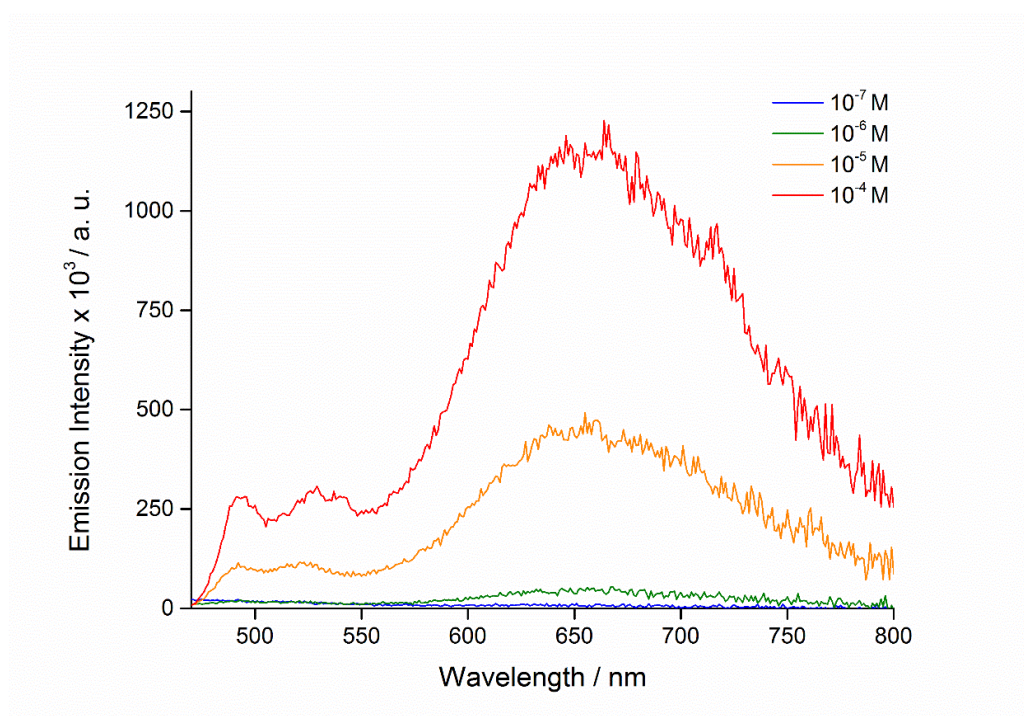


Figure 2.21 Emission spectra for [Pt(CNC)(Py-H)] at different concentrations in a Butyronitrile glass.

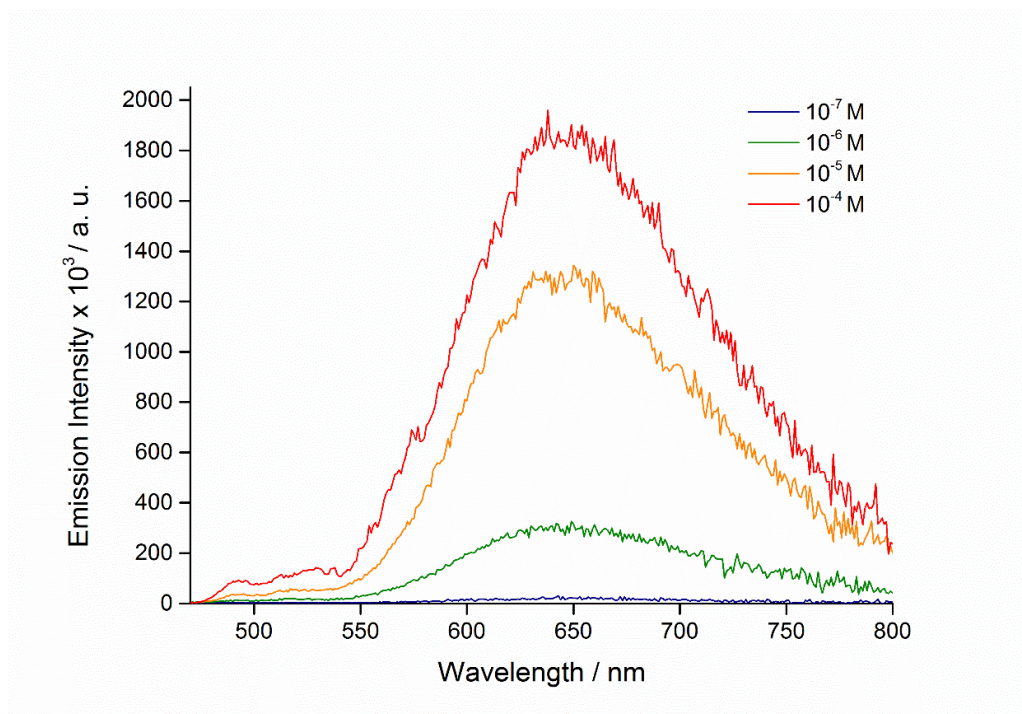


Figure 2.22 Emission spectra for [Pt(CNC)(Py-CO₂Me)] at different concentrations.

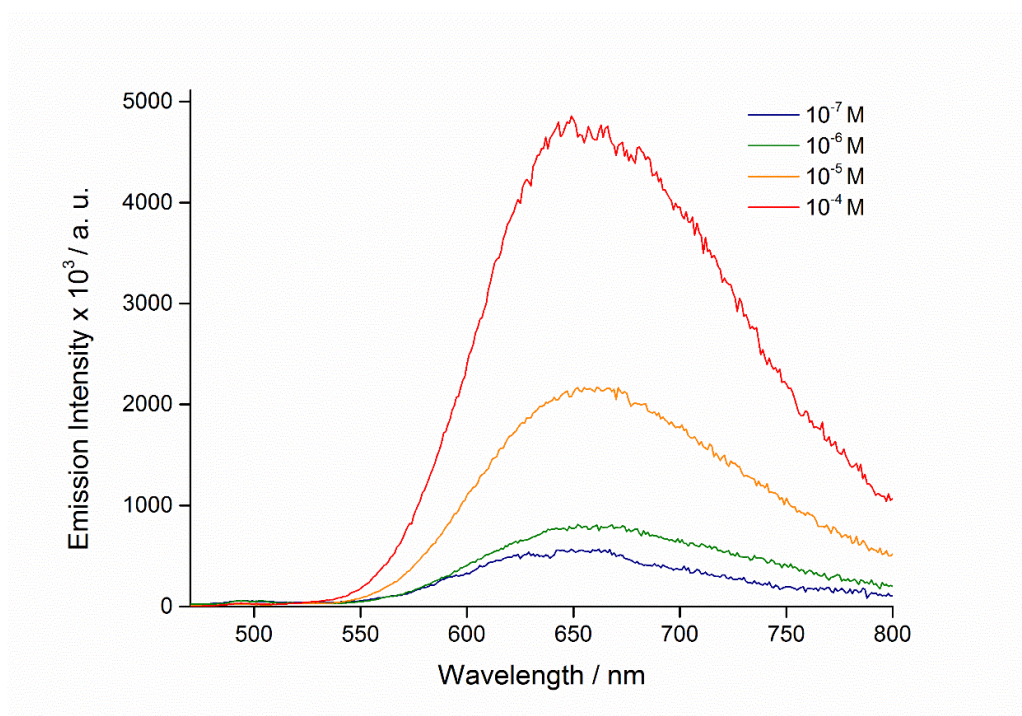


Figure 2.23 Emission spectra for [Pt(CNC)(Py-Ph)] at different concentrations.

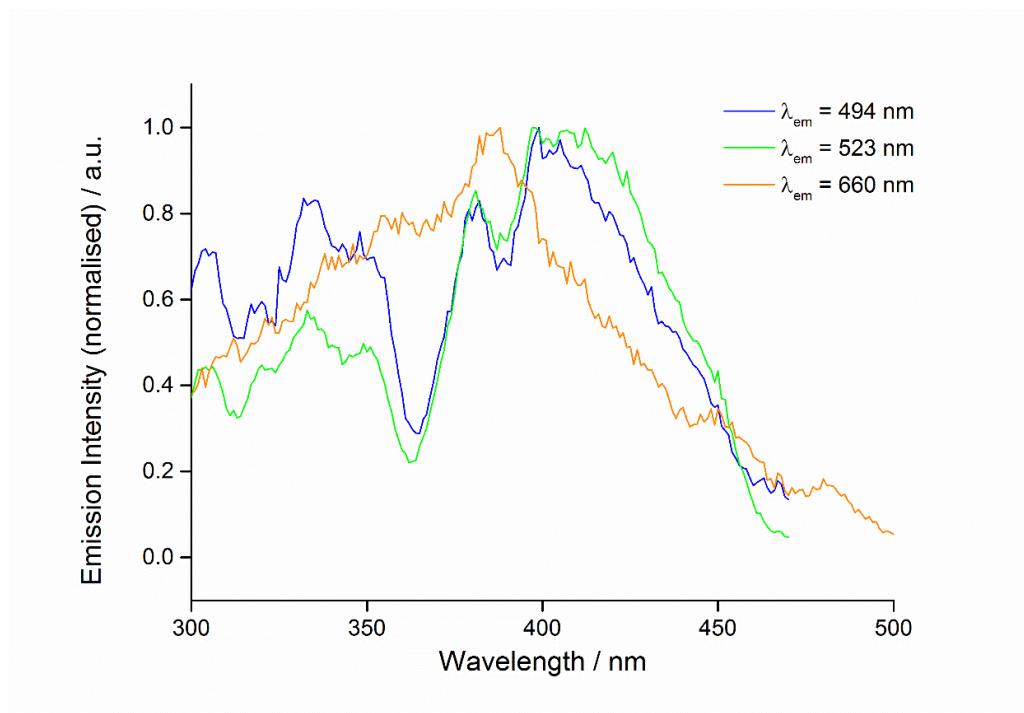


Figure 2.24 Excitation spectra for [Pt(CNC)(Py-H)] at the emission maxima.

2.6 Biological investigation of the neutral dicyclometalated platinum(II) complexes

2.6.1 Cellular uptake and cytotoxicity studies in eukaryotic cells

The cellular uptake for the synthesised platinum complexes was investigated by means of ICP-MS (**Figure 2.25**). Adenocarcinomic human alveolar basal epithelial A549 cells were used in this study, and the protocol for the uptake analyses is described in detail in the Experimental Section 2.8.5. In brief, the A549 cells were incubated with the complexes in cell culture medium (Dulbecco's Modified Eagle Medium – DMEM) at a concentration of 20 μM (0.1% DMSO) for 30 minutes at 37°C.

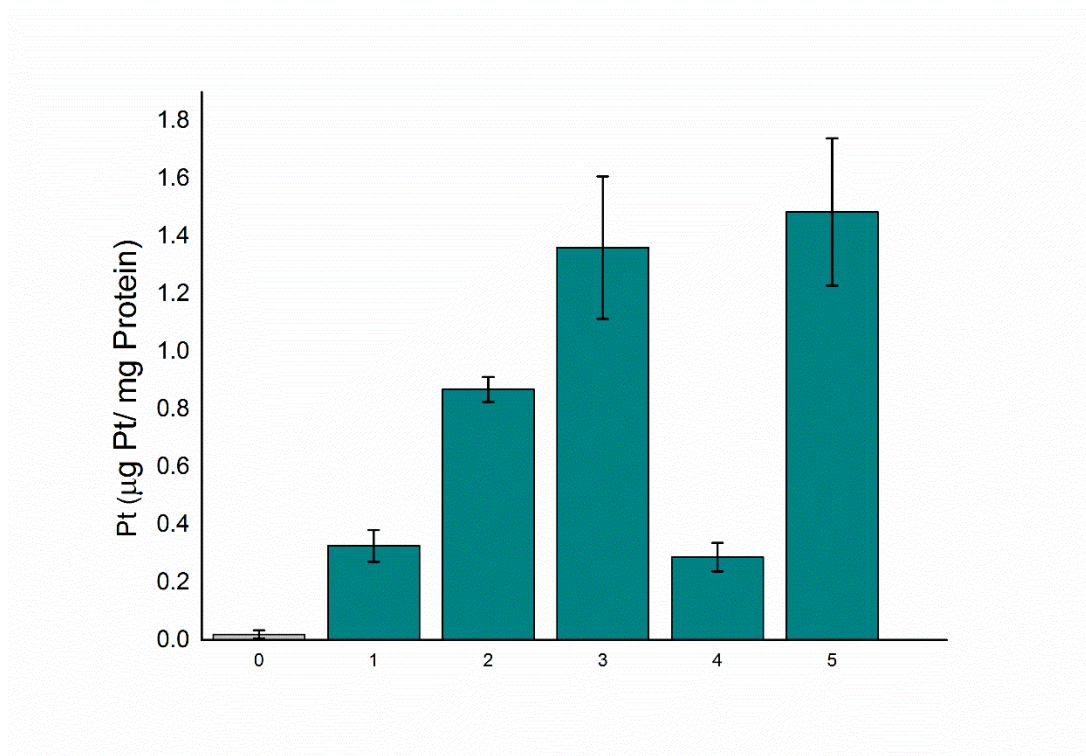


Figure 2.25 Accumulation of Pt reported as μg of Pt on mg of protein. 0) Control (0.1% DMSO in DMEM medium); 1) $[\text{Pt}(\text{CNC})(\text{DMSO})]$; 2) $[\text{Pt}(\text{CNC})(\text{Py-H})]$; 3) $[\text{Pt}(\text{CNC})(\text{Py-CO}_2\text{Me})]$, 4) $[\text{Pt}(\text{CNC})(\text{Py-Ph})]$; 5) $[\text{Pt}(\text{CNC})(\text{bpy-PPh}_3)^{2+} 2\text{I}^-]$.

After this time, cells lysates were prepared, and the amount of proteins determined with the Bradford Assay. The cell sample then underwent acid digestion and analysed with ICP-MS to determine the platinum content. Notably, all the complexes show relatively high cellular uptake after 30 minutes incubation, although a comparison with previously reported platinum(II) complex has not been attempted due to the lack of reports on uptake values for parent compounds. Amongst the complexes in the series, [Pt(CNC)(Py-CO₂Me)] and [Pt(CNC)(bpy-PPh₃)²⁺ 2I⁻] exhibit higher accumulation in cells. While for [Pt(CNC)(bpy-PPh₃)²⁺ 2I⁻] this could be due to the ancillary ligand being positively charged, the improved uptake of [Pt(CNC)(Py-CO₂Me)] could be due to the presence of the ester functionality. In fact, using ester bonds to promote the cellular uptake is a common strategy in the design of drugs and prodrugs, where the delivery pathway of the target small molecule exploits the activity of endogenous, non-specific esterases.^{153,154}

The cytotoxicity of the platinum complexes was assessed by incubating A549 cells with the complexes at 20 μM and 40 μM concentrations for 3 hours, followed by treatment with Alamar Blue cell viability reagent (**Figure 2.26**). [Pt(CNC)(DMSO)], [Pt(CNC)(Py-H)], [Pt(CNC)(Py-CO₂Me)] and [Pt(CNC)(Py-Ph)] did not show any effect on metabolic activity at the concentration used for cellular imaging (20 μM). These results are in line with the trend reported for related neutral platinum complex bearing N[^]C[^]N or N[^]N[^]C ligands, that showed minimal or no cytotoxic effect, with viability values ranging from 80% to 97% in a different range of incubation conditions.^{59,66,137,155,156} On the other hand, [Pt(CNC)(bpy-PPh₃)²⁺ 2I⁻] was found to be more cytotoxic at the same concentration, with a viability value of around 60% after 3 hours. This behaviour is likely to be due to the presence of the cationic triphenylphosphonium pendant causing the disruption of the mitochondrial membrane, as observed for a previously reported family of platinum(II) complexes.¹⁵⁷ All the synthesised complexes showed an increased toxic effect when dosed at a 40 μM concentration for 3 hours, conditions that far exceeded those used in the imaging studies. On comparing the ICP-MS and cytotoxicity data, it is not possible to correlate the cytotoxicity to the relative amount of complex that has been internalised within the cells. In fact, [Pt(CNC)(Py-CO₂Me)] does not exhibit any toxic effect at a 20 μM concentration, despite showing a relative uptake value that is comparable to the one found for the more cytotoxic [Pt(CNC)(bpy-PPh₃)²⁺ 2I⁻].

These results suggest that the cytotoxic effect for this family of complexes might be related to their different cellular localisation.

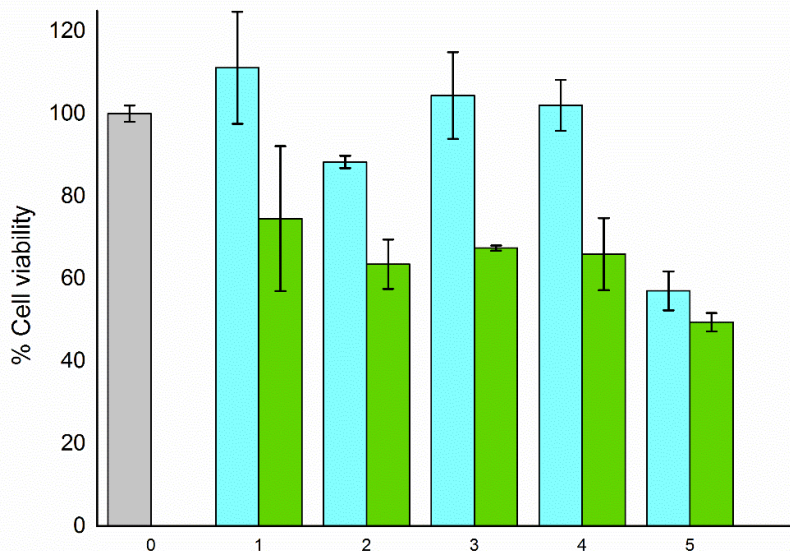


Figure 2.26 Alamar Blue Cytotoxicity Assay for the platinum(II) complexes in A549 cells, with fluorescence output reported as a percentage of the control cells. Pt(II) doses: 20 μM (light blue bars) and 40 μM (green bars). 0) Control (0.1% DMSO in DMEM medium); 1) [Pt(CNC)(DMSO)]; 2) [Pt(CNC)(Py-H)]; 3) [Pt(CNC)(Py-CO₂Me)], 4) [Pt(CNC)(Py-Ph)]; 5) [Pt(CNC)(bpy-PPh₃)²⁺2I⁻].

2.6.2 Cytotoxicity studies on bacterial cells

The toxicity of the platinum complexes towards bacterial cells was assessed by monitoring the bacterial growth rates in the presence of the complexes at the concentration used for the imaging experiments (20 μM in growth media, 0.1% DMSO). The gram-negative strain *Escherichia coli* (*E. coli*) and the gram-positive *Bacillus cereus* (*B. cereus*) were chosen as model species for this study and grown in Lysogeny Broth (LB Broth) and Nutrient Broth respectively. The protocol for determining the kinetics of growth is described in Experimental section 2.8.8, and the resulting graphs are reported in **Figure 2.27**. While the platinum complexes did not show any toxic effect towards A549 eukaryotic cells (Section 3.5.1), they completely inhibited the growth of *B. cereus* at a concentration of 20 μM (12 μg/mL).

As discussed in Chapter 1, Section 1.6.2, studies of transition metal complexes as antibacterial agents have been reported by Crowley *et al.* for a family of rhenium(I) and ruthenium(II) triazole complexes,^{108,110} as well as Keene and co-workers, that focus on a family of ruthenium(II) species.^{102,106} It should be noted however, that the antimicrobial activity of these compounds has been tested towards different microbial species, including *Staphylococcus aureus* (*S. aureus*) and methicillin-resistant *S. aureus*. On the other hand, the synthesised platinum complexes do not affect the growth of *E. coli*. Similar behavior is observed for some of the metal complexes reported by the groups mentioned above, and by our group, that recently reported about a family of methylated iridium complexes showing antimicrobial activity towards the gram-positive *Deinococcus radiodurans* (*D. radiodurans*) but observed no toxic effect towards *E. coli*.¹⁵⁸ While the mechanisms ruling the toxicity effect of transition metal complexes towards different bacterial strains are not well understood, the difference in toxicity towards gram-positive and gram-negative bacteria is likely to be due to their different cell wall.

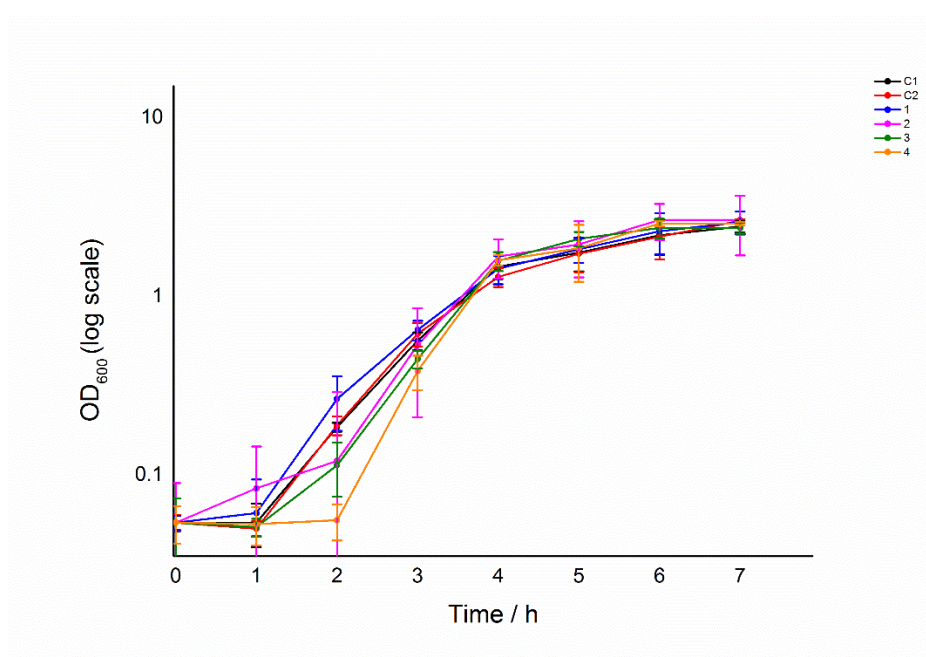
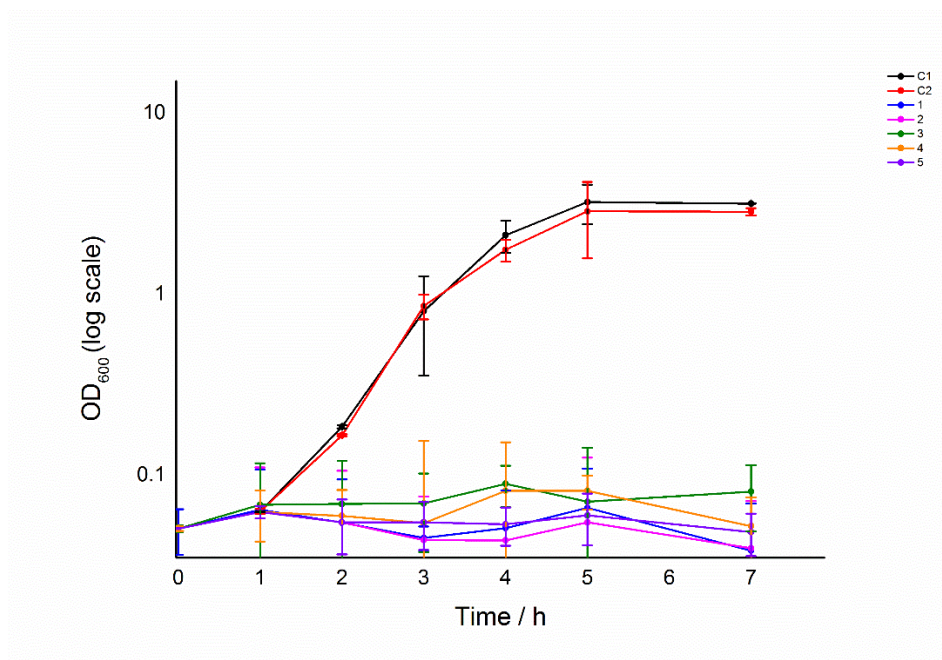


Figure 2.27 Kinetics of growth of *B. cereus* (top) and *E. coli* (bottom) at 37 °C in the presence of the platinum(II) complexes. C1) Untreated culture, C2) 0.1% DMSO control, 1) [Pt(CNC)(DMSO)]; 2) [Pt(CNC)(Py-H)]; 3) [Pt(CNC)(Py-CO₂Me)], 4) [Pt(CNC)(Py-Ph)]; 5) [Pt(CNC)(bpy-PPh₃)²⁺ 2I⁻]. Note: the experiment for [Pt(CNC)(bpy-PPh₃)²⁺ 2I⁻] incubated with *E. coli* was performed separately and the resulting growth curves are reported in Appendix A, Figure A7.).

2.6.3 Bio-imaging studies

The uptake of the platinum complexes within eukaryotic cells and bacterial cells was investigated *via* confocal microscopy. A549 cells were incubated with the complexes at a concentration of 20 μM in the growth media (0.1% DMSO) at 37°C. The complexes were excited at 405 nm and imaged in an interval consistent with the emission profile recorded from aqueous solution in a cuvette (section 2.5.2). Unfortunately, despite the same protocol described for ICP-MS being followed, no emission coming from the complexes could be detected in the expected emission interval, even by increasing the dosing or incubation time, raising the laser power and optimising the acquisition parameters. **Figure 2.28** shows confocal microscopy images are shown for [Pt(CNC)(DMSO)] as an example. Similarly, no emission from the complexes could be detected in *E. coli* and *B. cereus* (**Figure 2.29**). This result appears to be in contrast with the result obtained from the ICP-MS studies on eukaryotic cells, which instead showed that the platinum complexes were internalised within cells. As discussed in Section 2.5.2, however, these platinum complexes are emissive due to aggregation induced emission. Despite the complexes exhibiting cellular uptake, the aggregation process may not occur in the cellular or bacterial cytoplasm, or the quantum yield of the aggregate may be too low to be detectable.

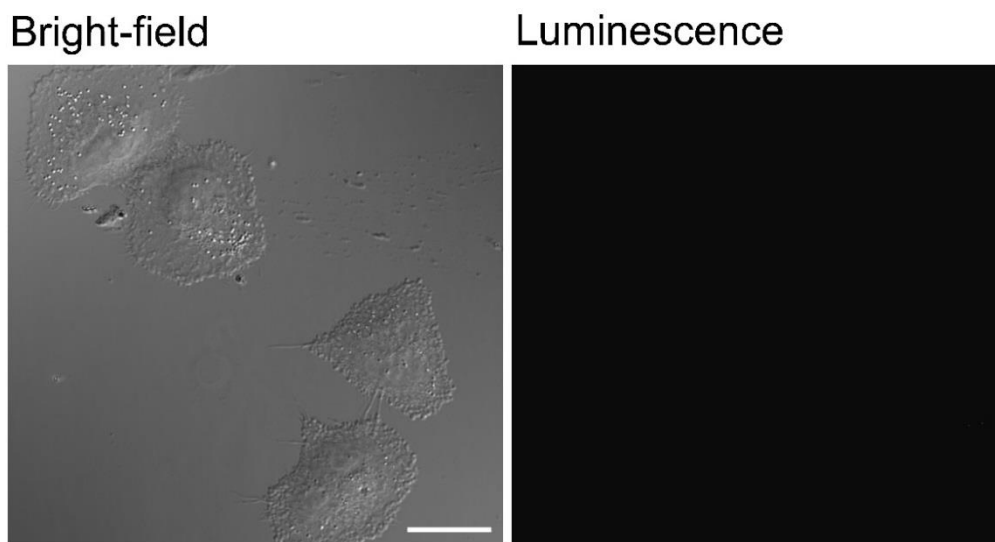


Figure 2.28 Confocal microscopy images of A549 cells dosed with [Pt(CNC)(DMSO)] ($\lambda_{\text{ex}} = 405 \text{ nm}$, $\lambda_{\text{em}} = 500\text{-}700 \text{ nm}$). Left: bright-field image showing A594 cells. Right: confocal image showing the absence of a detectable signal. Scalebar 20 μm .

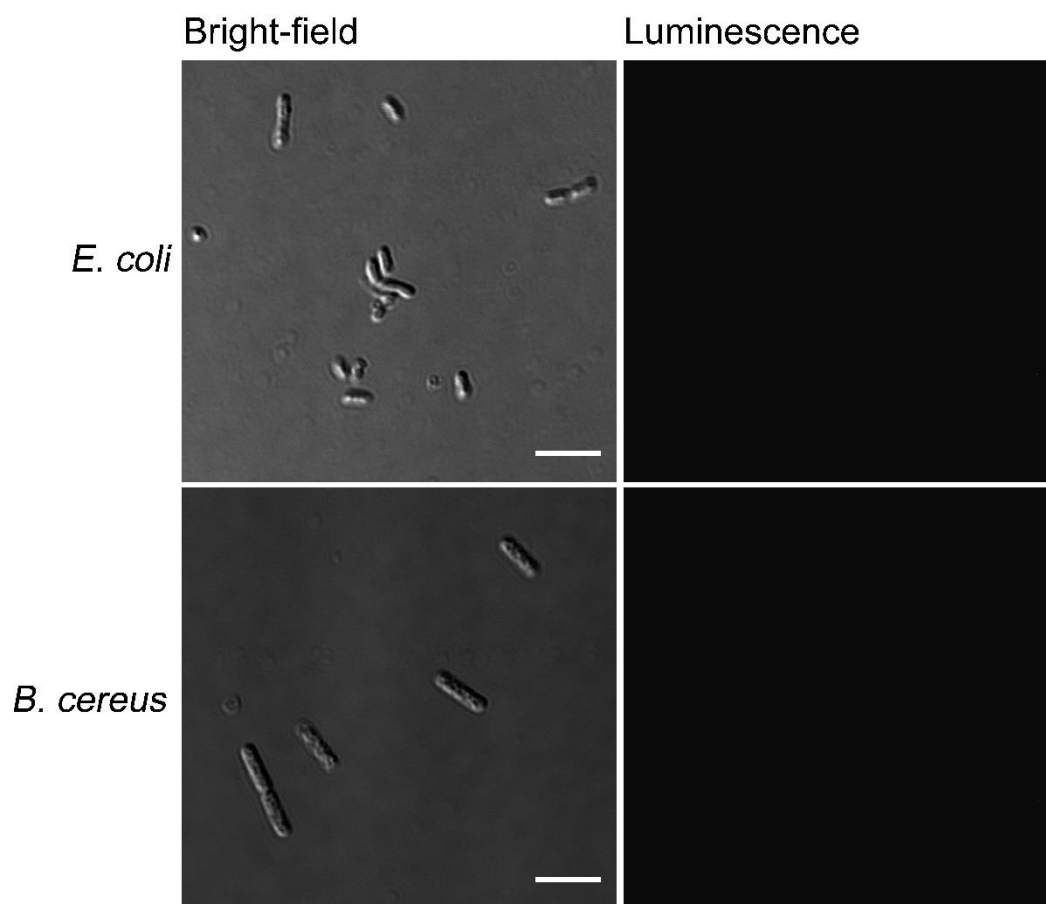


Figure 2.29 Confocal microscopy images of *B. cereus* (top) and *E. coli* (bottom) dosed with [Pt(CNC)(DMSO)] ($\lambda_{\text{ex}} = 405 \text{ nm}$, $\lambda_{\text{em}} = 525/50 \text{ nm}$ and $595/50 \text{ nm}$). Left: bright-field image showing bacterial cells. Right: confocal image showing the absence of a detectable signal. Scalebar $5 \mu\text{m}$.

2.7 Conclusions

In this chapter, a new family of neutral platinum(II) complexes has been synthesised and characterised. X-Ray crystallography analyses confirmed the formation of dicyclopentadienylated mononuclear complexes, where the different ancillary ligands occupying the fourth coordination site affect the packing of the complexes in the solid state. In general, no close Pt-Pt interaction is observed in the crystal packing.

The complexes are not emissive in organic solvents, due to the fact that the CNC ligand bound to the metal centre experiences a dramatic distortion in the excited state, hence promoting non-radiative decay. On the other hand, the emission of the complexes is revived upon aggregation. In fact, the complexes show an orange-red emission in aqueous solution (0.1% DMSO) and in a solid film. The only exception to this trend is [Pt(CNC)(bpy-PPh₃)] which is not emissive in H₂O or in the solid state, due to the positively charged, bulky ancillary ligand hindering the aggregation process. This further suggests how the monodentate ligand occupying the fourth coordination sphere is affecting not only the packing of the complexes in the solid state, as proved by inspection of the crystal structures, but also in different media. Indeed, [Pt(CNC)(DMSO)] and [Pt(CNC)(bpy-PPh₃)²⁺ 2I⁻] are emissive in their monomeric form in frozen matrix at 77K, whereas the rest of the complexes show a red-shifted and unstructured emission ascribed to the formation of aggregates.

The potential of the red-emissive aggregates to be used as imaging agents has been assessed by incubating the platinum complexes with eukaryotic cells and bacteria. Unfortunately, it was not possible to detect any emission from the aggregates from the biological substrates. This could be due to the fact that aggregation is not occurring within the cellular or bacterial cytoplasm. On the other hand, aggregates could be forming, but with a quantum yield too low to allow detection with confocal microscopy.

However, this family of complexes exhibited remarkably low toxicity, along with good accumulation within eukaryotic cells. This could open the route to the application of these platinum complexes as neutral, non-toxic biological carriers for Pt-bound therapeutic agents or fluorophores. Moreover, this series of complexes was found to inhibit the cellular growth for the gram-positive bacteria *B. cereus*. Following this result, the toxicity of these complexes could be tested in the future towards a broad

range of bacterial strains, to investigate a potential application as antimicrobial agents with advantageous low toxicity towards human cells.

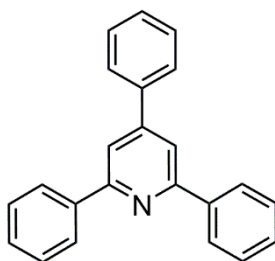
2.8 Experimental

2.8.1 General synthetic procedures

All reagents and solvents were purchased from Sigma Aldrich and used as received without further purification. 2,4,6-Triphenylpyridine (**CNCH₂**), and 4-(Pyridin-4'-yl)-1-[4''-(triphenylphosphonio)prop-1''-yl]pyridinium diiodide ligand (**bpy-PPh₃**)²⁺ 2I⁻ were synthesized according to previously published procedures^{139,159}. Nuclear magnetic resonance spectra, consisting of ¹H and ¹³C were recorded using a Bruker Advance 400 spectrometer (400.1 MHz for ¹H, 100 MHz for ¹³C) at 300K. ¹H and ¹³C chemical shifts were referenced to residual solvent signals. Elemental analyses were obtained at the School of Molecular and Life Sciences, Curtin University. ESI-Mass spectrometry analysis was performed at The University of Bologna and at The University of Sydney.

2.8.2 Synthesis

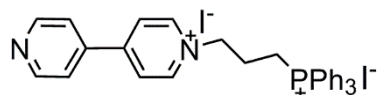
2,4,6-Triphenylpyridine (**CNCH₂**)



Benzaldehyde (1.000 g 9.42 mmol), Acetophenone (2.264 g, 18.85 mmol), and NaOH (s) (0.8 g, 20 mmol) were combined using a mortar and pestle, and the yellow medium was aggregated until a yellow-brown tacky solid formed. The solid was left to harden for 24h and then transferred to a suspension of ammonium acetate (5 g, excess) in acetic acid (25 ml). The mixture was heated to reflux (2 h). The product was precipitated out of solution via the addition of water, collected and washed with water and ethanol. (860 mg, 2.80 mmol, Yield: 30%). ¹H-NMR in CDCl₃ matches with previous reports of this compound. ¹H-NMR, 400 MHz, CDCl₃, δ

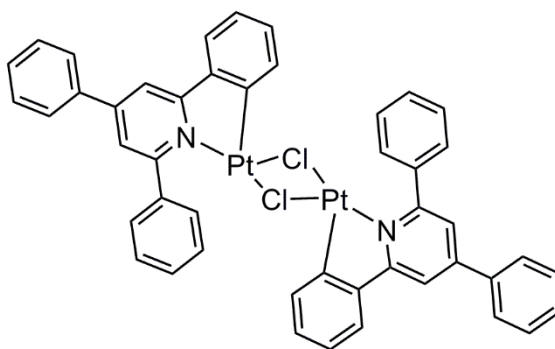
(ppm) = 8.21 (d, 4H, $J_{\text{H-H}} = 8.8$ Hz), 7.90 (s, 2H), 7.76 (d, 2H, $J_{\text{H-H}} = 8.4$ Hz); 7.57-7.48 (m, 6H), 7.37 (m, 3H).

4-(Pyridin-4'-yl)-1-[4''-(triphenylphosphonio)prop-1''-yl]pyridinium diiodide [(bpy-PPh₃)²⁺2I⁻].



4,4'-Bipyridine (200 mg, 1.27 mmol) was dissolved in 8 mL of dry acetonitrile. (4-Iodoprop-1-yl)triphenylphosphonium diiodide (362 g, 0.634 mmol) was added. The reaction mixture was refluxed for 54 h under a nitrogen atmosphere. The reaction mixture was allowed to cool at room temperature and the suspension was poured into Et₂O. The yellow-orange precipitate was filtered and washed with Et₂O and redissolved in dichloromethane. Evaporation of the dichloromethane under reduced pressure gave the crude product, containing a mixture of the target ligand and a 10% of starting 4,4'-Bipyridine. The crude ligand was used without further purification to synthesise [Pt(CNC)(bpy-PPh₃)]. ¹H-NMR, 400 MHz, CDCl₃, δ (ppm) = 10.22 (d, 2H, $J_{\text{H-H}} = 8.0$ Hz), 8.87 (d, 2H, $J_{\text{H-H}} = 8.0$ Hz), 8.24 (d, 2H, $J_{\text{H-H}} = 8.0$ Hz), 7.88-7.94 (m, broad, 6H), 7.85-7.79 (m, broad, 3H), 7.77-7.71 (m, broad, 6H), 7.66 (d, 2H, $J_{\text{H-H}} = 8.0$ Hz), 5.67-5.62 (m, 2H), 3.97-3.87 (m, 2H), 2.66-2.59 (m, 2H).

[Pt(CNC)(μ -Cl)]₂

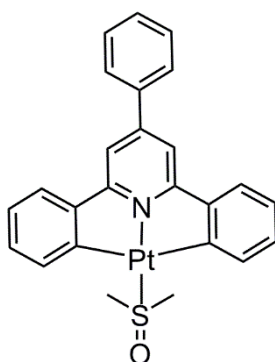


K₂PtCl₄ (0.280 g, 0.675 mmol) and the ligand precursor CNCH₂ (0.269 g, 0.876 mmol) were dissolved in 135 mL of acetic acid. The reaction mixture was stirred at 120 °C for 3 days under an argon atmosphere. The precipitated was filtered and washed

with water, acetone and diethyl ether. The desired product was then isolated by dissolution in dichloromethane.

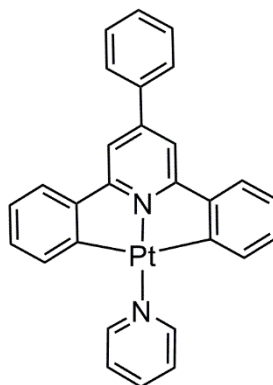
Yield: 0.211 g, 0.197 mmol, 70%. $\text{Pt}_2\text{C}_{47.5}\text{H}_{35}\text{N}_2\text{O}_{0.5}\text{Cl}_2$ Calc: C 51.73%, H 3.20%, N 2.54%. Found: C 51.96%, H 3.21%, N 2.46%. $^1\text{H-NMR}$, 400 MHz, acetone- d_6 , δ (ppm) = 8.25 (s, 2H); 8.08-8.02 (m, 5H); 7.95-7.92 (m, 4H); 7.78 (d, 3H, $J_{\text{H-H}} = 7.8$ Hz); 7.66 (s, 2H), 7.58-7.54 (m, 12H); 7.11-7.07 (m, 2H); 7.03-6.99 (m, 2H). Due to its poor solubility, the $^{13}\text{C-NMR}$ of this compound could not be recorded.

[Pt(CNC)(DMSO)]



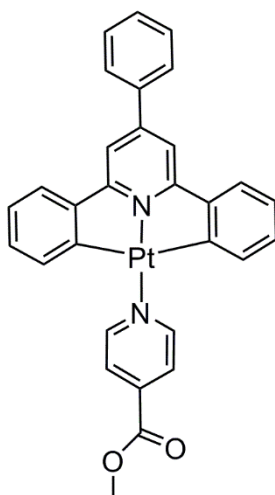
[Pt(CNC)(μ -Cl)]₂ (0.100 g, 0.093 mmol) was dissolved in 3 mL of DMSO at 150 °C and allowed to cool. Na₂CO₃ (0.010 g, 0.093 mmol,) and water (3 mL) were added to the solution. The reaction mixture was stirred at room temperature for 3 h and the precipitate was then filtered and washed with water and diethyl ether. Yield: 0.095 g, 0.164 mmol, 88%. $\text{PtNC}_{25}\text{H}_{21}\text{OS}$ Calc: C 51.90%, H 3.66%, N 2.42%, S 5.54%. Found: C 52.05%, H 3.74%, N 2.24%, S 5.6%. $^1\text{H-NMR}$, 400 MHz, acetone- d_6 , δ (ppm) = 8.00 (d, 2H, $J_{\text{H-H}} = 8.0$ Hz); 7.93 (d, 2H, $J_{\text{H-H}} = 8.0$ Hz); 7.87 (s, 2H); 7.80 (d, 2H, $J_{\text{H-H}} = 8.0$ Hz); 7.62-7.55 (broad m, 3H); 7.23 (t, 2H, $J_{\text{H-H}} = 8.0$ Hz); 7.10 (t, 2H, $J_{\text{H-H}} = 8.0$ Hz); 3.69 (s, 6H). $^{13}\text{C-NMR}$, 100 MHz, acetone- d_6 , δ (ppm) = 168.2, 168.1, 154.8, 150.7, 138.4, 137.5, 131.1, 130.9, 130.0, 128.3, 125.5, 125.3, 113.8, 48.6.

[Pt(CNC)(Py-H)]



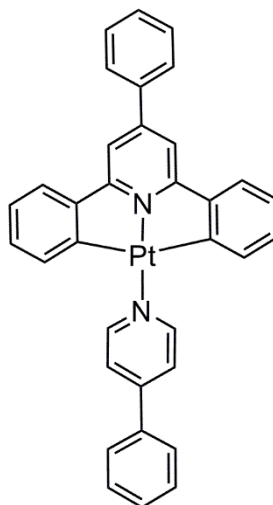
[Pt(CNC)(DMSO)] (0.050 g, 0.087 mmol) and pyridine (0.014g, 0.174 mmol) were dissolved in 5 mL of dichloromethane. The reaction mixture was stirred at room temperature for 3 hours. The solvent was then dried under reduced pressure, and 10 mL of diethyl ether were added to afford a bright orange precipitate, which was filtered and washed with diethyl ether (0.026g, 0.045 mmol, 53%). **[PtN₂C₂₈H₂₀]·0.1(CH₂Cl₂)**
Calc: C 57.39%, H 3.46%, N 4.76%. Found: C 57.07%, H 3.26%, N 4.61%. **¹H-NMR**, 400 MHz, acetone-d₆, δ (ppm): 9.08 (d, 2H, J_{H-H} = 8); 8.13 (t, 1H, J_{H-H} = 8.0 Hz); 7.98 (d, 2H, J_{H-H} = 12); 7.73 (m, 6H); 7.77-7.69 (m, 3H); 7.14 (t, 2H, J_{H-H} = 8.0 Hz); 7.02 (t, 2H, J_{H-H} = 8.0 Hz), 6.92 (d, 2H, J_{H-H} = 8.0 Hz). **¹³C-NMR**, 100 MHz, acetone-d₆, δ (ppm)= 174.01, 169.35, 154.55, 153.00, 150.16, 138.98, 137.63, 133.96, 131.04, 130.48, 129.90, 128.17, 127.56, 124.94, 123.95, 113.06.

[Pt(CNC)(Py-CO₂Me)]



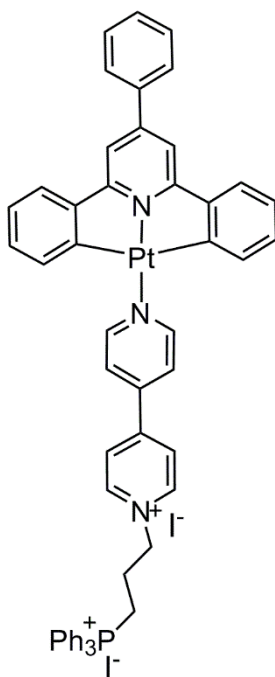
[Pt(CNC)(DMSO)] (0.065 g, 0.112 mmol) and methyl isonicotinate (0.031g, 0.225 mmol) were dissolved in 5 mL of dichloromethane. The reaction mixture was stirred at room temperature for 16 hours. The solvent was then dried under reduced pressure, and 15 mL of diethyl ether were added to afford a bright orange precipitate, which was filtered and washed with diethyl ether (0.056 g, 0.087 mmol, 78%). [**PtO₂N₂C₃₀H₂₂**] Calc: C 56.51%, H 3.48%, N 4.39%. Found: C 56.20%, H 3.16%, N 4.19%. **¹H-NMR**, 400 MHz, acetone-d₆, δ (ppm): 9.29 (d, 2H, J_{H-H} = 8Hz); 8.13 (d, 2H, J_{H-H} = 8Hz); 7.98 (d, 2H, J_{H-H} = 8Hz); 7.78 (s, 2H); 7.74 (d, 2H, J_{H-H} = 8Hz); 7.62-7.54 (m, 3H); 7.14 (t, 2H, J_{H-H} = 8.0 Hz); 7.03 (t, 2H, J_{H-H} = 8.0 Hz); 6.87 (d, 2H, J_{H-H} = 8Hz); 4.04 (s, 3H). **¹³C-NMR**, 100 MHz, acetone-d₆, δ (ppm)= 173.54, 169.24, 164.52, 155.31, 153.24, 150.07, 138.87, 137.90, 133.78, 131.13, 130.55, 129.91, 128.20, 126.57, 125.04, 124.15, 113.18, 53.48.

[Pt(CNC)(Py-Ph)]



[Pt(CNC)(DMSO)] (0.050 g, 0.087 mmol) and 4-phenylpyridine (0.027 g, 0.174 mmol) were dissolved in 5 mL of dichloromethane. The reaction mixture was stirred at room temperature overnight to afford a bright orange precipitate, which was filtered and washed with diethyl ether (0.026 g, 0.040 mmol, 46%). [PtC₃₄N₂H₂₄]·0.5(CH₂Cl₂) Calc: C 59.36%, H 3.61%, N 4.01%. Found: C 59.39%, H 3.25%, N 4.02%. ¹H-NMR, 400 MHz, acetone-d₆ δ (ppm): 9.11 (d, 2H, J_{H-H} = 8.0 Hz); 8.04 – 7.96 (broad m, 6H); 7.78 – 7.73 (m, 4H); 7.66-7.51 (m, broad, 6H); 7.15 (t, 2H, J_{H-H} = 8.0 Hz); 7.05 - 6.95 (broad m, 4H). ¹³C-NMR: Due to low solubility, the ¹³C-NMR of this compound could not be recorded.

[Pt(CNC)(bpy-PPh₃)]



[Pt(CNC)(DMSO)] (0.050 g, 0.087 mmol) and Bpy-PPh₃ (0.14 g, 0.173 mmol) were dissolved in 5 mL of dichloromethane. The reaction mixture was stirred at room temperature overnight. The solvent was then dried under reduced pressure, and 10 mL of diethyl ether were added to afford a red precipitate, which was filtered and washed with methanol and diethyl ether (0.030 g, 0.025 mmol, 28%). [PtPN₃I₂C₅₄H₄₄]**·1(CH₂Cl₂)** Calc C 50.83%, H 3.57%, N 3.23%. Found: C 50.45%, H 3.68%, N 3.26%.

¹H-NMR, 400 MHz, acetone-d₆, δ (ppm) = 9.21 (d, 2H, J_{H-H} = 8.0 Hz); 8.90 (2H, J_{H-H} = 8.0 Hz); 8.68 (d, 2H, J_{H-H} = 8.0 Hz); 8.12-8.03 (m, 4H); 7.99 (s, 2H); 7.95-7.89 (m, broad, 4H); 7.89-7.77 (m, broad, 15H); 7.60 (m, 3H); 7.22 (m, 2H); 7.13 (m, 2H); 4.80 (m, 2H); 3.73-3.66 (m, broad, 2H), 2.35-2.28 (m, broad, 2H). ¹³C-NMR, 100 MHz, acetone-d₆, δ (ppm) = 166.91, 153.51, 152.97, 151.55, 151.02, 149.98, 146.08, 141.18, 136.82, 135.65, 134.15, 134.04, 130.90, 130.78, 129.48, 128.02, 125.85, 125.51, 124.95, 122.28, 118.82, 117.96, 113.35, 60.29, 23.97, 18.44.

2.8.3 Photophysical measurements

Absorption spectra were recorded at room temperature using a Perkin Elmer Lambda 35 UV/Vis spectrometer. Uncorrected steady state emission and excitation spectra were recorded on an Edinburgh FLSP980 spectrometer equipped with a i) a temperature-monitored cuvette holder, ii) 450 W Xenon arc lamp, iii) double excitation and double emission monochromators, iv) Peltier cooled Hamamatsu R928P photomultiplier tube (185-850 nm). The emission and excitation spectra were corrected for source intensity (lamp and grating) and emission spectral response (detector and grating) by calibration curve supplied with the instrument. Emission lifetimes (τ) were determined by the single photon counting technique (TCSPC) with the same Edinburgh FLSP980 spectrometer using a pulsed picosecond LED (EPL 377 nm, FWHM <800 ps) as the excitation source and the above-mentioned R928P PMT as the detector. The goodness of fit was assessed by minimizing the reduced χ^2 function and by visual inspection of the weighted residuals. Experimental uncertainties were estimated to be $\pm 8\%$ for lifetime determinations and ± 2 nm and ± 5 nm for absorption and emission peaks, respectively. Photoluminescence Quantum Yields were determined using an integrating sphere.

2.8.4 Cell culture

The biological investigation regarding eukaryotic cells (Sections 2.8.4 - 2.8.7) was performed in collaboration with A/Prof Elizabeth New at the University of Sydney. adenocarcinomic human alveolar basal epithelial A549 cells were used in all experiments and maintained at 37 °C in 5% carbon dioxide. Cells were cultured in Advanced Dulbecco's Modified Eagle's Medium (DMEM, Thermo Fisher Scientific) supplemented with 2% foetal calf serum (FCS, Thermo Fisher Scientific) and 2.5 mM L-glutamine (G, Sigma-Aldrich). All the Pt complexes working solutions were prepared from fresh 1000X stocks in DMSO and diluted to the appropriate concentration in DMEM.

2.8.5 Uptake studies

Preparation of cell lysates: A549 cells were plated and in 6 well and grown until approximately 80% confluent. Cells were then dosed with the appropriate Pt complex (20 μM) for 30 minutes. After the incubation time, the medium was removed, and the cells washed with PBS (3 x 0.5 mL). 80 μL of lysis buffer was added to each well. The cells were immediately harvested by scraping; the scraper was washed in 2% nitric acid and MilliQ water pre-harvesting, and trace metal free tubes were used to minimise environmental Cu contamination. The cell lysates were stored at -20 $^{\circ}\text{C}$.

Bradford assay: 200 μL of Bradford reagent (1 in 5 dilution, Bio-Rad) was added to each well of a polystyrene 96 well plate (Greiner Bio-One). 1 μL of cell lysates was added to each well in duplicate and mixed with pipetting. Standards, containing bovine serum albumin (BSA), were prepared according to the manufacturer's protocols. The plate was incubated at room temperature for 5-30 min, and absorbance at 595 nm was measured. Protein concentration was determined by extrapolation from the BSA standard curve.

ICP-MS: To determine the relative amount of Pt in the lysates, 50 μL of cell lysates were added to 50 μL of 69% analytical grade nitric acid (Merck). The samples were heated at 50 $^{\circ}\text{C}$ overnight to ensure digestion and stored at 4 $^{\circ}\text{C}$ until measurement. The samples were diluted (1 in 50) in ultra-pure water and 10 ppb iridium was added as an internal standard. The samples were analysed by a Perkin-Elmer NexION 350X ICP-MS. The final Pt concentrations were normalised against the amount of protein in the sample and are expressed in μg of Pt per mg of protein.

2.8.6 Cell viability

A549 cells were plated and in 6 well and grown until approximately 80% confluent. Cells were incubated with each platinum complex (final concentrations 20 μM and 40

μM , 4 x repeats) for 3 h, alongside with control cells. Alamar Blue was then added and cells incubated for further 1-2 hours. Fluorescence output was read at 590 nm ($\lambda_{\text{exc}} = 570 \text{ nm}$) on a Perkin Elmer EnSpire Multimedia plate reader, and averaged value for repeats reported as a percentage of the control.

2.8.7 Confocal microscopy on eukaryotic cells

Cells were plated in 35 mm glass bottom MatTek dishes, and allowed to adhere overnight. Cells were dosed with 20 μM solution of the platinum complexes in the growth medium (section 2.8.4) for 30-60 minutes and then washed twice with an equal volume of PBS, then imaged in FluoroBrite DMEM media (supplemented with 10% fetal bovine serum - FBS and 1.25% Glutamine - G).

Confocal images were acquired using an Olympus Fluoroview FV3000 inverted light, fluorescence and confocal microscope and a UPLSAPO 60X water-immersion objective lens (NA = 1.15), in a temperature-controlled incubator at 37 °C. The complexes were excited at 405 nm and the emission was collected in the 500-700 nm region. Excitation at 405 nm was provided by a UV laser. Images were collected using FV10-ASW viewer software v1.7 (Olympus) and processed using image J.

2.8.8 Bacterial strains and growth conditions

The biological investigation regarding bacterial cells (Sections 2.8.8-2.8.10) was performed at Curtin University and at the Harry Perkins Institute of Medical Research, Perth.

B. cereus ATCC10876 was grown on Nutrient Broth agar plates at 37 °C. A bacterial culture was obtained by inoculating bacteria in Nutrient Broth media and incubating overnight in a shaking incubator at 37 °C.

E. coli NCTC 10418 was grown on LB agar plates at 37 °C. A bacterial culture was obtained by inoculating bacteria in LB media and incubating overnight in a shaking incubator at 37 °C.

All the Pt complexes working solutions were prepared from fresh 1000X stocks in DMSO and diluted in the appropriate growth medium.

2.8.9 Growth curves determination

An overnight culture of *B. cereus* or *E. coli* were diluted to a suspension with an optical density of approximately 0.1 at 600 nm (OD_{600}). Bacteria were incubated with the appropriate platinum complex in the growth medium (20 μ M, 0.1% DMSO) alongside control cultures, and the growth was monitored at appropriate time intervals measuring the culture OD_{600} .

2.8.10 Confocal microscopy on bacterial cells

Bacteria were dosed with a 20 μ M solution of the complexes in the appropriate growth medium (0.1% DMSO) for 30-60 minutes, then washed and imaged.

Confocal images were acquired using a Nikon A1R confocal microscope and a Plan Apo λ 100X oil-immersion objective lens (NA = 1.45). The complexes were excited at 405 nm and the emission was collected in the 525/50 nm and 595/50 nm regions. Images were collected using NIS-Element version 4.60.00 software and deconvolved using 3D Blind deconvolution. The images were processed using NIS-Element Viewer v.4.20 and the final preparation was conducted with Adobe Photoshop CC (Adobe Systems Inc., USA).

Chapter 3

Synthesis, Photophysical and Biological Investigation of a Platinum-Naphthalimide Complex.

3.1 Introduction

In the field of biological imaging, there is increasing interest in correlative methods, where a combination of techniques is applied to the same sample to generate a unique and complementary set of information that could not be obtained with the individual platforms.^{160–169} To this end, fluorescence microscopy has been coupled with a wide range of techniques including electron microscopy, magnetic resonance imaging and mass spectrometry. The main challenge in the development of correlative approaches is that different instruments and analyses require not only different sample preparation protocols, but also different labels.¹⁶⁹ As a consequence, for many correlative methods, multiple labels and labelling steps may be required. A solution to this is offered by correlative probes, the properties of which are specifically designed to allow simultaneous detection with multiple instruments of interest, hence allowing the use of a single label across different setups. Amongst the most commonly-used multimodal techniques are correlative fluorescence and electron microscopy (CFEM), but the luminescent dyes necessary for fluorescence microscopy (FM) are not all directly applicable to electron microscopy (EM), which requires the presence of electron dense particles or materials. This has been overcome by the development of combinatorial affinity labels such as those based on Fluoronano Gold^{167,169–171} and Quantum Dots.^{172–175} These materials are based on electron dense particles with luminescent properties, that are suitable for detection by both FM and EM. More recently, fluorescence microscopy has been coupled with nano-scale secondary ion mass spectrometry (NanoSIMS).^{176–178} NanoSIMS is particularly suitable to perform analysis of isotopes and trace elements^{81,179} and has previously been combined with confocal microscopy to elucidate the cellular uptake and sub-cellular accumulation of

platinum-based drugs in human cells and tissues.^{180,181} In contrast, probes for bacterial imaging that enable correlative imaging are far less developed. While not possessing the distinct compartmentalisation of eukaryotic cells, bacteria are nonetheless characterised by a rich and structured sub-cellular architecture. High resolution imaging of bacterial cells has contributed to great advances in prokaryotic cell biology, enabling the study of a wide range of sub-cellular structures that play a key role in the growth and pathogenesis of these unicellular organisms.^{12,26} Given the small size of bacterial cells, super-resolution microscopy is pivotal to visualise microbial specimens to a sub-cellular level.^{24,25} In the past decade, several super-resolution methods have been used to resolve structures and monitor dynamic processes in bacteria, such as stimulated emission-depletion (STED) microscopy, stochastic optical reconstruction microscopy (STORM), photoactivated localization microscopy (PALM) and structured illumination microscopy (SIM).^{12,24,25,182} Most of the fluorescence imaging on bacterial cells has to date been achieved using genetically encoded tags or commercially available dyes, and considerable recent research interest has focussed on the development of new fluorophores that can efficiently target bacteria.^{12,26,35,38,43,49,183–186} Since most of these probes are small organic molecules, however, their detection with other imaging techniques such as electron microscopy and mass spectrometry is not readily achievable. At the same time, nanoSIMS protocols applied to bacteria have relied so far on the more traditional approach based on the stable isotope labelling of target biological substrates.^{187–190} Given the lack of probes enabling correlative bacterial imaging, the aim of the work described in this chapter is to investigate the potential of a novel luminescent metal-based marker to act as a small-molecule correlative probe for bacteria. Specifically, the focus of this study is on the synthesis, characterisation and bacterial imaging applications of a neutral platinum(II)-naphthalimide metal complex of the general formula [Pt(CNC)(Py-Napht)], where CNC is a doubly deprotonated 2,4,6-triphenylpyridine, and Py-Napht is a N-3-pyridyl-4-butylamino-1,8-naphthalimide. The probe incorporates the luminescent 1,8-naphthalimide unit, exploited for fluorescent microscopy, in the coordination sphere of the platinum(II) complex acting as a metal-based carrier. The resulting complex has been tested towards the bacterial species *Bacillus cereus*, to validate the capability of this system to perform super-resolution microscopy (SIM) and nanoSIMS on bacteria.

3.2 Synthesis and characterisation

3.2.1 Synthesis of N-pyridyl-4-butylamino-1,8-naphthalimide

The N-3-Pyridyl-4-butylamino-1,8-naphthalimide (**Py-Napht**) was synthesised in collaboration with Kate Leslie, at the University of Sydney. Following a variation of a previously reported procedure,^{191,192} 4-nitro-naphthalic anhydride was reacted with 3-aminopyridine and then combined with butylamine (**Figure 3.1**). The target ligand was then purified *via* column chromatography using silica as stationary phase and DCM and MeOH as eluents, and obtained in a moderate yield, 35%, over two steps.

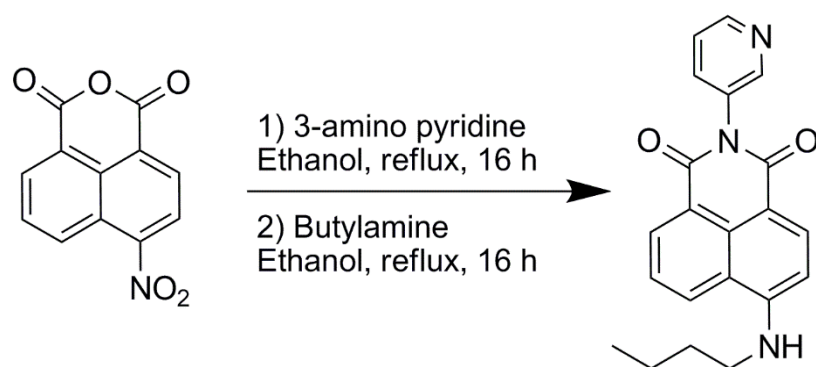


Figure 3.1 Synthetic scheme for the synthesis of **Py-Napht**.

The 1,8-naphthalimide was characterised by ¹H-NMR, ¹³C-NMR spectroscopy as well as high resolution mass spectrometry. The ¹H-NMR spectrum in CDCl₃ matched the proposed structure, confirming the success of the condensation reaction between the 3-aminopyridine and the anhydride, as well as the substitution of the nitro group with the butylamine. Indeed, the corresponding signals of the butyl chain were identified between 1.5 ppm and 3.5 ppm. The HR-ESI mass spectrum showed in the positive ions scan a predominant peak corresponding to $m/z = 368.13695$, that matched with the expected molecular mass with an additional sodium cation $[M+Na]^+$.

3.2.2 Synthesis of the platinum(II)-naphthalimide complex [Pt(CNC)(Py-Napht)]

Following the procedure described in Chapter 2, sections 2.4.1 and 2.4.2, the precursor [Pt(CNC)(DMSO)] was prepared from the platinum dimer and then dissolved in DCM. Two equivalents of **Py-Napht** were added and the reaction stirred overnight. The low solubility of the ligand however, limited the success of the reaction in these conditions. Indeed, after the reaction time, **Py-Napht** was still present as a suspension in the reaction mixture, and unreacted [Pt(CNC)(DMSO)] was recovered from the solution. The reaction was therefore attempted in an acetone/methanol (9:1 v/v) mixture, that allowed the almost complete dissolution of **Py-Napht** by refluxing overnight (**Figure 3.2**)

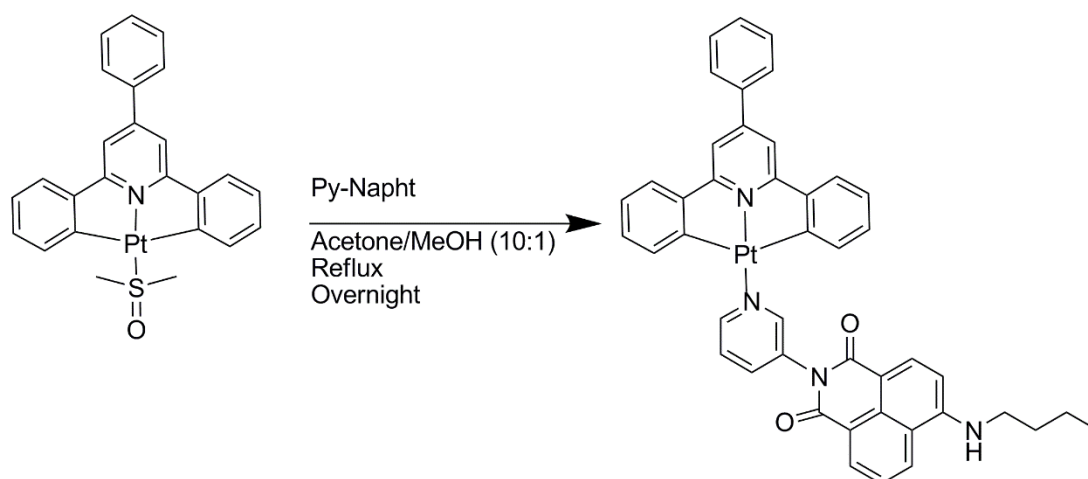


Figure 3.2 Scheme of the synthetic procedure for [Pt(CNC)(Py-Napht)].

Purification *via* column chromatography, using silica as stationary phase and acetone as eluent, was required to yield the pure [Pt(CNC)(Py-Napht)] (30%). ¹H-NMR spectroscopy confirmed the success of the reaction. Indeed, the presence of the signal belonging to the naphthalimide together with the absence of a singlet at 3.69 ppm, characteristic of platinum-bound DMSO, confirmed coordination of **Py-Napht** to a dicyclopalladated platinum(II) centre.

3.3 Photophysical investigation

3.3.1 Absorption properties

The photophysical properties of [Pt(CNC)(Py-Napht)] have been investigated to assess the applicability of the complex as a cellular and bacterial marker. The absorption data have been summarised in **Table 3.1**.

Table 3.1 Absorption data of diluted solution (10^{-5} M) of [Pt(CNC)(Py-Napht)] in different solvents.

Solvent	$\lambda_{\text{abs}} / \text{nm}$ ($10^4 \epsilon$ [$\text{M}^{-1} \text{cm}^{-1}$])
DCM	282 (15.26), 363 (3.55), 433 (5.04)
DMSO	287 (11.02), 348 (2.60), 448 (3.61)
H ₂ O (0.1% DMSO)	284 (7.59), 365sh (2.31), 461 (2.10)

The absorption spectrum of [Pt(CNC)(Py-Napht)] in DCM is depicted in **Figure 3.3**, blue line. The complex possesses a strong absorption band centred at 282 nm ($\epsilon = 15.26 \times 10^4 \text{ M}^{-1} \text{ cm}^{-1}$) followed by a less intense band at 363 nm ($\epsilon = 3.55 \times 10^4 \text{ M}^{-1} \text{ cm}^{-1}$) that are assigned to the π - π^* transitions of the diphenylpyridine ligand.^{145,150,193,194} Additionally, a relatively intense absorption band is observed at 433 nm, assigned to the lowest dipole-allowed transition in the 1,8-naphthalimide, a transition presenting a partial charge-transfer (CT) character.¹⁹⁴⁻¹⁹⁸ A very similar absorption band was observed by recording the absorption spectra of the uncoordinated **Py-Napht** in the same solvent (Appendix B, Figure B.1), showing that the contribution of this lower energy band is mainly ascribed to the naphthalimide moiety. For [Pt(CNC)(Py-Napht)] however this intense band is likely to be overlapping with the metal-to-ligand charge transfer ($^1\text{MLCT } 5d \rightarrow \pi^*$) that is expected in the same wavelength range, as discussed in Chapter 2, Section 2.5.1. The absorption spectra of the complex in DMSO and H₂O (0.1% DMSO) followed the same trend, with generally lower molar absorptivity values. This trend may be due to a lower solubility of the complex with increasing polarity of the solvent, resulting in a higher tendency to slightly aggregate or even precipitate in aqueous solution.

Moreover, with increasing polarity of the medium, a red-shift was observed for the low-energy band, that shifted from 433 nm to 460 nm going from dichloromethane to H₂O. This behaviour is ascribed to a strong solvatochromism that is typical of fluorophores characterised by ICT states,^{191,198} and that was confirmed by recording the emission spectra of the complex in the different solvents.

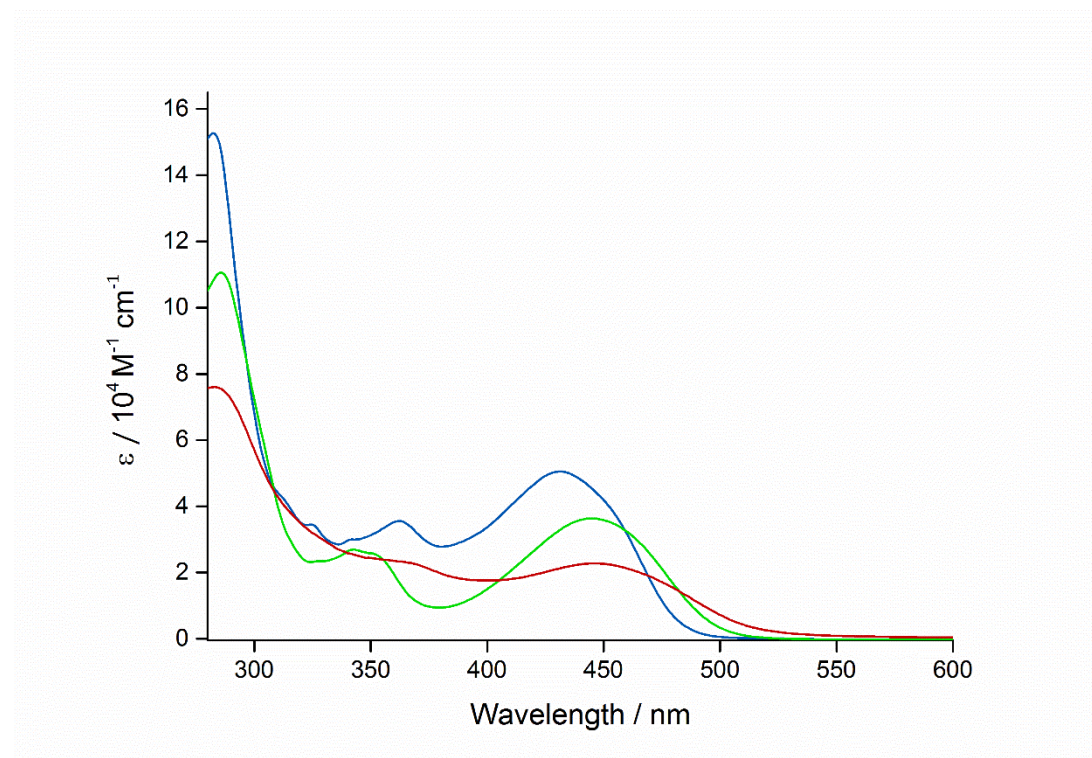


Figure 3.3 Absorption profiles for [Pt(CNC)(Py-Napht)] in dichloromethane (blue line), DMSO (green line) and H₂O (red line) solutions.

3.3.2 Emission properties in solution and in the solid state

The emission properties in solution as well as in the solid state have been summarised in **Table 3.2**. Excitation of a dichloromethane solution of the complex at 430 nm resulted in a broad emission band centred at 515 nm, again typical of the ICT emissive state of naphthalimide fluorophores. The excitation spectrum matched the ICT absorption band (**Figure 3.4**) suggesting that no electronic interaction existed between the platinum centre and the naphthalimide ligand.^{194,195} Moreover, the lifetime recorded on the emission maxima exhibited a value of 11 ns, closely matching the value observed for the uncoordinated **Py-Napht** (Appendix B, Table B.1). These

observations suggest that the emission observed for [Pt(CNC)(Py-Napht)] is dominated by the fluorescence of the 1,8-naphthalimide, in agreement with previously reported Re(I) and Pt(II) complexes bearing 1,8-naphthalimide ligands.^{194,195} Consistent with what was observed in the absorption spectra, a positive solvatochromism occurred with increasing solvent polarity, with a red-shift of 57 nm going from DCM to H₂O (**Figure 3.5**). The same trends are observed for the free naphthalimide ligand **Py-Napht** (Appendix B, Figure B.2). Interestingly, a very weak and broad emission band centred at 708 nm is observed for [Pt(CNC)(Py-Napht)] in the solid state (**Figure 3.6**), with a profile that resembled the one observed for the neutral platinum complexes described in Chapter 2, Section 2.5.2. This emission band, that is red-shifted in comparison to the emission observed in solution, is ascribed to the presence of a small amount of aggregation of the complex in the solid state. The fact that the emission intensity detected was extremely low suggests that the bulky naphthalimide ligand is hindering the aggregation process.

Table 3.2 Emission data for [Pt(CNC)(Py-Napht)]

	λ_{em} [nm]	τ_{aer} [ns]	Φ_{aer}^a %
DCM	515	11	28
DMSO	542	10	5
H ₂ O (0.1% DMSO)	572	3	2
Solid film	708	- ^b	-

[a] Measured versus [Ru(bpy)₃]²⁺ in H₂O ($\phi_r = 0.028$). [b] Too weak to be measured.

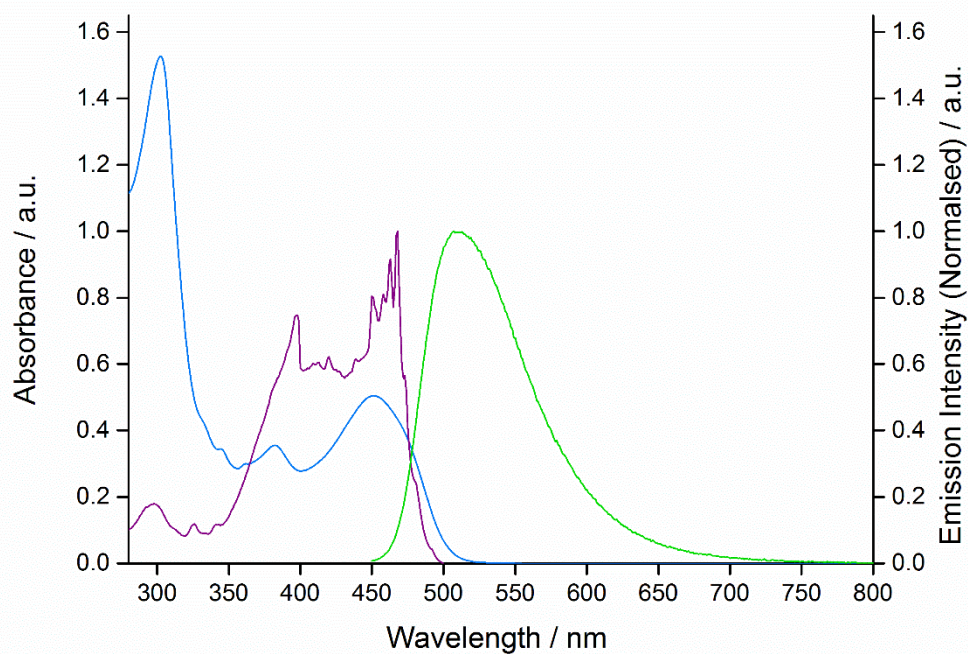


Figure 3.4 Absorption (blue line), excitation (purple line) and emission (green line) spectra of [Pt(CNC)(Py-Napht)] from a 10^{-5} DCM solution.

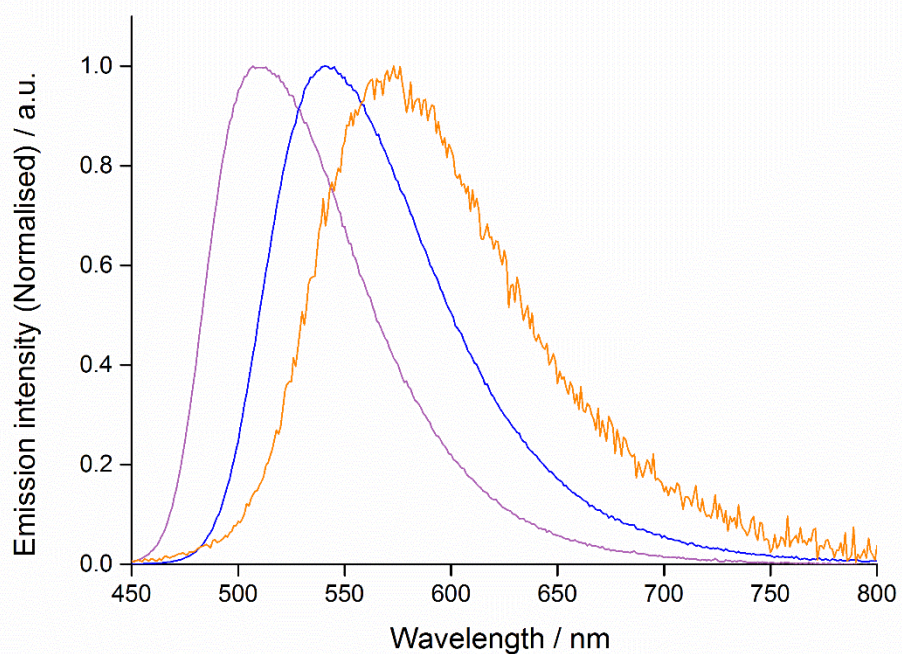


Figure 3.5 Emission profiles of [Pt(CNC)(Py-Napht)] from a DCM (violet line), DMSO (blue line) and H₂O (orange line) solutions.

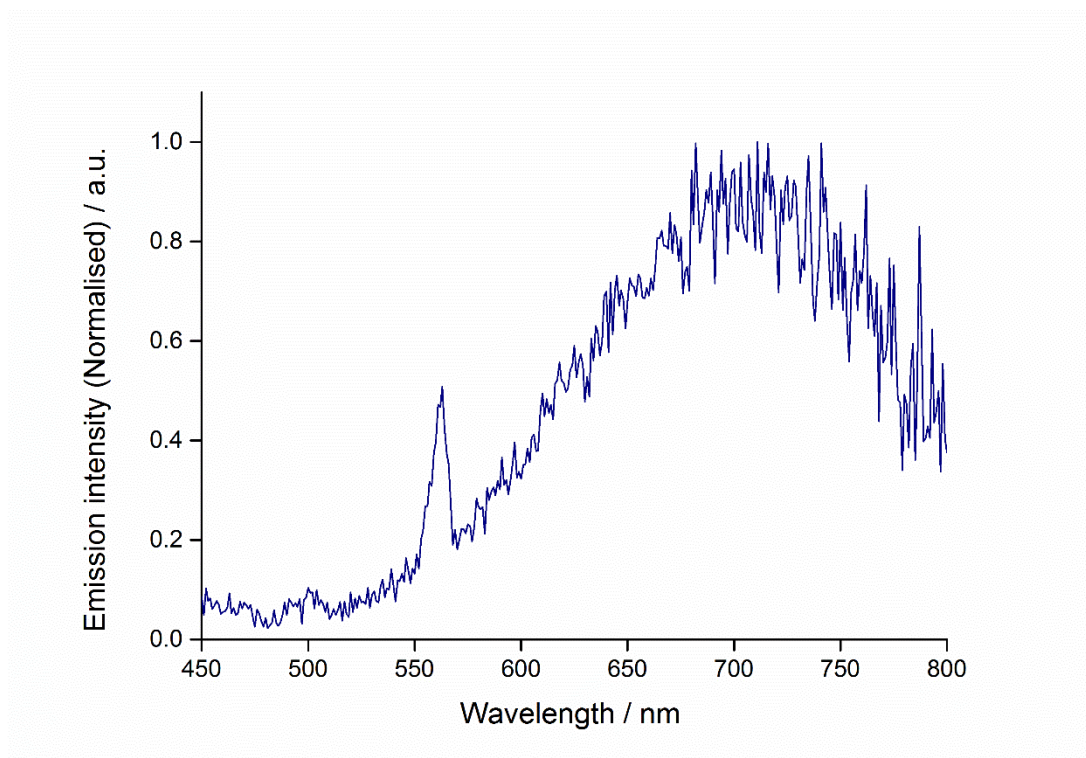


Figure 3.6 Emission profile of [Pt(CNC)(Py-Napht)] in the solid state.

3.4 Computational investigation

To further investigate the structural and photophysical properties of [Pt(CNC)(Py-Napht)] and **Py-Napht**, Time-Dependent Density Functional Theory (TD-DFT) calculations were performed in collaboration with Denis Jacquemin (Université de Nantes, France). For **Py-Napht**, the lowest state can be ascribed to a π - π^* transition, involving a CT of 0.60 e over 2.10 Å. The computed 0-0 energy is 2.77 eV, 0.19 eV off the experimental value (2.58 eV), an error typical of TD-DFT.^{199,200} In [Pt(CNC)(Py-Napht)], the dihedral angle between the pyridyl ring and the 1,8-naphthalimide (PT complex) plane is 62° (54°). This leads to a near orthogonality of the two chromophores (angle of 86.2°), preventing direct electronic interactions. The TD-DFT calculations reveal that lowest singlet state in [Pt(CNC)(Py-Napht)] is located on the 1,8-naphthalimide moiety (no lower CT-like state is found) and presents a 0-0 energy of 2.78 eV, almost identical to the one determined in **Py-Napht**. Overall, theory therefore confirms that there is almost no interaction between the two moieties in [Pt(CNC)(Py-Napht)] and that the lowest excited state is always located on the naphthalimide. For **Py-Napht**, TD-DFT found that the lowest singlet excited state is strongly dipole allowed ($f=0.46$ for absorption and $f=0.52$ for emission). The computed vertical transition energies are at 3.21 eV (386 nm) for absorption and 2.59 eV (478 nm) for emission, both values being significantly blue-shifted compared to the measurements, as a logical consequence of the lack of vibronic corrections in such vertical estimates. Turning to data more directly comparable to experiment, the expected accuracy of TD-DFT is recovered, with a computed Stokes shift (5000 cm⁻¹) that fits reasonably well experiment (3950 cm⁻¹), and a theoretical 0-0 energy (2.77 eV or 448 nm) within an quarter of an eV from the measured crossing point between the absorption and emission curves (2.58 eV of 480 nm). For **Py-Napht** the lowest excited-state present a strongly dominant HOMO-LUMO character. These orbitals are displayed in Figure S7, and, as expected they are localized on the naphthalimide moiety and have a clear $\pi^{(*)}$ character. The partial CT character is also obvious with the HOMO more localised on the amino-donor group and two *bottom* rings whereas the LUMO shows a stronger contribution from the diimide moiety. Using Le Bahers' model, we computed an ICT of 0.60 e over 2.10 Å, which is a moderate ICT character. For [Pt(CNC)(Py-Napht)], the ground-state geometry reveals weakly interacting chromophores (see Figure S8 and the main text). The lowest transition in

[Pt(CNC)(Py-Napht)] is computed at 3.19 eV (389 nm, $f=0.57$) and corresponds to a HOMO-1 to LUMO transition, which has can be seen in Figure S7 are naphthalimide-centred and present the same shape has in **Py-Napht**. The three next higher transitions (378 nm, $f=0.005$; 343 nm, $f=0.010$; 308 nm, $f=0.111$) are all located on the Pt complex and account for the additional absorption band noticed experimentally. Consistently with the above, the optimization of the lowest singlet state leads to a bright emission (oscillator strength of 0.53) with a 0-0 energy at 2.78 eV (446 nm), almost unchanged from **Py-Napht**, as expected.

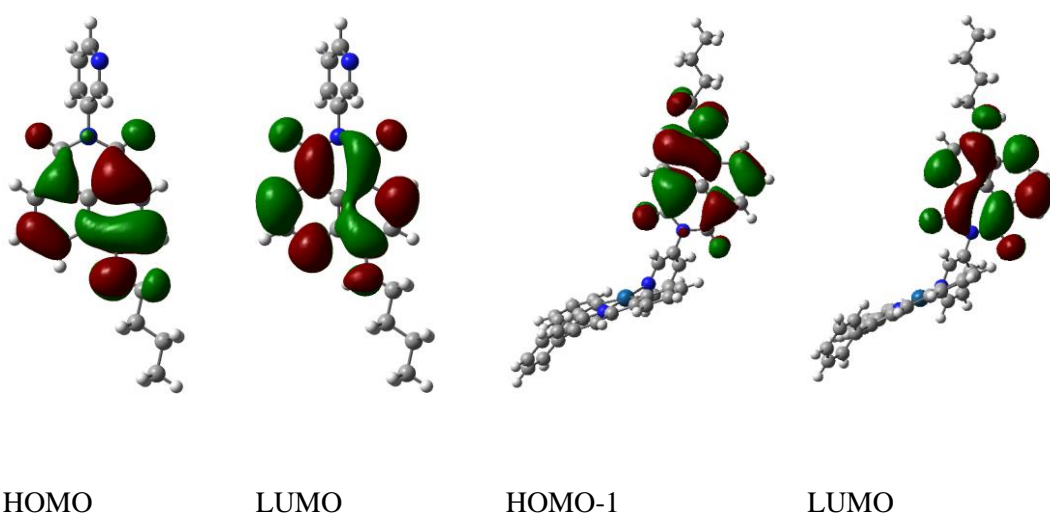


Figure 3.7 Relevant frontier MOs of **Py-Napht** (left) and [Pt(CNC)(**Py-Napht**)] (right).

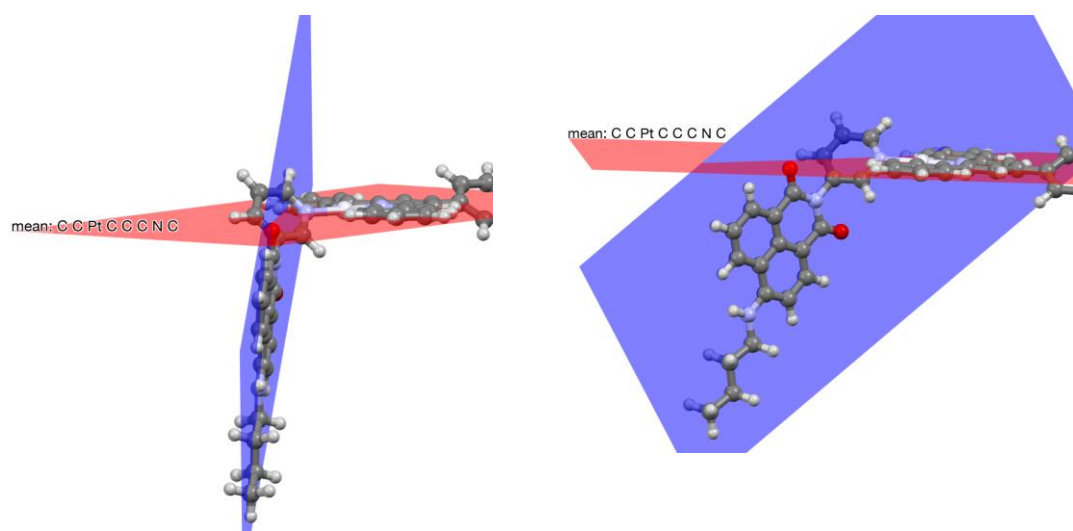


Figure 3.8 Two views of the optimal ground-state geometries of [Pt(CNC)(Py-Napht)], with representations of the 1,8-naphthamide and Pt-complex planes.

3.5 Biological investigation

3.5.1 Cellular uptake and cytotoxicity studies in eukaryotic cells

Following the approach outlined in Chapter 2, before investigating the biological properties of [Pt(CNC)(Py-Napht)] towards bacteria, the complex was tested in eukaryotic cells. The cellular uptake of [Pt(CNC)(Py-Napht)] was investigated by means of ICP-MS, following the same protocol and incubation conditions described in Chapter 2, section 2.6.1. The result obtained for the precursor [Pt(CNC)(DMSO)], previously discussed in Chapter 2, is reported here as a comparison.

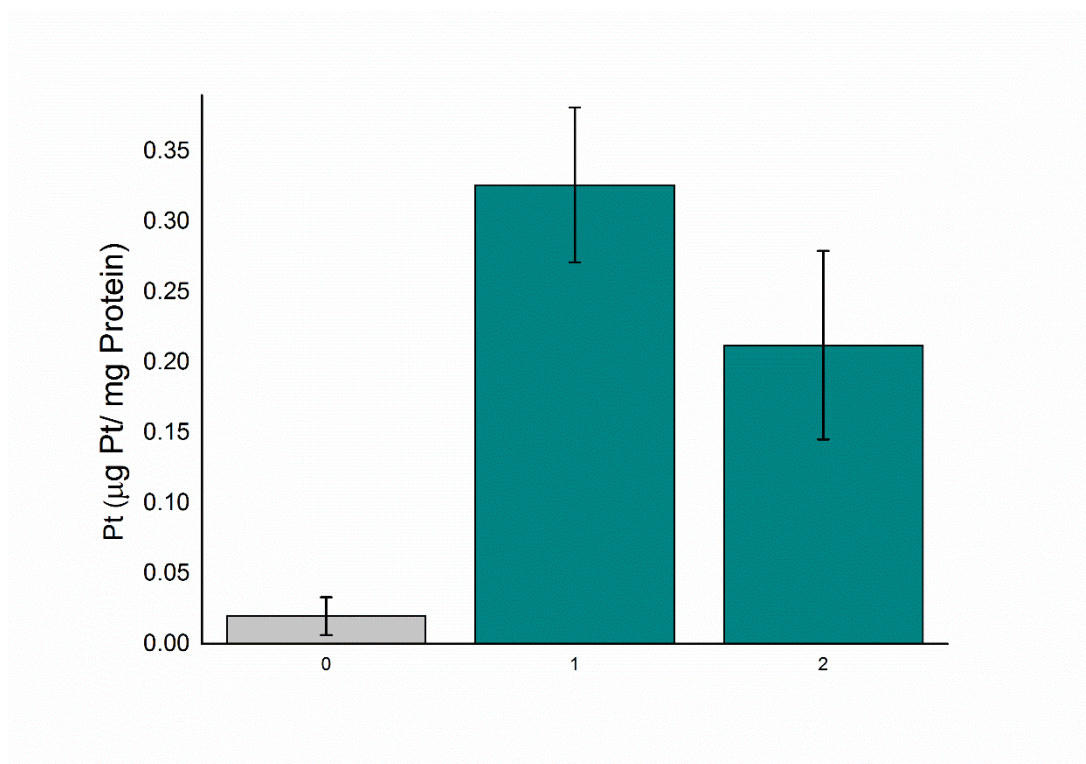


Figure 3.9 Accumulation of Pt reported as µg of Pt on mg of Protein. 0) Control (0.1% DMSO in DMEM medium); 1) [Pt(CNC)(DMSO)]; 2) [Pt(CNC)(Py-Napht)].

As shown in **Figure 3.9**, [Pt(CNC)(Py-Napht)] exhibited good cellular uptake in A549 cells, after incubation at a concentration of 20 µM at 37 °C. The cellular uptake of the complex is comparable to [Pt(CNC)(DMSO)], supporting the promising potential of using this scaffold as a carrier for the naphthalimide unit. The cytotoxicity

of the Pt-Naphthalimide adduct was assessed alongside both [Pt(CNC)(DMSO)] and **Py-Napht** as a comparison (**Figure 3.10**).

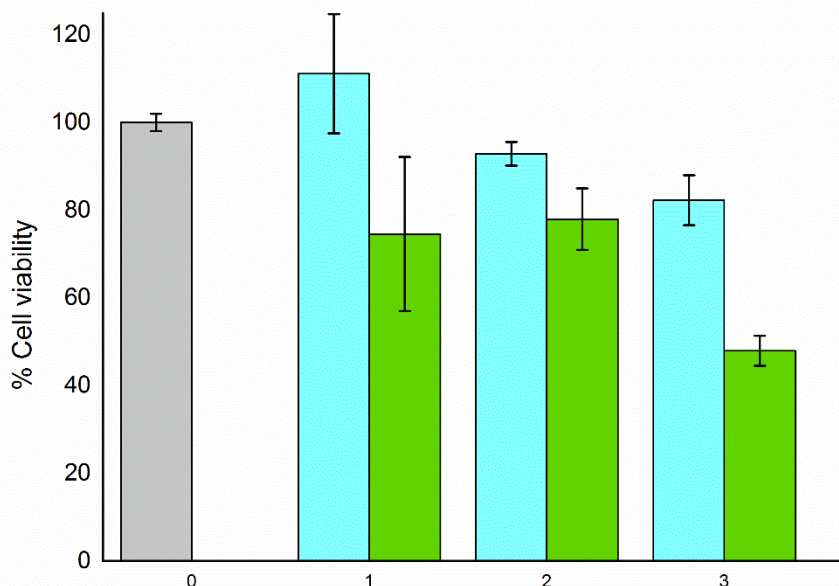


Figure 3.10 Alamar Blue Cytotoxicity Assay in A549 cells, with fluorescence output reported as a percentage of the control cells. Doses: 20 μM (light blue bars) and 40 μM (green bars). 0) Control (0.1% DMSO in DMEM medium); 1) [Pt(CNC)(DMSO)]; 2) **Py-Napht**; 3) [Pt(CNC)(**Py-Napht**)].

Good cellular viability was found in the presence of free **Py-Napht** at 20 μM and 40 μM (78% and 93% respectively). This result is in line with the trend previously observed for related naphthalimide derivatives, that were found to be non-toxic in similar conditions up to a concentration of 100 μM .¹⁹¹ Notably, this low toxicity was maintained even for [Pt(CNC)(**Py-Napht**)]. Indeed, similarly to what was observed for [Pt(CNC)(DMSO)] as well as the other neutral complexes tested in Chapter 2, at a concentration of 20 μM [Pt(CNC)(**Py-Napht**)] exhibited a cell viability value above 80%. These toxicity values are significantly lower than the ones reported for a related cationic platinum(II) N[^]N[^]N complex functionalised with a naphthalimide ligand, that showed toxicity values comparable to cisplatin.¹⁹⁴

3.5.2 Cellular staining

Naphthalimide-based dyes have been widely explored in bio-sensing and bio-imaging. The naphthalimide core allows relatively facile chemical functionalisation and tuning of the photophysical properties, offering a highly versatile building unit that has been exploited to develop a wide range of cation and anion sensors.^{198,201–206} Moreover, 1,8-naphthalimides have been further explored as DNA binders and anticancer agents.^{198,207,208} Diversely functionalised 1,8-naphthalimides have also been explored as cellular labels, where modifications within the chemical structure afforded cytoplasmic localisation, affinity for lipid droplets, as well as responsiveness to hypoxia.^{191,192} 1,8-Naphthalimides have been previously incorporated in the coordination sphere of transition metal complexes, including Ru(II), Re(II), Pt(II) dyes exploited for biological applications.^{194,195,209–211} With the promising uptake and cytotoxicity data in hand, [Pt(CNC)(Py-Napht)] has been investigated as a platinum-based fluorescent cellular marker. The complex was incubated with A549 cells for 30 minutes at a concentration of 20 μ M. The successful uptake of the probe has been confirmed by the recording the emission deriving from the stained cells *via* confocal microscopy. As shown in **Figure 3.11**, [Pt(CNC)(Py-Napht)] localised in the cytoplasm as well as in droplet-like vacuoles, with morphology and localisation that resembled lipid droplets.

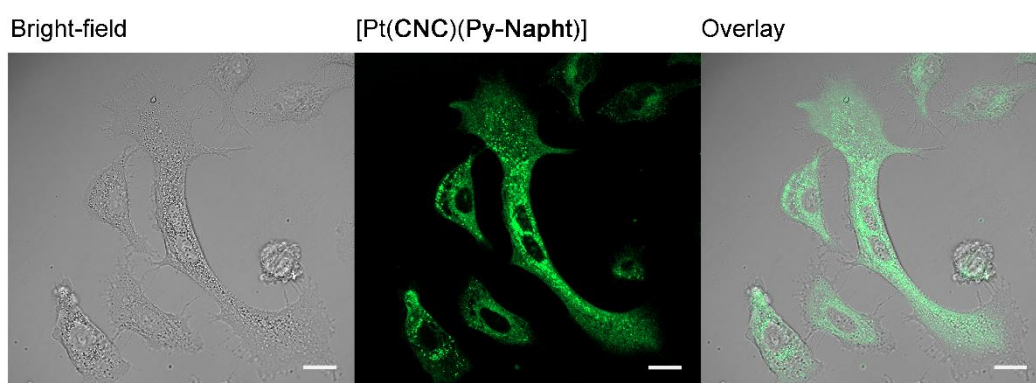


Figure 3.11 Confocal microscopy images of A549 cells incubated with [Pt(CNC)(Py-Napht)] Dose: 20 μ M, Scalebar 20 μ m.

By lowering the concentration of the dye to 10 μM , a preferential staining of the droplet-like sub-organelles was obtained, with a less intense luminescence signal detected from the cytoplasm. To verify the affinity of the dye for lipid droplets, preliminary co-localisation experiments have been attempted with the lipid stain Nile Red. A549 cells were incubated with a 10 μM solution of [Pt(CNC)(Py-Napht)] and then counter-stained with Nile-Red. The co-localisation experiments (**Figure 3.12**) showed a relatively high Pearson's coefficient, with a value of 0.67 ± 0.02 . Interestingly, in some of the lipid droplets only the [Pt(CNC)(Py-Napht)] green emission was observed, whereas no red emission coming from Nile Red was detected. This could suggest a certain degree of displacement by [Pt(CNC)(Py-Napht)] at the expense of Nile Red. Staining experiments have been carried out with **Py-Napht** in the same conditions. The free ligand showed a very similar staining pattern in comparison to the platinum(II) complex (Appendix B, Figure B.3-4). The naphthalimide moiety localised in the cytoplasm and in the lipid droplets, consistent with previous reports on similarly functionalised naphthalimides.

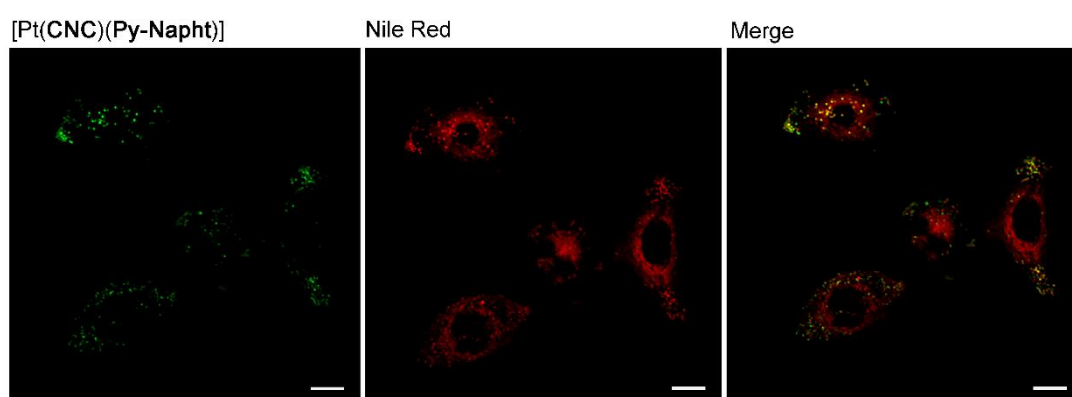


Figure 3.12 Co-staining experiment. Micrographs of A549 cells stained with [Pt(CNC)(Py-Napht)] (green) and counter-stained with Nile Red (Red). Dose: 10 μM , Scalebar 20 μm .

3.5.3 Cytotoxicity studies on bacterial cells

The cytotoxicity of [Pt(CNC)(Py-Napht)] towards *B. cereus* and *E. coli* has been evaluated by examination of the kinetics of bacterial growth in the presence of the complex. Following the protocol described in Chapter 2 - Section 2.8.9, an overnight culture of both species was inoculated in the appropriate fresh media containing 20 μM (0.1% DMSO) of the platinum complex, as well as of the free ligand **Py-Napht**. OD_{600} was then monitored at appropriate time intervals, to obtain the growth curves depicted in **Figure 3.13**. Consistently with what was observed for the parent complexes presented in Chapter 2, [Pt(CNC)(Py-Napht)] completely inhibited the bacterial growth of the gram-positive *B. cereus*. On the other hand, **Py-Napht** did not show any significant inhibitory effect. This difference is ascribed to a toxic effect of the platinum(II) complex in contrast to the free 1,8-naphthalimide. This result is intriguing, considering that [Pt(CNC)(Py-Napht)] and **Py-Napht** showed similar cell viability values for A549 cells. Similarly, neither [Pt(CNC)(Py-Napht)] or **Py-Napht** inhibited the growth of *E. coli*. The toxicity related to heavy metals is often ascribed to their accumulation and interference with various metabolic pathways. Cellular and bacterial response to heavy metals is complex.²¹² The response to metal stress in bacteria appears to be organism specific and the details of the resulting growth restriction have been intensively studied and are beginning to be understood.²¹²⁻²¹⁵ In general, metal excess induces the activation of varied efflux systems, as well as storage and sequestration mechanisms involving metal binding metabolites, that can be metal specific or non-specific.^{212,214} The different toxicity of [Pt(CNC)(Py-Napht)] to A549 cells, *B. cereus* and *E. coli* may be due to the different morphological and biochemical characteristics of the three organisms, leading to different responses to the accumulation of the platinum(II) complex. A possible reason for the opposite trends in toxicity exhibited for *B. cereus* and *E. coli* may be due to the difference in the bacterial cell envelope, which may affect the cellular uptake. Indeed, as discussed in Chapter 1, Section 1.1.1, gram-negative bacteria such as *E. coli* possess a second lipid membrane surrounding the peptidoglycan layer of the cell wall.

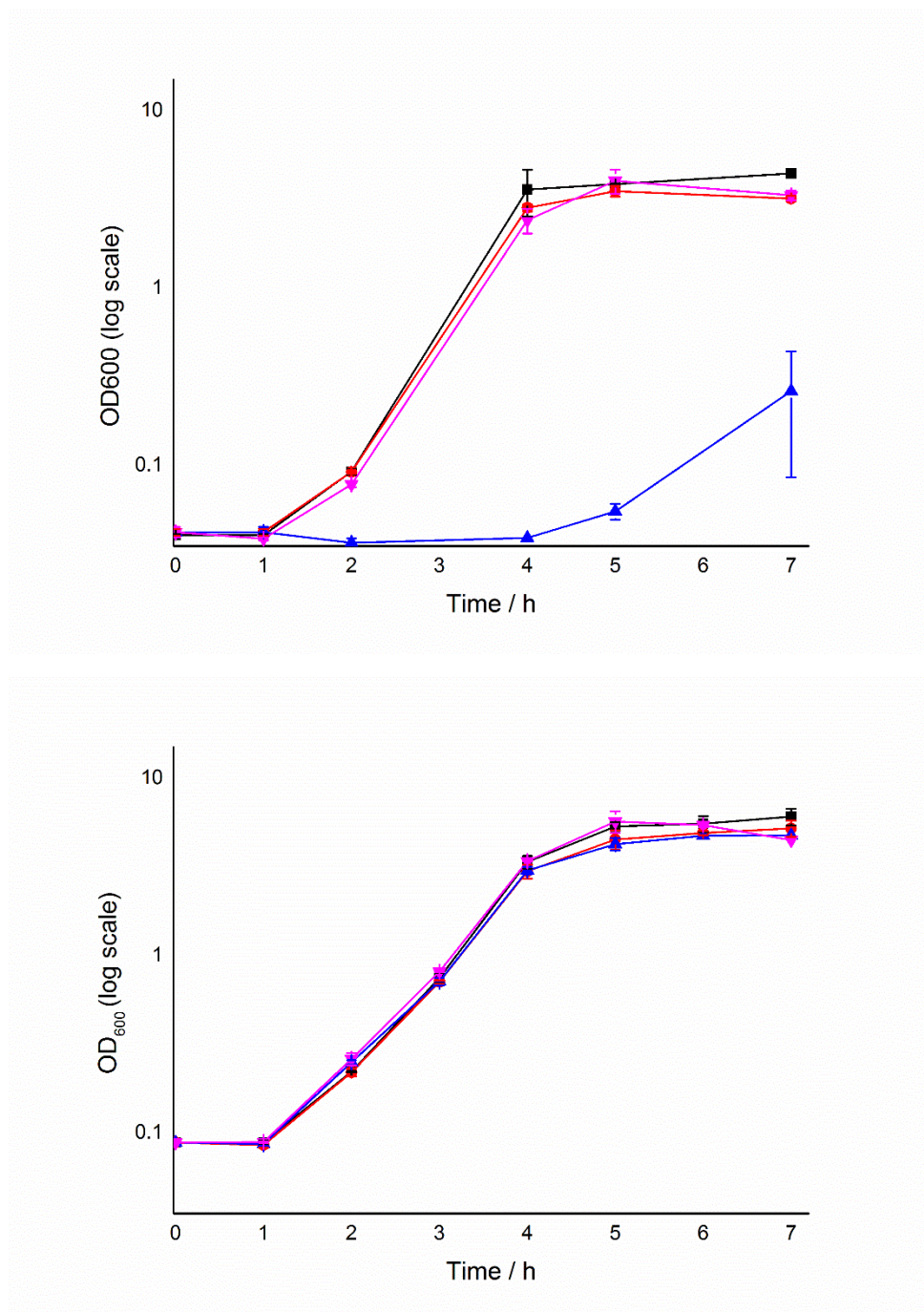


Figure 3.13 Kinetics of growth of *B. cereus* (top) and *E. coli* (bottom) at 37 °C in the presence of the platinum(II) complexes. C1) Untreated culture (black line), C2) 0.1% DMSO control (red line), 1) [Pt(CNC)(Py-Napht)] (blue line); 2) Py-Napht (pink line).

3.5.4 Bacterial staining and super-resolution Imaging

Bacteria are from five to ten times smaller than mammalian cells. Around 1 μm wide and up to 5 μm long, bacterial cells are particularly challenging to image using conventional, diffraction-limited microscopies such as wide-field epifluorescence microscopy and Laser scanning confocal microscopy (LCSM). LCSM can produce improved resolution and contrast, and in general the quality of the images can be improved in terms of signal-to-noise ratio using deconvolution algorithms. Overcoming the light diffraction limit, super-resolution microscopy techniques are suitable for bacterial imaging, particularly to visualise sub-cellular structures. Amongst the different super-resolution microscopies, Structured Illumination Microscopy (SIM) has been widely used to image bacterial substructures. SIM provides super-resolution images by applying illumination patterns to the specimen. The interaction between the illumination patterns and the sample results in a series of interference images, and the Fourier transforms of each image allows then the extraction of the spatial information that generates the super-resolution image. With this technique, super-resolution is solely achieved from the patterned illumination and data processing, without relying on photoactivatable or photoswitchable dyes. This is a great advantage, as conventional fluorophores can be used instead of dyes with particular requirements in terms of photophysical properties. To assess the potential of [Pt(CNC)(Py-Napht)] to be used as bacterial imaging agent for super-resolution microscopy, live *B. cereus* and *E. coli* were incubated with the complex and imaged *via* structured illumination microscopy (SIM). While for *E. coli* no uptake was observed even with longer incubation times, [Pt(CNC)(Py-Napht)] was successfully internalised by *B. cereus* after 15 minutes. The lack of uptake in *E. coli* may again be due to the presence of an additional external lipid membrane for gram-negative species. **Figure 3.14** shows micrographs of [Pt(CNC)(Py-Napht)] interacting with live *B. cereus*. Given the absence of a transmission detector in the SIM setup used for these experiments, the bacteria were co-stained with MitoTracker Red to gain improved spatial information. This commercial dye specifically stains the mitochondria in mammalian eukaryotic cells and while its use to label bacteria is quite limited,²¹⁶ MitoTracker could easily stain live *B. cereus* in the growth medium and compatibly with simultaneous staining with [Pt(CNC)(Py-Napht)].

More specifically, the complex seemed to localise in well-defined spherical microdomains within the bacterial cytoplasm that resembled lipid bodies. To gain further insight into the nature of these inclusions, *B. cereus* was also incubated with the lipophilic dye BODIPY 493/503. The commercial lipid stain exhibited a very similar punctate localisation pattern to [Pt(CNC)(Py-Napht)] (**Figure 3.15**), confirming the lipid nature of the vacuoles and suggesting that the platinum(II) complexes indeed possessed affinity for such lipid bodies within the bacterial cells.

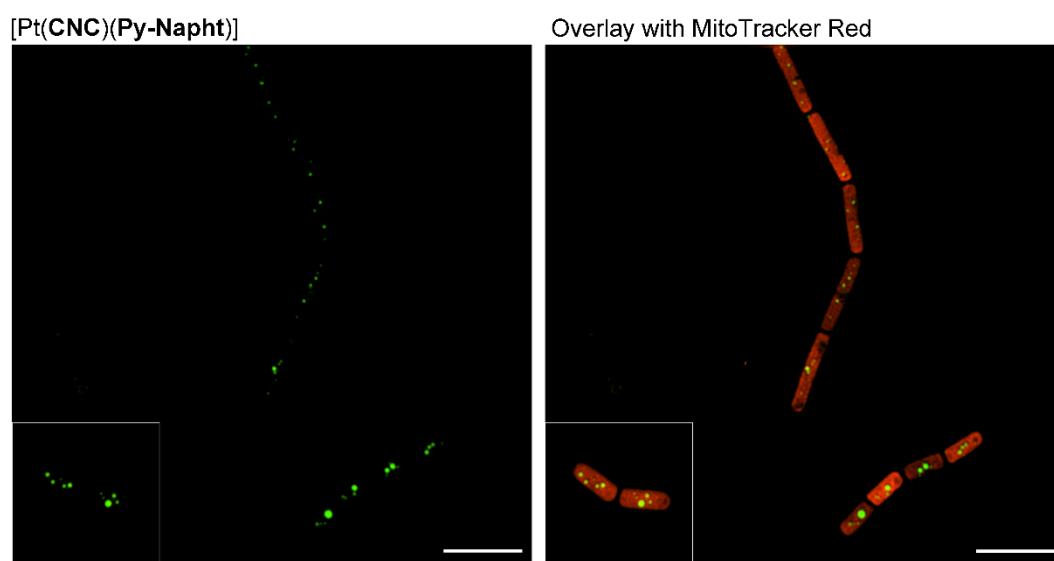


Figure 3.14 SIM images of *B. cereus* incubated with [Pt(CNC)(Py-Napht)] (left) and co-stained with MitoTracker Red (Right). Scalebars: 5 μ M.

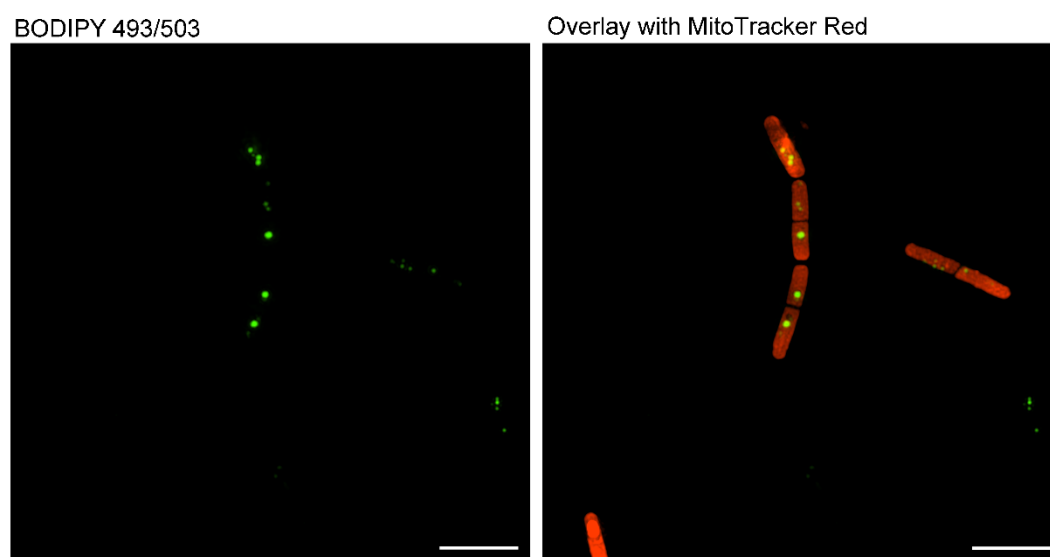


Figure 3.15 SIM images of *B. cereus* incubated with BODIPY 493/503 (left) and co-stained with MitoTracker Red (Right). Scalebars: 5 μ M.

This is remarkable, if one considers that lipid staining in bacteria has been achieved so far only with commercial organic dyes.^{15,186} Significantly, the study of lipid metabolism in bacteria is attracting an increasing interest in many fields of clinical and medical relevance.^{15,16,18,19} Indeed, lipid synthesis, storage and trafficking play a key role in the pathogenesis and antibiotic biosynthesis of many microorganism.²¹⁷⁻²¹⁹ Moreover, lipid-producing bacteria have the potential to be used for a wide range of industrial applications, including single-cell oil and biopolymers.^{17,20,22,220} Staining experiments with the free ligand **Py-Napht** were carried out as a comparison (Appendix B, Figure B.5).

Again, consistently with what was observed with A549 cells, the uncoordinated 1,8-naphthalimide showed a localisation pattern that was very similar to the one exhibited by the platinum(II) complex, suggesting that the [Pt(CNC)] fragment does not affect the sub-cellular affinity of the luminescent moiety bound in the fourth coordination site. Moreover, these results further highlight that the toxicity of these species is not purely related to their sub-cellular localisation. Indeed, [Pt(CNC)(**Py-Napht**)] and **Py-Napht** exhibited a similar sub-cellular localisation in A549 cells, and neither of them showed any toxic effects. On the other hand, the two species had opposite effects towards the bacterial cell growth of *B.cereus*, despite showing a similar staining pattern and lipid affinity.

Based on these data, a final conclusion about the toxicity trends of the synthesised compounds cannot be drawn, but further studies on a wider range of cell lines as well as bacterial strains can potentially define a trend about the toxicity of these species also with respect to their cellular localisation.

3.5.5 Bacterial imaging with NanoSIMS

In secondary ion mass spectrometry (SIMS), a section of the sample is irradiated with a primary ion beam (O^- or Cs^+) causing the release of secondary ions that are then identified based on mass-to-charge ratios.^{26,176} While NanoSIMS was initially used mainly in geochemistry and material science to measure trace elements and isotopic abundance, this powerful technique has attracted increasing attention as an imaging tool for biological samples.^{176,177,221} NanoSIMS is generally used by biologists in cell and tissue sample to image stable isotope-labeled molecules and provide an image of the sample composition.^{177,221} NanoSIMS can measure the overall abundance and distribution of native isotopes in the sample, or can be used to detect non-native isotopically labelled molecules. Therefore, one common approach to this technique is to generate an isotopically-labelled version of the biological molecule of interest (i.e. amino acids, proteins, lipids) which is then introduced into the sample prior to imaging.^{177,187,221} A similar approach has been used to monitor the accumulation of synthetic metal-based tags such as cisplatin.^{180,181} In this study, the potential of [Pt(CNC)(Py-Napht)] to be used as a correlative probe was assessed *via* NanoSIMS, that was exploited to confirm the uptake of the platinum-based dye in bacteria. Bacteria were fixed, dehydrated and embedded in resin, and semi-thin sections were cut for NanoSIMS imaging. $^{12}C^{14}N^-$ and $^{32}S^-$ secondary ions were used to show the morphology of single bacteria, and the $^{195}Pt^-$ secondary ion was used to indicate the distributions of [Pt(CNC)(Py-Napht)] (**Fig. 3.16**). As expected, NanoSIMS images confirmed the internalisation of [Pt(CNC)(Py-Napht)] within *B. cereus*. The distributions of [Pt(CNC)(Py-Napht)] in these cells are not homogenous, and there are some subcellular regions that yield higher $^{195}Pt^-$ signals, that could correspond to lipid enriched regions. However, the non-homogeneity of the sample may also be due to fixation and other preparation steps affecting the localisation of the probe, that need to be further investigated and optimised. For example, as shown in the confocal images of fixed *B. cereus* incubated with [Pt(CNC)(Py-Napht)], when the bacteria were fixed the localisation of the compound appeared to be slightly different in comparison to the one observed with live bacteria. While the localisation within lipid vacuoles was maintained, a weaker luminescent signal was detected (Appendix B – Figure B.6). This suggested that the fixation steps need to be adapted to better preserve the lipid structures.

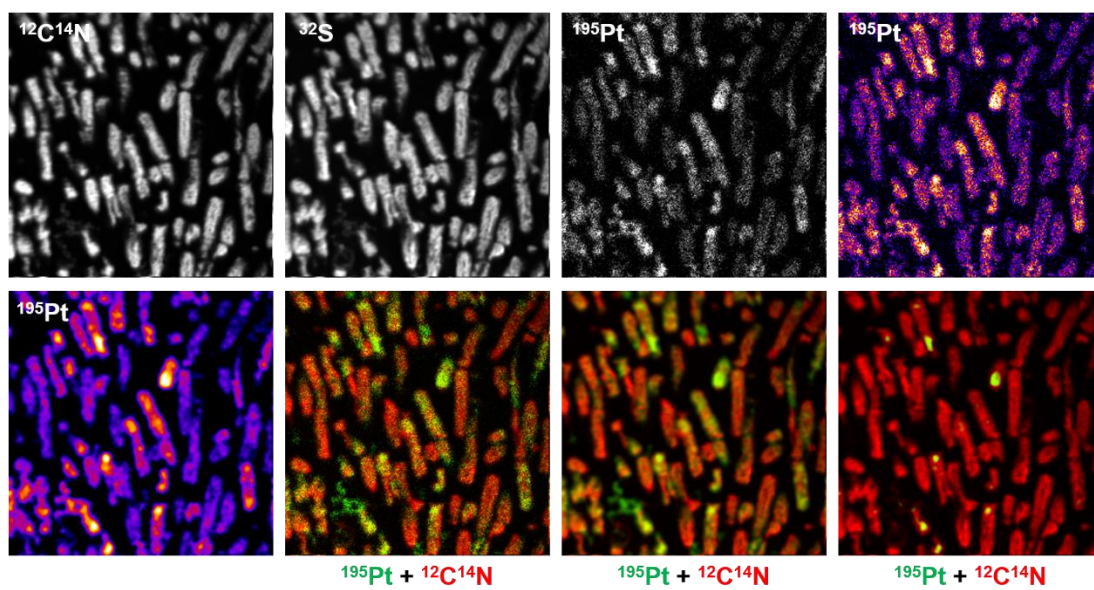


Figure 3.16 NanoSIMS micrographs of *B.cereus* incubated with [Pt(CNC)(Py-Napht)] for 15 min.

3.6 Conclusion

In this chapter, a new platinum(II) complex, [Pt(CNC)(Py-Napht)], has been synthesised and characterised. The photophysical properties of the complex have been investigated alongside the uncoordinated ligand, **Py-Napht**. Interestingly, the properties of the 1,8-naphthalamide are unaffected by the presence of the platinum(II) metal centre. Indeed, the photophysical trends observed for the complex in diluted DCM, DMSO and aqueous solutions are very similar to the one monitored for **Py-Napht**. Time-Dependent Density Functional Theory (TD-DFT) calculations confirmed that no electronic interaction is occurring between the naphthalimide moiety and the platinum(II) C^NC centre, and that the lowest excited state is always located on the naphthalimide. [Pt(CNC)(Py-Napht)] is weakly emissive in the solid state, showing a broad and unstructured emission profile that is typical of the emission arising from aggregated platinum(II) complexes bearing dicyclometalated ligands.

The platinum(II)-naphthalimide complex has been firstly tested towards eukaryotic cells, to validate its capability of being used as cellular label. The complex appeared to be non-toxic towards A549 cells, with viability values that were very similar to the one observed for the uncoordinated **Py-Napht**. Given the presence of the metal centre, it was possible to carry out ICP-MS analyses, which confirmed the uptake of the complex and prompted the investigation of its cellular behaviour via confocal microscopy. Inspection of the confocal images of A549 cells incubated with [Pt(CNC)(Py-Napht)] revealed a preferential localisation in lipid droplets, similar to that observed for **Py-Napht**. Preliminary co-localisation experiments with the lipophilic dye Nile Red confirmed the affinity of the reported dyes for lipid compartments within A549 cells. To further investigate the sub-cellular localisation of these dyes, different lipid droplet specific dye could be used as comparison, such as LipidSpot.

Based on the results obtained with eukaryotic cells, [Pt(CNC)(Py-Napht)] has been investigated as potential correlative probe for bacteria, using the model species *B. cereus*. The possibility of using the platinum(II)-naphthalimide complex for fluorescence microscopy has been confirmed via structured illumination microscopy (SIM), which importantly showed the applicability of the synthesised probe for super-resolution microscopy. Interestingly, [Pt(CNC)(Py-Napht)] showed sub-cellular

localisation in bacterial cells, staining spherical micro-domains resembling lipid inclusions.

Imaging experiments with the lipophilic dye BODIPY confirmed the lipid nature of these vacuoles, suggesting the affinity of the platinum(II) complexes for lipid inclusions within bacteria. Again, **Py-Napht** showed a similar staining pattern.

Unfortunately, while **Py-Napht** did not affect the bacterial growth, [Pt(CNC)(**Py-Napht**)] showed toxic effects towards *B. cereus*. Indeed, the platinum(II)-naphthalimide complex appeared to have inhibitory effects against this specie, as indicated by the growth curves. It is important to note however that [Pt(CNC)(**Py-Napht**)] showed uptake in *B. cereus* in incubation times (15 minutes) that are shorter than the doubling time of the bacteria in the growth conditions used for this study (around 30 minutes). The toxicity of [Pt(CNC)(**Py-Napht**)] will require further investigations to gain a better understanding about the mechanisms involved in the inhibitory effect against *B. cereus*, especially considering that the same complex did not show any toxic effect against the eukaryotic A549 cells. The potential of [Pt(CNC)(**Py-Napht**)] to be used as a correlative probe was assessed *via* nano-scale secondary ion mass spectrometry (NanoSIMS), that was exploited to confirm the uptake of the platinum-based dye in bacteria. Indeed, inspection of the NanoSIMS images confirmed the internalisation of [Pt(CNC)(**Py-Napht**)] within *B.cereus*. These results are remarkable, as they show that the [Pt(CNC)] fragment bound to the naphthalimide dye does not affect the photophysical properties and cellular localisation of Pt(CNC)(**Py-Napht**) in comparison to the free ligand, allowing the complex to be used as a carrier for the luminescent unit, while allowing detection with other techniques that are not readily accessible for traditional organic fluorophores, such as ICP-MS and NanoSIMS.

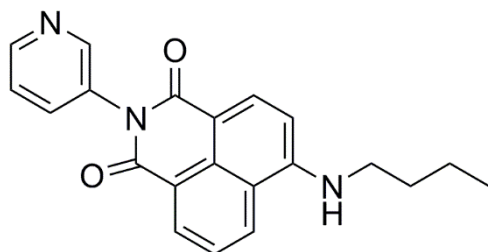
3.7 Experimental

3.7.1 General synthetic procedures

General procedures have been conducted as outlined in Chapter 2, section 2.8.1, unless otherwise stated.

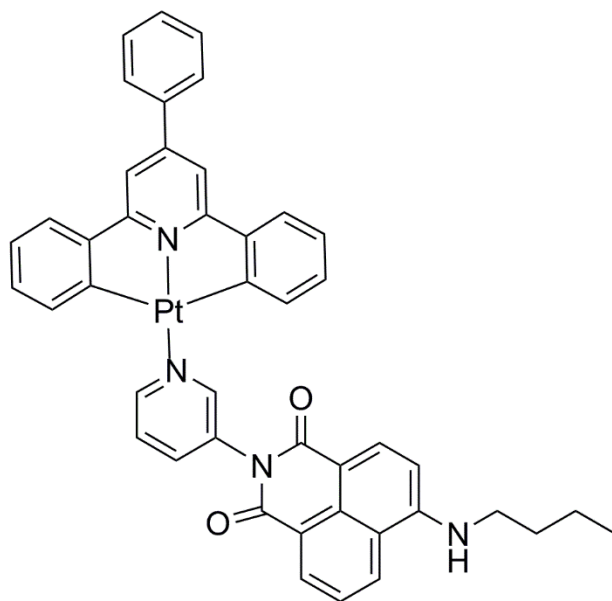
3.7.2 Synthesis

N-3-Aminopyridine-4-butylamino-1,8-naphthalimide (**Py-Napht**)



3-Aminopyridine (85 mg, 0.9 mmol) and 4-nitro-naphthalic anhydride (0.2 g, 0.82 mmol) in ethanol (30 mL) was stirred at reflux for 16 h, then cooled to room temperature and the precipitate filtered and then washed with cold ethanol and ether to give a beige solid. This crude residue (0.14 g) was then combined with butylamine (35 μ L, 3.5 mmol) in ethanol (30 mL) and stirred at reflux for 16 hours. The reaction mixture was cooled and filtered, and the filtrate evaporated under reduced pressure. The crude residue was purified using silica column chromatography (0-10% MeOH in CH_2Cl_2) to give **PyNapht** as a yellow solid (110 mg, 35 % over two steps). **HR-ESIMS**: calculated for $\text{O}_2\text{N}_3\text{C}_{21}\text{H}_{19}$: 345.402 (m/z), found: 368.13695 (m/z) [$\text{M}+\text{Na}$] $^+$. **$^1\text{H-NMR}$** , 500 MHz, CDCl_3 : δ (ppm) 8.68 (s, b, 1H), 8.64-8.59 (m, 2H), 8.50 (d, $J = 8.4$, 1H), 8.16 (dd, $J = 8.5, 0.9$, 1H), 7.72-7.68 (m, 1H), 7.66 (dd, $J = 8.5, 7.3$, 1H), 7.51-7.46 (m, 1H), 6.77 (d, $J = 8.4$, 1H), 5.40 (s, b, 1H), 3.47-3.41 (m, 2H), 1.86-1.78 (m, 2H), 1.59-1.51 (m, 2H), 1.04 (t, $J = 7.4$, 3H). **$^{13}\text{C-NMR}$** , 125 MHz, CDCl_3 : δ (ppm) 164.8, 164.1, 150.2, 150.0, 149.1, 137.0, 135.3, 131.9, 130.5, 126.6, 124.9, 124.0, 123.9, 123.1, 120.5, 109.8, 104.7, 43.6, 31.2, 20.5, 14.0.

[Pt(CNC)(Py-Napht)]



[Pt(CNC)(DMSO)] (0.050 g, 0.087 mmol) and **PyNapht** (0.060 g, 0.174 mmol) were dissolved in 5 mL of a acetone/methanol (9:1) mixture. The reaction mixture was stirred at reflux overnight. After the reaction time, the solvent was dried under reduced pressure. Purification *via* column chromatography, using silica as stationary phase and acetone as eluent, was required to yield the pure [Pt(CNC)(Py-Napht)]. (0.022 g, 0.026 mmol, 30%). [PtO₂N₄C₄₄H₃₅] Calc: C 62.40%, H 4.17%, N 6.62%. Found: C 62.69%, H 4.07%, N 6.61%. ¹H-NMR, 400 MHz, acetone-*d*₆, δ (ppm): 9.08 (d, 2H, J_{H-H} = 8); 8.13 (t, 1H, J_{H-H} = 8.0 Hz); 7.98 (d, 2H, J_{H-H} = 12); 7.73 (m, 6H); 7.59-7.51 (m, 3H); 7.14 (apparent t, 2H); 7.02 (apparent t, 2H), 6.92 (d, 2H, J_{H-H} = 8.0 Hz). ¹³C-NMR, 100 MHz, DMSO-*d*₆, δ (ppm) = 166.9, 163.7, 162.9, 153.5, 150.1, 149.9, 149.8, 137.3, 136.8, 136.7, 132.7, 132.2, 130.7, 130.6, 130.2, 129.5, 129.4, 129.3, 128.1, 127.5, 125.5, 124.9, 124.7, 124.4, 123.6, 123.3, 113.3, 30.9, 20.4, 16.2. Two quaternary C peaks were not visible in the spectrum. Aliphatic carbon peak overlapping with solvent signal.

3.7.3 Photophysical measurements

Photophysical measurements have been conducted as outlined in Chapter 2, section 2.8.3, with the exception of Photoluminescence Quantum Yields measurements. Photoluminescence Quantum Yields were determined according to the approach described by Demas and Crosby²²². Luminescence quantum yields (Φ_{em}) were measured in optically dilute solutions (O.D. < 0.1 at excitation wavelength) obtained from absorption spectra on a wavelength scale [nm] and compared to the reference emitter by Equation:

$$\Phi_x = \Phi_r \left[\frac{A_r(\lambda_r) I_r(\lambda_r) n_x^2 D_x}{A_x(\lambda_x) I_x(\lambda_x) n_r^2 D_r} \right]$$

where A is the absorbance at the excitation wavelength (λ), I is the intensity of the excitation light at the excitation wavelength (λ), n is the refractive index of the solvent, D is the integrated intensity of the luminescence and Φ is the quantum yield. The subscripts r and x refer to the reference and the sample, respectively. The quantum yield determinations were performed at identical excitation wavelength for the sample and the reference, therefore cancelling the $I(\lambda_r)/I(\lambda_x)$ term in the equation. The quantum yields of complexes were measured against an aqueous solution of [Ru(bipy)₃]Cl₂ (bipy = 2,2'-bipyridine; $\Phi_r = 0.028$)²²³.

3.7.4 Theoretical calculations

To perform DFT and TD-DFT calculations, we have used the Gaussian16 program.²²⁴ Our calculations consisted in geometry optimisations, vibrational spectra determinations, and TD-DFT calculations of **PyNaphth** and Pt-**PyNaphth**. We have applied default procedures, integration grids, algorithms and parameters, except for tighten energy (typically 10^{-10} a.u.) and internal forces (10^{-5} a.u.) convergence thresholds. The ground-state (S_0) and excited-state (S_1) geometrical parameters have been determined with the M06-2X exchange-correlation functional.²²⁵ This choice was motivated by its relative high ratio of *exact* exchange (54%) limiting the formation of spurious charge-transfer excited-state that can sometimes be obtained with functionals

encompassing smaller exact exchange ratio. The vibrational spectrum has been subsequently determined analytically at the same level of theory and it has been checked that all structures correspond to true minima of the potential energy surface for both S_0 and S_1 . At least, the first thirty low-lying excited-states have been determined within the vertical TD-DFT approximation using the same functional, that is suited for optical spectra, though it tends to provide slightly too large transition energies.²²⁶ For the structural and vibrational calculations, we have selected the 6-31G(d) atomic basis set for all atoms, but Pt that was treated with the LanL2DZ atomic basis set and pseudo-potential. For the TD-DFT calculations, we used the 6-311+G(2d,p) atomic basis set (light atoms) and the LanL08(f) basis/pseudopotential (Pt). During all steps, a modelling of bulk solvent effects (here DMSO) was achieved through the Polarizable Continuum Model (PCM).²²⁷ For the TD-DFT calculations, we applied the linear-response²²⁸ approach in its *non-equilibrium* limit and applied further corrections using the corrected linear-response²²⁹ approach, so that all our values are “LR+cLR”. The contour threshold used to draw the MOs was set to 0.02 au.

3.7.5 Cell Culture

The biological investigation regarding eukaryotic cells in this chapter was performed in collaboration with A/Prof Elizabeth New at the University of Sydney. A549 cells were used and cultured following the protocol described in Chapter 2, section 2.8.

3.7.6 Uptake studies

Uptake studies were carried out following the protocol described in Chapter 2, section 2.8.5.

3.7.7 Cell viability

Cell viability was determined by Alamar Blue assay according to the protocol described in Chapter 2, section 2.8.6.

3.7.8 Confocal microscopy on eukaryotic cells

A549 Cells were stained following the protocol described in Chapter 2, section 2.8.7. Staining with Nile Red was performed according to the Manufacturer's protocol (ThermoFisher). Confocal images were acquired with the experimental setup described in Chapter 2, section 2.8.7.

3.7.9 Bacterial strains and growth conditions

The biological investigation regarding bacterial cells (Sections 2.8.8-2.8.10) was performed at Curtin University and at the Harry Perkins Institute of Medical Research, Perth. Bacterial strains and growth conditions were described in Chapter 2, section 2.8.8.

3.7.10 Growth curves determination

Bacterial cell growth was monitored following the protocol described in Chapter 2, section 2.8.9.

3.7.11 Confocal microscopy on bacterial cells

Super-resolution imaging of live *B.cereus*:

Live bacteria were dosed with a 10 μ M solution of Pt-PyNapht and PyNapht in Nutrient Broth (0.1% DMSO) for 15 minutes, then washed with Nutrient Broth and imaged. Staining with BODIPY 493/503 and MitoTracker Red (3 μ M) was performed

following the same protocol. Before imaging, bacteria were immobilized in a 1.5% Nutrient Agar gel.

Super-resolution images were acquired using a Nikon SIM Ti2 inverted microscope and a SR Apo TIRF AC 100xH oil immersion objective lens (NA = 1.49). Pt-PyNapht, PyNapht and BODIPY were excited at 488 nm and the emission was collected in the 525/50 nm region. MytoTracker Red was excited at 561 nm and the emission collected in the 605/50 nm region. Images were collected and reconstructed using NIS-Element version 4.60.00 software. The images were processed using NIS-Element Viewer v.4.20 and the final preparation was conducted with Adobe Photoshop CC (Adobe Systems Inc., USA).

Imaging of fixed *B.cereus*:

Bacteria were stained prior to fixation following the protocol described above, and then fixed with PFA (2% in PBS). Bacteria were resuspended in fresh PBS before imaging.

Fixed *B. cereus* stained with Pt-PyNapht, were imaged with a Nikon A1 confocal microscope with a Plan Apo VC 60x water immersion objective lens (NA = 1.2). Pt-PyNapht was excited at 488 nm and the emission was collected in the 525/50 nm region.

3.7.12 NanoSIMS

500-nm sample sections were cut with a Leica UC6 ultramicrotome and mounted on silicon wafers. Sections were coated with a thin layer of gold and imaged with NanoSIMS 50 (CAMECA). Secondary ions ($^{12}\text{C}^{14}\text{N}^-$, $^{32}\text{S}^-$ and $^{195}\text{Pt}^-$) were collected. Selected regions of the section was scanned before imaging (primary aperture D1=1) to remove the gold coating and ensure a steady state of secondary ion release.

A $15 \times 15 \mu\text{m}$ region was imaged with an ~ 3 pA beam current (primary aperture D1=2) and a dwell time of 30 ms/pixel per frame for four frames. 256×256 -pixel images were obtained. Images were prepared using the OpenMIMS plugin in ImageJ.

Chapter 4

Anionic Cyclometalated Platinum(II) Tetrazolato Complexes as Viable Photoredox Catalysts

4.1 Introduction

The development of platinum complexes has attracted a great deal of attention in the past few years, with a number of investigations focusing on the design principles for platinum(II) complexes^{57,70,125} containing N-donor and/or cyclometalated ligands, in order to tune their photophysical and aggregation properties.^{61,65,115,128} Platinum(II) complexes bearing chelating ligands such as terpyridine derivatives (N[^]N[^]N), and mono-deprotonated cyclometalated ligands such as diversely functionalised 1,3-bis-(2-pyridyl)benzene (N[^]C[^]N) or 6-phenyl-2,2'-bipyridine (C[^]N[^]N), have been widely explored for a variety of applications, including biosensing and bioimaging,^{54,59,66,88,146} fabrication of organic light-emitting devices (OLEDs)^{69,70,230} and photocatalysis.^{231–234} On the other hand, doubly deprotonated tridentate C[^]N[^]C ligands have been generally less investigated. This type of dicyclometalated ligands offers a facile route to the preparation of anionic platinum(II) complexes, which can be simply obtained by the successive addition of a negatively charged ancillary ligand to coordination sphere. The majority of the reported platinum(II) C[^]N[^]C species are neutral or cationic, whereas reports that explore anionic platinum(II) complexes are quite rare.^{151,235} In this chapter, the synthesis, characterisation, photophysical and photochemical studies are reported of the first examples of anionic Pt(II) tetrazolato complexes, [Pt(CNC)TzR]TBA, bearing a doubly deprotonated 2,4,6-triphenylpyridine (CNCH₂) as a terdentate ligand, a tetrazolato ligand (TzR⁻) in the fourth coordination site and tetrabutylammonium (TBA⁺) as counterion (**Figure 4.1**). While the synthesis of these complexes was motivated by their potential use as probes for organisms characterised by a reverse membrane potential, prompted by the relatively small number of reports exploring the applications of homogeneous platinum-based photoredox catalysts in

organic synthesis^{236–239}, the capacity of these novel Pt(II) complexes to serve as catalysts in a number of fundamental classes of visible-light-mediated photoredox-catalyzed reactions has been evaluated.^{240–242} Specifically, the viability of the complexes in different types of α -amino C–H functionalization reactions, an atom-transfer radical addition (ATRA), and a hydrodehalogenation reaction was explored.

Target compounds

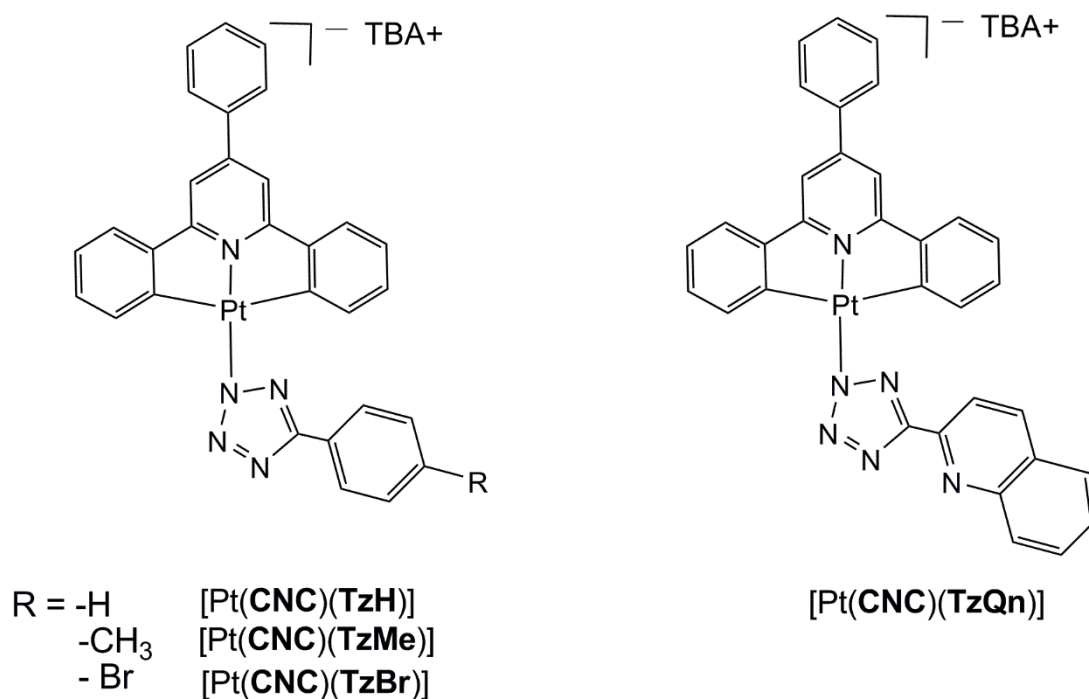


Figure 4.1 Chemical structure of the anionic platinum(II) complexes presented in this chapter.

4.2 Synthesis and characterization of the anionic platinum complexes.

The first attempt to synthesise the anionic platinum(II) species involved the generation of the triethylammonium salt of the appropriate tetrazole, [TEA][TzR], following previously reported procedures used for Ru(II), Re(I) and Ir(III) complexes^{84,243,244}. The deprotonated tetrazole was then added to a solution of the precursor [Pt(CNC)(DMSO)], however the target complexes could not be isolated from the reaction mixture. The ¹H-NMR of the crude [Pt(CNC)(TzMe)][TEA], precipitated from the reaction mixture, is shown in **Figure 4.2** as an example.

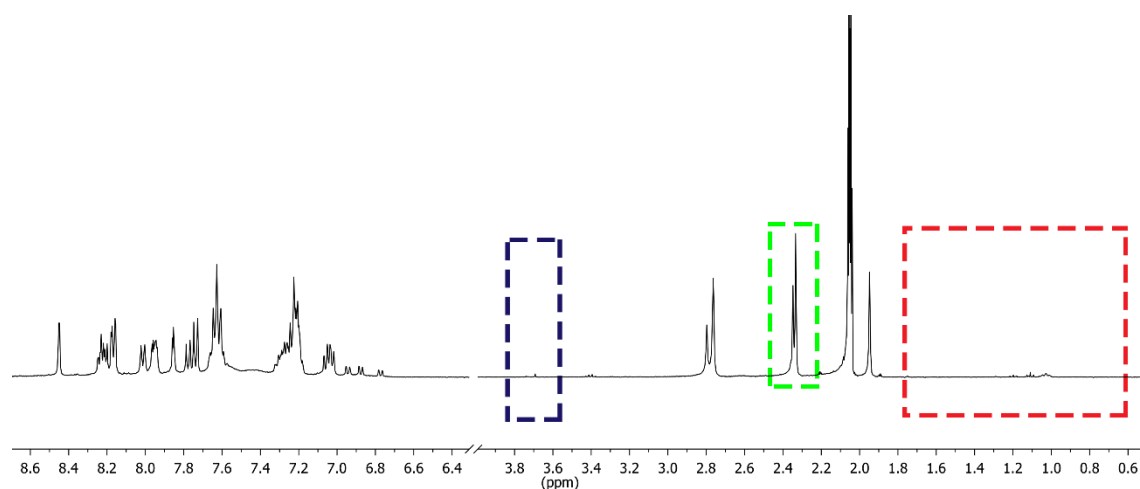


Figure 4.2 ¹H-NMR in acetone-*d*⁶ for the crude [Pt(CNC)(TzMe)][TEA]. The area in which the singlet of the DMSO ligand is expected (blue line), the singlets of the methyl group on the tetrazole (green line) and the area in which the peaks corresponding to the triethylammonium counterion are expected (red line) are highlighted in boxes.

As discussed in the previous chapters, the absence of a singlet at 3.69 ppm indicated that the DMSO ligand was displaced from the coordination sphere of the platinum(II) centre. However, inspection of the aromatic region did not show a set of signals matching with a doubly cyclometalated structure as described in Chapter 2, Section 2.4.1. The *para*-methyl substituted tetrazolato ligand typically shows a single at around 2.39 ppm, corresponding to the -CH₃ group, whereas the ¹H-NMR of the reaction

mixture showed two singlets, at 2.35 and 2.33 ppm respectively. This suggests the presence of at least two different species in solution, which could be due to ligand exchange processes. Moreover, the spectrum did not confirm the presence of the TEA⁺ counterion, which is normally characterised by two signals at around 1.15 ppm (-CH₂) and 3.36 ppm (-CH₃). This observation did not support the formation of an anionic compound. This result was in contrast with the ESI-MS analysis of the same sample, that showed the presence of a predominant signal for 659 *m/z* in the negative ions scan, corresponding to the expected [Pt(CNC)(TzMe)]⁻ fragment, together with a peak at 102 *m/z* (TEA⁺) in the positive ions scan. The targeted anionic complexes were successfully isolated by using a stronger base such as tetrabutylammonium hydroxide (TBAOH), which also offered a more coordinating counterion. A large excess of the appropriate tetrabutylammonium tetrazolate salt [TBA][TzR] was generated in H₂O and then combined with a MeOH solution of [Pt(CNC)(DMSO)] (Figure 4.3).

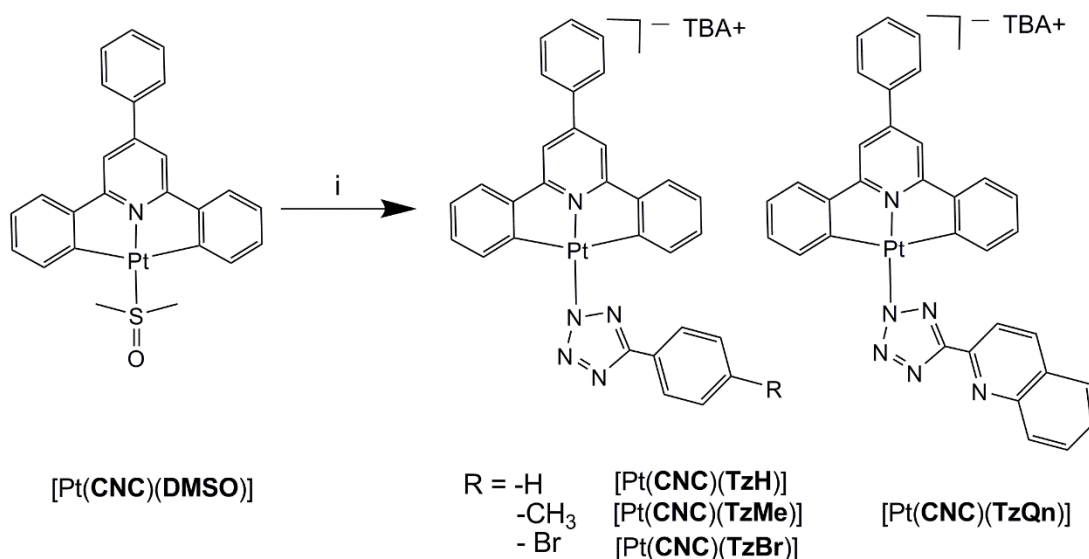


Figure 4.3 Scheme of the synthetic procedure for the anionic complexes. Reagent and conditions: i) tetrazole ligand, TBAOH, MeOH/H₂O 6:1, reflux, 20 h.

After heating at reflux for 20 hours, the final complexes were filtered off and did not require any further purification. ¹H and ¹³C-NMR characterisation confirmed the coordination of the tetrazolato ligand to a doubly cyclometalated species. The ¹H-NMR spectrum of [Pt(CNC)(TzMe)][TBA] is reported, as an example, in Figure 4.4. The presence of the TBA⁺ as counterion was confirmed *via* ¹H-NMR and ¹³C-NMR,

as well as ESI-MS. Indeed, the cationic molecular ion corresponding to the TBA^+ was detected, alongside the molecular ion of the complex $[\text{Pt}(\text{CNC})(\text{TzMe})]^-$ (Figure 4.5). ESI-MS spectra for the remaining anionic compounds can be found in Appendix C – Figures C.1 – C.3.

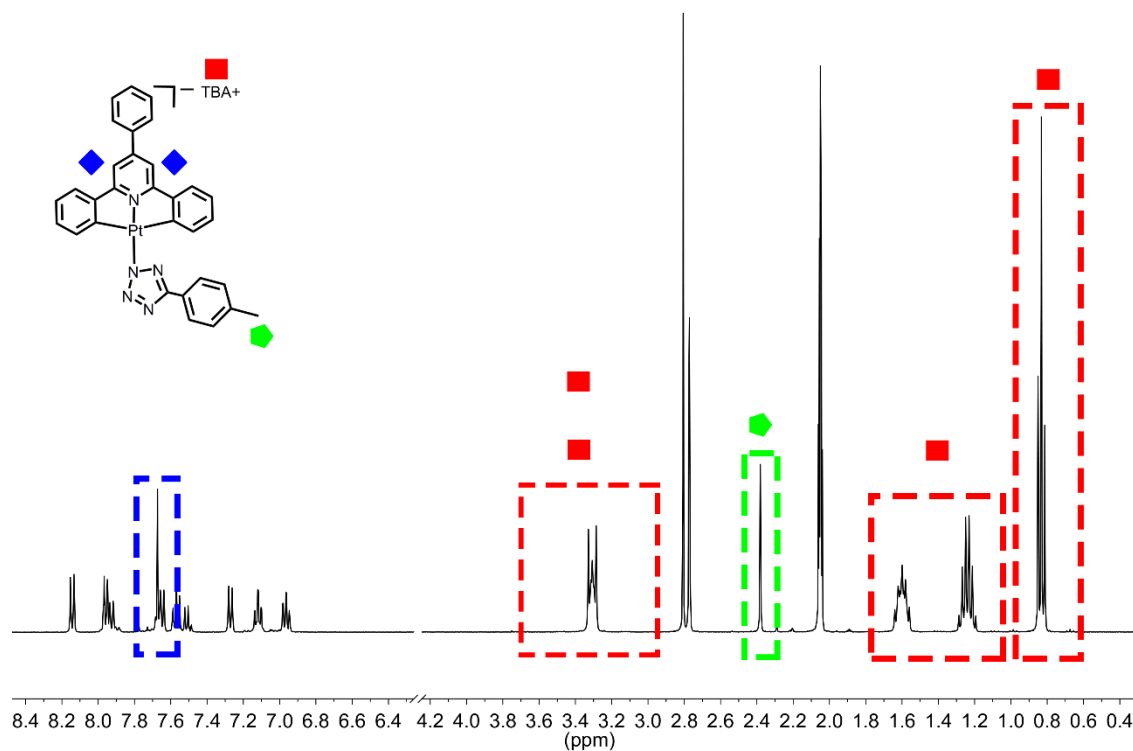


Figure 4.4 $^1\text{H-NMR}$ in acetone- d_6 for $[\text{Pt}(\text{CNC})(\text{TzMe})][\text{TBA}]$. The singlet of the central pyridine (blue line), the singlet of the methyl group on the tetrazole (green line) and the peaks corresponding to the tetrabutylammonium counterion (red line) are highlighted in boxes.

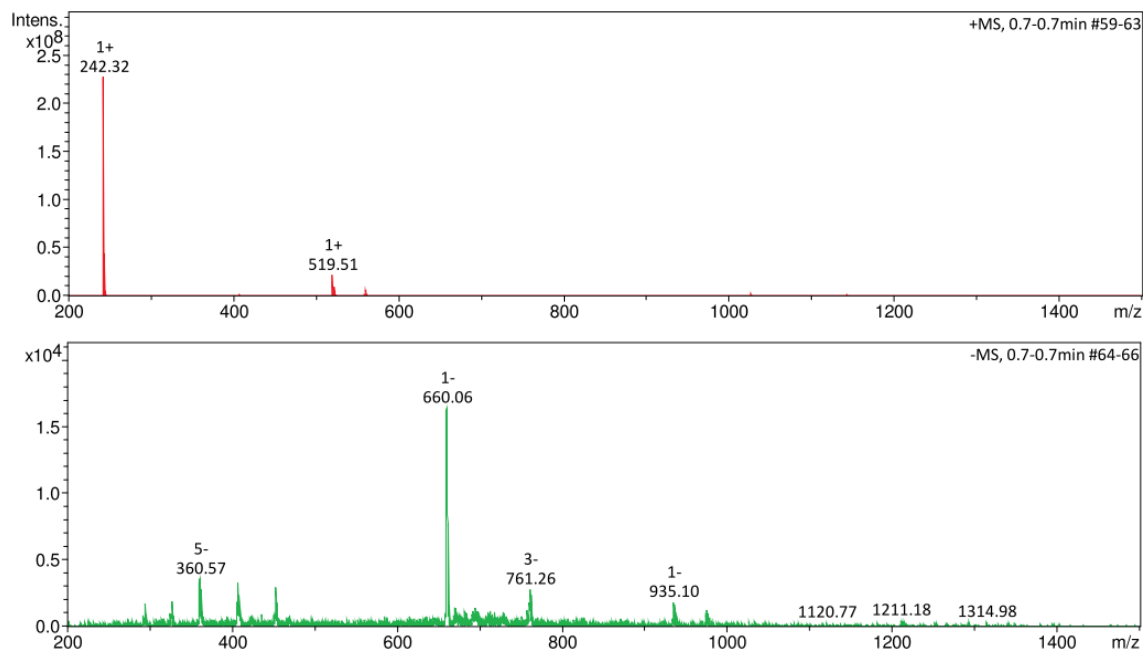


Figure 4.5 ESI-MS spectrum of [Pt(CNC)(TzMe)][TBA]. Top: positive ion region; bottom: negative ion region.

4.3 Photophysical properties

4.3.1 Absorption properties

The photophysical properties of the anionic complexes in solution have been assessed in DMF, used for the photocatalysis experiment, as well as DMSO and H₂O (0.1% DMSO). The UV-Vis absorption data obtained from 10⁻⁵ M DMF solutions of the complexes are summarized in **Table 4.1** along with the corresponding absorption spectra shown in **Figure 4.6**. The absorption profiles display intense absorption bands with maxima around 284 nm ($\epsilon = 1\text{--}2 \cdot 10^4 \text{ M}^{-1} \text{ cm}^{-1}$) and in the 330–350 nm region ($\epsilon = 0.3\text{--}0.7 \cdot 10^4 \text{ M}^{-1} \text{ cm}^{-1}$) nm. Tailing from these bands, the anionic complexes show an additional shoulder centered around 375 nm ($\epsilon = 0.2\text{--}0.5 \cdot 10^4 \text{ M}^{-1} \text{ cm}^{-1}$). With reference to related platinum(II) cyclometalated complexes, the high energy bands ($\lambda < 400 \text{ nm}$) are assigned to $\pi \rightarrow \pi^*$ ligand-centered transitions (LC).^{61,142,143,145,151,193} The bands at lower energy ($\lambda > 400 \text{ nm}$) are assigned to spin-allowed (singlet to singlet) and spin-forbidden (singlet to triplet) metal-to-ligand-charge-transfer transitions (MLCT).^{68,142,145,151} The absorption profiles of the complexes in DMSO, and H₂O (0.1% DMSO), followed the same trend (See Appendix C – Figures C.4 - C.5).

Table 4.1 Absorption data for the anionic platinum complexes from a 10⁻⁵ M DMF solution.

Complex	λ_{abs} [nm] ($10^4\epsilon$ [$\text{M}^{-1} \text{ cm}^{-1}$])
[Pt(CNC)(DMSO)]	284 (1.272), 347 (0.460), 437 (0.031), 470 (0.015), 565 (0.001)
[Pt(CNC)(TzH)]	284 (2.267), 327 (0.591), 371 (0.490), 411 (0.219), 531 (0.012)
[Pt(CNC)(TzMe)]	284 (1.037), 331 (0.256), 373 (0.216), 412 (0.099), 536 (0.002)
[Pt(CNC)(TzBr)]	284 (1.700), 325 (0.462), 372 (0.350), 407 (0.165), 533 (0.002)
[Pt(CNC)(TzQn)]	284 (2.047), 333 (0.736), 372 (0.519), 415 (0.195), 531 (0.007)

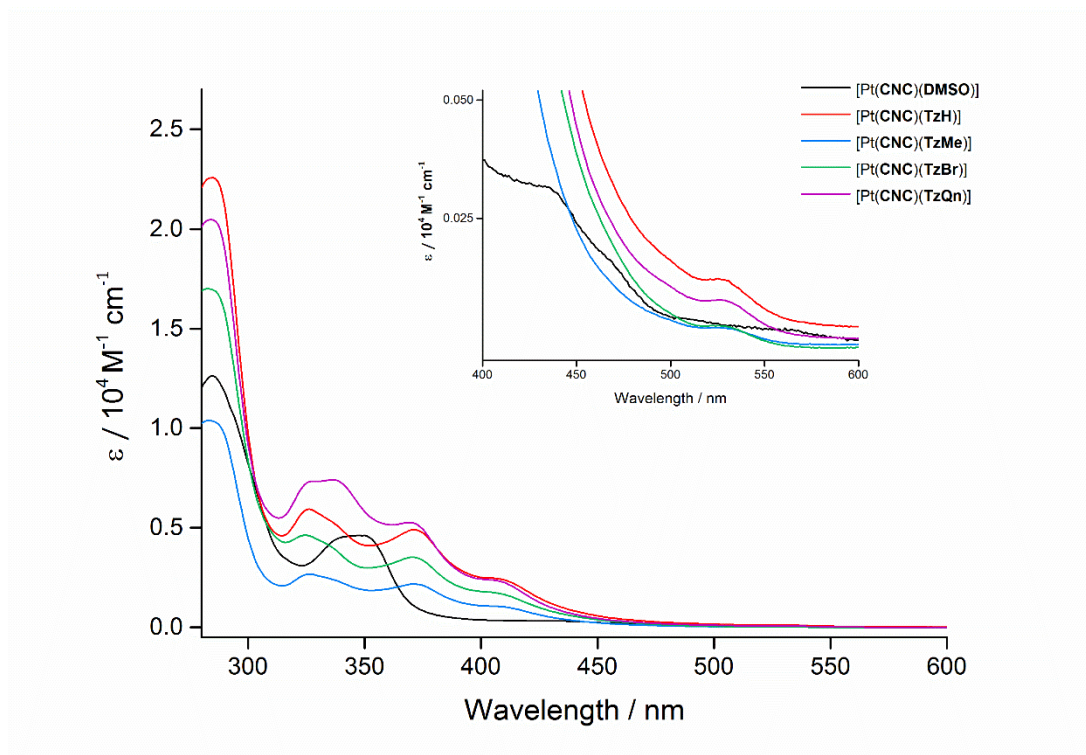


Figure 4.6 Absorption spectra of 10^{-5} M solutions of the platinum complexes in DMF.

4.3.2 Emission properties in solution

While none of the complexes displayed photoluminescence in DMF or DMSO fluid solution at room temperature, a switch-on in the emission is observed in H₂O (0.1% DMSO). In agreement with what was observed for the neutral complexes described in Chapter 2, the lack of emission in pure organic solvents at room temperature is ascribed to the fact that the triplet excited state of the complexes undergoes a strong distortion, favouring therefore nonradiative decay.^{57,61} Again, introducing H₂O in the solvent system caused a decrease in solubility, inducing aggregation. As a result, a broad emission band centred at 700 nm was observed for the anionic complexes (**Figure 4.7**), with emission maxima and excited state lifetime values in agreement to the ones observed for the neutral parent complexes (**Table 4.2**).

Table 4.2 Emission data for the anionic platinum complexes from a 10⁻⁵ M H₂O (0.1% DMSO) solution.

Complex	λ_{em} [nm]	τ_{aer} [ns]	Φ_{aer}^a %
[Pt(CNC)(TzH)]	703	20	0.93
[Pt(CNC)(TzMe)]	700	28	0.44
[Pt(CNC)(TzBr)]	693	19	0.51
[Pt(CNC)(TzQn)]	709	23	0.53

^aMeasured with an integrating sphere.

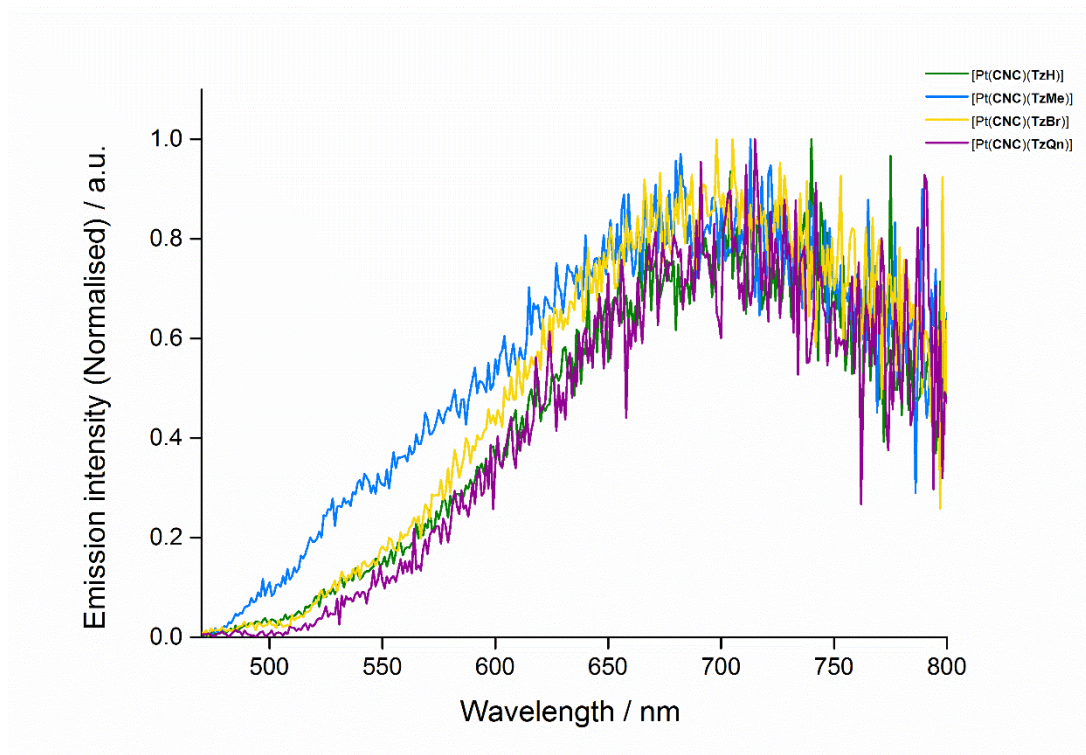


Figure 4.7 Emission profiles for the anionic platinum complexes from a 10^{-5} M H_2O (0.1% DMSO) solution.

4.3.3 Emission properties in solid state and frozen matrix

The emission properties of the complexes could be measured from solid state and frozen matrix at 77 K (**Table 4.3**). In the solid state, the anionic complexes displayed broad and unstructured bands with red-shifted maxima in the 600-750 nm region (**Figure 4.8**). These emission bands are again likely to arise from the formation of aggregates, in agreement with related platinum(II) complexes bearing analogous CNC^{2-} cyclometallating ligands.^{142,145,151} The red-shift is ascribed to the stronger σ -donation on the anionic tetrazolato ligands compared to DMSO. The quantum yields are relatively low and the value of excited state lifetimes decays are in agreement with previously reported compounds.^{143,149} The emission from aggregated species for the anionic complexes is also supported from the photophysical studies performed in frozen butyronitrile glass at 77 K, where the intensity of the broad and red-shifted emission band is enhanced upon increasing the concentration of the platinum(II) complex from 10^{-7} to 10^{-4} M.

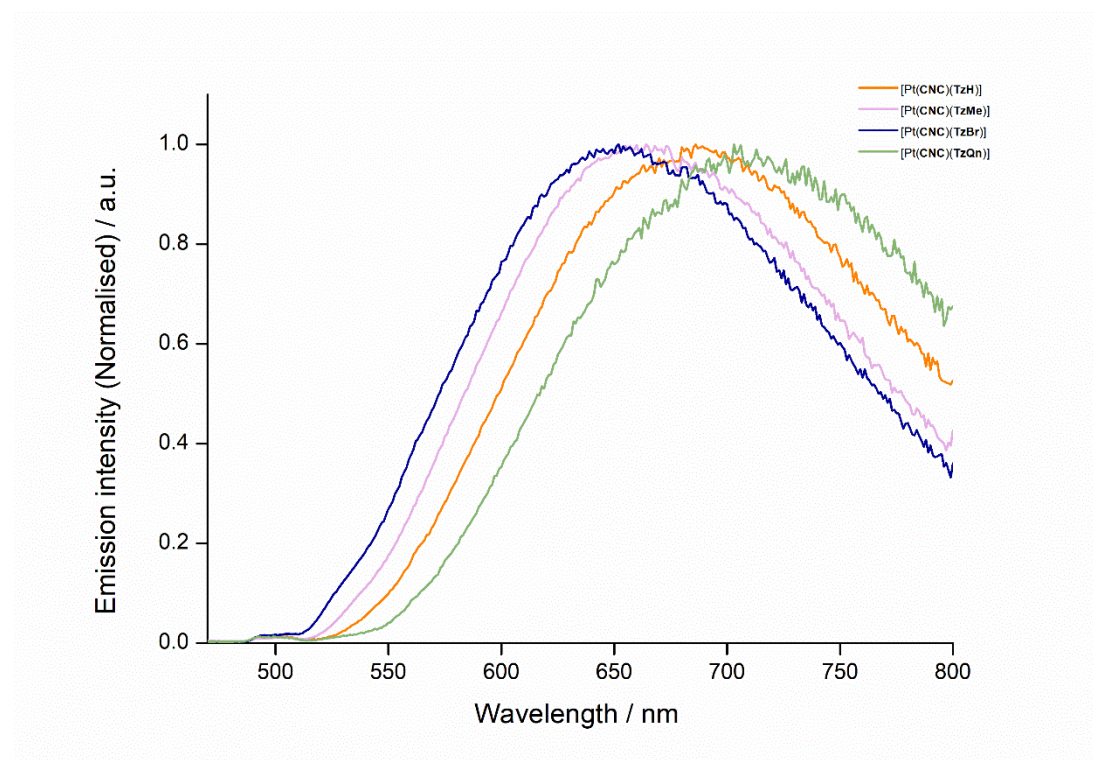


Figure 4.8 Emission profile for the complexes in the solid state.

Table 4.3 Emission data for the platinum complexes in the solid state and frozen matrix.

Complex	Medium (T/K)	λ_{em} [nm]	τ [μ s] ^a (%)	Φ % ^b
[Pt(CNC)(TzH)]	Solid film (298)	690	0.24	1.51
	Butyronitrile (77)	685	1.9 (49), 6 (51)	
[Pt(CNC)(TzMe)]	Solid film (298)	662	0.09	0.56
	Butyronitrile (77)	488	15.6	
		519	16.4	
		686	2.2 (63) 8.1 (37)	
[Pt(CNC)(TzBr)]	Solid film (298)	654	0.10	0.63
	Butyronitrile (77)	683	2.9	
[Pt(CNC)(TzQn)]	Solid film (298)	712	0.17	1.08
	Butyronitrile (77)	690	6.5 (51), 2 (49)	

^aFor the biexponential excited state lifetime (τ), the relative weights of the exponential curves are reported in parentheses. ^bMeasured with an integrating sphere.

Similarly to what was observed in Chapter 2, the low energy emission band remains dominant even at a concentration of 10^{-6} M, with a marked contribution of the high energy bands visible for [Pt(CNC)(TzMe)]. Emission spectra in a 10^{-7} - 10^{-4} M concentration range are depicted in **Figure 4.9** for [Pt(CNC)(TzMe)] as an example. For this complex, the excitation spectra and lifetimes have been monitored on the high energy bands, 488 nm and 519 nm respectively, and compared to the ones obtained at 686 nm (**Figure 4.10**). Given the shorter lifetimes and the difference in excitation spectra, the low energy bands exhibited by the synthesised platinum anionic species are ascribed to the formation of aggregates in the frozen matrix⁶⁷. The same emission spectra for the other complexes are reported in Appendix C, Figures C.6 – C.8.

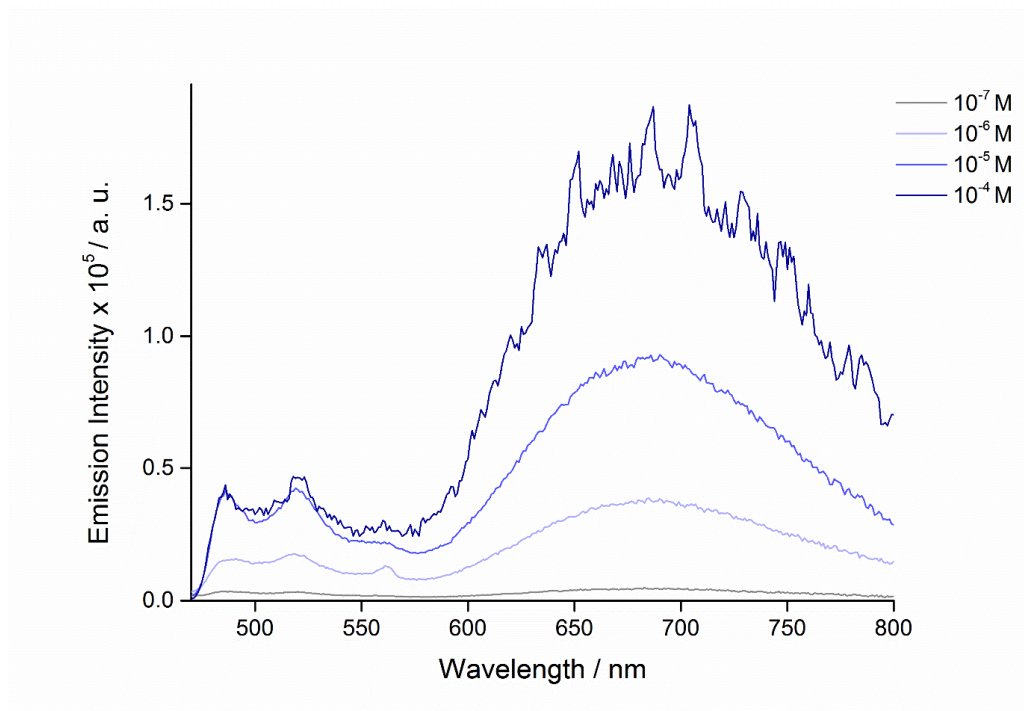


Figure 4.9 Emission spectra of [Pt(CNC)(TzMe)] at different concentrations in a butyronitrile glass (77 K).

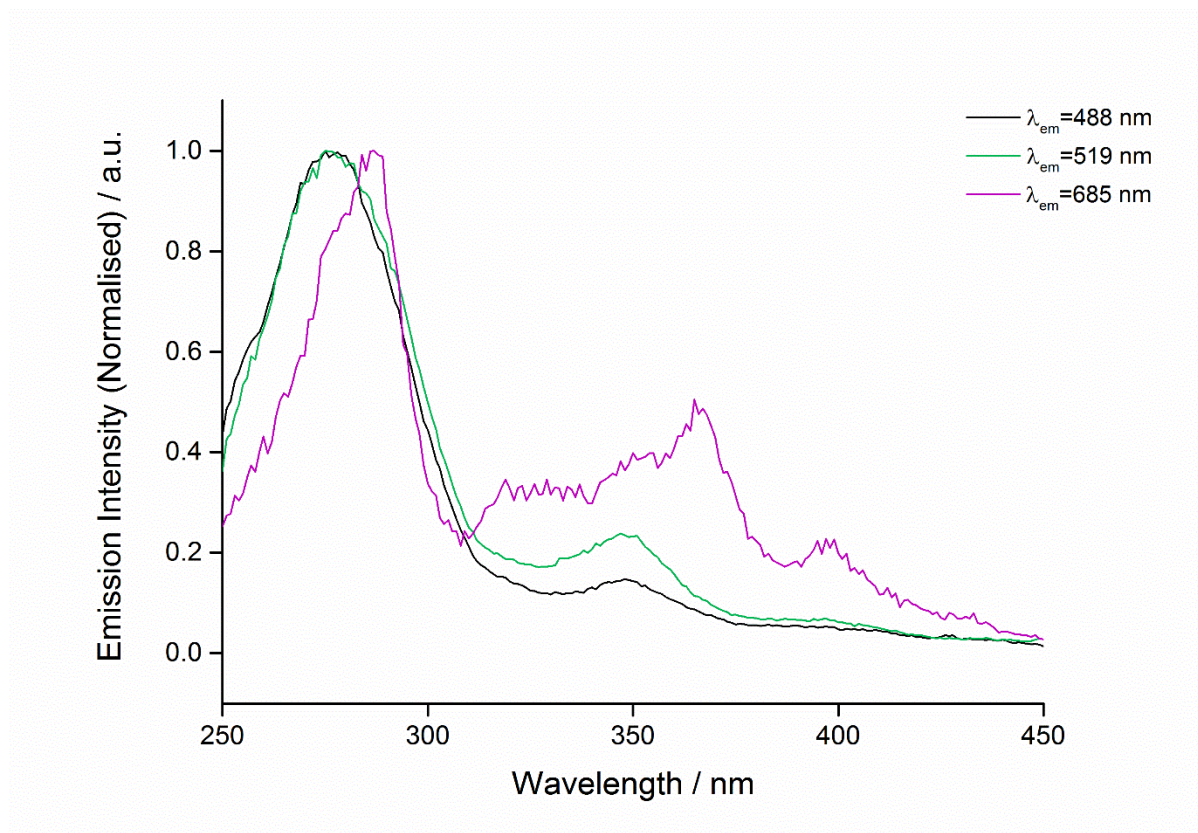


Figure 4.10 Excitation spectra of [Pt(CNC)(TzMe)] (at the emission maxima).

4.4 Electrochemical measurements

The electrochemical measurements presented in this section have been conducted in collaboration with Liam Burt, University of Tasmania. The redox potentials were measured directly by cyclic voltammetry for all of the synthesised platinum(II) complexes. A representative cyclic voltammogram is shown in **Figure 4.11** for [Pt(CNC)(TzMe)], while the voltammograms for the other complexes are reported in Appendix C, Figure C.9 - C.13. The anionic complexes maintained very similar reversible behaviour for their respective reduction potentials, with $E_{1/2} = ca. -1.95$ V vs. SCE (**Table 4.4**). Notable differences were observed for [Pt(CNC)(DMSO)], which displayed a lower reduction potential, with $E_{pc} = -1.64$ V vs. SCE, in agreement with the charge neutral nature of this complex. However, as all the Pt(II) complexes were not emissive in solution at r.t., it was not possible to estimate the excited state redox potentials for the respective Pt^{II*}/Pt^I couples associated with these species.

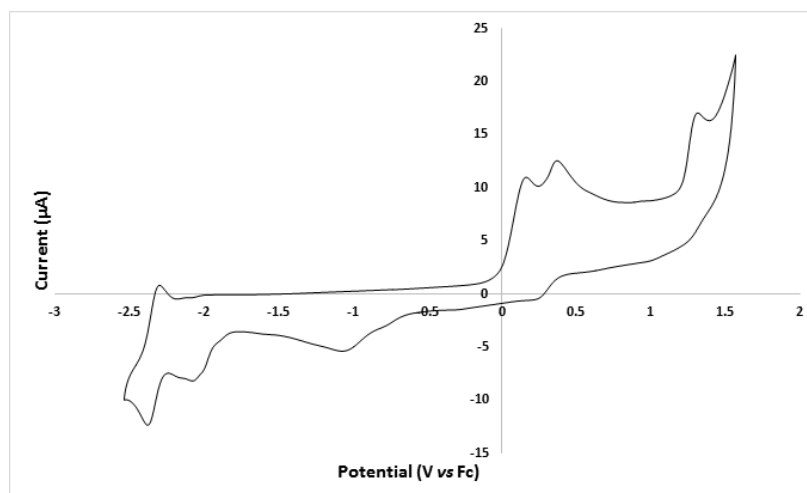


Figure 4.11 Cyclic voltammogram for [Pt(CNC)(TzMe)] in CH₃CN (500 μm); NBu₄PF₆ (0.1 M) supporting electrolyte.

Table 4.4. Electrochemical data for the platinum complexes in degassed CH₃CN at ambient temperature. All potentials are given in volts (V) versus the saturated calomel electrode (SCE).

Entry	Complex	E _{1/2} (M/M ⁻)
1	[Pt(CNC)(DMSO)]	-1.64
2	[Pt(CNC)(TzH)]	-1.95
3	[Pt(CNC)(TzMe)]	-1.96
4	[Pt(CNC)(TzBr)]	-1.95
5	[Pt(CNC)(TzQn)]	-1.94

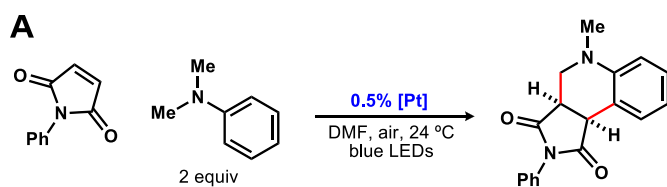
4.5 Photoredox catalysis

The photoredox catalysis experiment presented herein have been conducted in collaboration with Liam Burt, University of Tasmania.²⁴⁵ Visible light photoredox catalysis plays a central role in current organic chemistry, due to the potential activation of a wide range of transformations under mild reaction conditions.^{1,2} A variety of investigations have focused on the application of transition metal complexes as photoactivated catalysts, with a major focus on polypyridyl ruthenium(II) and cyclometalated iridium(III) systems.^{240,246} In contrast, a smaller number of studies exploring the application of homogeneous platinum(II)-based photoredox catalysts in organic synthesis have been reported to date. This is somewhat surprising, given that the photophysical properties of platinum(II) complexes have been extensively investigated in the past decades, including the effect of exchanging pyridine rings with cyclometalating phenyl rings in the conjugated terdentate ligand. In fact, the large variety of luminescent platinum(II) complexes reported to date have potential applications in a variety of technologies, including biosensing and bioimaging,^{54,59,66,88,113,146} as well as organic light-emitting devices (OLEDs).^{69,70,230} The investigation of platinum(II) complexes in photoredox catalysis has mostly been centered around the archetypal family of platinum(II) cations bound to diversely functionalised 2,2':6',2''-terpyridine (N[^]N[^]N) ligands. These complexes have been exploited to promote a wide range of reactions,^{247,248} including synthesis of 3,4-diarylthiophenes,²⁴⁹ oxidation of alkanes²⁵⁰ and photocatalytic generation of molecular hydrogen.^{233,234} Examples of platinum(II) cyclometalated complexes, where one pyridine ring in N[^]N[^]N is substituted for a phenyl ring, have been explored as photocatalysts for oxidation of sulfides²⁵¹ or trifluoromethylation reactions²⁵². Che *et al.* reported on the photoreductive catalytic activity of pincer and tetradentate platinum(II) complexes^{239,253}, as well as new terdentate complexes bearing a 6-phenyl-2,2'-bipyridine (C[^]N[^]N) ligand for difluoroalkylation reactions.²⁵⁴ The same group focused on platinum(II) complexes bound to the bis-cyclometalating terdentate ligand 2,6-diphenylpyridine (C[^]N[^]C). The photophysical properties of these complexes highlighted pronounced structural distortion in the excited state, with consequent enhancement of non-radiative decay pathways. While this characteristic is detrimental for the design and synthesis of highly luminescent platinum(II) complexes, these systems have never been assessed in the area of photoredox catalysis. Therefore, the

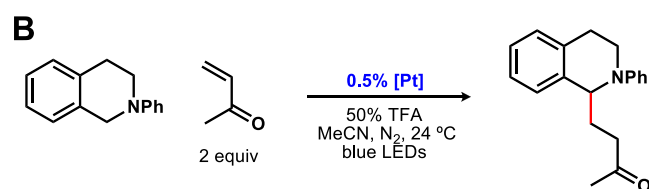
investigation described in this section originated from the lack of data relative to the photocatalytic properties of platinum(II) complexes bound to the doubly cyclometallated 2,6-diphenylpyridine ligand. This study focused on three fundamental classes of photocatalytic reactions, including: α -amino C–H functionalization, ATRA, and hydrodehalogenation reactions. Consequently, this section focuses on the capacity of the air-stable anionic platinum(II) species as well as the neutral precursor [Pt(CNC)(DMSO)] to facilitate photoredox-catalyzed Povarov-type reactions employing *N*-phenylmaleimide and *N,N*-dimethylaniline (**Table 4.5, A**).^{255,256} In each of the transformations studied, no reaction was observed in the absence of light or in the absence of the Pt complex. These experiments utilised 0.5% catalyst loadings and product yields were monitored over 5, 8, and 24 h. All the complexes efficiently facilitated this α -amino C–H functionalisation reaction, in yields ranging from 76–89%. The capacity of these catalysts to mediate photoredox-catalyzed radical additions of *N*-phenyl-1,2,3,4-tetrahydroisoquinoline to methyl vinyl ketone (**Table 4.5, B**) was also evaluated.²⁵⁷ This transformation could also be promoted by all of the complexes. In these experiments, the complex [Pt(CNC)(TzH)] afforded the best results (86% yield), while [Pt(CNC)(TzQn)] only provided a 38% yield of the Michael addition product. It is generally accepted that in both these α -amino C–H functionalization processes the photoredox catalyst serves to oxidize the amine-containing molecules.^{40–42} This leads to the formation of putative nucleophilic α -aminoalkyl radicals, which add to Michael acceptors en route to the final products. Thus, the results in Table 5 indicate that these novel platinum(II) complexes can mediate photoredox-catalysed reactions efficiently via their capacity to oxidise organic substrates.

Next, the ability of the complexes to promote photoredox-catalyzed hydrodeiodination of methyl 4-iodobenzoate ($E_{\text{red}} = -1.95$ V vs. SCE) (**Table 4.6, A** - entries 1–5) was investigated.^{258–260} In each case, a 0.5% catalyst loading did not allow for an efficient reduction to take place and these reactions proceeded at low conversion and thus afforded poor yields (21–26%). When this process was performed in the presence of 1% of [Pt(CNC)(TzH)], a 36% yield was obtained (entry 6).

Table 4.5. A: Photoredox-catalyzed Povarov-type reactions. **B:** Photoredox-catalyzed radical addition reactions.



entry	[Pt]	yield (%) ^a		
		5 h	8 h	24 h
1	Pt-dmso	30	48	81
2	Pt-TzH	40	55	89
3	Pt-TzMe	54	77	84
4	Pt-TzBr	37	53	76
5	Pt-TzQn	50	70	81

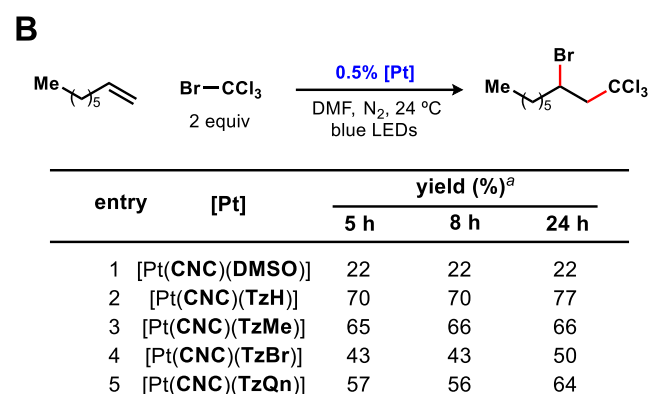
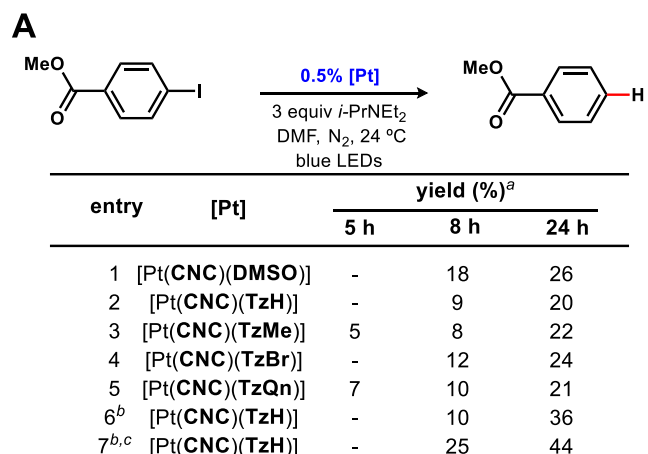


entry	[Pt]	yield (%) ^a		
		5 h	8 h	24 h
1	Pt-dmso	21	30	63
2	Pt-TzH	29	42	86
3	Pt-TzMe	28	43	68
4	Pt-TzBr	24	38	62
5	Pt-TzQn	15	22	38

^aYields determined via GC with the aid of a calibrated internal standard (average of 2 experiments).

The results of other photoredox-catalysed hydrodehalogenation reactions suggested that heating this reaction above ambient temperature could significantly improve the efficiency of this process.^{258–260} However, performing this reaction at 45 °C, afforded only a modest improvement (entry 7). These data suggest that higher Pt catalyst loadings are required to effect higher yielding hydrodeiodination processes. Finally, the capacity of the complexes to facilitate photoredox-catalyzed ATRA reactions employing bromotrichloromethane and 1-octene (**Table 4.6, B**) was explored.^{261–263} The anionic tetrazolato derivatives facilitated this process in generally moderate to good yields. Notably, [Pt(CNC)(TzH)] provided the best results (77% yield), while [Pt(CNC)(DMSO)] only provided a 22% yield of the addition product.

Table 4.6 A: Photoredox-catalyzed hydrodeiodination **B:** Photoredox-catalyzed ATRA reactions.



^aYields determined via GC with the aid of a calibrated internal standard (average of 2 experiments). ^b1% of [Pt(CNC)(TzH)], employed in this reaction. ^cReaction performed at 45 °C.

It is proposed that in hydrodehalogenation and ATRA processes the photoredox catalyst operates by reducing the aryl halide or transfer agent, respectively. In the former transformation, it is generally accepted that fragmentation of the ensuing anionic radical leads to a putative aryl radical that abstracts a proton from a trialkylamine to ultimately provide the hydrodehalogenated product.^{43–45} In ATRA reactions, the catalyst is sought to reduce the transfer agent (i.e., bromotrichloromethane) to generate radical species which then add to the olefin.^{46–48} Thus, the results in Table 6 indicate that these novel platinum(II) complexes can also facilitate photoredox-catalysed reactions through their capacity to reduce organic substrates.

4.6 Conclusions

In this Chapter, the development of a new class of anionic cyclometalated platinum(II) complexes has been presented. The complexes, with the general formula [TBA][Pt(CNC)(TzR)], can be conveniently prepared by substitution of the DMSO ligand with the corresponding tetrazolato ligand in [Pt(CNC)(DMSO)]. Attempt to obtain stable triethylammonium salt analogues were unsuccessful. The photophysical properties of the synthesised anionic complexes have been evaluated in solution as well as in the solid state and in a 77 K glass. As is typical for this class of cyclometalated platinum(II) complexes, no emission was detected at room temperature from diluted DMF solutions. On the other hand, the photophysical properties could be assessed in aqueous media, solid state and frozen matrix, where all the complexes display emission bands attributed to aggregates. In addition, we demonstrated that these air-stable platinum(II) complexes represent viable catalysts that can facilitate a range of fundamental classes of visible-light-mediated photoredox-catalyzed reactions. Specifically, we determined that this new family of complexes facilitated α -amino C–H functionalization processes, such as Povarov-type reactions and the addition of α -amino C–H bonds across Michael acceptors, in addition to an ATRA chemistry, and a hydrodeiodination. With the exception of hydrodeiodination process, the best Pt(II) catalysts provided turnover numbers of 150–175 in each of these transformations.

4.7 Experimental

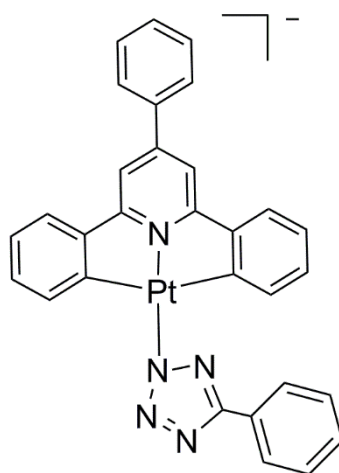
4.7.1 General synthetic procedures

General procedures have been conducted as outlined in Chapter 2, Section 2.8.1. unless otherwise stated.

1H-5-phenyltetrazole (**HTzH**), 1H-5-(4-methylphenyl)tetrazole (**HTzMe**), 1H-5-(4-bromophenyl)tetrazole (**HTzBr**) and 1H-5-(quinol-2-yl)tetrazole (**HTzQn**) were synthesized according to previously published procedures.^{139,264}

ESI-Mass spectrometry analysis was performed at The University of Bologna and at The University of Sydney.

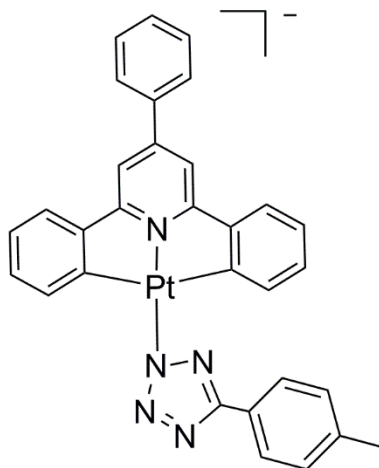
[Pt(**CNC**)(**TzH**)]



[Pt(**CNC**)(**DMSO**)] (0.050 g, 0.087 mmol) was dissolved in 12 mL of methanol. An aqueous solution of **HTzH** (0.140 g, 0.952 mmol) and TBAOH (2 mL of a 40 wt% water solution) was added. The reaction mixture was stirred at reflux for 20 hours to obtain an orange precipitate, which was filtered and washed with diethyl ether. Yield: 0.050 g, 0.056 mmol, 64%. PtC₄₆H₅₆N₆ Calc: C 62.21%, H 6.36%, N 9.46%. Found: C 61.86%, H 6.45%, N 9.46%. ESI-MS: Calculated for PtC₃₀H₂₀N₅ (M⁻): 645.61 m/z, C₁₆H₃₆N (M⁺): 242.47 m/z. Found: 645.67 m/z (M⁻), 242.31 m/z (M⁺). ¹H-NMR, 400 MHz, acetone-*d*₆, δ (ppm) = 8.26 (d, 2H, J_{H-H} = 8.0 Hz); 7.97-7.90 (m, 4H), 7.67-7.63 (m, 4H), 7.57-7.52 (m, 3H), 7.50-7.43 (m, 2H), 7.36-7.31 (m, 1H), 7.12 (t, 2H, J_{H-H} = 8.0 Hz), 6.96 (t, 2H, J_{H-H} = 8.0 Hz), 3.33-3.29 (m, 8H), 1.65-1.57 (m, 8H), 1.29-1.20

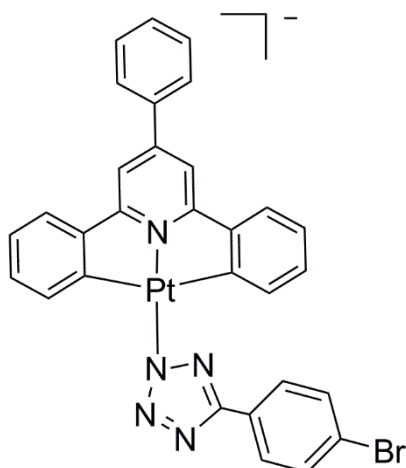
(m, 8H), 0.83 (t, 12H, $J_{\text{H-H}} = 4.0$ Hz). $^{13}\text{C-NMR}$, 100 MHz, acetone- d_6 , δ (ppm) = 175.5, 169.9, 163.9, 151.9, 150.0, 139.6, 138.00, 133.0, 130.3, 130.1, 129.9, 129.2, 128.4, 128.0, 127.0, 124.0, 122.9, 112.3, 59.2, 24.4, 20.3, 13.9.

[Pt(CNC)(TzMe)]



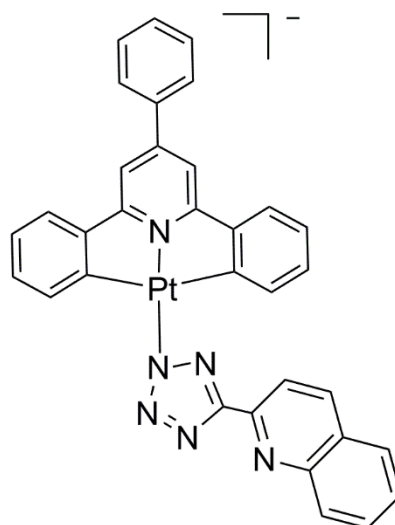
[Pt(CNC)(DMSO)] (0.050 g, 0.087 mmol) was dissolved in 15 ml of methanol. An aqueous solution of HTzMe (0.153 g, 0.97 mmol) and TBAOH (2 mL of a 40 wt% water solution) were added. The reaction mixture was stirred at reflux for 20 hours to obtain a yellow-orange precipitate, which was filtered and washed with methanol and diethyl ether. Yield: 0.065 g, 0.072 mmol, 83%. $\text{PtC}_{47}\text{H}_{58}\text{N}_6$ Calc: C 62.57%, H 6.49%, N 9.32%. Found: C 62.21%, H 6.15%, N 9.05%. ESI-MS: Calculated for $\text{PtC}_{31}\text{H}_{22}\text{N}_5$ (M^+): 659.63 m/z, $\text{C}_{16}\text{H}_{36}\text{N}$ (M^+): 242.47 m/z. Found: 660.06 m/z (M^+), 242.32 m/z (M^+). $^1\text{H-NMR}$, 400 MHz, acetone- d_6 , δ (ppm) = 8.14 (d, 2H, $J_{\text{H-H}} = 8.0$ Hz); 7.97-7.92 (m, 4H); 7.67-7.64 (m, 4H); 7.59-7.50 (m, broad, 3H); 7.27 (d, 2H, $J_{\text{H-H}} = 8.0$ Hz); 7.12 (t, 2H, $J_{\text{H-H}} = 8.0$ Hz), 6.96 (t, 2H, $J_{\text{H-H}} = 8.0$ Hz), 3.33-3.29 (m, 8H); 2.38 (s, 3H); 1.62-1.58 (m, 8H); 1.27-1.21 (m, 8H), 0.83 (t, 12H, $J_{\text{H-H}} = 8.0$ Hz). $^{13}\text{C-NMR}$, 100 MHz, acetone- d_6 , δ (ppm) = 175.6, 169.9, 163.9, 151.8, 149.9, 139.6, 138.0, 137.9, 130.3, 130.1, 129.9, 128.0, 127.0, 124.01, 122.9, 112.3, 59.2, 24.4, 21.4, 20.3, 13.87. Two quaternary C peaks were not visible in the spectrum.

[Pt(CNC)(TzBr)]



[Pt(CNC)(DMSO)] (0.050 g, 0.087 mmol) was dissolved in 15 ml of methanol. An aqueous solution of HTzBr (0.214 g, 0.952 mmol) and TBAOH (2 mL of a 40 wt% water solution) were added. The reaction mixture was stirred at reflux for 20 hours to obtain a yellow precipitate, which was filtered and washed with diethyl ether. Yield: 0.048 g, 0.049 mmol, 57%. [PtC₄₆H₅₅N₆Br](CH₃OH)·Calc: C 56.51%, H 5.95%, N 8.41%. Found: C 56.44%, H 5.76%, N 8.03%. ESI-MS: Calculated for PtC₃₀H₁₉N₅Br (M⁻): 724.50 m/z, C₁₆H₃₆N (M⁺): 242.47 m/z. Found: 724.60 m/z (M⁻), 242.31 m/z (M⁺). ¹H-NMR, 400 MHz, acetone-*d*₆, δ (ppm) = 8.19 (d, 2H, J_{H-H} = 8.0 Hz); 7.96 (d, 2H, J_{H-H} = 8.0 Hz); 7.85 (d, 2H, J_{H-H} = 8.0 Hz); 7.68-7.64 (m, 6H); 7.57-7.51 (m, 3H); 7.12 (t, 2H, J_{H-H} = 8.0 Hz), 6.97 (t, 2H, J_{H-H} = 8.0 Hz), 3.31-3.27(m, 8H); 1.60-1.54 (m, 8H); 1.25-1.19 (m, 8H), 0.83 (t, 12H, J_{H-H} = 4.0 Hz). ¹³C-NMR, 100 MHz, acetone-*d*₆, δ (ppm) = 174.6, 169.5, 163.3, 152.3, 150.0, 139.4, 137.2, 132.6, 131.4, 130.7, 130.4, 129.9, 128.8, 128.2, 124.3, 123.4, 122.3, 113.0, 59.2, 24.2, 20.2, 13.7.

[Pt(CNC)(TzQn)]



[Pt(CNC)(DMSO)] (0.050 g, 0.087 mmol) was dissolved in 15 ml of methanol. An aqueous solution of HTzQn (0.153 g, 0.952 mmol) and TBAOH (2 mL of a 40 wt% water solution) were added. The reaction mixture was stirred at reflux for 20 hours to obtain a dark orange precipitate, which was filtered and washed with diethyl ether. Yield: 0.063 g, 0.067 mmol, 77%. [PtC₄₉H₅₇N₇](CH₃OH) Calc: C 61.84%, H 6.33%, N 10.10%. Found: C 61.78%, H 6.40%, N 10.36%. ESI-MS: Calculated for PtC₃₃H₂₁N₆ (M⁻): 696.65 m/z, C₁₆H₃₆N (M⁺): 242.47 m/z. Found: 645.57 m/z (M⁻), 242.30 m/z (M⁺). ¹H-NMR, 400 MHz, acetone-*d*₆, δ (ppm) = 8.48 (d, 1H, J_{H-H} = 8.0 Hz); 8.39 (d, 1H, J_{H-H} = 8.0 Hz); 8.12 (d, 1H, J_{H-H} = 8.0 Hz); 7.96 (d, 3H, J_{H-H} = 8 Hz); 7.80 (d, 2H, J_{H-H} = 8 Hz); 7.77-7.73 (m, 1H), 7.69-7.65 (m, 4H), 7.59-7.51 (m, 4H), 7.12 (t, 2H, J_{H-H} = 8.0 Hz), 6.97 (t, 2H, J_{H-H} = 8.0 Hz) 3.37-3.33 (m, 8H); 1.64-1.60 (m, 8H); 1.26-1.21 (m, 8H), 0.83 (t, 12H, J_{H-H} = 4.0 Hz). ¹³C-NMR, 100 MHz, acetone-*d*₆, δ (ppm) = 175.5, 169.9, 164.8, 152.0, 151.9, 150.0, 149.3, 139.5, 137.9, 137.0, 130.4, 130.4, 130.2, 129.9, 128.7, 128.1, 126.9, 124.1, 123.0, 121.5, 112.4, 59.2, 24.4, 20.3, 13.9. Two quaternary C peaks were not visible in the spectrum.

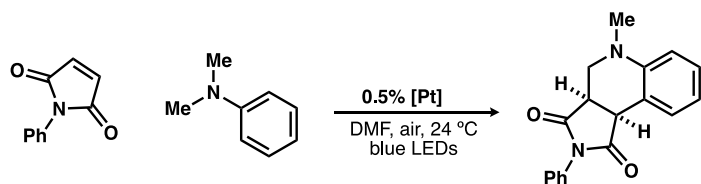
4.7.2 Photophysical measurements

Photophysical measurements have been conducted as outlined in Chapter 2, section 2.8.3.

4.7.3 Photoredox-catalyzed reactions

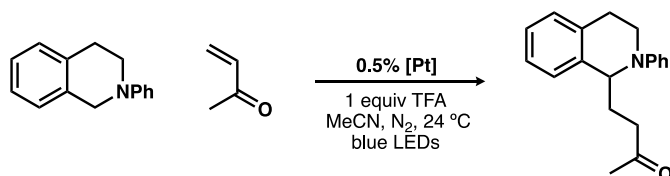
GC data were obtained on a Shimadzu GC-2014 System using an Agilent HP-5 ms capillary column. Unless otherwise specified all reagents employed in these studies were used as received from Sigma-Aldrich, AK Scientific, Combi-Blocks, and Oakwood and were used without purification. *i*-Pr₂NEt and *N,N*-dimethylaniline were distilled prior to use. Custom blue LED (467 nm) photoreactor #1 was constructed using blue LEDs strips purchased from aliexpress.com (Appendix C, Figures C.14 – C.15). The 11-W blue LED photoreactor provides ~14,000 lux (measured at the center of the photoreactor). The glass photoreactor features a condenser jacket that allows water cooling to maintain a constant temperature (24 °C) inside the reactor during irradiation. When the blue LED photoreactor was in use, it was completely covered in foil to block ambient light.

General Procedure A



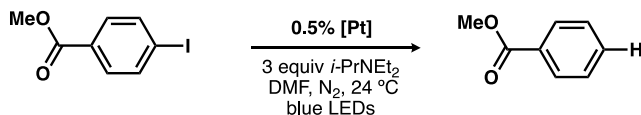
In air (in the dark), *N*-phenylmaleimide (100 μmol; 500 μL of a 200 mM solution in DMF {this solution also contained tridecane (100 μmol, 200 mM); internal standard}, *N,N*-dimethylaniline (200 μmol; 500 μL of a 400 mM solution in DMF), and the Pt catalyst (0.5 μmol, 500 μL, 1 mM solution in DMF) were successively added to a 4-mL glass vial containing a magnetic stir bar. This vial was then capped and placed in blue LED photoreactor #1 and magnetically stirred. The vial was irradiated and maintained at 24 °C. Aliquots (100 μL) were obtained from the reaction mixture at the specified times (5, 8, 24 h) and analyzed by GC.

General Procedure B



In a nitrogen-filled glovebox (in the dark), *N*-phenyl-1,2,3,4-tetrahydroisoquinoline (100 μmol ; 500 μL of a 200 mM solution in MeCN {this solution also contained 1,4-dimethoxybenzene or naphthalene (100 μmol , 200 mM); internal standard}, methyl vinyl ketone (200 μmol ; 500 μL of a 200 mM solution in MeCN), TFA (200 μmol ; 250 μL of a 800 mM solution in MeCN), and the Pt catalyst (0.5 μmol , 250 μL , 2 mM solution in MeCN) were successively added to a 4-mL glass vial containing a magnetic stir bar. The vial was then capped with a septum-containing cap, removed from the glovebox, and placed in blue LED photoreactor #1 and magnetically stirred. The vial was irradiated and maintained at 24 $^\circ\text{C}$. Aliquots (100 μL) were obtained from the reaction mixture at the specified times (5, 8, 24 h) and analyzed by GC.

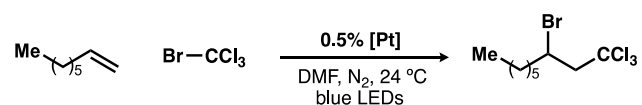
General Procedure C



In a nitrogen-filled glovebox (in the dark), methyl 4-iodobenzoate (100 μmol ; 1.0 mL of a 100 mM solution in DMF {this solution also contained 1,4-dimethoxybenzene or naphthalene (20 μmol , 20 mM); internal standard}, *i*-Pr₂NEt (300 μmol ; 250 μL of a 1.2 M solution in DMF) and the Pt catalyst (0.5 μmol , 250 μL , 2 mM solution in DMF) were successively added to a 4-mL glass vial containing a magnetic stir bar. The vial

was then capped with a septum-containing cap, removed from the glovebox, and placed in blue LED photoreactor #1 and magnetically stirred. The vial was irradiated and maintained at 24 °C. Aliquots (100 μ L) were obtained from the reaction mixture at the specified times (5, 8, 24 h) and analyzed by GC.

General Procedure D



In a nitrogen-filled glovebox (in the dark), 1-octene (1.5 mmol; 240 μ L), tridecane {(0.3 mmol, 73 μ L); internal standard}, bromotrichloromethane (3.0 mmol; 300 μ L) were combined with DMF (2.4 mL) to make a stock solution. This stock solution was dispensed as 0.3 mL into Pt catalyst (2.25 μ mol) and homogenised. 0.1 mL of this solution was then added to a 4-mL glass vial containing a magnetic stir bar. This vial was then capped, removed from the glovebox, and placed in blue LED photoreactor #2 and magnetically stirred. The vial was irradiated and maintained at 24 °C. Aliquots (100 μ L) were obtained from the reaction mixture at the specified times (5, 8, 24 h) and analyzed by GC.

Chapter 5

Interrogating the sub-cellular architecture of bacteria using a family of phosphorescent iridium complexes

5.1 Introduction

Optical imaging is well suited to interrogate the chemical biology of living systems and has found extensive use to characterise cellular environments, with nanometer precision and high temporal resolution. The majority of the imaging techniques exploit the use of molecular probes, the design of which is an ongoing challenge, dictated by increasingly ambitious analyses requiring precise target specificity. At the same time, direct label-free analytical methods that will complement the use of molecular probes, is an emerging field (i.e. multimodal microscopy).^{265,266} Amongst other techniques, Raman spectroscopy is particularly attractive; because it provides sub-micron spatial resolution and does not suffer spectral interferences from H₂O. In this context, metal-based probes are attracting increasing attention as innovative imaging agents, due to their advantageous photophysical properties and their potential to be used as correlative probes with other imaging techniques such as electron microscopy.^{72,73} A wide range of new imaging tools has been developed from phosphorescent metal complexes which selectively target sub-cellular organelles (e.g., mitochondria, nucleic acids, ribosomes, lipid droplets) in multicellular systems.^{54,71,269,270,74,75,77,83,86,114,267,268} In contrast, sub-cellular imaging tools for bacteria are less well developed. A deeper understanding of prokaryotic cell biology is required to advance in many clinical and industrial settings. Unfortunately however, despite the continuous advances in genome sequencing, many molecular mechanisms in prokaryotes are yet unknown, and improved bacterial imaging techniques have the potential to delineate key dynamics and biological functions. Compared to cellular and tissue imaging, bacterial imaging has several additional challenges, the most significant of which is represented by the robust bacterial cell envelope. An increasing research effort is focusing on developing

new molecules to stain bacteria, and a wide range of fluorophores^{35,38,41–44,271–273} and bio-functionalised nanoparticles^{14,48} has been reported. However, most of these systems can only interact with the bacterial cell wall and are not internalised within the bacterial cells. This approach, therefore, limits the staining to the cell surface and hinders the visualisation of any sub-cellular environment or event. Moreover, production of these dyes can be synthetically demanding due to their complex molecular architecture. This factor might limit mass production for widespread use and tunability to obtain a platform of bacterial markers with complementary properties. Hence, to date, most of the current protocols to image bacterial substructures rely on the use of a relatively limited number of commercial organic dyes^{185,274–276} or on the genetic manipulation of target proteins.^{12,24,183,184,277–280} The use of genetically encoded tags, however, can lead to artefacts or mislocalisation of the encoded tag. Moreover, this approach is not applicable to label non-proteinaceous biomolecules such as glycans, nucleic acids and lipids.^{26,281} To date, there is a recognised lack of new small molecules that are able to interact with bacteria, readily penetrating the bacterial cell wall to enable the visualisation of bacterial substructures.²⁶ In this context, it is interesting to note that transition metal complexes have not yet been explored as bacterial imaging agents. This is quite surprising, if one considers that complexes of Ru(II), Re(I), Ir(III) with luminescent properties have been investigated in detail as potential antibacterial agents.^{90,99,108,110,100–107} Given the lack of reports on luminescent metal complexes for bacterial imaging, the aim of this chapter is to investigate the potential of a suite of phosphorescent metal complexes to act as molecular probes for bacteria. Specifically, the presented methods centre on a family of phosphorescent Ir(III) tetrazolato complexes that have been reported by our group.^{84,158} Previous reports have shown that a series of cationic iridium(III) complexes exhibited antimicrobial activity towards *Deinococcus radiodurans* (*D. radiodurans*), whereas the neutral analogues did not show any cytotoxic effect towards the same species.¹⁵⁸ Based on these results, the non-toxic, neutral iridium complexes have been tested as molecular probes for the live imaging of the bacterial species *Bacillus cereus*. In addition, Raman microscopy has been used on live bacteria to complement the use of luminescent metal complex probes. In order to begin development of structure-activity relationships, the cationic analogues of the iridium(III) complexes have also been considered in this study, to assess if a different trend in toxicity corresponded to a different sub-cellular localisation.

5.2 Interaction of live *Bacillus cereus* with neutral iridium(III) tetrazolato complexes

5.2.1 Photophysical properties and toxicity

The iridium complexes investigated as imaging agents in this section (**Figure 5.1**) were selected as they have strong potential to be developed into easily accessible probes for bacterial imaging. The probes, with the general formula $[\text{Ir}(\text{C}^{\wedge}\text{N})(\text{TzR})]$, can be readily synthesised starting from the appropriate chloro-bridged dimer $[\text{Ir}(\text{C}^{\wedge}\text{N})_2\text{Cl}]_2$ where $\text{C}^{\wedge}\text{N}$ is 2-phenylpyridine (**ppy**) or 2-(2,4-difluorophenyl)pyridine (**F₂ppy**), that is reacted with an excess of the corresponding tetrazolato ligand (**TzR**) at room temperature.^{84,158} Importantly, minor modifications in the chemical structure allow the tuning of the emission colour, while using the same excitation wavelength. Indeed, upon excitation at 405 nm, the emission maxima range from 520 nm to 600 nm in aqueous media (**Table 5.1**).

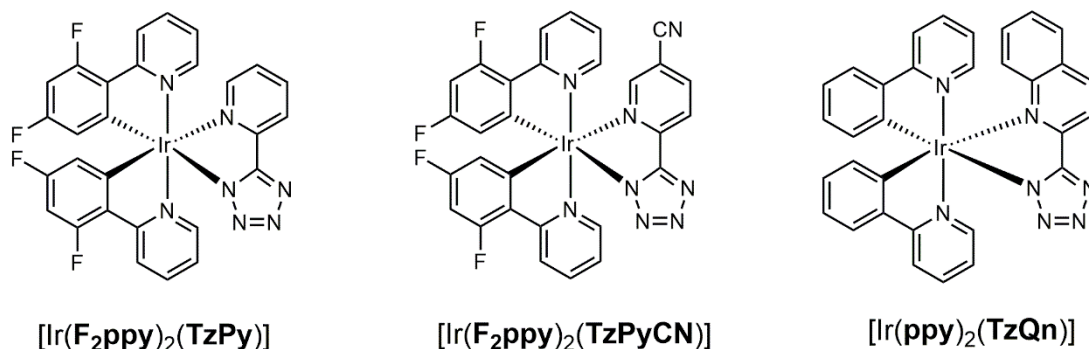


Figure 5.1 Chemical structure of the neutral iridium(III) tetrazolato complexes

As the intention of this work was to develop probes for live-imaging of bacteria, an important initial step was to determine their impact on the bacterial growth. The toxicity of the complexes towards *B. cereus* was determined by monitoring the kinetics of growth in the presence of the complexes at the concentration used for the imaging experiments (20 μM in Nutrient Broth, 0.1% DMSO). Notably, the complexes do not significantly affect maximum cell yield (**Figure 5.2**).

Table 5.1 Photophysical properties of the neutral iridium(III) complexes from 10^{-5} M aqueous solutions (0.1% DMSO)

Complex	λ_{em} [nm]	τ_{aer} [ns] ^a	Φ_{aer}
[Ir(F ₂ ppy) ₂ (TzPy)]	520	38 (12), 332 (88)	0.062
[Ir(F ₂ ppy) ₂ (TzPyCN)]	552	189 (41), 628 (59)	0.057
[Ir(ppy) ₂ (TzQn)]	600	305 (25), 928 (75)	0.039

[a] For the biexponential excited state lifetime (τ), the relative weights of the exponential curves are reported in parentheses. [b] Measured versus [Ru(bpy)₃]²⁺ in H₂O ($\Phi_r = 0.028$).

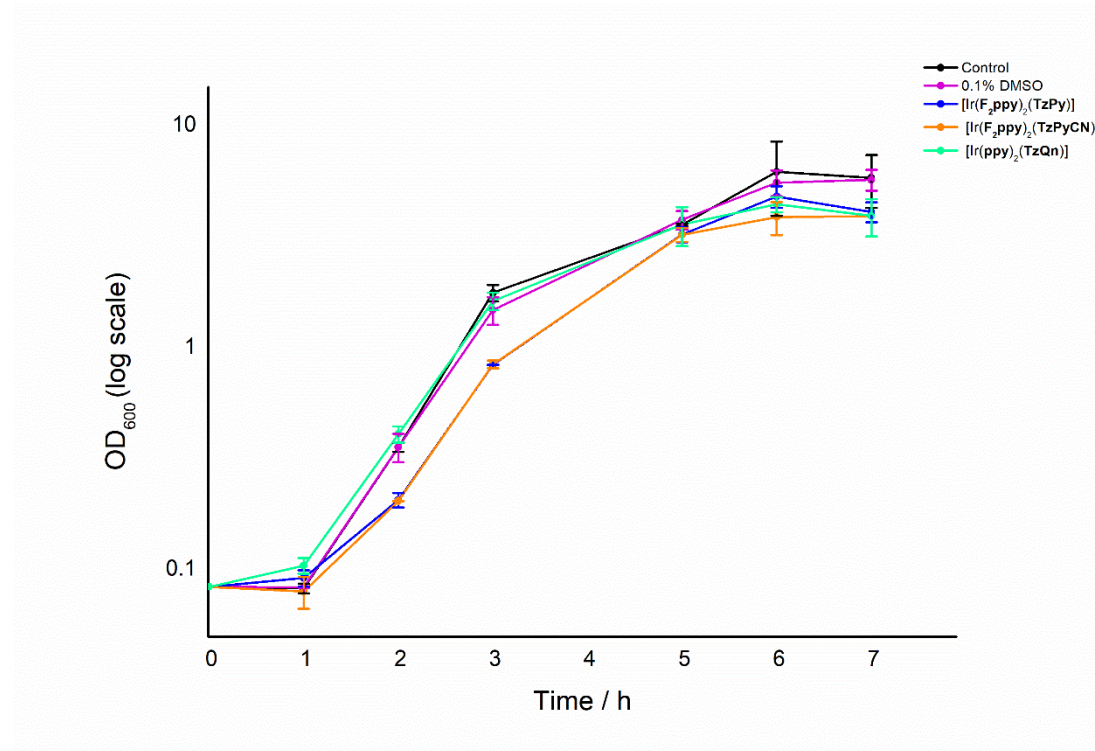


Figure 5.2 Growth curves of *B. cereus* in the presence of the neutral iridium(III) complexes. Unstained and DMSO treated bacterial cultures were also monitored.

5.2.2 Confocal imaging

With the fundamental requirements of synthetic accessibility and non-toxicity confirmed, the potential of $[\text{Ir}(\text{F}_2\text{ppy})_2(\text{TzPy})]$, $[\text{Ir}(\text{F}_2\text{ppy})_2(\text{TzPyCN})]$ and $[\text{Ir}(\text{F}_2\text{ppy})_2(\text{TzQn})]$ as molecular probes for bacteria was assessed by confocal microscopy (**Figure 5.3**). The complexes were incubated with live *B. cereus* directly in the growth medium (Nutrient Broth, 0.1% DMSO). The emission of the complexes was detected after only one minute of dosing at room temperature (See link to Supporting Video 1, Appendix D). This extremely fast cellular uptake is remarkable, if one considers that previously reported protocols involve from 30 minutes up to two hours incubation time.^{103,104,186} Acquisition of *z-stacks* images confirmed that the complexes were effectively internalised within the live bacteria and were not interacting with the outer side of the membrane (See link to Supporting Video 2, Appendix D).

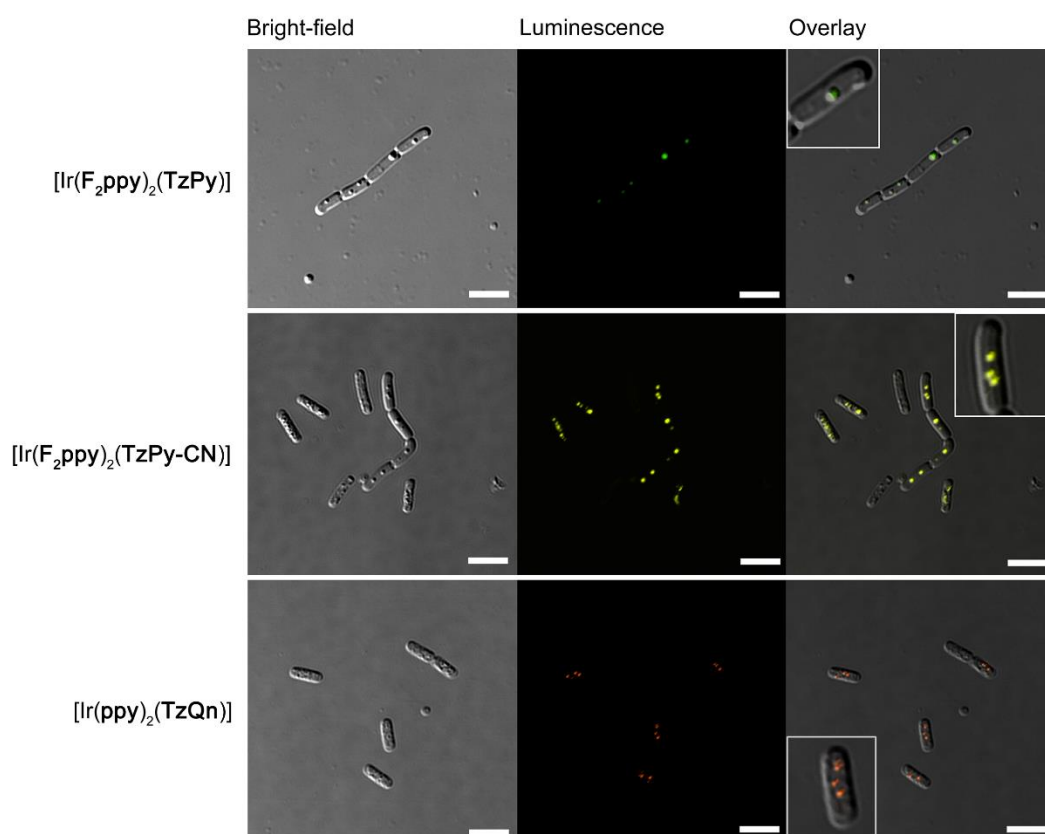


Figure 5.3 Confocal fluorescence microscopy demonstrates the uptake and compartmentalisation of the neutral iridium complexes in *B. cereus* (dose: 20 μM , 0.1% DMSO). Scalebars 5 μm .

Importantly, time-lapse experiments showed that no evident photobleaching from the complexes was observed after imaging over one hour period, acquiring a z-stack every minute (See link to Supporting Video 3, Appendix D). The resolution of the images showed that all of the complexes were highly localised to the same well defined, droplet-like micro domains within *B. cereus*. The spherical shape of the inclusions within the bacterial cytoplasm resemble lipid vacuoles. In order to prove our conclusion of lipid staining, a further staining experiment was trialled with BODIPY (**Figure 5.3**), showing a very similar localisation pattern and therefore suggesting that the iridium complexes show specificity for lipid bodies in the bacteria. Importantly, the three complexes exhibit the same sub-cellular localisation. The ability to have probes with a wide range of emission profiles but consistent sub-cellular localisation is beneficial when considering experiments with multiple probes, so that the specific emission of each marker can be easily discriminated, as they can be excited and/or detected independently. To the best of our knowledge, this protocol is the first ever to image lipid distributions within prokaryotes using phosphorescent metal complexes. Indeed, imaging of lipid inclusions in bacteria has to date only been achieved with traditional organic dyes.^{15,186} Significantly, an increasing research effort has focused on the study of the lipid metabolism in bacterial cells.^{15,16,18,19} In fact, the role of neutral lipids both in the pathogenesis or in the antibiotic biosynthesis of different microorganisms has been investigated.²¹⁷⁻²¹⁹ Moreover, further studies on bacterial lipid accumulation have been prompted by the potential use of prokaryotes as a source of single cell oil or biopolymers (e. g. Exopolysaccharides, EPS or Polyhydroxyalkanoates, PHAs) for a wide range of derived industrial products.^{17,20,22,220} To date, however, many dynamics involving lipid production, trafficking and storage in bacteria are poorly understood, and the capability of imaging lipid distribution in live bacteria is of key importance.

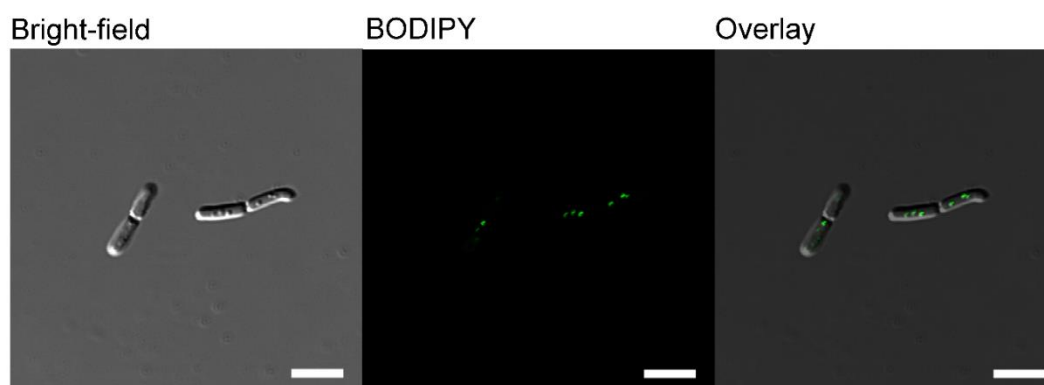


Figure 5.4 *B. cereus* dosed with 3 μ M BODIPY 493/503. BODIPY 493/503 was excited at 488 nm and the emission was collected in the region 525/50 nm. Scalebar 5 μ M.

5.3 Confocal Raman imaging of lipid inclusions in live *Bacillus cereus*

Direct lipid imaging in living cells is also possible with vibrational spectroscopies such as Raman spectroscopy. The sub-micron spot sizes achieved with confocal Raman microscopy are well suited to studying sub-cellular lipid distributions, hence this technique has previously been applied *in situ* within *ex vivo* tissue sections,²⁶⁶ and living cell culture,²⁸² but is yet to be applied to image sub-cellular lipid distributions in bacterial cells. Classical bulk analyses of *Bacillus* species has been used to study lipophilic inclusions or granules that are enriched in lipids and other lipophilic compounds, such as polyhydroxybutyrate (PHB).²⁸³ Raman spectroscopic mapping was used in this study to provide direct biochemical imaging of lipid-enriched inclusions within live *B. cereus* (**Figure 5.5**).

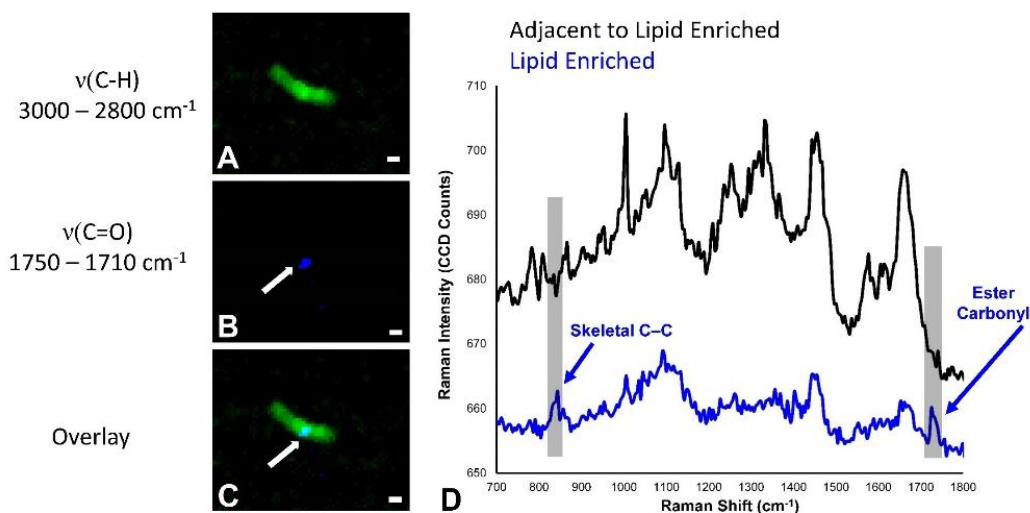


Figure 5.5 Direct detection of lipid inclusions in living bacteria using confocal Raman microscopy. (A-C) Confocal Raman microscopy images showing outline of bacterial cell (A, intensity of $\nu(\text{C-H})$), lipid esters (B), intensity of ester $\nu(\text{C=O})$, and overlay (C). Representative Raman spectra of bacterial cell body and lipid enriched inclusion (D, spectra offset for clarity). Spectra within the lipid-enriched region show characteristic ester $\nu(\text{C=O})$ and skeletal $\nu(\text{C-C})$, consistent with presence of lipids or lipophilic substances such as PHBs. Scale bar in A-C = 1 μm .

The ester carbonyl band which is an established spectroscopic marker for lipophilic environments in bacteria,^{284,285} was detected with confocal Raman mapping at 1725 cm^{-1} , (shoulder at 1735 cm^{-1}), revealing distinct lipid enriched regions within live *B.cereus*. The lipid enriched domains display similar morphology to those observed in the imaging experiments with the iridium complexes and BODIPY. Further examination of the Raman spectra suggest that the lipid enriched regions may contain PHBs, based on the pronounced characteristic peak observed at 843 cm^{-1} .²⁸⁵ To the best of our knowledge, this is the first time that confocal Raman microscopy has been used to image lipids at sub-cellular spatial resolution in living bacteria. Many previous studies using Raman spectroscopy to analyse biological samples report strong spectral interference from autofluorescence of endogenous fluorophores.²⁸⁶ To overcome endogenous autofluorescence longer excitation wavelengths are typically used, but this worsens spatial resolution and decreases Raman scattering power. Alternatively, sophisticated coherent anti-stokes Raman scattering has been developed to overcome endogenous autofluorescence in biological samples,²⁸⁷ but such methods do not reveal the complete Raman spectrum, and the instrumentation is highly specialised. The collection of Raman spectra with a 532 nm excitation wavelength in this study, is possible with routinely available benchtop Raman equipment, thus allowing accessible opportunities to image lipids at sub-cellular spatial resolution in a relatively quick time frame (~1 hour per bacteria). Although Raman microscopy has a number of limitations compared to fluorescence microscopy, (e.g. longer data acquisition times, poorer detection limits), the direct imaging capability makes the technique ideal to validate and gain further insight about the chemical specificity of luminescent complexes. Moreover, it allows a facile, label-free complementary route to monitor the morphology of live bacteria over time, to assess any effect of the dyes on the lipid metabolism.

5.4 Interaction of live *Bacillus cereus* with cationic iridium(III) tetrazolato complexes

5.4.1 Photophysical properties and toxicity

As previously reported by our group, the neutral iridium(III) complexes described in Section 4.2 can be easily methylated^{84,158}, to afford the cationic analogues depicted in **Figure 5.6**. The positively charged iridium(III) complexes experience a red-shift of the emission, with emission maxima range from 540 nm to 640 nm in aqueous media upon excitation at 405 nm (**Table 5.2**).

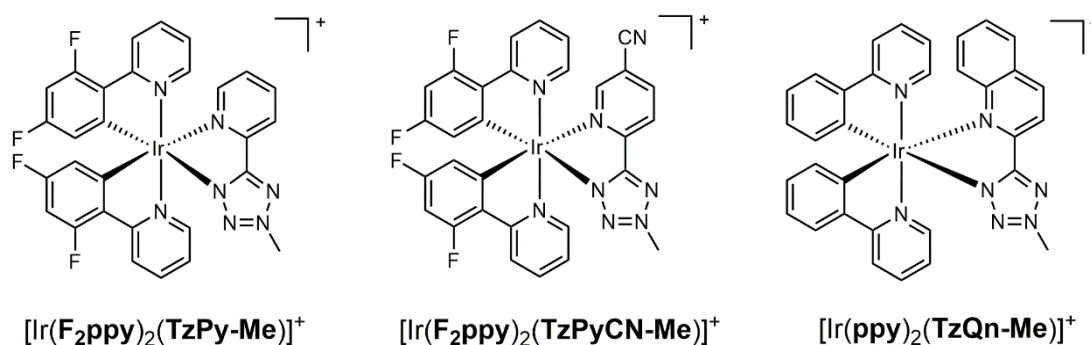


Figure 5.6 Chemical structure of the cationic iridium(III) tetrazolato complexes

Table 5.2 Photophysical properties of the neutral iridium(III) complexes from 10⁻⁵ M aqueous solutions (0.1% DMSO)

Complex	λ_{em} [nm]	τ_{aer} [ns] ^a	$\Phi_{\text{aer}}^{\text{b}}$
$[\text{Ir}(\text{F}_2\text{ppy})_2(\text{TzPy-Me})]^+$	540	15 (29), 98 (71)	0.003
$[\text{Ir}(\text{F}_2\text{ppy})_2(\text{TzPyCN-Me})]^+$	640	11 (76), 56 (24)	0.005
$[\text{Ir}(\text{ppy})_2(\text{TzQn-Me})]^+$	630	17 (39), 134 (61)	0.004

[a] For the biexponential excited state lifetime (τ), the relative weights of the exponential curves are reported in parentheses. [b] Measured versus $[\text{Ru}(\text{bpy})_3]^{2+}$ in H₂O ($\Phi_{\text{r}} = 0.028$).

Fiorini *et al* investigated how the conversion of the neutral iridium(III) tetrazolato complexes into cationic iridium(III) tetrazolates translated into a turn-on in the antimicrobial activity against the gram-positive bacterial species *D. radiodurans*. This antimicrobial activity was ascribed to the ability of the charged complexes to disrupt the cell envelope of *D. radiodurans*, although other concomitant mechanisms accounting for this inhibitory behaviour were not excluded. The aim of this section is to gain further insight into the biological behaviour of the charged complexes $[\text{Ir}(\text{F}_2\text{ppy})_2(\text{TzPy-Me})]^+$, $[\text{Ir}(\text{F}_2\text{ppy})_2(\text{TzPyCN-Me})]^+$, $[\text{Ir}(\text{F}_2\text{ppy})_2(\text{TzQn-Me})]^+$ assessing *via* preliminary confocal microscopy experiments whether the different trend in toxicity compared to the corresponding neutral analogues is linked to a different interaction with the bacterial cells. First, the toxicity of the cationic species has been confirmed against *B. cereus*, the model used in this study. The kinetics of bacterial growth in the presence of $[\text{Ir}(\text{F}_2\text{ppy})_2(\text{TzPy-Me})]^+$, $[\text{Ir}(\text{F}_2\text{ppy})_2(\text{TzPyCN-Me})]^+$, $[\text{Ir}(\text{F}_2\text{ppy})_2(\text{TzQn-Me})]^+$ are depicted in **Figure 5.7**. In contrast to the trend observed for the neutral complexes in Section 5.2, and as expected, the growth of *B. cereus* is inhibited by the presence of the complexes in the growth medium.

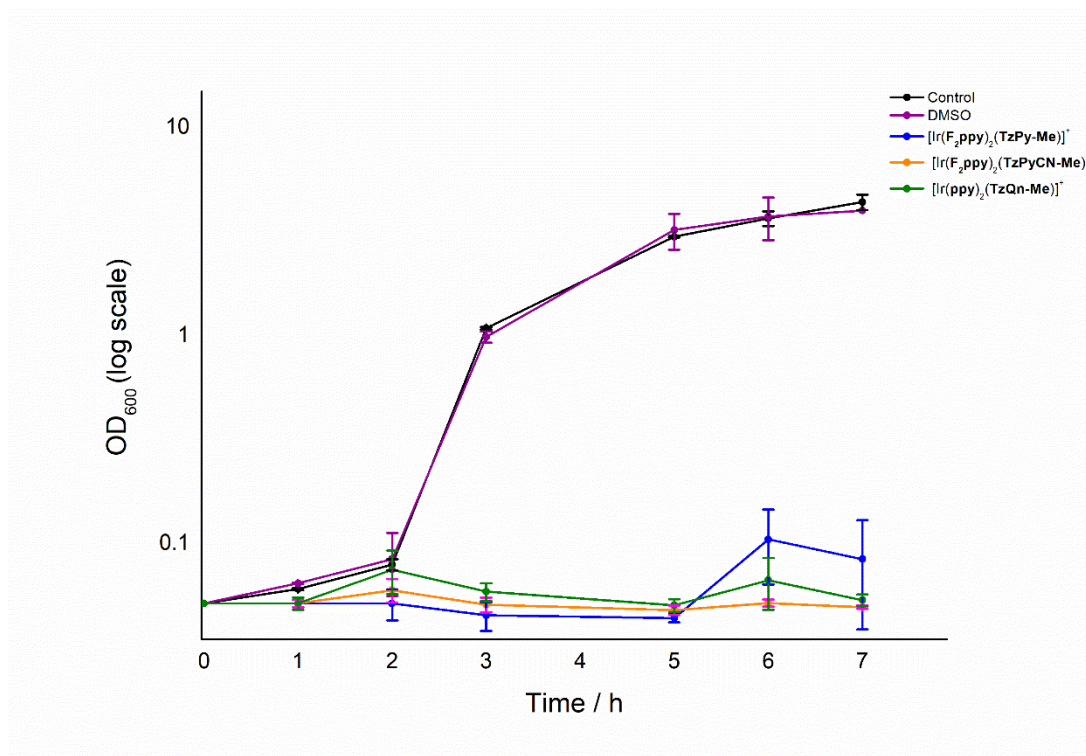


Figure 5.7 Growth curves of *B. cereus* in the presence of the cationic iridium(III) complexes. Unstained and DMSO treated bacterial cultures were also monitored.

5.4.2 Confocal imaging

Following the same staining protocol described in the previous section, live *B. cereus* were incubated with a 20 μM solution of the complexes (Nutrient Broth, 0.1% DMSO) and the stained culture was imaged via confocal microscopy. Indeed, $[\text{Ir}(\text{F}_2\text{ppy})_2(\text{TzPy-Me})]^+$, $[\text{Ir}(\text{F}_2\text{ppy})_2(\text{TzPyCN-Me})]^+$, $[\text{Ir}(\text{F}_2\text{ppy})_2(\text{TzQn-Me})]^+$ were quickly internalised within bacteria and showed a sub-cellular localisation that were different to the staining profiles observed for the neutral analogues or BODIPY. Indeed, the cationic complexes appeared to stain a fine sub-cellular structure present throughout the bacterial cell (**Figure 5.8**).

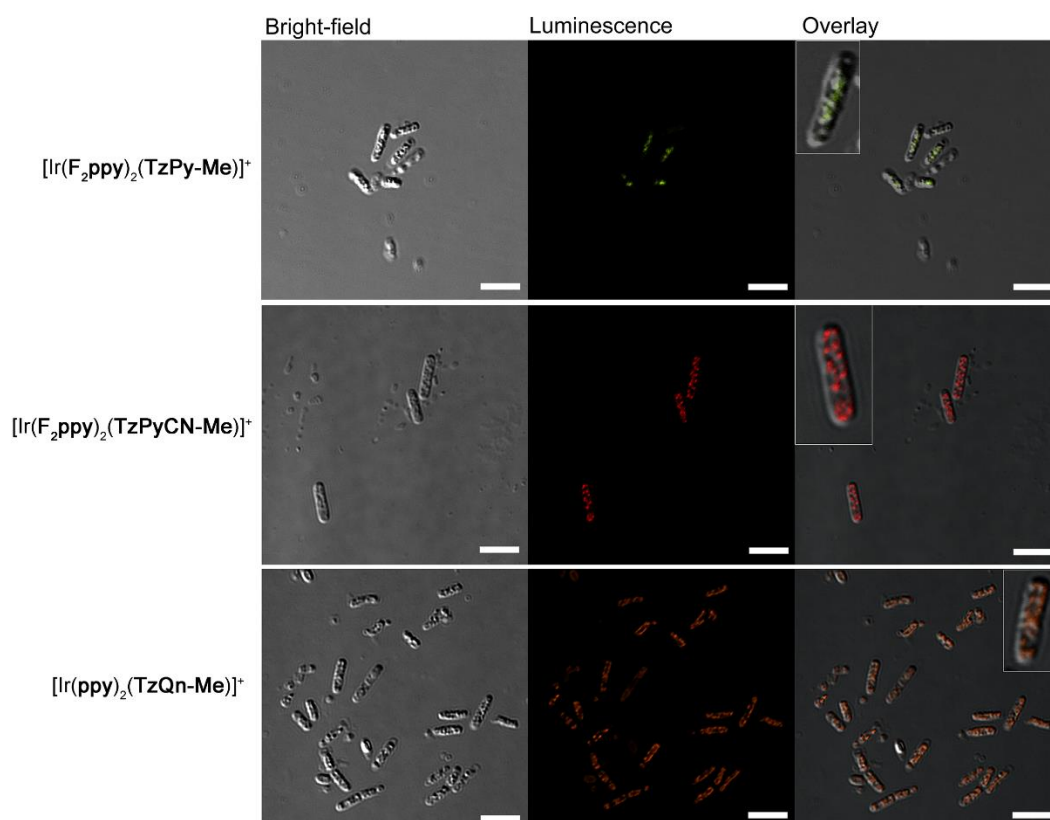


Figure 5.8 Confocal fluorescence microscopy shows the uptake and interaction of the cationic iridium complexes in *B. cereus* (dose: 20 μM , 0.1% DMSO, 1 minute incubation time). Scalebars 5 μm .

In the attempt to gain a better understanding of the eventual affinity of $[\text{Ir}(\text{F}_2\text{ppy})_2(\text{TzPy-Me})]^+$, $[\text{Ir}(\text{F}_2\text{ppy})_2(\text{TzPyCN-Me})]^+$, $[\text{Ir}(\text{F}_2\text{ppy})_2(\text{TzQn-Me})]^+$ for a particular bacterial substructure, further staining experiments have been conducted with the commercial stain SYTO 9. This green fluorescent dye shows preferential affinity for DNA and RNA in bacteria as well as in eukaryotic cells, and it is commonly used in confocal microscopy and flow cytometry. At first inspection of the confocal images, SYTO 9 showed a staining pattern that resembled the one observed for the cationic iridium(III) complexes. However, the complexes appeared to show a more defined and punctate localisation pattern spread throughout the bacterial cytoplasm that extended to the peripheral area of the cell. It could be hypothesised that the cationic iridium(III) complexes interacted with bacterial proteins in *B. cereus*. Several imaging studies focused on bacterial proteins commonly identified as MreB and Mbl are actin homologs that control cell morphogenesis in a wide range of rod-shaped bacteria. These proteins play a critical role in various processes, in particular for maintenance of cell width and cell viability.^{6,279,280,288} Many investigations focus on the function of MreB and Mbl as an actin-like cytoskeleton in bacteria, also involved in the synthesis of the peptidoglycan cell wall.^{6,280} Moreover, it has been reported that other integral membrane proteins like YueB also play a key role in the interaction of bacterial cell with bacterial viruses such as bacteriophages.²⁸⁹⁻²⁹¹ An intense research effort is focusing on the dynamics of these actin-like proteins, as they are yet not fully understood.

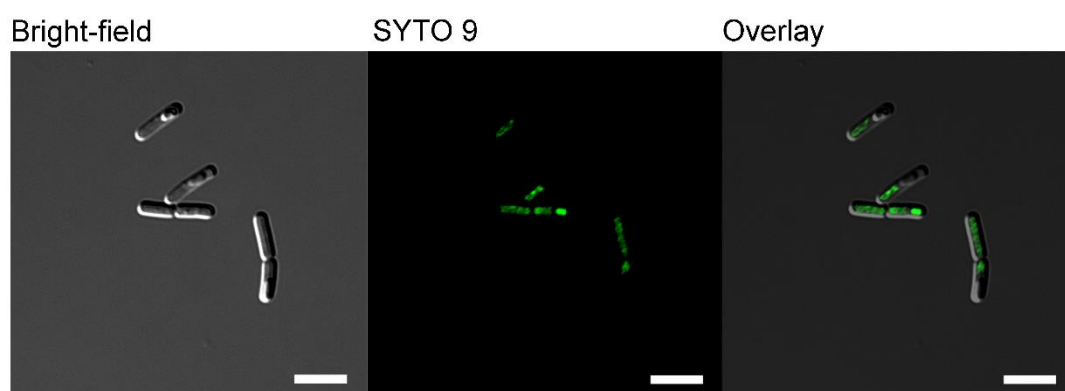


Figure 5.9 *B. cereus* dosed with 3 μM SYTO 9. SYTO 9 was excited at 488 nm and the emission was collected in the region 525/50 nm. Scalebar 5 μM .

Carballido-López and other authors have used a variety of microscopic approaches to study the molecular mechanisms related to MreB, Mbl and YueB in the gram-positive model *B. subtilis*, and all of these are based on the generation of fluorescent proteins.^{6,12,279,280,289} GFP-fused versions of MreB, Mbl and YueB have been used to monitor their localisation, to study their motion and mode of action. In this context, inspection of previously reported confocal or superresolution images of *B. subtilis*, revealed that GFP-adducts of MreB, Mbl or YueB often exhibit a punctate staining pattern along the bacterial sidewalls and cytoplasmic region,^{12,279,280,289} that resembles the localisation pattern of $[\text{Ir}(\mathbf{F}_2\mathbf{ppy})_2(\mathbf{TzPy-Me})]^+$, $[\text{Ir}(\mathbf{F}_2\mathbf{ppy})_2(\mathbf{TzPyCN-Me})]^+$, $[\text{Ir}(\mathbf{F}_2\mathbf{ppy})_2(\mathbf{TzQn-Me})]^+$. It could be hypothesised that the cationic iridium(III) complexes considered in this study interacted with proteinaceous substrates within *B. cereus*. The interaction of $[\text{Ir}(\mathbf{F}_2\mathbf{ppy})_2(\mathbf{TzPy-Me})]^+$, $[\text{Ir}(\mathbf{F}_2\mathbf{ppy})_2(\mathbf{TzPyCN-Me})]^+$, $[\text{Ir}(\mathbf{F}_2\mathbf{ppy})_2(\mathbf{TzQn-Me})]^+$ with proteins like MreB, Mbl and YueB, vital for the maintenance of a viable cell wall, could explain the antimicrobial effect exhibited for *B. cereus*. The lack of readily available commercial dyes to stain these substrates impeded co-localisation experiments to prove this hypothesis. Further imaging studies are required using antibodies-based dyes and GFP-fusion techniques to prove the affinity of the complexes for the protein of interest.

5.5 Conclusion

The results discussed in this chapter strongly suggest that the three neutral iridium(III) tetrazolato complexes, $[\text{Ir}(\mathbf{F}_2\mathbf{ppy})_2(\mathbf{TzPy})]$, $\text{Ir}(\mathbf{F}_2\mathbf{ppy})_2(\mathbf{TzPyCN})$, $[\text{Ir}(\mathbf{F}_2\mathbf{ppy})_2(\mathbf{TzQn})]$, not only successfully act as stains for living bacteria, but they also show a lipid-specific affinity and sub-cellular localisation. The lipid nature of the inclusions has been confirmed by means of Raman spectroscopy, used for the first time to image lipids in live bacteria, complementing the use of luminescent probes. Chemical modifications of the complexes allow a facile colour tuning of the emission by using the same excitation wavelength, without affecting the sub-cellular localisation. Critically, the three complexes investigated do not inhibit the cell growth for the strain object of this study. These results highlight the potential to use this family of complexes as non-toxic labels for *in-vivo* imaging of bacteria, offering widely varying emission colour and consistent sub-cellular specificity. There has also been preliminary investigation into the sub-cellular localisation of the cationic analogues, $[\text{Ir}(\mathbf{F}_2\mathbf{ppy})_2(\mathbf{TzPy})]^+$, $[\text{Ir}(\mathbf{F}_2\mathbf{ppy})_2(\mathbf{TzPyCN})]^+$, $[\text{Ir}(\mathbf{F}_2\mathbf{ppy})_2(\mathbf{TzQn})]^+$. The results discussed in this chapter strongly suggest that the three neutral iridium(III) tetrazolato complexes, $[\text{Ir}(\mathbf{F}_2\mathbf{ppy})_2(\mathbf{TzPy})]$, $\text{Ir}(\mathbf{F}_2\mathbf{ppy})_2(\mathbf{TzPyCN})$, $[\text{Ir}(\mathbf{F}_2\mathbf{ppy})_2(\mathbf{TzQn})]$, to try and delineate a structure-activity relationship in order to explain the cellular behaviour of the complexes. If a trend can be identified, this could be exploited in the future to develop an expanded library of metal-based bacterial imaging agents. Confocal microscopy experiments proved that the cationic iridium(III) complexes indeed showed a remarkably different sub-cellular localisation within *B. cereus*, with a well-defined punctate staining pattern along the cytoplasmic region including the bacterial sidewalls. Staining experiments with the DNA/RNA stain SYTO 9 suggested that the observed staining pattern was unlikely to be due to interaction with bacterial DNA and/or RNA. The results discussed in this chapter strongly suggest that the three cationic iridium(III) tetrazolato complexes, $[\text{Ir}(\mathbf{F}_2\mathbf{ppy})_2(\mathbf{TzPy})]^+$, $[\text{Ir}(\mathbf{F}_2\mathbf{ppy})_2(\mathbf{TzPyCN})]^+$, $[\text{Ir}(\mathbf{F}_2\mathbf{ppy})_2(\mathbf{TzQn})]^+$, showed affinity for essential proteins like MreB, Mbl or YueB. This interaction could explain the inhibitory effect that these complexes exhibited towards *B. cereus*. Further in-depth studies are needed to confirm this hypothesis and expand the current understanding of the interaction of this new class of metal-based probes with bacterial cells.

5.6 Experimental

5.6.1 Photophysical measurements

Photophysical measurements have been conducted as outlined in Chapter 3, Section 3.7.3.

5.6.2 Bacterial strains and growth conditions

Bacterial strains and growth conditions were described in Chapter 2, section 2.8.8.

5.6.3 Growth curves determination

Bacterial cell growth was monitored following the protocol described in Chapter 2, Section 2.8.9.

5.6.4 Confocal microscopy

Bacterial cultures were dosed with a 20 μM solution of the complexes in Nutrient Broth (0.1% DMSO) for 1 minute, then washed with Nutrient Broth and imaged. Staining with BODIPY 493/503 (ThermoFischer) and SYTO 9 (ThermoFischer) at a concentration of 3 μM were performed following the same protocol.

Confocal images were acquired using a Nikon A1R confocal microscope and a Plan Apo λ 100X oil-immersion objective lens (NA = 1.45). The complexes were excited at 405 nm and the emission was collected in the 525/50 nm and 595/50 nm regions. BODIPY 493/503 and SYTO 9 were excited at 488 nm and the emission collected in the 525/50 nm region. Images were collected using NIS-Element version 4.60.00 software and deconvolved using 3D Blind deconvolution. The images were processed using NIS-Element Viewer v.4.20 and the final preparation was conducted with Adobe Photoshop CC (Adobe Systems Inc., USA).

5.6.5 Raman imaging

Raman spectroscopic maps of living bacteria were collected with a WITec Alpha 300 SAR, using confocal modality. Bacteria were immobilised in 1.5% agarose, sandwiched between a glass microscope slide and coverslip. Maps were collected with 532 nm excitation, with a 60x Nikon objective (N.A. 0.8, with glass coverslip correction) and 300 nm laser spot. Raman maps were collected with either 0.1 or 0.25 μm steps and a 200 ms dwell time per pixel. Raman spectroscopic false colour images of lipid ester distribution were generated from the area under the curve of the ester carbonyl $\nu(\text{C}=\text{O})$ band with a linear baseline subtraction (1755 - 1715 cm^{-1}). Project 4 WITec Suite 4.0 software was used for analysis and post processing of Raman spectra and image generation. Image overlays were prepared using ImageJ.

Chapter 6

Development of a protocol to stain live acidophilic bacteria for confocal microscopy

6.1 Introduction

Acidophiles are acidophilic microorganisms that have pH optimum for growth that is less than pH 3.^{7,292,293} These organisms are abundant in the biosphere, inhabiting natural environments associated with pyritic ore bodies or coal deposits,^{7,10} and man-made acidic environments such as acid mine drainage. Iron and/or sulfur oxidising acidophilic bacteria have application in biomining, that is the process of using microorganisms to extract metals from rock ores or mine waste.^{10,294} The ability of micro-organisms to solubilise metals from insoluble ores is known as bioleaching.^{10,23,295} This process is currently used on a commercial scale to recover metals from copper, gold and uranium ores and it has potential for recovering other metals including for example Ni(II) and Co(II) from low-grade sulfide containing ores. Acidophiles such as *Acidithiobacillus ferrooxidans* and related species have an active role in biomining, and they have been subject to a large body of research to fully understand how these species survive and leach in extreme conditions.^{7,10} While thriving at pH 1-2, acidophiles require a circumneutral intracellular pH, therefore they experience and maintain a pH gradient of around 6 orders of magnitude across the cytoplasmic membrane.⁷

pH homeostasis in acidophiles is very complex and involves several homeostatic mechanisms, one of which is based on the presence of a reversed transmembrane potential.^{7,296} Neutrophilic organisms maintain a negative membrane potential, that is characterised by a negative charge on the internal surface of the membrane and a positive charge on the external one. On the other hand, with a reverse membrane potential, acidophiles bear a positive charge in the inner side of the membrane and a negative charge on the outer side (**Figure 6.1**)

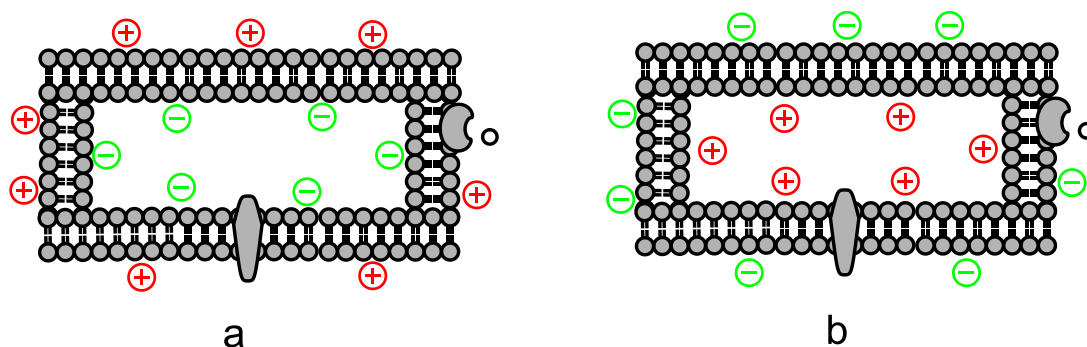


Figure 6.1 Schematic representation of cell membrane with: **a** *negative* membrane potential **b.** *positive* membrane potential.

The reverse transmembrane potential inhibits the entry of H^+ from the external environment across the membrane and aids the maintenance of the pH gradient. However, pH homeostasis mechanisms in acidophiles are not fully delineated, and a better understanding of these processes is vital for the biomining industry, as they play a key role in the bioleaching capability of acidophiles. Flow cytometry is a technique routinely used to assess viability and membrane potential in neutrophilic microorganisms. This laser-based technique uses specific fluorophores to measure a wide range of physical and chemical parameters such as size, viability and different physical attributes.²⁹⁷ Previous work has focused on the development of a dye-based protocol for flow cytometry with acidophiles, so that the technique could be exploited for viability assays and to gain further insights into the membrane potential of these species.²⁹⁸ The challenge in applying flow cytometry to acidophiles was mainly related to the fact that there is to date no dye available to readily stain live acidophiles. This is likely to be due to the presence of the reversed membrane potential, previously discussed, that is inhibiting cellular uptake. Furthermore, operating with live acidophiles requires a pH ranging from pH 1 to pH 2. These experimental conditions can dramatically affect the performance of fluorescent probes, as in the case of propidium iodide (PI). Indeed, while this dye is commonly used in live/dead flow cytometric assays for neutrophiles²⁹⁹, previous reports demonstrate strong quenching of PI due to low pH.^{300,301}

The new developed protocol for flow cytometry was based on the structural properties of the commercially available dye SYTO 9. This dye is commonly used to stain nucleic acids in a wide range of live and dead, gram-positive and gram-negative bacteria.

Importantly, SYTO 9 is natively very weakly fluorescent, but it experiences a 10-fold increase in fluorescence intensity signal when bound to double stranded DNA or RNA.³¹ The chemical structure of SYTO 9 has not been yet disclosed, however it is known to be a positively charged, membrane-permeable rhodamine derivative.³¹ In species with a negative membrane potential like neutrophiles, the negative charge on the internal side of the membrane drives the uptake of the positively charged SYTO 9, which then binds to DNA or RNA producing an increase in the fluorescence intensity output. However, in cells with a positive membrane potential such as acidophiles, the inner side of the membrane is positively charged. Due to this, it could be expected that the interaction of SYTO 9 with live acidophiles would be limited to the outer side of the membrane, resulting in the visualisation of an extremely weak, faded signal. On the other hand, in non-viable or compromised populations of acidophiles, SYTO 9 would be capable of staining nucleic acids as the membrane potential is no longer maintained. Based on this rationale, a first gating strategy has been developed to discriminate viable and non-viable population of acidophiles *via* flow cytometry.²⁹⁸

Besides flow cytometric techniques, optical imaging is a promising approach to gain further understanding of the complex microbiology of acidophiles. Again, the challenge in this context is the absence of a probe able to stain live acidophiles. First, it is vital to have a probe that can cross the cell membrane of live acidophiles, so that intracellular events and features can be monitored. Secondly, such a probe should be emissive at pH as low as pH 1-2, so that experiments can be conducted in the optimal growth conditions. Indeed, even though it can be assumed that upon internalisation within acidophiles the probe would be exposed to a circumneutral intracellular pH, it is important to use a probe that is also emissive at the intracellular pH. In this way, the probe could be detected in the internal cytoplasmic region and interaction with the outer side of the membrane could be monitored.

Based on the results previously obtained with flow cytometry using SYTO 9, it can be assumed that to stain live acidophiles, cellular uptake needs to be promoted by overcoming or exploiting the reversed membrane potential. If the positively charged SYTO 9 could not cross the bacterial membrane due to charge effects, then the staining strategy should be directed towards the use of neutral and anionic probes. In this chapter, the first steps to delineate a protocol for imaging live acidophiles via confocal microscopy have been undertaken. The model species *Acidithiobacillus ferrooxidans* (*At. ferrooxidans*) has been considered throughout this study. Firstly, confocal imaging

experiments with SYTO 9 on *At. ferrooxidans* were conducted. This was to test the applicability of SYTO 9 for confocal imaging on *At. ferrooxidans* and to assess the role of the bacterial cell membrane in the cellular uptake. Secondly, a family of reference transition metal complexes bearing neutral and negative and positive overall charges (**Figure 6.2**) have been tested for imaging live *At. Ferrooxidans*. This was to assess whether the charge of the probes influenced cellular uptake in the live model specie. Prior to the imaging experiments, the emission properties of all the considered dyes, including SYTO 9, have been monitored at low pH.

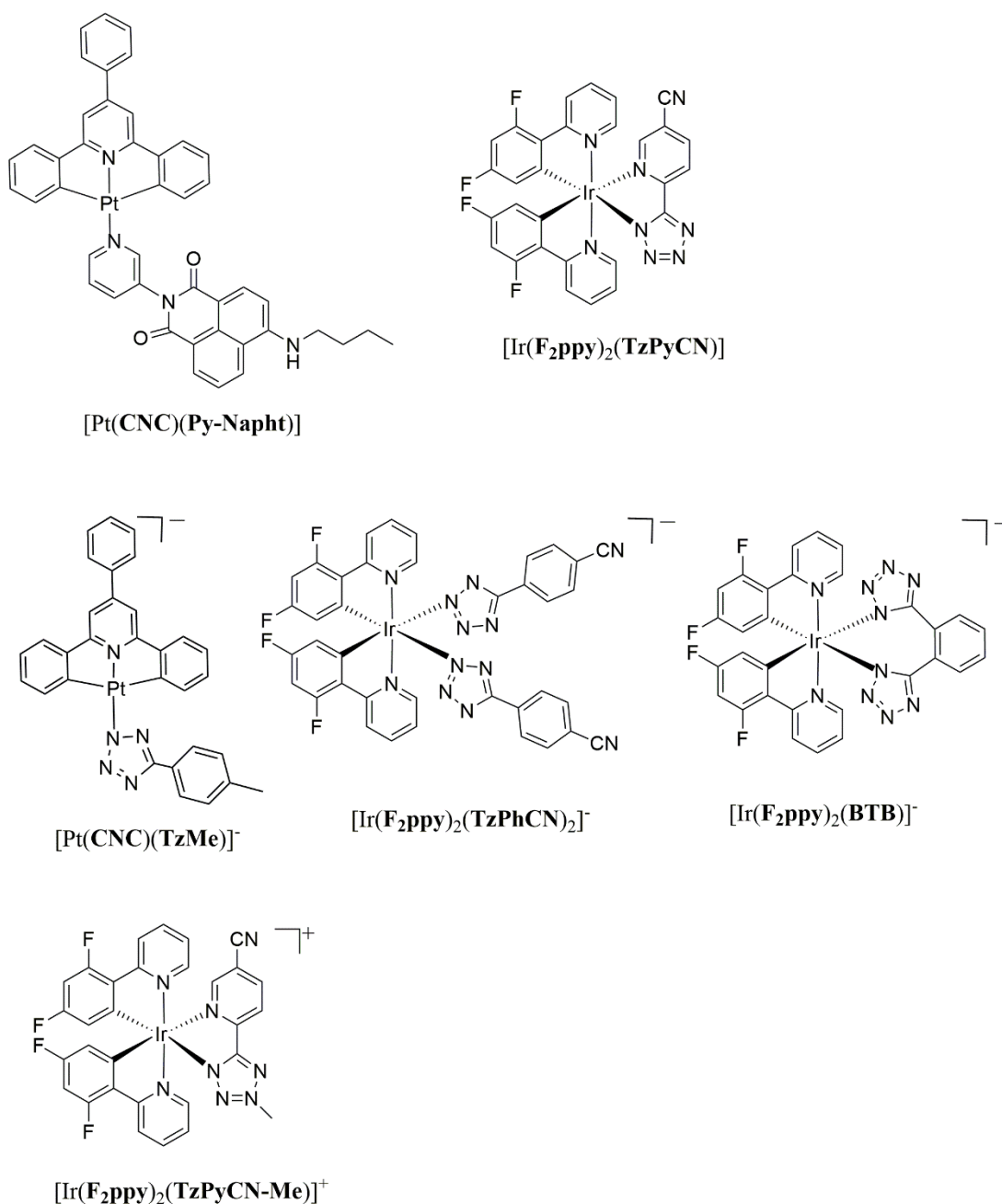


Figure 6.2 Chemical structure of the complexes considered in this study. Top: neutrally charged complexes. Middle: Anionically charged complexes. **BTB** represents the doubly deprotonated form of 1,2 bis-(1 H -tetrazol-5-yl)-benzene (1,2- H_2 **BTB**). Bottom: Positively charged control.

6.2 Photophysical properties at low pH

Before treating *At. ferrooxidans* with the model dyes, the emission properties at low pH have been assessed (**Table 6.1**). In order to closely mimic the staining conditions, the photophysical measurements have been carried out in the growth medium used to culture *At. ferrooxidans*, that is in standard basal salts media (BSM). It is to be noted that the solubility of all the compounds decreased in this medium. DMSO (1%) was used to facilitate the dissolution of the species, and visible turbidity was observed when the compounds were dissolved in BSM for the neutral species [Pt(CNC)(Py-Napht)] and [Ir(F₂ppy)₂(TzPyCN)]. Despite the solubility issues, all the model compounds maintained emission properties that were consistent with those observed at neutral pH in terms of emission profiles (**Figure 6.3**) and excited state lifetime decays. The emission properties of [Ir(F₂ppy)₂(TzPhCN)₂]⁻ and [Ir(F₂ppy)₂(BTB)]⁻ in aqueous media at a neutral pH have also been assessed, as they have not been reported in the literature previously (Appendix E, Table E.1). The photophysical properties of SYTO 9 and the other model compounds at neutral pH are also reported in Appendix E, Table E.1. In general, the quantum yield values at low pH experienced an overall 3-fold decrease. Despite a general emission quenching due to the decrease in solubility as well as the low pH of the solution³⁰², the dyes considered in this chapter were still performing in extremely acidic environments, therefore they were tested for the staining experiments with *At. ferrooxidans*.

Table 6.1 Emission data for the tested compounds in BSM (1% DMSO, pH = 1.8).

Complex	λ_{em} [nm]	τ_{aer}^a [ns]	Φ_{aer}^b %
SYTO 9	550	3	0.4
[Pt(CNC)(Py-Napht)]	570	2	0.7
[Pt(CNC)(TzMe)] ⁻	705	21	0.4
[Ir(F ₂ ppy) ₂ (TzPyCN)]	550	174	1.5
[Ir(F ₂ ppy) ₂ (TzPyCN-Me)] ⁺	645	25	0.5
[Ir(F ₂ ppy) ₂ (TzPhCN) ₂] ⁻	520	25 (59), 5 (41)	0.2
[Ir(F ₂ ppy) ₂ (BTB)] ⁻	460, 487	55 (84), 6 (16)	1.1

[a] For the biexponential excited state lifetime (τ), the relative weights of the exponential curves are reported in parentheses. [b] Measured versus [Ru(bpy)₃]²⁺ in H₂O ($\Phi_r = 0.028$).

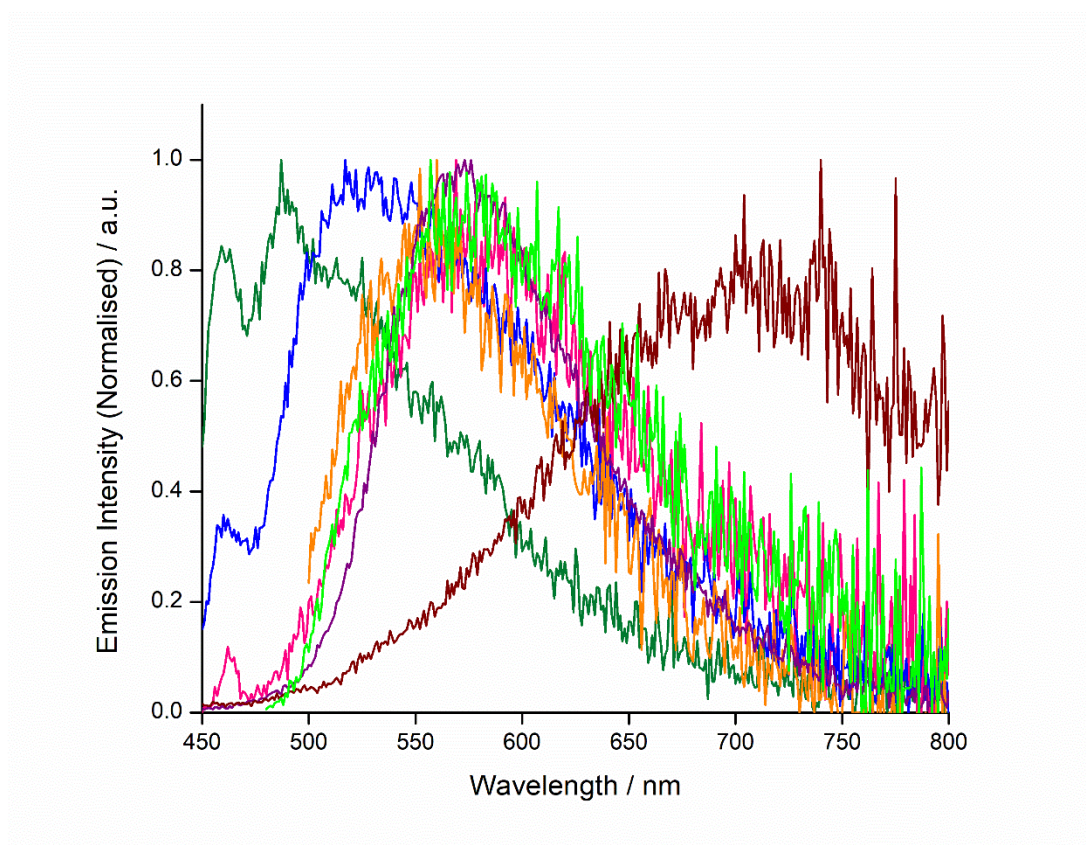


Figure 6.3 Emission profiles of SYTO 9 (bright green line) and the model complexes considered in this study in BSM, pH 1.8. [Pt(CNC)(Py-Napht)]: purple line; [Pt(CNC)(TzMe)]⁻: brown line; [Ir(F2ppy)₂(TzPyCN)]: orange line; [Ir(F2ppy)₂(TzPyCN-Me)]⁺: pink line; [Ir(F2ppy)₂(TzPhCN)₂]⁻: blue line; [Ir(F2ppy)₂(BTB)]⁻: dark green line.

6.3 Imaging of *At. ferrooxidans* with MitoTracker Red and SYTO 9

6.3.1 Incubation test with MitoTracker Red

There are a very limited number of reports regarding the staining of extremophile bacteria. Maslov *et al* reported in 2018 the use of a commercially available organic dye, MitoTracker, to stain the halophilic bacteria *Halobacterium salinarum*.²¹⁶ This membrane-potential sensitive dyes exists with a range of colours (e.g MitoTracker Red, MitoTracker Orange) and it is normally used to stain mitochondria in eukaryotic cells. Following the same approach, *At. ferrooxidans* was dosed with a 3 μM solution of MitoTracker Red, and different incubation times were tested ranging from 15 minutes up to 3 hours. Unfortunately, MitoTracker Red could not be detected in these conditions, indicating that it was unlikely to penetrate or interact with the cell wall of live *At. ferrooxidans* (**Figure 6.4**).

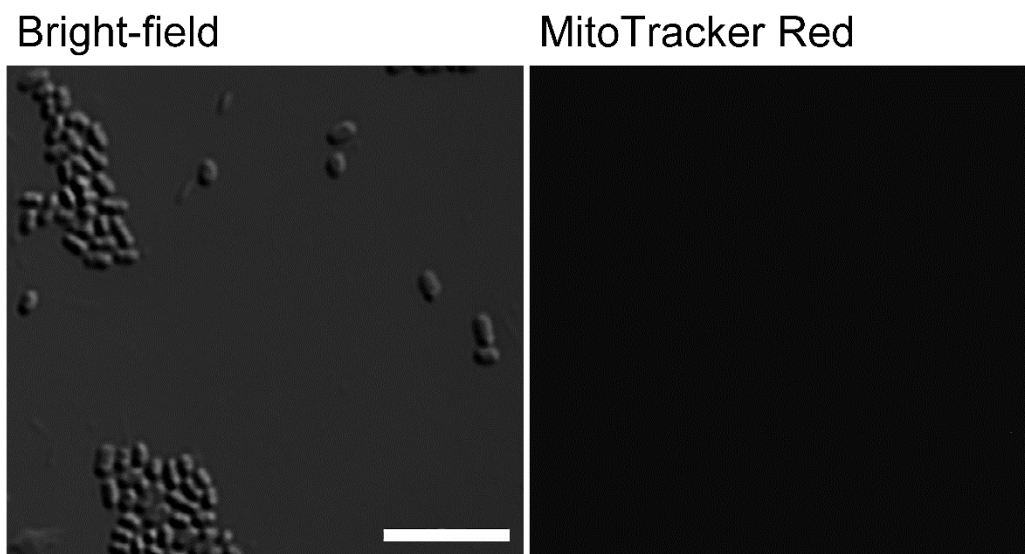


Figure 6.4 Micrographs showing live *At. ferrooxidans* dosed with MitoTracker Red. Scalebars 5 μm .

6.3.2 Incubation tests with SYTO 9

6.3.2.1 SYTO 9 and live *At. ferrooxidans*

Before treating acidophiles with SYTO 9, control experiments with *B. cereus* and *E. coli* were performed to confirm that the commercial stain worked as per manufacturer's protocol (Appendix E, Figure E.2 – E.3). Live *At. ferrooxidans* was then dosed with SYTO 9 in BSM for an incubation time ranging from 15 min to 3 hours. Imaging of the samples with confocal laser scanning microscopy suggested that no detectable interaction occurred between SYTO 9 and *At. ferrooxidans*, as no fluorescence signal could be detected. This may appear in contrast with the flow cytometry analyses previously reported,²⁹⁸ where a very weak signal corresponding to SYTO 9 could be detected with live *At. ferrooxidans*, due to the organic dye stuck to the external surface of the bacteria. It should be noted however that flow cytometric techniques generally analyse bulk samples, therefore they record the signal originating from the entire bacterial sample and not from the single cell. Hence, in a case of poor staining, even though each individual cell would provide an extremely faded signal, the overall intensity could still be sufficient to yield a detectable signal *via* flow cytometry. This is not true for confocal microscopy which, on the contrary, detects the signal originating from the single specimen.

6.3.2.2 SYTO 9 and membrane-compromised *At. ferrooxidans*

It can be hypothesised that staining with SYTO 9 would be achievable if the membrane integrity in *At. ferrooxidans* is compromised, and therefore the positive membrane potential no longer maintained. The most commonly used method to obtain membrane-compromised cells or bacteria is via fixation. *At. ferrooxidans* was fixed *via* a standard method involving treatment with 4% formaldehyde, washing with H₂O and final dehydration steps with EtOH. The fixed sample was then incubated with a 3 µM solution of SYTO 9 and imaged. As shown in **Figure 6.5**, SYTO 9 could be easily detected via confocal microscopy, showing a similar performance to the one observed for *B. cereus* and *E. coli*. This suggests that in presence of a compromised membrane, SYTO 9 could interact with fixed *At. ferrooxidans* staining nucleic acids.

To further confirm this, a verification test has been carried out preparing a membrane-compromised sample of *At. ferrooxidans* via heat treatment. An aliquot of *At. ferrooxidans* was heated at 60°C for 180 minutes, and then incubated with 70% EtOH. To confirm the non-viability of the culture, an aliquot was inoculated in fresh growth media to verify the absence of any cell growth. Heat-treated *At. ferrooxidans* was incubated with SYTO 9 and similarly to what was observed after cell fixation, staining was readily observed via confocal microscopy (Appendix E, Figure E.4) This suggests that the lack of uptake of SYTO 9 in live *At. ferrooxidans* is likely to be due to the presence of the intact cell membrane, and staining can be easily achieved when the membrane is compromised.

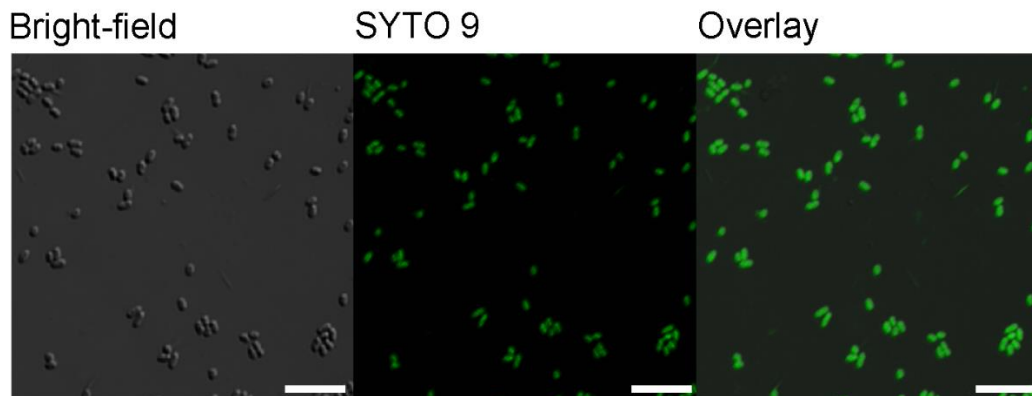


Figure 6.5 Micrographs showing fixed *At. ferrooxidans* dosed with SYTO 9. Scalebars 5 μm .

6.4 Imaging of *At. ferrooxidans* with transition metal complexes

In this section, different platinum(II) and iridium(III) complexes were tested on live *At. ferrooxidans*. Based on the negative results obtained with the positively charged SYTO 9 (Section 6.3.2), a range of neutral and anionic complexes has been chosen to assess whether the overall charge of the dyes had an effect on the uptake in the acidophiles. For neutral complexes, given the absence of a cationic charge, it could be hypothesised that the uptake would be driven by permeability effects through the membrane. For anionic species instead, the positive membrane potential of live *At. ferrooxidans* could be exploited for the uptake, opposite to that which was observed with SYTO 9. Indeed, when considering a positive membrane potential, it can be hypothesised that the anionic complexes would be attracted by the positive charge in the internal surface of the membrane and therefore be internalised within the bacteria. Hence, the neutral species [Pt(CNC)(Py-Napht)] and [Ir(F₂ppy)₂(TzPyCN)] have been tested alongside anionic species such as [Pt(CNC)(TzMe)]⁻, [Ir(F₂ppy)₂(TzPhCN)₂]⁻ and [Ir(F₂ppy)₂(BTB)]⁻. As a negative control, the cationic iridium(III) analogue [Ir(F₂ppy)₂(TzPyCN-Me)]⁺ has been also considered. All the complexes were tested at a 20 μM concentration in BSM and incubated with live *At. ferrooxidans* from 15 minutes up to 3 hours, following washing and imaging via confocal microscopy. The neutral species [Pt(CNC)(Py-Napht)] and [Ir(F₂ppy)₂(TzPyCN)]. could not be detected in live *At. ferrooxidans* even after 3 hours incubation. Similarly, [Pt(CNC)(TzMe)]⁻ did not exhibit any cellular uptake. Remarkably, uptake was instead observed for the anionic species [Ir(F₂ppy)₂(TzPhCN)₂]⁻ and [Ir(F₂ppy)₂(BTB)]⁻. Indeed, a green emission could be detected from the cytoplasm of live *At. ferrooxidans*. Interestingly, inspection of the whole image field clearly showed that not all the bacteria were stained (**Figure 6.6**). This indicated the need of further studies to assess whether the uptake is affected by different factors linked to the metabolic state of the species. However, as a negative control, [Ir(F₂ppy)₂(TzPyCN-Me)]⁺ was incubated with live *At. ferrooxidans*. Again, as was observed with the neutral analogue [Ir(F₂ppy)₂(TzPyCN)], the absence of any uptake was confirmed.

Similarly to what was observed in Chapter 2, the fact that no signal could be detected for $[\text{Pt}(\text{CNC})(\text{TzMe})]^-$ could be due to the absence of aggregation induced emission in the bacterial cytoplasm, although the lack of uptake within *At. ferrooxidans* cannot be excluded without ICP-MS studies. Nonetheless, these results are remarkable, as they showed clear evidence that indeed the charge of the iridium(III) complexes played an important role in promoting cellular uptake within *At. ferrooxidans*, allowing for the first time staining of the species in live cultures.

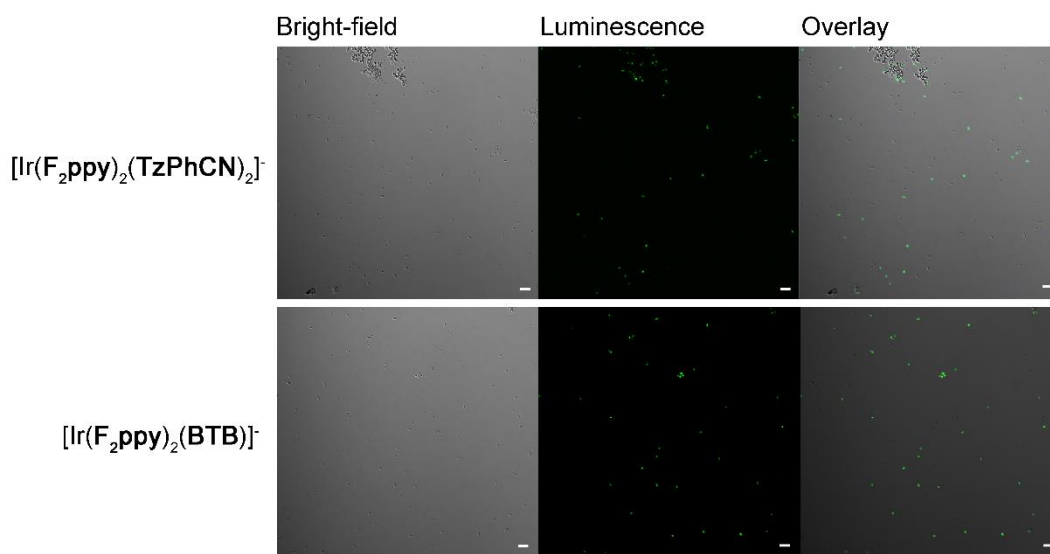


Figure 6.6 Micrographs showing live *At. ferrooxidans* dosed with $[\text{Ir}(\text{F}_2\text{ppy})_2(\text{TzPhCN})_2]^-$ (top) and $[\text{Ir}(\text{F}_2\text{ppy})_2(\text{BTB})]^-$ (bottom). Scalebars 5 μm .

6.5 Conclusion

In this chapter, the base for a new protocol to stain acidophiles has been set, considering the *At. ferrooxidans* as a model. For this study, the nucleic acid stain SYTO 9 has been used, alongside platinum(II) and iridium(III) reference complexes. The complexes that have been considered in this set of experiments have been chosen based on their overall charge, to assess whether this factor played a role in the biological behaviour of the complexes in terms of cellular uptake. Two neutral species, [Pt(CNC)(Py-Napht)] and [Ir(F₂ppy)₂(TzPyCN)], have been tested, as well as the anionic species [Pt(CNC)(TzMe)]⁻, [Ir(F₂ppy)₂(TzPhCN)₂]⁻ and [Ir(F₂ppy)₂(BTB)]⁻. Furthermore, the cationic complex [Ir(F₂ppy)₂(TzPyCN-Me)]⁺ has been considered. First of all the emission properties of SYTO 9 as well as the platinum(II) and iridium(III) complexes have been tested in BSM at pH 1.8, to confirm that the selected dyes were emissive despite the extremely acidic conditions. With this information in hand, SYTO 9 has been tested on live *At. ferrooxidans*. While this commonly used commercial dye is suitable to stain a wide range of gram-positive and gram-negative bacteria characterised by a positive membrane potential, no uptake was observed in *At. ferrooxidans*. This was ascribed to the fact that the positive membrane potential maintained by the acidophilic species in optimal growth conditions was inhibiting the uptake of the positively charged SYTO 9. To confirm this, membrane-compromised samples of *At. ferrooxidans* have been prepared via chemical fixation as well as heat treatment. In the presence of a compromised cell membrane, SYTO 9 was able to stain acidophiles and the green emission of the dye from the cytoplasmic region of *At. ferrooxidans* could be easily detected. Following these results, the neutrally charged [Pt(CNC)(Py-Napht)] and [Ir(F₂ppy)₂(TzPyCN)] were tested, to assess whether in the absence of a positive charge, uptake could be promoted simply by permeability effects. Unfortunately, these complexes did not appear to interact with live *At. ferrooxidans*. On the other hand, the anionic iridium(III) complexes [Ir(F₂ppy)₂(TzPhCN)₂]⁻ and [Ir(F₂ppy)₂(BTB)]⁻ could be internalised in live *At. ferrooxidans*, even though the bacterial culture could not be homogeneously stained. The cationic complex [Ir(F₂ppy)₂(TzPyCN-Me)]⁺ was used as a negative control. Indeed, no uptake was observed in live *At. ferrooxidans* for this positively charged dye, similarly to what was observed with SYTO 9. These results suggest that a negatively charged probe is preferred to stain *At. ferrooxidans*, so that the positive

membrane potential can be exploited to attract the anionic species to the inner side of the cellular membrane and promote cellular uptake. Future work will be focused on the design of an extended library of anionic probes to be tested towards *At. ferrooxidans* and other acidophiles strains. In particular, the probe design will be directed towards the functionalisation of the ligands with anionic functionalities as for example SO_3^- groups, to try and increase the overall negative charge of the complexes. Moreover, extensive studies are required to delineate the uptake mechanism as well as potential effects of the complexes on the bacterial growth.

6.6 Experimental

6.6.1 Photophysical properties

Photophysical measurements in BSM at pH = 1.8 have been conducted as outlined in Chapter 3, Section 3.7.3.

6.6.2 Bacterial strain and growth conditions

At. ferrooxidans DSM 14882 was cultured in standard basal salts media, BSM, (0.4 g/L NH₄SO₄, 0.4 g/L MgSO₄, 0.4 g/L KH₂PO₄) and adjusted to pH 1.8 with H₂SO₄. The culture was supplemented with 50mM FeSO₄ · 7H₂O, 5mM K₂S₄O₆ and 1% v/v trace elements from a stock solution²⁹⁸, and then incubated at 30 °C with shaking at 100 RPM.

6.6.3 Confocal microscopy

Bacterial cultures were dosed with a 20 μM solution of the complexes in Nutrient Broth (1% DMSO) for 15 minutes – 3 hours, to be then washed with BSM and imaged. Staining with MitoTracker Red (ThermoFischer) and SYTO 9 (ThermoFischer) at a concentration of 3 μM was performed following the same protocol.

When required, bacterial cultures were fixed in 4% PFA at pH 1.8 and resuspended in fresh BSM. When required, heat treated samples of live *At. ferrooxidans* were prepared heating a 2 mL aliquot to 60 °C for 3 hours, then incubated with 70% biology grade ethanol at room temperature for 60 minutes. To confirm the non-viability of the sample, a 1 mL aliquot was inoculated in fresh media for 48 hours at 60 °C.

MytoTracker Red was excited at 561 nm and the emission collected in the 605/50 nm region. SYTO 9 was excited at 488 nm and the emission collected in the 525/50 nm region. Images were collected and reconstructed using NIS-Element version 4.60.00 software. The images were processed using NIS-Element Viewer v.4.20 and the final preparation was conducted with Adobe Photoshop CC (Adobe Systems Inc., USA).

The complexes were excited at 405 nm and the emission was collected in the 525/50 nm and 595/50 nm regions

Chapter 7

Conclusion and future work

The research presented in this thesis was intended to explore the application of transition metal complexes as bacterial imaging agents. Novel platinum(II) complexes as well as iridium(III) complexes previously reported by our research group have been tested to image neutrophilic and acidophilic bacteria.

This aim was dictated by the recognised need for efficient small-molecule probes to image bacteria,²⁶ and by the lack of literature regarding transition metal complexes explored purely for this scope. Indeed, on the one hand, improved imaging agents able to readily cross the bacterial cell wall and image different sub-cellular structures are required to gain a better understanding of many molecular mechanisms in prokaryotic systems. On the other hand, transition metal complexes have been studied as antibacterial agents, with several examples focusing on iridium(III), rhenium(I) and ruthenium(II) metal ions.^{90,95,102,103,108–110} The favourable properties of transition metal complexes, such as easy target and emission tunability, resistance to self-quenching and photobleaching, have been exploited to image eukaryotic cells and tissues. Expanding these imaging studies towards bacterial cells aims to lay the foundation for future investigations to leverage the advantage of luminescent metal complexes for imaging applied to bacteria.

The first series of platinum(II) complexes presented in this work (**Figure 7.1**, left) focused on a dicyclopalladated system based on the tridentate 2,4,6-triphenylpyridine ligand (CNCH₂). Photophysical studies on the first family of neutral platinum(II) complexes confirmed that these species are emissive in aqueous media due to aggregation induced emission. De Cola and co-workers reported the application of platinum(II) aggregates as cellular imaging agents,^{76,88} showing how aggregated N[^]C[^]N systems could readily penetrate the cell membrane in eukaryotic systems and stain cellular components. Based on these results, and prompted by the lack of biological investigations on platinum(II) C[^]N[^]C derivatives in comparison to the more studied N[^]N[^]N[^]^{54,66} or N[^]C[^]N[^]^{54,59,88,155} complexes, the biological properties of the neutral C[^]N[^]C complexes reported in this study have been assessed against eukaryotic cells as well as on bacteria.

The emission of the platinum(II) aggregates could not be detected from the cellular or bacterial cytoplasm. However, ICP-MS analyses on A549 cells confirmed the uptake of the complexes in cells, demonstrating that the platinum(II) species could effectively cross the cellular membrane. Moreover, cytotoxicity assays revealed that the platinum(II) complexes were not cytotoxic towards A549 cells, with the exception of [Pt(CNC)(bpy-PPh₃)²⁺2I⁻]. As for bacterial species, the platinum(II) C^NC complexes showed inhibitory effects towards the gram-positive bacteria *Bacillus cereus*, while they did not affect the growth of the gram-negative specie *Escherichia coli*. The different in toxicity between the gram-positive and gram-negative bacteria tested is likely to be due to their different cell envelope. The antimicrobial activity of the platinum(II) complexes needs to be further investigated testing the platinum(II) species towards a wider range of bacterial strains. If the trend in toxicity against bacteria can be confirmed, this could be combined with the non-toxicity against A549 cells and exploited in the future to develop new non-toxic platinum(II) complexes with advantageous antimicrobial properties. With these results in hand, the investigation on platinum(II) C^NC complexes for biological imaging has been expanded towards the design of a new platinum(II)-naphthalimide probe, [Pt(CNC)(Py-Napht)]. (**Figure 7.1**, right). In this system, the 1,8-naphthalimide luminescent unit was coordinated to the non-luminescent platinum(II) C^NC fragment. Photophysical and theoretical studies confirmed that the emission properties of the naphthalimide were not affected by the coordination to the Pt(II) metal ion. The platinum(II)-naphthalimide adduct was first tested as cellular label on A549 cell. Confirming the trend observed for the parent platinum(II) C^NC complexes, ICP-MS analyses and Alamar Blue assays proved that [Pt(CNC)(Py-Napht)] accumulated into live cells with low cytotoxicity effects. Imaging of A549 cells incubated with [Pt(CNC)(Py-Napht)] showed sub-cellular localisation in lipid droplets. Interestingly, staining experiments with **Py-Napht** revealed that the free ligand accumulated into live cells showing the same localisation pattern. [Pt(CNC)(Py-Napht)] and **Py-Napht** were then incubated with live *B. cereus* and imaged via structured illumination microscopy (SIM). Remarkably, both the dyes were suitable for super-resolution imaging and showed the same sub-cellular localisation in lipid vacuoles within live bacteria.

Neutral Pt(II) C^NC complexes

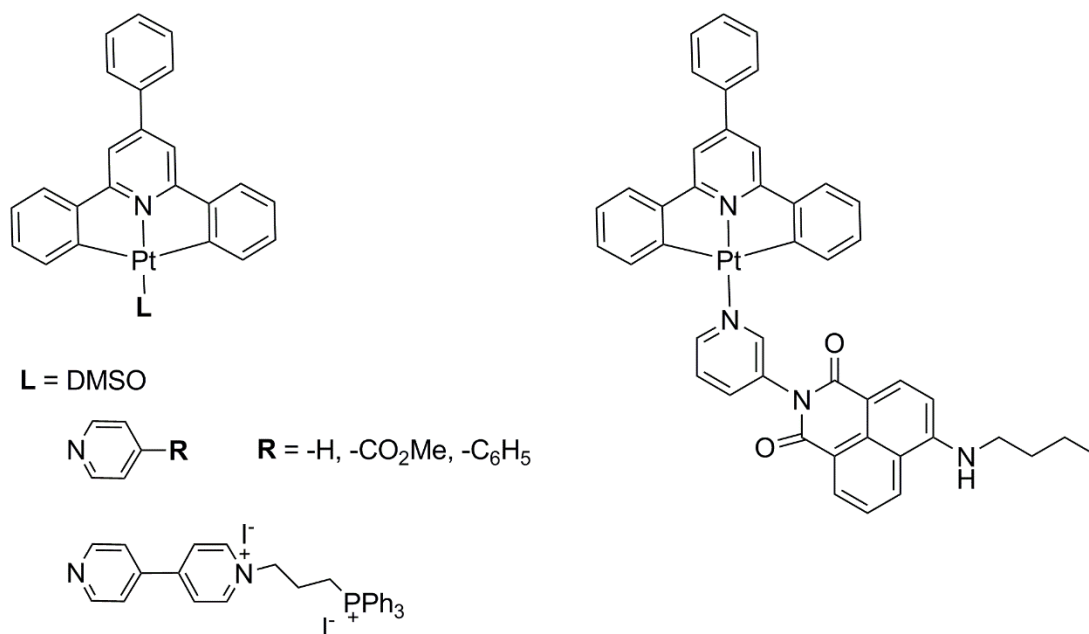


Figure 7.1 Left: first series of platinum(II) neutral complexes. Right: platinum(II)-naphthalimide complex.

The imaging experiments on A549 cells and *B. cereus* confirmed that not only the emission properties, but also the sub-cellular localisation of the 1,8-naphthalimide was unaffected by the coordination to the metal centre. The presence of the platinum(II) complex was then exploited for the detection of the complex via ion nanoscopy, that confirmed the uptake of [Pt(CNC)(Py-Napht)] within bacteria and showed its potential use as a correlative probe. Overall, the biological studies on [Pt(CNC)(Py-Napht)] showed how with this design rationale, the platinum(II) C^NC complex can act as a silent carrier for the naphthalimide unit and enabling detection via other important techniques such as ICP-MS or NanoSIMS. Following this approach, a new library of related platinum(II)-naphthalimide probes is currently being developed in the Massi group, with the aim of tuning the emission and sub-cellular specificity of the naphthalimide to have a family of platinum(II)-based correlative probes with different emission colour and affinity for different cellular components. Moreover, the same naphthalimide-type ligands could be coordinated to other metal centres such as

rhenium(I), to assess how a different metal ion leads to different localisation and/or toxicity effects (**Figure 7.2**).

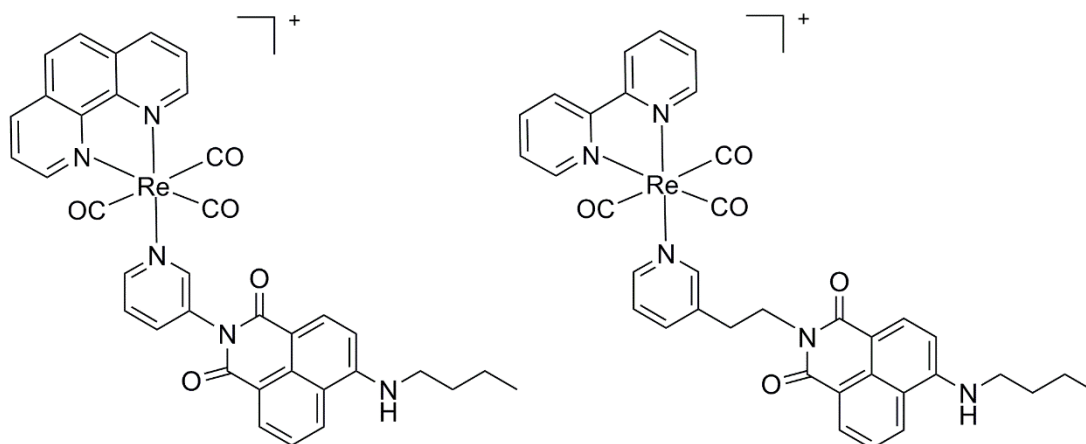


Figure 7.2 Proposed structures of rhenium(I)-naphthalimide probes to be investigated as correlative probes.

To further expand the library of platinum(II) $C^{\wedge}N^{\wedge}C$ complexes, a new family of anionic species has been synthesised and characterised. The synthesis of the anionic $[Pt(CNC)(TzR)]^{-}$ complexes (**Figure 7.3**) was motivated by their potential use as imaging agents for species endowed with a reverse membrane potential.

Moreover, their capability to serve as photoredox catalysts for organic synthesis has been evaluated, showing promising results for a number of α -amino C–H functionalization reactions, as well as atom-transfer radical addition (ATRA), and a hydrodehalogenation reaction.²⁴⁵

Anionic Pt(II) C^NC complexes

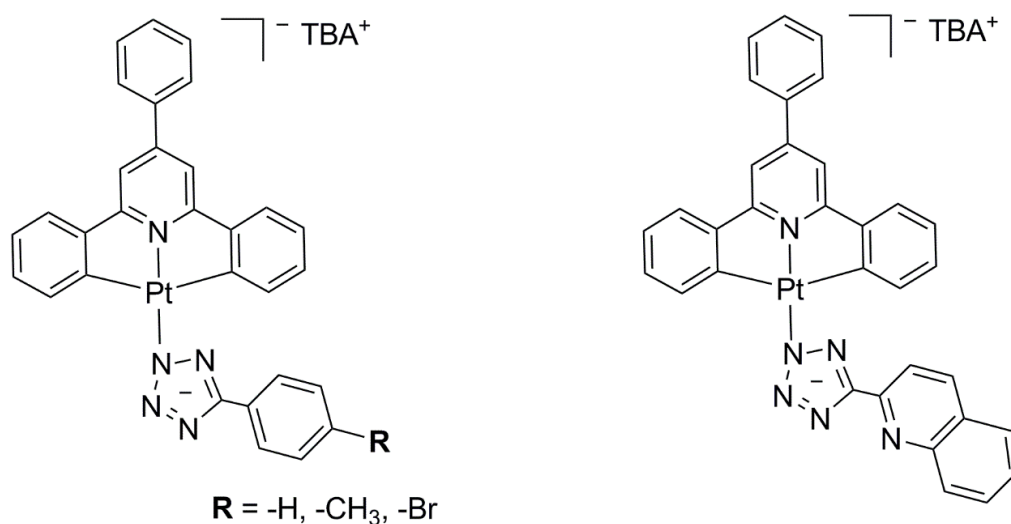


Figure 7.3 Chemical structure of the anionic Pt(II) tetrazolato complexes.

Further, the study on transition metal complexes as imaging agents was extended to include iridium(III) species. Previous investigations in our groups had shown how neutral and cationic iridium(III) tetrazolato complexes³⁰³ had opposite trends in antimicrobial activity against the gram-positive specie *Deinococcus radiodurans*. Based on the hypothesis that this could be due to different sub-cellular localisation within bacteria, a family of three neutral and three cationic (methylated) iridium tetrazolato complexes (**Figure 7.4**) was tested against live *B. cereus*. As for the neutral complexes, the absence of any antimicrobial effect was first confirmed, and the species were then incubated with live bacteria. The three complexes showed extremely fast (1 minute) cellular uptake and sub-cellular localisation in lipid vacuoles. The lipid nature of the cellular components was not only confirmed via staining experiments with BODIPY, but also via confocal Raman imaging. The use of confocal Raman spectroscopy to image lipid inclusions in live bacteria was unprecedented, and these results demonstrated the potential of this technique to be used as a facile, label-free complementary method to the imaging of lipids with luminescent probes. Moving to the cationic species, the three methylated iridium(III) complexes were found to inhibit the growth of *B. cereus*, as expected. Confocal imaging experiments demonstrated that the sub-cellular localisation of the cationic iridium(III) complexes was indeed different to the one observed for the neutral species. The methylated complexes appeared to

stain very fine sub-cellular structures, whose shape and distribution resembled essential membrane proteins such as MreB or Mbl. While co-localisation and imaging experiments are needed to confirm the affinity of the cationic complexes for bacterial membrane proteins, it can be concluded that the different localisation in comparison to the neutral species could be one of the main factors affecting the toxicity of the cationic derivatives.

Ir(III) complexes

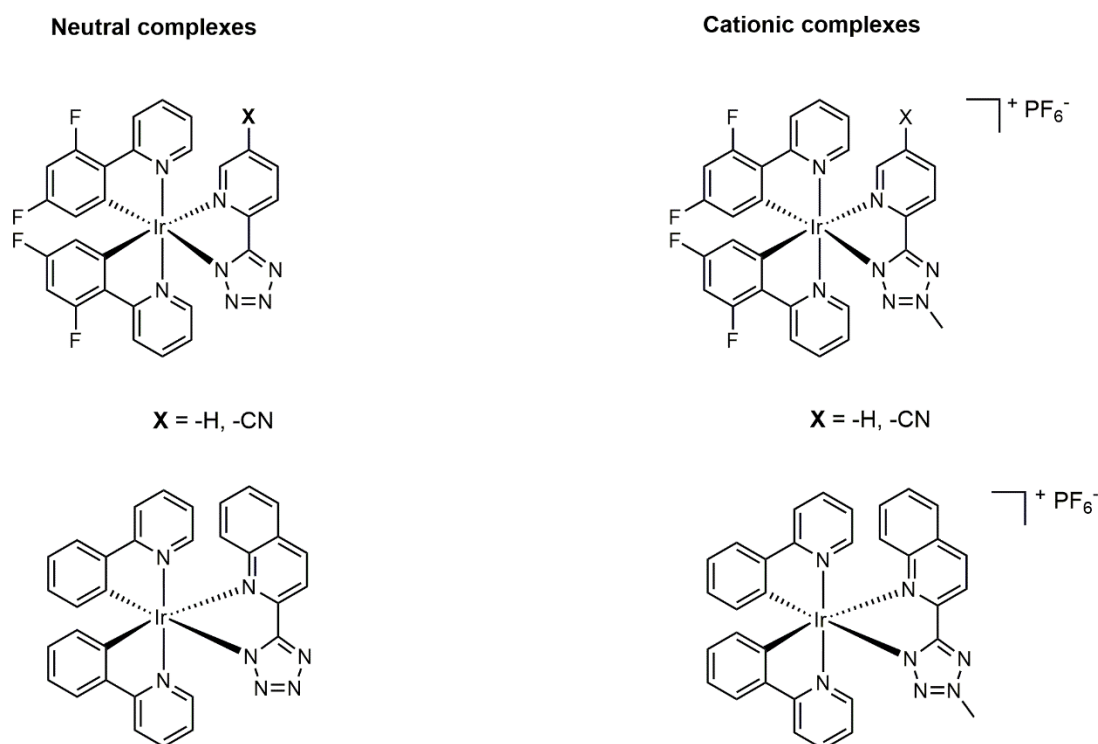


Figure 7.4 Chemical structures of the neutral and cationic iridium(III) complexes.

Finally, a series of platinum(II) and iridium(III) complexes (**Figure 7.5**) have been used to lay the foundations for a new protocol to stain live acidophilic bacteria, which thrive at $\text{pH} < 2$. There is currently no report about markers available to stain live acidophiles, and the main obstacle to this achievement appears to be the presence of a reverse membrane potential. Based on this hypothesis, this fundamental study aimed to define whether altering the overall charge of the probe (i.e. using neutral or anionic species) could overcome or even exploit the reverse membrane potential. First, the capability of the selected probes to emit light at $\text{pH} 2$ was confirmed. After staining

tests of membrane-compromised *Acidithiobacillus ferrooxidans* with the organic (cationic) dye SYTO 9, the selected neutral and anionic complexes were tested towards live *At. ferrooxidans*. The imaging experiments conducted proved that the anionic iridium(III) complexes could stain live acidophiles, although only a portion of the culture in the fields of view appeared to be stained, revealing a non-homogeneous behaviour. Control experiments with neutral or cationic iridium(III) analogues showed no staining of live *At. ferrooxidans*, suggesting that the anionic charge of the complexes may be driving the uptake in to these extremophilic species.

In this regard, future work will be directed towards expanding the library of anionic complexes, with focus on chemical modifications that, while maintaining the anionic charge as well as good emission properties at low pH, will be able to improve the uptake and staining capability of the complexes towards live acidophilic bacteria.

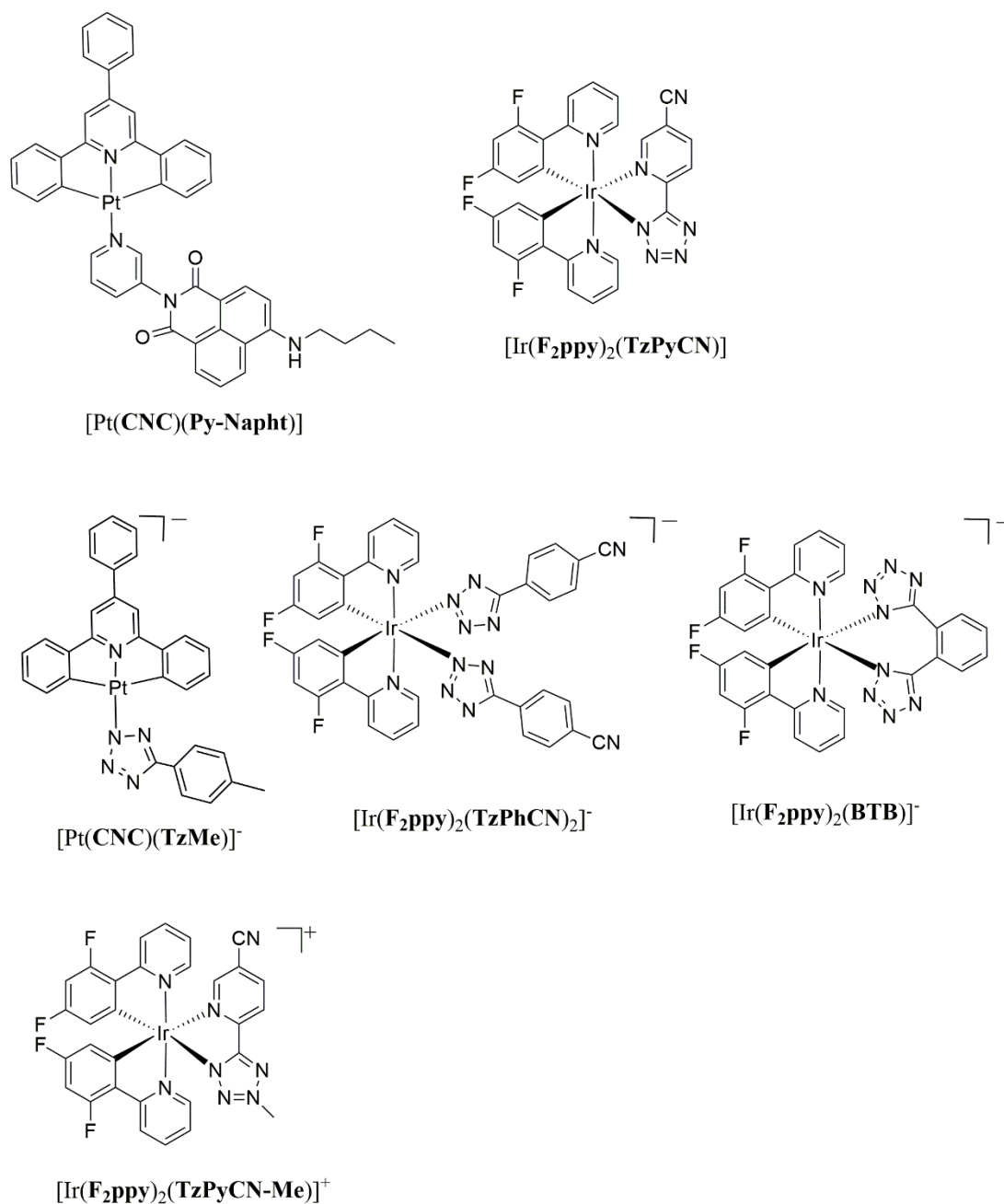


Figure 7.5 Selected transition metal complexes tested as imaging agents for the acidophilic specie *At. ferrooxidans*.

Increasing the negative charge of the complexes by adding negatively charged functional groups in the ligand system may be useful to improve the uptake, as for example in the proposed structures showed in **Figure 7.6**.

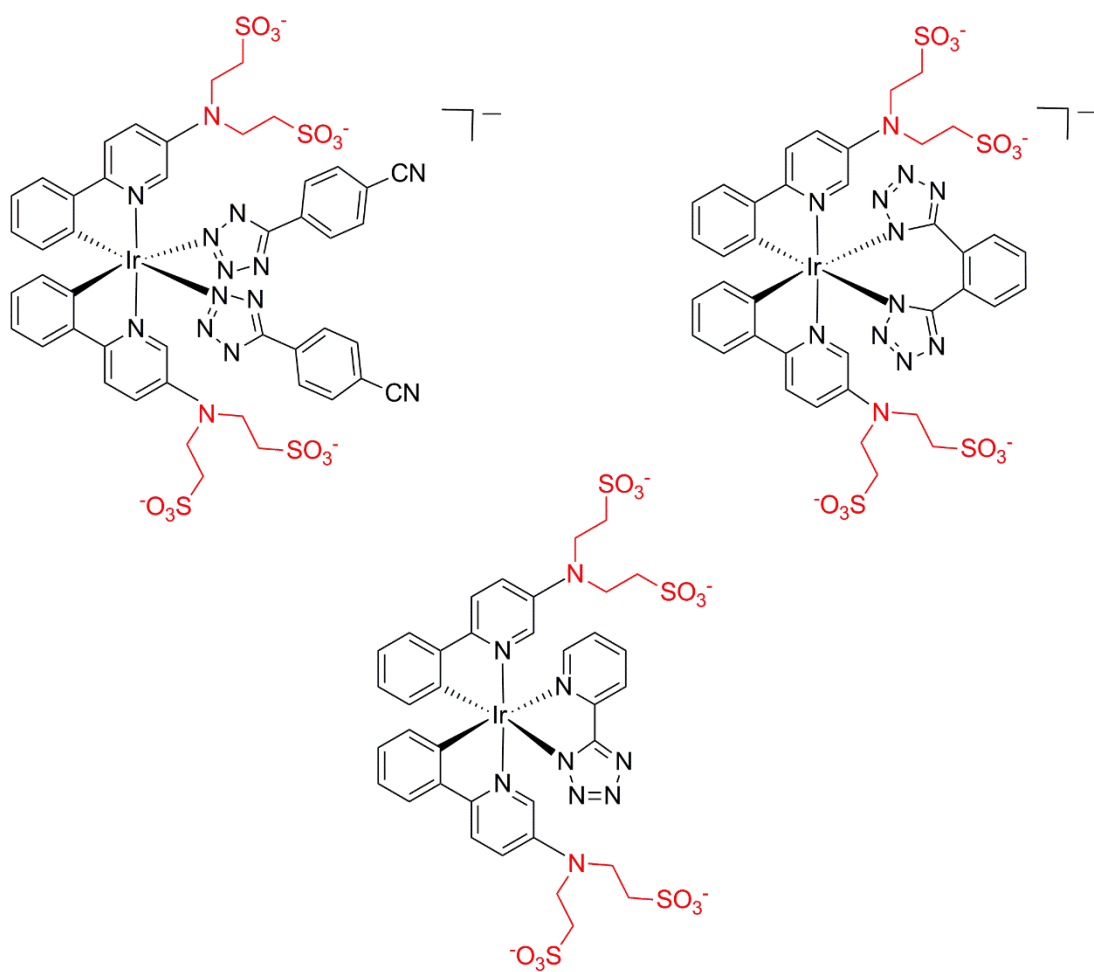


Figure 7.6 Proposed structures of new anionic iridium(III) species, appended with anionic functional groups.

References

- 1 M. T. Madigan, J. M. Martinko, K. S. Bender, D. H. Buckley and D. A. Stahl, *Brock biology of microorganisms - Fourteenth Edition*, 2010.
- 2 M. J. Daly, F. J. Brockman, H. M. Kostandarithes, M. F. Romine, D. Kennedy, J. M. Zachara, S. -M. W. Li, D. L. Balkwill and J. K. Fredrickson, *Appl. Environ. Microbiol.*, 2004, **70**, 4230–4241.
- 3 T. J. Silhavy, D. Kahne and S. Walker, *Cold Spring Harb. Perspect. Biol.*, 2010, **2**, 1–16.
- 4 A. H. Delcour, *Biochim. Biophys. Acta*, 2009, **1794**, 808–816.
- 5 M. Yilmaz, H. Soran and Y. Beyatli, *World J. Microbiol. Biotechnol.*, 2005, **21**, 565–566.
- 6 R. M. Figge, A. V Divakaruni and J. W. Guber, *Genomics*, 2004, **51**, 1–47.
- 7 C. Baker-Austin and M. Dopson, *Trends Microbiol.*, 2007, **15**, 165–171.
- 8 H. Huber and K. O. Stetter, *Arch. Microbiol.*, 1989, **151**, 479–485.
- 9 J. P. Cárdenas, R. Ortiz, P. R. Norris, E. Watkin and D. S. Holmes, *Int. J. Syst. Evol. Microbiol.*, 2015, **65**, 3641–3644.
- 10 D. B. Johnson, *Curr. Opin. Biotechnol.*, 2014, **30**, 24–31.
- 11 D. B. Johnson, *FEMS Microbiol. Ecol.*, 1998, **27**, 307–317.
- 12 Z. Yao and R. Carballido-López, *Annu. Rev. Microbiol.*, 2014, **68**, 459–476.
- 13 M. van Oosten, M. Hahn, L. M. A. Crane, R. G. Pleijhuis, K. P. Francis, J. M. van Dijk and G. M. van Dam, *FEMS Microbiol. Rev.*, 2015, **39**, 892–916.
- 14 V. Hoerr, L. Tuchscher, J. Hüve, N. Nippe, K. Loser, N. Glyvuk, Y. Tsytsyura, M. Holtkamp, C. Sunderkötter, U. Karst, J. Klingauf, G. Peters, B. Löffler and C. Faber, *BMC Biol.*, 2013, **11**, 1–13.

- 15 M. Wältermann, A. Hinz, H. Robenek, D. Troyer, R. Reichelt, U. Malkus, H. J. Galla, R. Kalscheuer, T. Stöveken, P. Von Landenberg and A. Steinbüchel, *Mol. Microbiol.*, 2005, **55**, 750–763.
- 16 Hector M. Alvarez, *Biochimie*, 2016, **120**, 28–39.
- 17 I. Voss and A. Steinbüchel, *Appl. Microbiol. Biotechnol.*, 2001, **55**, 547–555.
- 18 Y. Chen, Y. Ding, L. Yang, J. Yu, G. Liu, X. Wang, S. Zhang, D. Yu, L. Song, H. Zhang, C. Zhang, L. Huo, C. Huo, Y. Wang, Y. Du, H. Zhang, P. Zhang, H. Na, S. Xu, Y. Zhu, Z. Xie, T. He, Y. Zhang, G. Wang, Z. Fan, F. Yang, H. Liu, X. Wang, X. Zhang, M. Q. Zhang, Y. Li, A. Steinbüchel, F. Toyoshi, C. Simon, J. Yu and P. Liu, *Nucleic Acids Res.*, 2014, **42**, 1052–1064.
- 19 D. J. Murphy, *Protoplasma*, 2012, **249**, 541–585.
- 20 R. Subramaniam, S. Dufreche, M. Zappi and R. Bajpai, *J. Ind. Microbiol. Biotechnol.*, 2010, **37**, 1271–1287.
- 21 G. Singh, A. Kumari, A. Mittal, V. Goel, A. Yadav and N. K. Aggarwal, *J. Polym. Environ.*, 2013, **21**, 441–449.
- 22 M. I. Torino, G. F. de Valdez and F. Mozzi, *Front. Microbiol.*, 2015, **6**, 1–16.
- 23 D. E. Rawlings and D. B. Johnson, *Microbiology*, 2007, **153**, 315–324.
- 24 J. P. Schneider and M. Basler, *Philos. Trans. R. Soc. B Biol. Sci.*, 2016, **371**, 1-11.
- 25 C. Coltharp and J. Xiao, *Cell. Microbiol.*, 2012, **14**, 1808–1818.
- 26 O. Kocaoglu and E. E. Carlson, *Nat. Chem. Biol.*, 2016, **12**, 472–478.
- 27 E. Snapp, *Curr. Protoc. Cell Biol.*, 2005, **21.4**, 1-13.
- 28 R. Y. Tsien, *Annu. Rev. Biochem.*, 1998, **67**, 509–544.
- 29 O. Shimomura, F. H. Johnson and Y. Saiga, *J. Cell. Comp. Physiol.*, 1962, **59**, 223–39.
- 30 W. M. Leevy, N. Serazin and B. D. Smith, *Drug Discov. Today*, 2007, **4**, 91–97.
- 31 S. Stains, *Mol. Biol. Cell*, 2003, 4–6.
- 32 K. R. Gee, H. C. Kang, T. I. Meier, G. Zhao and L. C. Blaszcak, 2001, **22**, 960–965.

- 33 G. Zhao, T. I. Meier, S. D. Kahl, K. R. Gee, L. C. Blaszcak and E. Lilly, 1999, **43**, 1124–1128.
- 34 W. Phetsang, M. A. T. Blaskovich, M. S. Butler, J. X. Huang, J. Zuegg, S. K. Mamidyala, S. Ramu, A. M. Kavanagh and M. A. Cooper, *Bioorg. Med. Chem.*, 2014, **22**, 4490–4498.
- 35 P. Shieh, M. S. Siegrist, A. J. Cullen and C. R. Bertozzi, *Proc. Natl. Acad. Sci.*, 2014, **111**, 5456–5461.
- 36 E. Kuru, H. V. Hughes, P. J. Brown, E. Hall, S. Tekkam, F. Cava, M. A. De Pedro, Y. V Brun and M. S. Vannieuwenhze, *Angew. Chemie - Int. Ed.*, 2012, **51**, 12519–12523.
- 37 N. K. Olrichs, M. E. G. Aarsman, J. Verheul, C. J. Arnusch, N. I. Martin, M. Hervø, W. Vollmer and B. De Kruijff, *ChemBioChem*, 2011, **12**, 1124–1133.
- 38 X. Ning, S. Lee, Z. Wang, D. Kim, B. Stubblefield, E. Gilbert and N. Murthy, *Nat. Mater.*, 2011, **10**, 602–607.
- 39 K. M. Backus, H. Boshoff, C. S. Barry, O. Boutureira, M. K. Patel, F. D. Hooge, S. S. Lee, L. E. Via, K. Tahlan, C. E. B. Iii and B. G. Davis, *Nat. Chem. Biol.*, 2011, **7**, 228–235.
- 40 A. Dumont, A. Malleron, M. Awwad, S. Dukan and B. Vauzeilles, *Angew. Chem. Int. Ed.*, 2012, **51**, 3143–3146.
- 41 D. R. Rice, H. Gan and B. D. Smith, *Photochem. Photobiol. Sci.*, 2015, **14**, 1271–1281.
- 42 D. R. Rice, P. Vacchina, B. Norris-Mullins, M. A. Morales and B. D. Smith, *Antimicrob. Agents Chemother.*, 2016, **60**, 2932–2940.
- 43 A. G. White, N. Fu, W. M. Leevy, J.-J. Lee, M. A. Blasco and B. D. Smith, *Bioconjug. Chem.*, 2010, **21**, 1297–1304.
- 44 W. M. Leevy, S. T. Gammon, H. Jiang, J. R. Johnson, D. J. Maxwell, E. N. Jackson, M. Marquez, D. Piwnica-Worms and B. D. Smith, *J. Am. Chem. Soc.*, 2006, **128**, 16476–16477.
- 45 E. Zhao, Y. Hong, S. Chen, C. W. T. Leung, C. Y. K. Chan, R. T. K. Kwok, J. W. Y. Lam and B. Z. Tang, *Adv. Healthc. Mater.*, 2014, **3**, 88–96.

- 46 E. Zhao, Y. Chen, H. Wang, S. Chen, J. W. Y. Lam, C. W. T. Leung, Y. Hong and B. Z. Tang, *ACS Appl. Mater. Interfaces*, 2015, **7**, 7180–7188.
- 47 E. Zhao, Y. Chen, S. Chen, H. Deng, C. Gui, C. W. T. Leung, Y. Hong, J. W. Y. Lam and B. Z. Tang, *Adv. Mater.*, 2015, **27**, 4931–4937.
- 48 C. A. Strassert, M. Otter, R. Q. Albuquerque, A. Hone, Y. Vida, B. Maier and L. De Cola, *Angew. Chem. Int. Ed.*, 2009, **48**, 7928–7931.
- 49 L. C. Ong, L. Y. Ang, S. Alonso and Y. Zhang, *Biomaterials*, 2014, **35**, 2987–2998.
- 50 F. P. V. Balzani, G. Bergamini, S. Campagna, *Top. Curr. Chem.*, 2007, **280**, 1–36.
- 51 J. R. Lakowicz, *Principles of Fluorescence Spectroscopy, 3rd Edition*, 2006.
- 52 J. V Caspar and T. J. Meyer, *J. Phys. Chem.*, 1983, **87**, 952–957.
- 53 F. B. L. Flamigni, A. Barbieri, C. Sabatini, B. Ventura, *Top. Curr. Chem.*, 2007, **281**, 143–203.
- 54 M. Mauro, A. Aliprandi, D. Septiadi, N. S. Kehr and L. De Cola, *Chem. Soc. Rev.*, 2014, **43**, 4144–4166.
- 55 J. A. G. Williams, *Top. Curr. Chem.*, 2007, **281**, 205–268.
- 56 G. S. M. Tong and C. M. Che, *Chem. - A Eur. J.*, 2009, **15**, 7225–7237.
- 57 K. Li, G. S. Ming Tong, Q. Wan, G. Cheng, W. Y. Tong, W. H. Ang, W. L. Kwong and C. M. Che, *Chem. Sci.*, 2016, **7**, 1653–1673.
- 58 T. Morgan and F. H. Burstall, *J. Chem. Soc.*, 1934, 1498–1500.
- 59 S. W. Botchway, M. Charnley, J. W. Haycock, A. W. Parker, D. L. Rochester, J. A. Weinstein and J. A. G. Williams, *Proc. Natl. Acad. Sci.*, 2008, **105**, 16071–16076.
- 60 C. C.-M. Cheung T-S, Cheung K-K, Peng S-M, *J. Chem. Soc., Dalt. Trans.*, 1996, 1645–1651.
- 61 S. C. F. Kui, F. F. Hung, S. L. Lai, M. Y. Yuen, C. C. Kwok, K. H. Low, S. S. Y. Chui and C. M. Che, *Chem. - Eur. J.*, 2012, **18**, 96–109.
- 62 J. Mei, Y. Hong, J. W. Y. Lam, A. Qin, Y. Tang and B. Z. Tang, *Adv. Mater.*, 2014, **26**, 5429–5479.

- 63 J. A. G. Williams, *Top. Curr. Chem.*, 2007, **281**, 205–268.
- 64 K. M. Wong and V. W. Yam, *Acc. Chem. Res.*, 2010, **44**, 424–434.
- 65 V. W. W. Yam, K. M. C. Wong and N. Zhu, *J. Am. Chem. Soc.*, 2002, **124**, 6506–6507.
- 66 C. Y. S. Chung, S. P. Y. Li, J. A. Morris, D. Sale and V. W. W. Yam, *Chem. Sci.*, 2013, **4**, 2453–2462.
- 67 V. W. Yam, R. P. Tang, K. M. Wong and X. Lu, *Chem. Eur. J.*, 2002, **8**, 4066–4076.
- 68 V. W. W. Yam, H. O. Song, S. T. W. Chan, N. Zhu, C. H. Tao, K. M. C. Wong and L. X. Wu, *J. Phys. Chem. C*, 2009, **113**, 11674–11682.
- 69 W. Mróz, C. Botta, U. Giovanella, E. Rossi, A. Colombo, C. Dragonetti, D. Roberto, R. Ugo, A. Valore and J. A. G. Williams, *J. Mater. Chem.*, 2011, **21**, 8653–8661.
- 70 J. A. Gareth Williams, S. Develay, D. L. Rochester and L. Murphy, *Coord. Chem. Rev.*, 2008, **252**, 2596–2611.
- 71 M. P. Coogan and V. Fernández-Moreira, *Chem. Commun.*, 2014, **50**, 384–399.
- 72 J. R. Shewring, A. J. Cankut, L. K. McKenzie, B. J. Crowston, S. W. Botchway, J. A. Weinstein, E. Edwards and M. D. Ward, *Inorg. Chem.*, 2017, **56**, 15259–15270.
- 73 R. E. Daniels, L. K. McKenzie, J. R. Shewring, J. A. Weinstein, V. N. Kozhevnikov and H. E. Bryant, *RSC Adv.*, 2018, **8**, 9670–9676.
- 74 C. Caporale and M. Massi, *Coord. Chem. Rev.*, 2018, **363**, 71–91.
- 75 V. Fernández-Moreira, F. L. Thorp-Greenwood and M. P. Coogan, *Chem. Commun.*, 2010, **46**, 186–202.
- 76 A. Aliprandi, D. Genovese, M. Mauro and L. De Cola, *Chem. Lett.*, 2015, **44**, 1152–1169.
- 77 K. K. W. Lo, A. W. T. Choi and W. H. T. Law, *Dalt. Trans.*, 2012, **41**, 6021–6047.
- 78 K. K. W. Lo, *Acc. Chem. Res.*, 2015, **48**, 2985–2995.
- 79 D. Parker, *Aust. J. Chem.*, 2011, **64**, 239–243.
- 80 N. P. E. Barry and P. J. Sadler, *Chem. Commun.*, 2013, **49**, 5106–5131.

- 81 A. C. Komor and J. K. Barton, *Chem. Commun.*, 2013, **49**, 3617–3630.
- 82 T. Chen, W. J. Mei, Y. S. Wong, J. Liu, Y. Liu, H. S. Xie and W. J. Zheng, *Medchemcomm*, 2010, **1**, 73–75.
- 83 A. Sorvina, C. A. Bader, J. R. T. Darby, M. C. Lock, J. Y. Soo, I. R. D. Johnson, C. Caporale, N. H. Voelcker, S. Stagni, M. Massi, J. L. Morrison, S. E. Plush and D. A. Brooks, *Sci. Rep.*, 2018, **8**, 1–8.
- 84 C. Caporale, C. A. Bader, A. Sorvina, K. D. M. MaGee, B. W. Skelton, T. A. Gillam, P. J. Wright, P. Raiteri, S. Stagni, J. L. Morrison, S. E. Plush, D. A. Brooks and M. Massi, *Chem. - Eur. J.*, 2017, **23**, 15666–15679.
- 85 J. Li, Z. Tian, Z. Xu, S. Zhang, Y. Feng, L. Zhang and Z. Liu, *Dalton Trans.*, 2018, **47**, 15772–15782.
- 86 C. A. Bader, R. D. Brooks, Y. S. Ng, A. Sorvina, M. V. Werrett, P. J. Wright, A. G. Anwer, D. A. Brooks, S. Stagni, S. Muzzioli, M. Silberstein, B. W. Skelton, E. M. Goldys, S. E. Plush, T. Shandala and M. Massi, *RSC Adv.*, 2014, **4**, 16345–16351.
- 87 K. E. Erkkila, D. T. Odom and J. K. Barton, *Chem. Rev.*, 1999, **99**, 2777–2796.
- 88 D. Septiadi, A. Aliprandi, M. Mauro and L. De Cola, *RSC Adv.*, 2014, **4**, 25709–25718.
- 89 T. Zou, C. T. Lum, S. S. Chui and C. Che, *Angew. Chemie - Int. Ed.*, 2013, **52**, 2930–2933.
- 90 L. Lu, L. J. Liu, W. C. Chao, H. J. Zhong, M. Wang, X. P. Chen, J. J. Lu, R. N. Li, D. L. Ma and C. H. Leung, *Sci. Rep.*, 2015, **5**, 1–9.
- 91 A. D. Richards, A. Rodger, M. J. Hannon and A. Bolhuis, *Int. J. Antimicrob. Agents*, 2009, **33**, 469–472.
- 92 S. E. Howson, A. Bolhuis, V. Brabec, G. J. Clarkson, J. Malina, A. Rodger and P. Scott, *Nat. Chem.*, 2011, **4**, 31–36.
- 93 P. Lam, G. Lu, K. Hon, K. Lee, C. Ho, X. Wang and J. C. Tang, *Dalt. Trans.*, 2014, **43**, 3949–3957.
- 94 A. Bolhuis, L. Hand, J. E. Marshall, A. D. Richards, A. Rodger and J. Aldrich-wright, *Eur. J. Pharm. Sci.*, 2011, **42**, 313–317.

- 95 L. F., C. J. G. and K. F. R., *Chem. Soc. Rev.*, 2015, **44**, 2529–2542.
- 96 A. Bolhuis and J. R. Aldrich-wright, *Bioorg. Chem.*, 2014, **55**, 51–59.
- 97 N. L. Kilah and E. Meggers, *Aust. J. Chem.*, 2012, **65**, 1325–1332.
- 98 P. M., G. G. and M.-N. N., *Dalton*, 2012, **41**, 6350.
- 99 F. Li, M. Feterl, J. M. Warner, A. I. Day, F. R. Keene and J. G. Collins, *Dalt. Trans.*, 2013, **42**, 8868–8877.
- 100 F. Li, Y. Mulyana, M. Feterl, J. M. Warner, J. G. Collins and F. R. Keene, *Dalt. Trans.*, 2011, **40**, 5032–5038.
- 101 F. Li, M. Feterl, J. M. Warner, F. R. Keene and J. Grant Collins, *J. Antimicrob. Chemother.*, 2013, **68**, 2825–2833.
- 102 A. K. Gorle, X. Li, S. Primrose, F. Li, M. Feterl, R. T. Kinobe, K. Heimann, J. M. Warner, F. Richard Keene and J. Grant Collins, *J. Antimicrob. Chemother.*, 2016, **71**, 1547–1555.
- 103 A. K. Gorle, M. Feterl, J. M. Warner, S. Primrose, C. C. Constantinoiu, F. R. Keene and J. G. Collins, *Chem. - A Eur. J.*, 2015, **21**, 10472–10481.
- 104 F. Li, M. Feterl, Y. Mulyana, J. M. Warner, J. G. Collins and F. R. Keene, *J. Antimicrob. Chemother.*, 2012, **67**, 2686–2695.
- 105 F. Li, E. J. Harry, A. L. Bottomley, M. D. Edstein, G. W. Birrell, C. E. Woodward, F. R. Keene and J. G. Collins, *Chem. Sci.*, 2014, **5**, 685–693.
- 106 A. K. Gorle, M. Feterl, J. M. Warner, L. Wallace, F. R. Keene and J. G. Collins, *Dalt. Trans.*, 2014, **43**, 16713–16725.
- 107 M. Pandrala, F. Li, M. Feterl, Y. Mulyana, J. M. Warner, L. Wallace, F. R. Keene and J. G. Collins, *Dalt. Trans.*, 2013, **42**, 4686–4694.
- 108 S. V. Kumar, S. O. Scottwell, E. Waugh, C. J. McAdam, L. R. Hanton, H. J. L. Brooks and J. D. Crowley, *Inorg. Chem.*, 2016, **55**, 9767–9777.
- 109 S. V. Kumar, W. K. C. Lo, H. J. L. Brooks and J. D. Crowley, *Inorganica Chim. Acta*, 2015, **425**, 1–6.

- 110 S. V. Kumar, W. K. C. Lo, H. J. L. Brooks, L. R. Hanton and J. D. Crowley, *Aust. J. Chem.*, 2016, **69**, 489–498.
- 111 A. Noor, G. S. Huff, S. V. Kumar, J. E. M. Lewis, B. M. Paterson, C. Schieber, P. S. Donnelly, H. J. L. Brooks, K. C. Gordon, S. C. Moratti and J. D. Crowley, *Organometallics*, 2014, **33**, 7031–7043.
- 112 K. K. W. Lo, M. W. Louie and K. Y. Zhang, *Coord. Chem. Rev.*, 2010, **254**, 2603–2622.
- 113 K. K. W. Lo, S. P. Y. Li and K. Y. Zhang, *New J. Chem.*, 2011, **35**, 265–287.
- 114 K. K. W. Lo, W. K. Hui, C. K. Chung, K. H. K. Tsang, D. C. M. Ng, N. Zhu and K. K. Cheung, *Coord. Chem. Rev.*, 2005, **249**, 1434–1450.
- 115 A. Aliprandi, M. Mauro and L. De Cola, *Nat. Chem.*, 2016, **8**, 10–15.
- 116 M. Bachmann, D. Suter, O. Blacque and K. Venkatesan, *Inorg. Chem.*, 2016, **55**, 4733–4745.
- 117 M. Mydlak, M. Mauro, F. Polo, M. Felicetti, J. Leonhardt, G. Diener, L. De Cola and C. A. Strassert, *Chem. Mater.*, 2011, **23**, 3659–3667.
- 118 C. A. Strassert, C. H. Chien, M. D. Galvez Lopez, D. Kourkoulos, D. Hertel, K. Meerholz and L. De Cola, *Angew. Chemie - Int. Ed.*, 2011, **50**, 946–950.
- 119 C. Alexander, A. Nithyakumar and N. Arockia Samy, *Inorg. Chem. Commun.*, 2017, **78**, 17–20.
- 120 B. A. Iglesias, J. F. B. Barata, P. M. R. Pereira, H. Girão, R. Fernandes, J. P. C. Tomé, M. G. P. M. S. Neves and J. A. S. Cavaleiro, *J. Inorg. Biochem.*, 2015, **153**, 32–41.
- 121 K. Ypsilantis, T. Tsohis, A. Kourtellaris, M. J. Manos, J. C. Plakatouras and A. Garoufis, *Dalt. Trans.*, 2017, **46**, 1467–1480.
- 122 C. O'Brien, M. Y. Wong, D. B. Cordes, A. M. Z. Slawin and E. Zysman-Colman, *Organometallics*, 2015, **34**, 13–22.
- 123 Z. M. Hudson, C. Sun, M. G. Helander, H. Amarne, Z. H. Lu and S. Wang, *Adv. Funct. Mater.*, 2010, **20**, 3426–3439.

- 124 J. Brooks, Y. Babayan, S. Lamansky, P. I. Djurovich, I. Tsyba, R. Bau and M. E. Thompson, *Inorg. Chem.*, 2002, **41**, 3055–3066.
- 125 K. M. C. Wong and V. W. W. Yam, *Coord. Chem. Rev.*, 2007, **251**, 2477–2488.
- 126 F. K. W. Kong, M. C. Tang, Y. C. Wong, M. Y. Chan and V. W. W. Yam, *J. Am. Chem. Soc.*, 2016, **138**, 6281–6291.
- 127 H. L. Au-Yeung, A. Y. Y. Tam, S. Y. L. Leung and V. W. W. Yam, *Chem. Sci.*, 2017, **8**, 2267–2276.
- 128 C. Po, A. Y.-Y. Tam and V. W.-W. Yam, *Chem. Sci.*, 2014, **5**, 2688–2695.
- 129 A. Y. Y. Tam, W. H. Lam, K. M. C. Wong, N. Zhu and V. W. W. Yam, *Chem. - A Eur. J.*, 2008, **14**, 4562–4576.
- 130 W. A. Tarran, G. R. Freeman, L. Murphy, A. M. Benham, R. Katakay and J. A. G. Williams, *Inorg. Chem.*, 2014, **53**, 5738–5749.
- 131 S. J. Farley, D. L. Rochester, A. L. Thompson, J. A. K. Howard and J. A. G. Williams, *Inorg. Chem.*, 2005, **44**, 9690–9703.
- 132 J. A. G. Williams, A. Beeby, E. S. Davies, J. A. Weinstein and C. Wilson, *Inorg. Chem.*, 2003, **42**, 8609–8611.
- 133 J. Moussa, T. Cheminel, G. R. Freeman, L. M. Chamoreau, J. A. G. Williams and H. Amouri, *Dalt. Trans.*, 2014, **43**, 8162–8165.
- 134 A. Rodrigue-Witchel, D. L. Rochester, S. Bin Zhao, K. B. Lavelle, J. A. G. Williams, S. Wang, W. B. Connick and C. Reber, *Polyhedron*, 2016, **108**, 151–155.
- 135 D. L. Ma and C. M. Che, *Chem. Eur. J.*, 2003, **9**, 6133–6144.
- 136 S.-W. Lai, M. C.-W. Chan, T.-C. Cheung, S.-M. Peng and C.-M. Che, *Inorg. Chem.*, 1999, **38**, 4046–4055.
- 137 C. K. Koo, K. L. Wong, C. W. Y. Man, H. L. Tam, S. W. Tsao, K. W. Cheah and M. H. W. Lam, *Inorg. Chem.*, 2009, **48**, 7501–7503.
- 138 C. K. Koo, Y. M. Ho, C. F. Chow, M. H. W. Lam, T. C. Lau and W. Y. Wong, *Inorg. Chem.*, 2007, **46**, 3603–3612.

- 139 G. W. V. Cave and C. L. Raston, *J. Chem. Soc. Perkin Trans. 1*, 2001, **24**, 3258–3264.
- 140 G. W. V. Cave, N. W. Alcock and J. P. Rourke, *Organometallics*, 1999, **18**, 1801–1803.
- 141 G. W. V. Cave, F. P. Fanizzi, R. J. Deeth, W. Errington and J. P. Rourke, *Organometallics*, 2000, **19**, 1355–1364.
- 142 S. C. F. Kui, S. S. Y. Chui, C. M. Che and N. Zhu, *J. Am. Chem. Soc.*, 2006, **128**, 8297–8309.
- 143 W. Lu, M. W. C. Chan, K. Cheung and C. Che, *Organometallics*, 2001, 2477–2486.
- 144 M. Krause, D. Kourkoulos, D. González-Abradelo, K. Meerholz, C. A. Strassert and A. Klein, *Eur. J. Inorg. Chem.*, , DOI:10.1002/ejic.201700792.
- 145 S. Fuertes, S. K. Brayshaw, P. R. Raithby, S. Schiffers and M. R. Warren, *Organometallics*, 2012, **31**, 105–119.
- 146 J. L. L. Tsai, T. Zou, J. Liu, T. Chen, A. O. Y. Chan, C. Yang, C. N. Lok and C. M. Che, *Chem. Sci.*, 2015, **6**, 3823–3830.
- 147 N. K. Allampally, C. A. Strassert and L. De Cola, *Dalt. Trans.*, 2012, **41**, 13132–13137.
- 148 P. Wu, E. L. M. Wong, D. L. Ma, G. S. M. Tong, K. M. Ng and C. M. Che, *Chem. Eur. J.*, 2009, **15**, 3652–3656.
- 149 A. Y. Y. Tam, K. M. C. Wong, N. Zhu, G. Wang and V. W. W. Yam, *Langmuir*, 2009, **25**, 8685–8695.
- 150 W. Lu, M. C. W. Chan, K. K. Cheung and C. M. Che, *Organometallics*, 2001, **20**, 2477–2486.
- 151 J. R. Berenguer, E. Lalinde and J. Torroba, *Inorg. Chem.*, 2007, **46**, 9919–9930.
- 152 R. Soldati, A. Aliprandi, M. Mauro, L. De Cola and D. Giacomini, *Eur. J. Org. Chem.*, 2014, **2014**, 7113–7121.
- 153 L. D. Lavis, *ACS Chem. Biol.*, 2008, **3**, 203–206.
- 154 M. Scherer, C. Kappel, N. Mohr, K. Fischer, P. Heller, R. Forst, F. Depoix, M. Bros and R. Zentel, *Biomacromolecules*, 2016, **17**, 3305–3317.

- 155 E. Baggaley, S. W. Botchway, J. W. Haycock, H. Morris, I. V. Sazanovich, J. A. G. Williams and J. A. Weinstein, *Chem. Sci.*, 2014, **5**, 879–886.
- 156 C. K. Koo, K. L. Wong, C. W. Y. Man, Y. W. Lam, L. K. Y. So, H. L. Tam, S. W. Tsao, K. W. Cheah, K. C. Lau, Y. Y. Yang, J. C. Chen and M. H. W. Lam, *Inorg. Chem.*, 2009, **48**, 872–878.
- 157 C. K. Koo, L. K. Y. So, K. L. Wong, Y. M. Ho, Y. W. Lam, M. H. W. Lam, K. W. Cheah, C. C. W. Cheng and W. M. Kwok, *Chem. Eur. J.*, 2010, **16**, 3942–3950.
- 158 V. Fiorini, I. Zanoni, S. Zacchini, A. L. Costa, A. Hochkoeppler, V. Zanotti, A. M. Ranieri, M. Massi, A. Stefan and S. Stagni, *Dalton Trans.*, 2017, **46**, 12328–12338.
- 159 E. L. Robb, J. M. Gawel, D. Aksentijević, H. M. Cochemé, T. S. Stewart, M. M. Shchepinova, H. Qiang, T. A. Prime, T. P. Bright, A. M. James, M. J. Shattock, H. M. Senn, R. C. Hartley and M. P. Murphy, *Free Radic. Biol. Med.*, 2015, **89**, 883–894.
- 160 S. Li, G. Ji, Y. Shi, L. H. Klausen, T. Niu, S. Wang, X. Huang, W. Ding, X. Zhang, M. Dong, W. Xu and F. Sun, *J. Struct. Biol.*, 2018, **201**, 63–75.
- 161 P. Schellenberger, R. Kaufmann, C. A. Siebert, C. Hagen, H. Wodrich and K. Grünewald, *Ultramicroscopy*, 2014, **143**, 41–51.
- 162 S. Halary, S. Duperron and T. Boudier, *Appl. Environ. Microbiol.*, 2011, **77**, 4172–4179.
- 163 J. M. Plitzko, A. Rigort and A. Leis, *Curr. Opin. Biotechnol.*, 2009, **20**, 83–89.
- 164 T. Ando, S. P. Bhamidimarri and N. Brending, *J. Phys. D: Appl. Phys.*, 2018, **51**, 1–42.
- 165 J. Caplan, M. Niethammer, R. M. Taylor and K. J. Czymmek, *Curr. Opin. Struct. Biol.*, 2011, **21**, 686–693.
- 166 K. Cortese, A. Diaspro and C. Tacchetti, *J. Histochem. Cytochem.*, 2009, **57**, 1103–1112.
- 167 E. Brown, J. Mantell, D. Carter, G. Tilly and P. Verkade, *Semin. Cell Dev. Biol.*, 2009, **20**, 910–919.
- 168 E. Brown and P. Verkade, *Protoplasma*, 2010, **244**, 91–97.
- 169 P. Z. T. Randall, Jr. Schirra, *Curr Protoc Cytom*, 2014, **70**, 1–10.

- 170 T. Takizawa and J. M. Robinson, *J. Histochem. Cytochem.*, 2000, **48**, 481–485.
- 171 J. M. Robinson and D. D. Vandr , *J. Histochem. Cytochem.*, 1997, **45**, 631–642.
- 172 M. J. Dukes, D. B. Peckys and N. De Jonge, *ACS Nano*, 2010, **4**, 4110–4116.
- 173 F. F. Marshall, X. Gao, S. Nie, J. W. Simons, J. A. Petros and L. Yang, *Curr. Opin. Biotechnol.*, 2004, **16**, 63–72.
- 174 B. N. G. Giepmans, T. J. Deerinck, B. L. Smarr, Y. Z. Jones and M. H. Ellisman, *Nat. Methods*, 2005, **2**, 743–749.
- 175 R. Nisman, D. P. Bazett-Jones, R. Li, G. Dellaire and Y. Ren, *J. Histochem. Cytochem.*, 2011, **52**, 13–18.
- 176 S. K. Saka, A. Vogts, K. Kr hnert, F. Hillion, S. O. Rizzoli and J. T. Wessels, *Nat. Commun.*, 2014, **5**, 3664.
- 177 C. H schen, F. Opazo, S. O. Rizzoli, U. Diederichsen, I. C. Vreja, K. Kr hnert, S. Kabatas and S. K. Saka, *Angew. Chem. Int. Ed.*, 2015, **54**, 5784–5788.
- 178 P. Ag i-Gonzalez, F. Opazo, K.-A. Saal, S. J hne, S. Kabatas, N. T. N. Phan and S. O. Rizzoli, *Angew. Chem. Int. Ed.*, 2019, **58**, 1–7.
- 179 L. E. Wedlock, M. R. Kilburn, J. B. Cliff, L. Filgueira, M. Saunders and S. J. Berners-Price, *Metallomics*, 2011, **3**, 917–925.
- 180 M. T. Proetto, C. E. Callmann, J. Cliff, C. J. Szymanski, D. Hu, S. B. Howell, J. E. Evans, G. Orr and N. C. Gianneschi, *ACS Cent. Sci.*, 2018, **4**, 1477–1484.
- 181 B. K. Keppler, M. Galanski, A. A. Legin, I. Lichtscheidl, A. Schintlmeister, M. Wagner and M. A. Jakupec, *Chem. Sci.*, 2014, **5**, 3135.
- 182 K. Ritchie, Y. Lill, C. Sood, H. Lee and S. Zhang, *Philos. Trans. R. Soc. B Biol. Sci.*, 2013, **368**, 1–8.
- 183 L. Li, Y. Li, T. M. Lim and S. Q. Pan, *FEMS Microbiol. Lett.*, 1999, **179**, 141–146.
- 184 C. Reimold, H. J. Defeu Soufo, F. Dempwolff and P. L. Graumann, *Mol. Biol. Cell*, 2013, **24**, 2340–2349.

- 185 P. Stiefel, S. Schmidt-Emrich, K. Maniura-Weber and Q. Ren, *BMC Microbiol.*, 2015, **15**, 1–9.
- 186 C. Zhang, L. Yang, Y. Ding, Y. Wang, L. Lan, Q. Ma, X. Chi, P. Wei, Y. Zhao, A. Steinbüchel, H. Zhang and P. Liu, *Nat. Commun.*, 2017, **8:15979**, 1-15.
- 187 D. M. Doughty, M. Dieterle, A. L. Sessions, W. W. Fischer and D. K. Newman, *PLOS One*, 2014, **9**, 1-8.
- 188 N. Musat, R. Foster, T. Vagner, B. Adam and M. M. M. Kuypers, *FEMS Microbiol. Rev.*, 2012, **36**, 486–511.
- 189 S. E. McGlynn, G. L. Chadwick, C. P. Kempes and V. J. Orphan, *Nature*, 2015, **526**, 531–535.
- 190 V. J. O. Silvan Scheller, Hang Yu, Grayson L. Chadwick, Shawn E. McGlynn, *Science*, 2016, **351**, 703–707.
- 191 K. G. Leslie, D. Jacquemin, E. J. New and K. A. Jolliffe, *Chem. Eur. J.*, 2018, **24**, 5569–5573.
- 192 K. Yang, K. G. Leslie, S. Y. Kim, B. Kalionis, W. Chrzanowski, K. A. Jolliffe and E. J. New, *Org. Biomol. Chem.*, 2018, **16**, 619–624.
- 193 M. Krause, D. Kourkoulos, D. González-Abradelo, K. Meerholz, C. A. Strassert and A. Klein, *Eur. J. Inorg. Chem.*, 2017, 5215–5223.
- 194 S. Banerjee, J. A. Kitchen, S. A. Bright, J. E. O’Brien, D. C. Williams, J. M. Kelly and T. Gunnlaugsson, *Chem. Commun.*, 2013, **49**, 8522–8524.
- 195 E. Langdon-Jones, C. Williams, A. Hayes, D. Lloyd, S. Coles, P. Horton, L. Groves and S. J. Pope, *Eur. J. Inorg. Chem.*, 2017, 5279–5287.
- 196 H. Guo, M. L. Muro-Small, S. Ji, J. Zhao and F. N. Castellano, *Inorg. Chem.*, 2010, **49**, 6802–6804.
- 197 F. Zhong and J. Zhao, *Eur. J. Inorg. Chem.*, 2017, 5196–5204.
- 198 R. M. Duke, E. B. Veale, F. M. Pfeffer, P. E. Kruger and T. Gunnlaugsson, *Chem. Soc. Rev.*, 2010, **39**, 3936–3953.

- 199 D. Jacquemin, B. Moore, C. Adamo and J. Autschbach, *J. Chem. Theory Comput.*, 2014, **10**, 1677-1685.
- 200 D. Jacquemin, A. Planchat, C. Adamo and B. Mennucci, *J. Chem. Theory Comput.*, 2012, **8**, 2359–2372.
- 201 J. F. Zhang, S. Kim, J. H. Han, S. J. Lee, T. Pradhan, Q. Y. Cao, S. J. Lee, C. Kang and J. S. Kim, *Org. Lett.*, 2011, **13**, 5294–5297.
- 202 M. H. Lee, J. H. Han, P. S. Kwon, S. Bhuniya, J. Y. Kim, J. L. Sessler, C. Kang and J. S. Kim, *J. Am. Chem. Soc.*, 2012, **134**, 1316–1322.
- 203 J. Wang and X. Qian, *Chem. Commun.*, 2006, **1**, 109–111.
- 204 Z. Xu, Y. Xiao, X. Qian, J. Cui and D. Cui, *Org. Lett.*, 2005, **7**, 889–892.
- 205 P. A. Panchenko, Y. V. Fedorov, V. P. Perevalov, G. Jonusauskas and O. A. Fedorova, *J. Phys. Chem. A*, 2010, **114**, 4118–4122.
- 206 R. K. Jackson, Y. Shi, X. Yao and S. C. Burdette, *Dalt. Trans.*, 2010, **39**, 4155–4161.
- 207 I. Ott, Y. Xu, J. Liu, M. Kokoschka, M. Harlos, W. S. Sheldrick and X. Qian, *Bioorganic Med. Chem.*, 2008, **16**, 7107–7116.
- 208 S. Banerjee, E. B. Veale, C. M. Phelan, S. A. Murphy, G. M. Tocci, L. J. Gillespie, D. O. Frimannsson, J. M. Kelly and T. Gunnlaugsson, *Chem. Soc. Rev.*, 2013, **42**, 1601–1618.
- 209 J. M. Pérez, I. López-Solera, E. I. Montero, M. F. Braña, C. Alonso, S. P. Robinson and C. Navarro-Ranninger, *J. Med. Chem.*, 1999, **42**, 5482–5486.
- 210 G. J. Ryan, S. Quinn and T. Gunnlaugsson, *Inorg. Chem.*, 2008, **47**, 401–403.
- 211 R. B. P. Elmes, M. Erby, S. A. Bright, D. C. Williams and T. Gunnlaugsson, *Chem. Commun.*, 2012, **48**, 2588–2590.
- 212 P. Chandrangsu, C. Rensing and J. D. Helmann, *Nat. Rev. Microbiol.*, 2017, **15**, 338–350.
- 213 I. V Rathnayake, M. Megharaj, G. S. Krishnamurti, N. S. Bolan and R. Naidu, *Chemosphere*, 2013, **90**, 1195–1200.

- 214 R. M. Sterritt and J. N. Lester, *Sci. Total Environ.*, 1980, **14**, 5–17.
- 215 L. D. Palmer and E. P. Skaar, *Annu. Rev. Genet.*, 2016, **50**, 67–91.
- 216 I. Maslov, A. Bogorodskiy, A. Mishin, I. Okhrimenko, I. Gushchin, S. Kalenov, N. A. Dencher, C. Fahlke, G. Büldt, V. Gordeliy, T. Gensch and V. Borshevskiy, *Sci. Rep.*, 2018, **8**, 1–12.
- 217 J. L. Cocchiario, Y. Kumar, E. R. Fischer, T. Hackstadt and R. H. Valdivia, *Proc. Natl. Acad. Sci.*, 2008, **105**, 9379–9384.
- 218 Y. Kumar, J. Cocchiario and R. H. Valdivia, *Curr. Biol.*, 2006, **16**, 1646–1651.
- 219 A. B. F. Barletta, L. R. Alves, M. C. L. Nascimento Silva, S. Sim, G. Dimopoulos, S. Liechocki, C. M. Maya-Monteiro and M. H. F. Sorgine, *Sci. Rep.*, 2016, **6**, 1–13.
- 220 A. Sukan, I. Roy and T. Keshavarz, *Carbohydr. Polym.*, 2015, **126**, 47–51.
- 221 C. He, L. G. Fong, S. G. Young and H. Jiang, *J. Investig. Med.*, 2017, **65**, 669–672.
- 222 G. A. Crosby and J. N. Demas, *J. Phys. Chem.*, 1971, **75**, 991–1024.
- 223 K. Nakamaru, *Bull. Chem. Soc. JPN*, 1982, **55**, 2697–2705.
- 224 M. J. Frisch, 2016, Wallingford, USA.
- 225 Zhao, Y. and D. G. Truhlar, *Theor Chem Acc.*, 2008, **120**, 215–241.
- 226 D. Jacquemin, E. A. Perpète, I. Ciofini, C. Adamo, R. Valero, Y. Zhao and D. G. Truhlar, *J. Chem. Theory Comput.*, 2010, **6**, 2071–2085.
- 227 J. Tomasi, B. Mennucci and R. Cammi, *Chem. Rev.*, 2005, **105**, 2999–3094.
- 228 R. Cammi and B. Mennucci, *J. Chem. Phys.*, 1999, **110**, 9877–9886.
- 229 M. Caricato, B. Mennucci, J. Tomasi, F. Ingrosso, R. Cammi, S. Corni and G. Scalmani, *J. Chem. Phys.*, 2006, **124**, 1-13.
- 230 C. Cebrián, M. Mauro, D. Kourkoulos, P. Mercandelli, D. Hertel, K. Meerholz, C. A. Strassert and L. De Cola, *Adv. Mater.*, 2013, **25**, 437–442.
- 231 J. J. Zhong, Q. Y. Meng, G. X. Wang, Q. Liu, B. Chen, K. Feng, C. H. Tung and L. Z. Wu, *Chem. Eur. J.*, 2013, **19**, 6443–6450.

- 232 J. E. McGarrah, Y. J. Kim, M. Hissler and R. Eisenberg, *Inorg. Chem.*, 2001, **40**, 4510–4511.
- 233 D. Zhang, L. Z. Wu, L. Zhou, X. Han, Q. Z. Yang, L. P. Zhang and C. H. Tung, *J. Am. Chem. Soc.*, 2004, **126**, 3440–3441.
- 234 P. Du, J. Schneider, P. Jarosz and R. Eisenberg, *J. Am. Chem. Soc.*, 2006, **128**, 7726–7727.
- 235 C. Po, A. Y. Y. Tam, K. M. C. Wong and V. W. W. Yam, *J. Am. Chem. Soc.*, 2011, **133**, 12136–12143.
- 236 J. J. Zhong, C. Yang, X. Y. Chang, C. Zou, W. Lu and C. M. Che, *Chem. Commun.*, 2017, **53**, 8948–8951.
- 237 P. Ye, D. H. Wang, B. Chen, Q. Y. Meng, C. H. Tung and L. Z. Wu, *Sci. China Chem.*, 2016, **59**, 175–179.
- 238 A. Casado-Sánchez, R. Gómez-Ballesteros, F. Tato, F. J. Soriano, G. Pascual-Coca, S. Cabrera and J. Alemán, *Chem. Commun.*, 2016, **52**, 9137–9140.
- 239 P. K. Chow, G. Cheng, G. S. M. T. Ong, W. P. To, W. L. Kwong, C. C. Kowk, C. Ma and C. M. Che, *Angew. Chem. Int. Ed.*, 2015, **54**, 2084–2089.
- 240 C. K. Prier, D. A. Rankic and D. W. C. MacMillan, *Chem. Rev.*, 2013, **113**, 5322–5363.
- 241 N. A. Romero and D. A. Nicewicz, *Chem. Rev.*, 2016, **116**, 10075–10166.
- 242 K. L. Skubi, T. R. Blum and T. P. Yoon, *Chem. Rev.*, 2016, **116**, 10035–10074.
- 243 S. Stagni, A. Palazzi, P. Brulatti, M. Salmi, S. Muzzioli, S. Zacchini, M. Marcaccio and F. Paolucci, *Eur. J. Inorg. Chem.*, 2010, 4643–4657.
- 244 V. Fiorini, A. M. Ranieri, S. Muzzioli, K. D. M. Magee, S. Zacchini, N. Akabar, A. Stefan, M. I. Ogden, M. Massi and S. Stagni, *Dalt. Trans.*, 2015, **44**, 20597–20608.
- 245 A. M. Ranieri, L. K. Burt, S. Stagni, S. Zacchini, B. W. Skelton, M. I. Ogden, A. C. Bissember and M. Massi, *Organometallics*, 2019, **38**, 1108–1117.
- 246 T. P. Nicholls, D. Leonori and A. C. Bissember, *Nat. Prod. Rep.*, 2016, **33**, 1248–1254.

- 247 Y. Yang, D. Zhang, L. Z. Wu, B. Chen, L. P. Zhang and C. H. Tung, *J. Org. Chem.*, 2004, **69**, 4788–4791.
- 248 P. Ye, D. H. Wang, B. Chen, Q. Y. Meng, C. H. Tung and L. Z. Wu, *Sci. China Chem.*, 2016, **59**, 175–179.
- 249 Y. Z. Chen, D. H. Wang, B. Chen, J. J. Zhong, C. H. Tung and L. Z. Wu, *J. Org. Chem.*, 2012, **77**, 6773–6777.
- 250 D. Zhang, L. Z. Wu, Q. Z. Yang, X. H. Li, L. P. Zhang and C. H. Tung, *Org. Lett.*, 2003, **5**, 3221–3224.
- 251 A. Casado-Sánchez, R. Gómez-Ballesteros, F. Tato, F. J. Soriano, G. Pascual-Coca, S. Cabrera and J. Alemán, *Chem. Commun.*, 2016, **52**, 9137–9140.
- 252 W. J. Choi, S. Choi, K. Ohkubo, S. Fukuzumi, E. J. Cho and Y. You, *Chem. Sci.*, 2015, **6**, 1454–1464.
- 253 K. Li, Q. Wan, C. Yang, X.-Y. Chang, K.-H. Low and C.-M. Che, *Angew. Chem. - Int. Ed.*, 2018, 1–6.
- 254 J. J. Zhong, C. Yang, X. Y. Chang, C. Zou, W. Lu and C. M. Che, *Chem. Commun.*, 2017, **53**, 8948–8951.
- 255 X. Ju, D. Li, W. Li, W. Yu and F. Bian, *Adv. Synth. Catal.*, 2012, **354**, 3561–3567.
- 256 T. P. Nicholls, G. E. Constable, J. C. Robertson, M. G. Gardiner and A. C. Bissember, *ACS Catal.*, 2016, **6**, 451–457.
- 257 L. Ruiz Espelt, E. M. Wiensch and T. P. Yoon, *J. Org. Chem.*, 2013, **78**, 4107–4114.
- 258 J. D. Nguyen, E. M. D’Amato, J. M. R. Narayanam and C. R. J. Stephenson, *Nat. Chem.*, 2012, **4**, 854–859.
- 259 I. Ghosh, T. Ghosh, J. I. Bardagi and B. König, 2014, **346**, 725–728.
- 260 T. P. Nicholls, J. C. Robertson, M. G. Gardiner and A. C. Bissember, *Chem. Commun.*, 2018, **54**, 4589–4592.
- 261 J. D. Nguyen, J. W. Tucker, M. D. Konieczynska and C. R. J. Stephenson, *J. Am. Chem. Soc.*, 2011, **133**, 4160–4163.

- 262 M. Pirtsch, S. Paria, T. Matsuno, H. Isobe and O. Reiser, *Chem. Eur. J.*, 2012, **18**, 7336–7340.
- 263 L. Li, M. Huang, C. Liu, J. C. Xiao, Q. Y. Chen, Y. Guo and Z. G. Zhao, *Org. Lett.*, 2015, **17**, 4714–4717.
- 264 K. Koguro, T. Oga, S. Mitsui and R. Orita, *Synthesis (Stuttg)*, **1998**, 910–914.
- 265 D. P. Bishop, N. Cole, T. Zhang, P. A. Doble and D. J. Hare, *Chem. Soc. Rev.*, 2018, **47**, 3770–3787.
- 266 S. Caine, M. J. Hackett, H. Hou, S. Kumar, J. Maley, Z. Ivanishvili, B. Suen, A. Szmigielski, Z. Jiang, N. J. Sylvain, H. Nichol and M. E. Kelly, *Neurobiol. Dis.*, 2016, **91**, 132–142.
- 267 Z. Liu, W. He and Z. Guo, *Chem. Soc. Rev.*, 2013, **42**, 1568–1600.
- 268 Q. Zhao, C. Huang and F. Li, *Chem. Soc. Rev.*, 2011, **40**, 2508–2524.
- 269 F. L. Thorp-Greenwood, R. G. Balasingham and M. P. Coogan, *J. Organomet. Chem.*, 2012, **714**, 12–21.
- 270 A. M. H. Yip and K. K. W. Lo, *Coord. Chem. Rev.*, 2018, **361**, 138–163.
- 271 G. Ferro-Flores, M. A. Avila-Rodríguez and F. O. García-Pérez, *Clin. Transl. Imaging*, 2016, **4**, 175–182.
- 272 S. Saurabh, A. M. Perez, C. J. Comerci, L. Shapiro and W. E. Moerner, *J. Am. Chem. Soc.*, 2016, **138**, 10398–10401.
- 273 W. Phetsang, M. A. T. Blaskovich, M. S. Butler, J. X. Huang, J. Zuegg, S. K. Mamidyala, S. Ramu, A. M. Kavanagh and M. A. Cooper, *Bioorganic Med. Chem.*, 2014, **22**, 4490–4498.
- 274 L. P. Partida-Martinez and C. Hertweck, *Nature*, 2005, **437**, 884–888.
- 275 S. Schlafer and R. L. Meyer, *J. Microbiol. Methods*, 2017, **138**, 50–59.
- 276 J. R. Lawrence, T. R. Neu and G. D. W. Swerhone, *J. Microbiol. Methods*, 1998, **32**, 253–261.

- 277 P. Bettencourt, D. Pires, N. Carmo and E. Anes, *Microsc. Sci. Technol. Appl. Educ.*, 2010, 614–621.
- 278 W. Jackson, M. Yamada, T. Moninger and C. Grose, *J. Virol. Methods*, 2013, **193**, 244–250.
- 279 E. C. Garner, R. Bernard, W. Wang, X. Zhuang, D. Z. Rudner and T. Mitchison, *Science*, 2011, **333**, 222–225.
- 280 R. Carballido-Lopez and J. Errington, *Dev. Cell*, 2003, **4**, 19–28.
- 281 P. V. Chang and C. R. Bertozzi, *Chem. Commun.*, 2012, **48**, 8864–8879.
- 282 H.-J. van Manen, Y. M. Kraan, D. Roos and C. Otto, *Proc. Natl. Acad. Sci.*, 2005, **102**, 10159–10164.
- 283 2016, 198–209.
- 284 V. Ciobotă, E. M. Burkhardt, W. Schumacher, P. Rösch, K. Küsel and J. Popp, *Anal. Bioanal. Chem.*, 2010, **397**, 2929–2937.
- 285 J. De Gelder, D. Willemse-Erix, M. J. Scholtes, J. I. Sanchez, K. Maquelin, P. Vandenamee, P. De Boever, G. J. Puppels, L. Moens and P. De Vos, *Anal. Chem.*, 2008, **80**, 2155–2160.
- 286 K. L. Summers, N. Fimognari, A. Hollings, M. Kiernan, V. Lam, R. J. Tidy, D. Paterson, M. J. Tobin, R. Takechi, G. N. George, I. J. Pickering, J. C. Mamo, H. H. Harris and M. J. Hackett, *Biochemistry*, 2017, **56**, 4107–4116.
- 287 J. P. Pezacki, J. A. Blake, D. C. Danielson, D. C. Kennedy, R. K. Lyn and R. Singaravelu, *Nat. Chem. Biol.*, 2011, **7**, 137–145.
- 288 H. Strahl, F. Bürmann and L. W. Hamoen, *Nat. Commun.*, 2014, **5**, 1–11.
- 289 P. Tavares, L. Jakutyte, R. Carballido-Lopez, R. Daugelavicius, C. Sao-Jose and C. Baptista, *J. Bacteriol.*, 2011, **193**, 4893–4903.
- 290 C. São-José, S. Lhuillier, R. Lurz, R. Melki, J. Lepault, M. A. Santos and P. Tavares, *J. Biol. Chem.*, 2006, **281**, 11464–11470.
- 291 C. São-José, C. Baptista and M. A. Santos, *J. Bacteriol.*, 2004, **186**, 8337–8346.

- 292 D. B. Johnson and K. B. Hallberg, *Res. Microbiol.*, 2003, **154**, 466–473.
- 293 D. B. Johnson, *J. Microbiol. Methods*, 1995, **23**, 205–218.
- 294 F. J. Ossandon, P. Cárdenas, M. Corbett, R. Quatrini and D. S. Holmes, *Genome Announc.*, 2014, **2**, 5–6.
- 295 C. M. Zammit, S. Mangold, V. Rao Jonna, L. A. Mutch, H. R. Watling, M. Dopson and E. L. J. Watkin, *Appl. Microbiol. Biotechnol.*, 2012, **93**, 319–329.
- 296 J. C. Cox, D. G. Nicholls and W. J. Ingledew, *Biochem. J.*, 1979, **178**, 195–200.
- 297 L. Judson, P. L., Van Le, *Flow Cytometry. Primary Care Update for OB/GYNS*, 1997, **4**, 87–91.
- 298 E. Mulrone, K., Jackman, C., Nelson, D., Watkin, *Honours Thesis, CHRI Biosci. Precinct, Sch. Biomed. Sci. Curtin Univ. Perth, West. Aust.*
- 299 Life Technologies, LIVE/DEAD Bac Light Bacterial Viability and Counting Kit (L34856), 2004.
- 300 G. Cosa, K. S. Focsaneanu, J. R. McLean, J. P. McNamee and J. C. Scaiano, *Photochem. Photobio.*, 2001, **73**, 585.
- 301 L. Shi, H. Harms, S. Müller, T. Hübschmann, S. Günther and L. Y. Wick, *Cytom. Part A*, 2007, **71A**, 592–598.
- 302 V. Fiorini, S. Zacchini, P. Raiteri, R. Mazzoni, V. Zanotti, M. Massi and S. Stagni, *Dalt. Trans.*, 2016, **45**, 12884–12896.
- 303 V. Fiorini, I. Zanoni, S. Zacchini, A. L. Costa, A. Hochkoepler, V. Zanotti, A. M. Ranieri, M. Massi, A. Stefan and S. Stagni, *Dalt. Trans.*, 2017, **46**, 12328–12338.
- 304 G. M. Sheldrick, *Acta Crystallogr. Sect. C Struct. Chem.*, 2015, **71**, 3–8.

Every reasonable effort had been made to acknowledge the owners of the copyright material. I would be pleased to hear from any copyright owner who has been omitted or incorrectly acknowledge.

Appendix A

Table A.1 Crystal data and structure refinement for [Pt(CNC)(μ -Cl)]₂.

Empirical formula	C₄₆H₃₂Cl₂N₂Pt₂
Formula weight	1073.81
Temperature/ K	295(2)
Wavelength/ Å	1.54184
Crystal system	Orthorhombic
Space group	<i>Pbcn</i>
Unit cell dimensions/ Å	<i>a</i> = 20.8521(4) <i>b</i> = 7.4582(2) <i>c</i> = 24.0550(5)
Volume/ Å³	3741.01(15)
Z	4
Calculated density/ Mg/m³	1.907
μ/ mm⁻¹	15.374
Crystal size /mm	0.120 x 0.103 x 0.068
θ range for data collection	3.675 to 67.22°.
Index ranges	-24 ≤ <i>h</i> ≤ 23, -8 ≤ <i>k</i> ≤ 8, -28 ≤ <i>l</i> ≤ 21
Reflections collected	9792
Independent reflections	3326 [<i>R</i> (int) = 0.0330]
Completeness to $\theta = 67.22^\circ$	99.2 %
Absorption correction	Analytical
Max. and min. transmission	0.458 and 0.262
Refinement method	Full-matrix least-squares on <i>F</i> ²
Data / restraints / parameters	3326 / 0 / 235
Goodness-of-fit on <i>F</i>²	1.188
Final <i>R</i> indices [<i>I</i> > 2σ(<i>I</i>)]	<i>R</i> 1 = 0.0552, <i>wR</i> 2 = 0.1275
<i>R</i> indices (all data)	<i>R</i> 1 = 0.0730, <i>wR</i> 2 = 0.1372
Largest diff. peak and hole/ e.Å⁻³	1.375 and -0.602
CCDC no.	1551633

Table A.2 Selected bond lengths [\AA] and angles [$^\circ$] for $[\text{Pt}(\text{CNC})(\mu\text{-Cl})_2]$.

Pt(1)-C(21)	1.986(9)	C(21)-Pt(1)-N(1)	81.1(3)
Pt(1)-N(1)	2.057(6)	C(21)-Pt(1)-Cl(1)	94.7(3)
Pt(1)-Cl(1)	2.303(2)	N(1)-Pt(1)-Cl(1)	175.2(2)
Pt(1)-Cl(1) ¹	2.466(3)	C(21)-Pt(1)-Cl(1) ¹	172.2(3)
		N(1)-Pt(1)-Cl(1) ¹	103.08(19)
		Cl(1)-Pt(1)-Cl(1) ¹	80.92(9)
		Pt(1)-Cl(1)-Pt(1) ¹	99.08(9)

The data for the structure were collected at 295(2) K on an Oxford Diffraction Gemini diffractometer using Cu- $K\alpha$ radiation. Following analytical absorption corrections and solution by direct methods, the structure was refined against F^2 with full-matrix least-squares using the program SHELXL-2014.³⁰⁴ All hydrogen atoms were added at calculated positions and refined by use of riding models with isotropic displacement parameters based on those of the parent atoms. Anisotropic displacement parameters were employed throughout for the non-hydrogen atoms. The molecule lies on a crystallographic inversion centre.

Table A.3 Crystal data and structure refinement for [Pt(CNC)(DMSO)].

Empirical formula	C₂₆H₂₃Cl₂NOPtS
Formula weight	663.50
Temperature/ K	293
Wavelength/ Å	0.71073
Crystal system	Triclinic
Space group	<i>P</i> 1
Unit cell dimensions/ Å, deg	<i>a</i> = 11.1705(5) α = 87.379(3) <i>b</i> = 14.5717(6) β = 83.506(3) <i>c</i> = 15.9969(7) γ = 83.578(3)
Volume/ Å³	2569.48(19)
Z	4
Calculated density/ Mg/m³	1.715
μ/ mm⁻¹	5.768
Crystal size/ mm	0.150 x 0.110 x 0.090
θ range for data collection (deg)	1.407 to 25.023
Index ranges	-13 ≤ <i>h</i> ≤ 13 -17 ≤ <i>k</i> ≤ 17 -19 ≤ <i>l</i> ≤ 19
Reflections collected	36804
Independent reflections	9061 [<i>R</i> (int) = 0.1084]
Absorption correction	Empirical
Max./min. transmission	0.7455/ 0.4269
Refinement method	Full-matrix least-squares on <i>F</i> ²
Data / restraints / parameters	9061 / 354/ 560
Goodness-of-fit on <i>F</i>²	1.018
Final <i>R</i> indices [<i>I</i> > 2σ(<i>I</i>)]	<i>R</i> 1 = 0.0551, <i>wR</i> 2 = 0.1486
<i>R</i> indices (all data)	<i>R</i> 1 = 0.1030, <i>wR</i> 2 = 0.1712
Largest diff. peak and hole/ e.Å⁻³	1.922 and -1.478
CCDC No.	1551634

Table A.4 Selected bond lengths [Å] and angles [°] for [Pt(CNC)(DMSO)].

Pt(1)-N(1)	2.018(9)	N(1)-Pt(1)-C(1)	80.8(4)
Pt(1)-C(1)	2.074(12)	N(1)-Pt(1)-C(17)	80.8(4)
Pt(1)-C(17)	2.135(17)	C(1)-Pt(1)-C(17)	161.5(5)
Pt(1)-S(1)	2.195(3)	N(1)-Pt(1)-S(1)	175.4(3)
Pt(2)-N(2)	1.993(9)	C(1)-Pt(1)-S(1)	99.3(3)
Pt(2)-C(101)	2.112(13)	N(2)-Pt(2)-C(101)	80.9(4)
Pt(2)-C(117)	2.043(13)	N(2)-Pt(2)-C(117)	80.3(5)
Pt(2)-S(2)	2.192(3)	C(101)-Pt(2)- C(117)	161.2(5)
		N(2)-Pt(2)-S(2)	174.8(3)
		C(101)-Pt(2)-S(2)	100.4(3)

Symmetry transformations used to generate equivalent atoms: ¹ 1-x,1-y,1-z.

The data were collected at 293(2) K on a Bruker APEX II diffractometer equipped with a CCD detector using Mo-K α radiation. The data were corrected for Lorentz polarization and absorption effects (empirical absorption correction SADABS).³⁰⁴ The structure was solved by direct methods and refined by full-matrix least-squares based on all data using F^2 . All hydrogen atoms were added at calculated positions and refined by use of riding models with isotropic displacement parameters based on those of the parent atoms. Anisotropic displacement parameters were employed throughout for the non-hydrogen atoms.

Table A.5 Crystal data and structure refinement for [Pt(CNC)(Py-H)].

Empirical formula	C₂₈H₂₀N₂Pt
Formula weight	579.55
Temperature/ K	100
Wavelength/ Å	0.71073
Crystal system	Hexagonal
Space group	<i>P</i> 6 ₂
Unit cell dimensions/ Å	<i>a</i> = 10.01370(10) <i>b</i> = 10.01370(10) <i>c</i> = 17.9391(2)
Volume/ Å³	1557.83(4)
Z	3
Calculated density/ Mg/m³	1.853
Abs. coefficient/ mm⁻¹	6.774
Crystal size/ mm	0.632 x 0.362 x 0.266
θ range for data collection (deg)	3.268 to 31.00
Index ranges	-14 ≤ <i>h</i> ≤ 14 -14 ≤ <i>k</i> ≤ 14 -25 ≤ <i>l</i> ≤ 25
Reflections collected	37779
Independent reflections	3324 [<i>R</i> (int) = 0.0375]
Absorption correction	Analytical
Max. and min. transmission	0.329 and 0.107
Refinement method	Full-matrix least-squares on <i>F</i> ²
Data / restraints / parameters	3324 / 1 / 144
Goodness-of-fit on <i>F</i>²	1.157
Final <i>R</i> indices [<i>I</i> > 2σ(<i>I</i>)]	<i>R</i> 1 = 0.0162, <i>wR</i> 2 = 0.0400
<i>R</i> indices (all data)	<i>R</i> 1 = 0.0168, <i>wR</i> 2 = 0.0402
Largest diff. peak and hole/ e.Å⁻³	0.940 and -0.463

Table A.6 Selected bond lengths [Å] and angles [°] for [Pt(CNC)(Py-H)].

Pt(1)-N(1)	1.963(11)
Pt(1)-N(11)	2.015(10)
Pt(1)-C(21)	2.060(4)
N(1)-Pt(1)-C(21)	81.34(10)
N(11)-Pt(1)-C(21)	98.66(10)
C(21)-Pt(1)-C(21) ¹	162.68(19)
C(2) ¹ -N(1)-C(2)	122.3(9)
C(2)-N(1)-Pt(1)	118.9(4)

Symmetry transformations used to generate equivalent atoms: ¹1-x,-y,z

Crystallographic data for the structure were collected at 100(2) K on an Oxford Diffraction Xcalibur diffractometer fitted with Mo K α radiation. Following analytical absorption corrections and solution by direct methods, the structure was refined against F^2 with full-matrix least-squares using the program SHELXL-2014. All hydrogen atoms were added at calculated positions and refined by use of riding models with isotropic displacement parameters based on those of the parent atoms. Anisotropic displacement parameters were employed throughout for the non-hydrogen atoms. The molecule is situated on a crystallographic 2-fold axis.

Table A.7 Crystal data and structure refinement for [Pt(CNC)(Py-CO₂Me)].

Empirical formula	C₃₀H₂₂N₂O₂Pt
Formula weight	637.58
Temperature/ K	100
Wavelength/ Å	0.71073
Crystal system	Monoclinic
Space group	<i>P</i> 2 ₁ / <i>c</i>
Unit cell dimensions/ Å	<i>a</i> = 14.0693(5) <i>b</i> = 9.6768(4) <i>c</i> = 17.4961(7)
Volume/ Å³	2245.92(16)
Z	4
Calculated density/ Mg/m³	1.886
Abs. coefficient/ mm⁻¹	6.280
Crystal size/ mm	0.816 x 0.235 x 0.066
θ range for data collection (deg)	2.435 to 29.00
Index ranges	-19 ≤ <i>h</i> ≤ 18 -13 ≤ <i>k</i> ≤ 13 -21 ≤ <i>l</i> ≤ 23
Reflections collected	21331
Independent reflections	5964 [<i>R</i> (int) = 0.0316]
Absorption correction	Analytical
Max. and min. transmission	0.678 and 0.121
Refinement method	Full-matrix least-squares on <i>F</i> ²
Data / restraints / parameters	5964 / 0 / 317
Goodness-of-fit on <i>F</i>²	1.069
Final <i>R</i> indices [<i>I</i> > 2σ(<i>I</i>)]	<i>R</i> 1 = 0.0233, <i>wR</i> 2 = 0.0541
<i>R</i> indices (all data)	<i>R</i> 1 = 0.0291, <i>wR</i> 2 = 0.0568
Largest diff. peak and hole/ e.Å⁻³	2.442 and -0.696

Table A.8 Selected bond lengths [Å] and angles [°] for [Pt(CNC)(Py-CO₂Me)].

Pt(1)-N(1)	1.955(3)
Pt(1)-N(11)	2.013(3)
Pt(1)-C(61)	2.059(3)
Pt(1)-C(21)	2.064(3)
N(1)-Pt(1)-N(11)	177.76(9)
N(1)-Pt(1)-C(61)	81.32(11)
N(11)-Pt(1)-C(61)	97.44(11)
N(1)-Pt(1)-C(21)	81.17(11)
N(11)-Pt(1)-C(21)	99.96(11)
C(61)-Pt(1)-C(21)	162.23(12)

Crystallographic data for the structure were collected at 100(2) K on an Oxford Diffraction Xcalibur diffractometer fitted with Mo K α radiation. Following analytical absorption corrections and solution by direct methods, the structure was refined against F₂ with full-matrix least-squares using the program SHELXL-2014.2 All hydrogen atoms were added at calculated positions and refined by use of riding models with isotropic displacement parameters based on those of the parent atoms. Anisotropic displacement parameters were employed throughout for the non-hydrogen atoms.

Table A.9 Crystal data and structure refinement for [Pt(CNC)(Py-Ph)].

Empirical formula	C_{34.50}H₂₅ClN₂Pt
Formula weight	698.10
Temperature/ K	100
Wavelength/ Å	0.71073
Crystal system	Monoclinic
Space group	<i>P</i> 2 ₁ / <i>c</i>
Unit cell dimensions/ Å	<i>a</i> = 16.1601(3) <i>b</i> = 11.96420(10) <i>c</i> = 14.8487(2)
Volume/ Å³	2588.97(7)
Z	4
Calculated density/ Mg/m³	1.791
Abs. coefficient/ mm⁻¹	5.551
Crystal size/ mm	0.633 x 0.135 x 0.058
θ range for data collection (deg)	2.308 to 34.993
Index ranges	-24 ≤ <i>h</i> ≤ 25 -9 ≤ <i>k</i> ≤ 19 -23 ≤ <i>l</i> ≤ 22
Reflections collected	41550
Independent reflections	10783 [<i>R</i> (int) = 0.0419]
Absorption correction	Analytical
Max. and min. transmission	0.741 and 0.241
Refinement method	Full-matrix least-squares on <i>F</i> ²
Data / restraints / parameters	10783 / 0 / 361
Goodness-of-fit on <i>F</i>²	1.061
Final <i>R</i> indices [<i>I</i> > 2σ(<i>I</i>)]	<i>R</i> 1 = 0.0272, <i>wR</i> 2 = 0.0512
<i>R</i> indices (all data)	<i>R</i> 1 = 0.0381, <i>wR</i> 2 = 0.0548
Largest diff. peak and hole/ e.Å⁻³	1.784 and -1.531

Table A.10 Selected bond lengths [Å] and angles [°] for [Pt(CNC)(Py-Ph)].

Pt(1)-N(1)	1.9688(18)
Pt(1)-N(11)	2.0291(19)
Pt(1)-C(61)	2.059(2)
Pt(1)-C(21)	2.061(2)
N(1)-Pt(1)-N(11)	178.61(7)
N(1)-Pt(1)-C(61)	81.14(8)
N(11)-Pt(1)-C(61)	98.57(8)
N(1)-Pt(1)-C(21)	81.03(8)
N(11)-Pt(1)-C(21)	99.27(8)
C(61)-Pt(1)-C(21)	162.17(9)

Crystallographic data for the structure were collected at 100(2) K on an Oxford Diffraction Gemini diffractometer using Mo K α radiation. Following analytical absorption corrections and solution by direct methods, the structure was refined against F^2 with full-matrix least-squares using the program SHELXL-2014.² The dichloromethane solvent molecule was modelled as being disordered about a crystallographic inversion centre. All hydrogen atoms were added at calculated positions and refined by use of riding models with isotropic displacement parameters based on those of the parent atoms. Anisotropic displacement parameters were employed throughout for the non-hydrogen atoms. The central pyridine ring and the two pendant phenyl rings 2n and 6n are essentially coplanar the dihedral angles being 2.74(8) and 3.00(8)° between the py ring and the two pendant rings with the dihedral angle between the two pendant rings being 0.74(8)°. The dihedral angle between the plane of the phenyl ring 4n and that of the coordination plane 31.04(8)°. The dihedral angle between the py ring 1n and the coordination plane is 55.00(8)°.

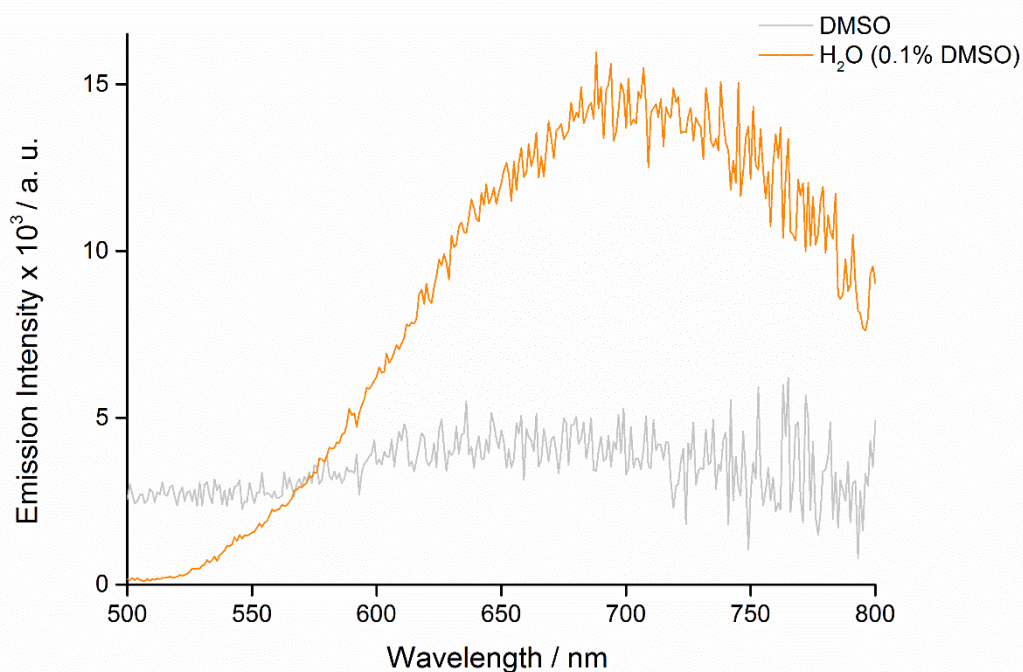


Figure A.1 Emission profiles of [Pt(CNC)(Py-H)] from a diluted (10^{-5} M) DMSO (grey trace) and H₂O (0.1% DMSO, orange trace) solution.

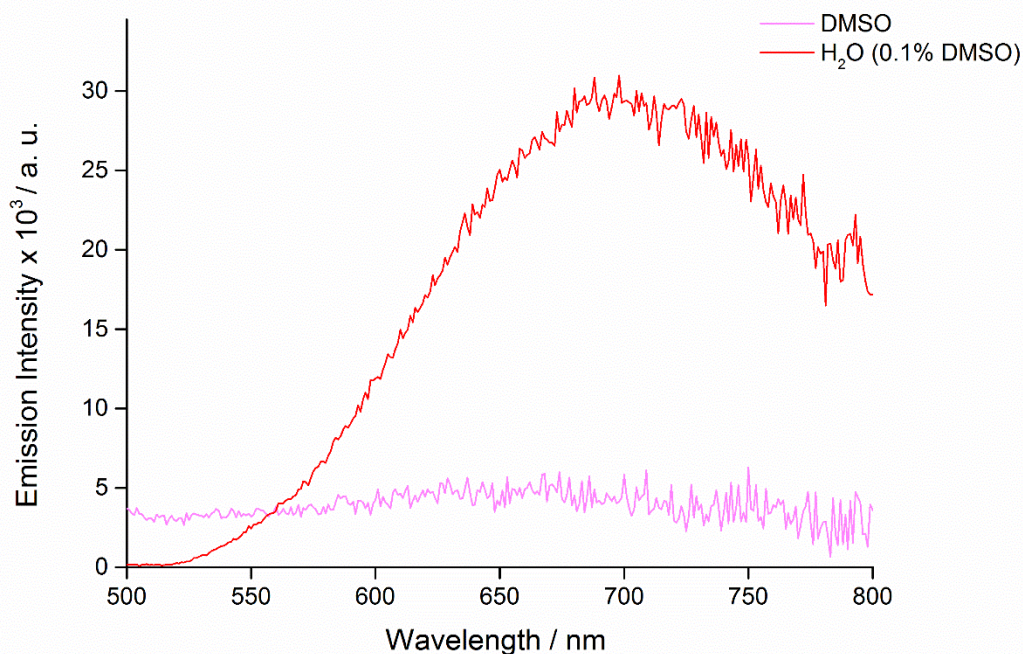


Figure A.2 Emission profiles of [Pt(CNC)(Py-H)] from a diluted (10^{-5} M) DMSO (pink trace) and H₂O (0.1% DMSO, red trace) solution.

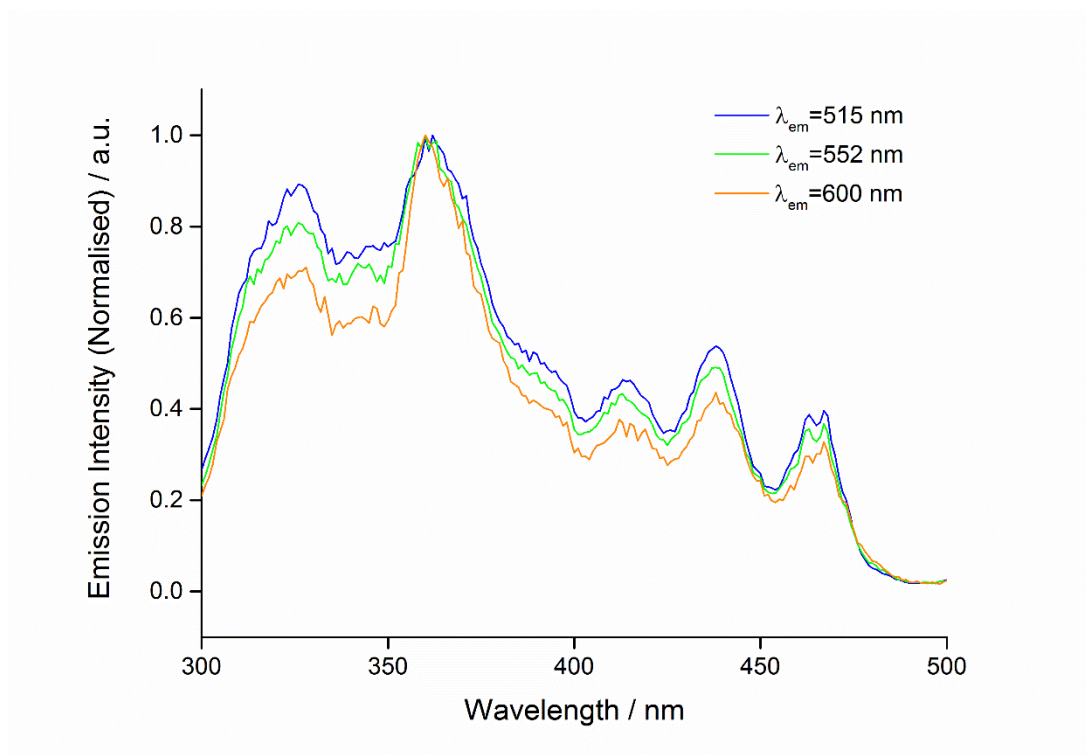


Figure A.3 Normalised excitation profile of [Pt(CNC)(DMSO)], recorded at the emission maxima, from a 10^{-5} butyronitrile glass at 77K.

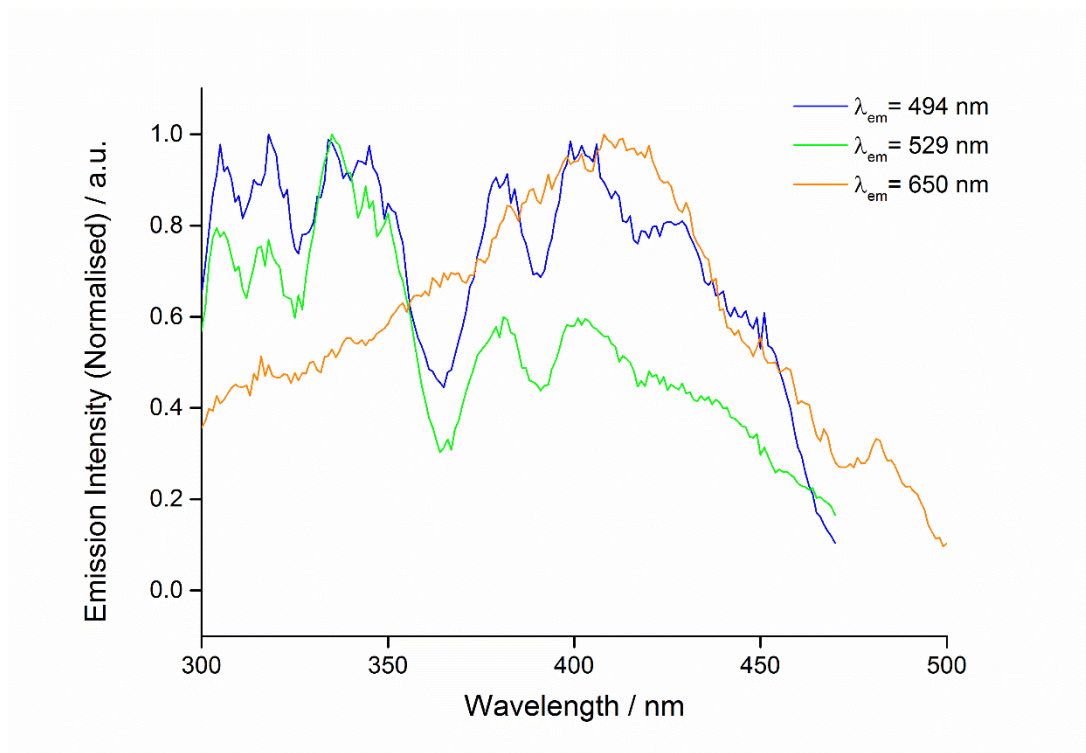


Figure A.4 Normalised excitation profile of [Pt(CNC)(Py-CO₂Me)], recorded at the emission maxima, from a 10^{-5} butyronitrile glass at 77K.

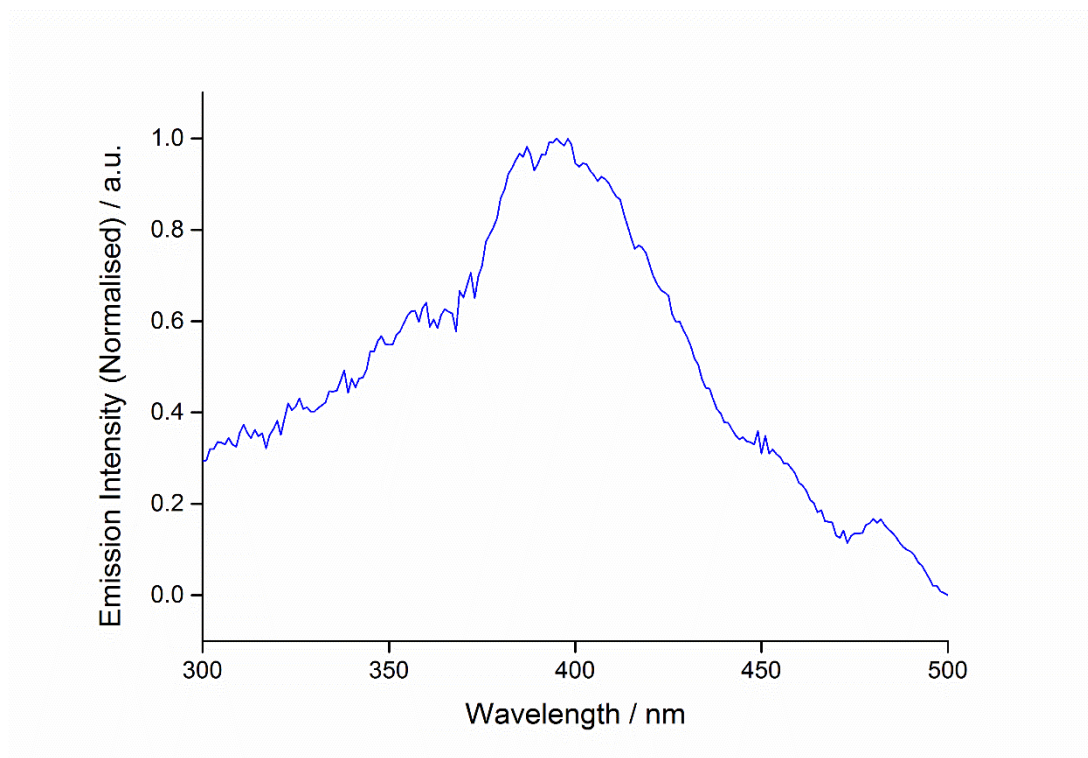


Figure A.5 Normalised excitation profile of [Pt(CNC)(Py-Ph)], recorded at the emission maxima ($\lambda_{em} = 657$ nm), from a 10^{-5} butyronitrile glass at 77K.

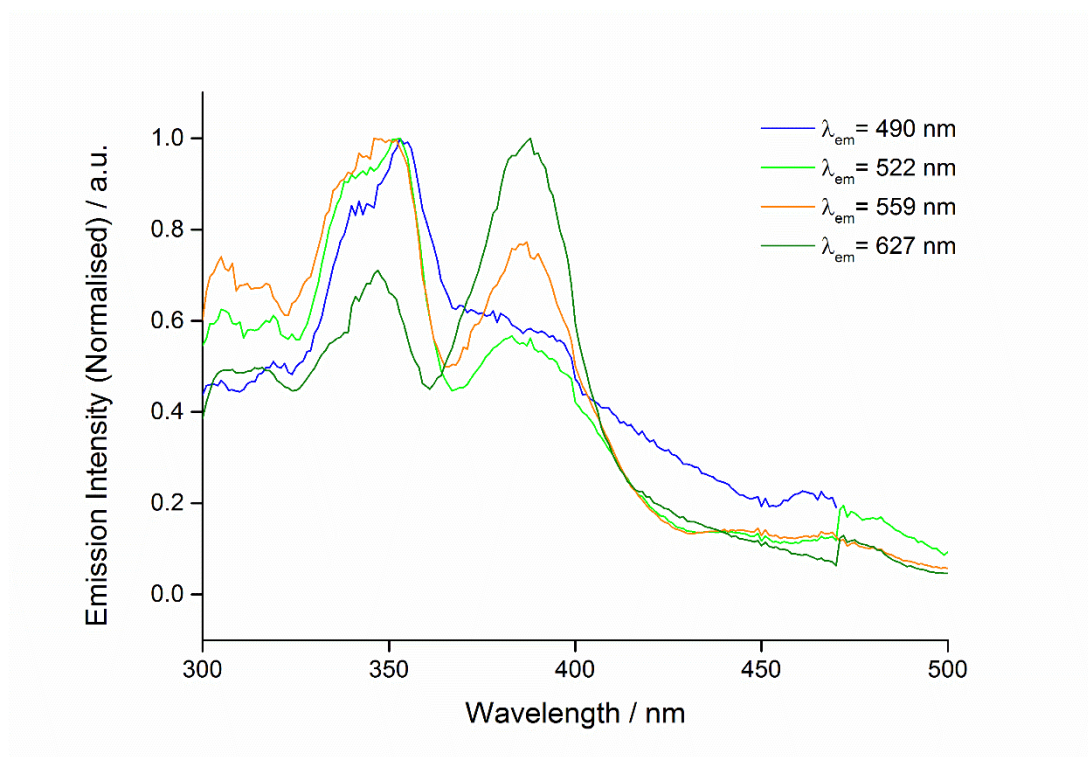


Figure A.6 Normalised excitation profile of [Pt(CNC)(bpy-PPh₃)], recorded at the emission maxima, from a 10^{-5} butyronitrile glass at 77K.

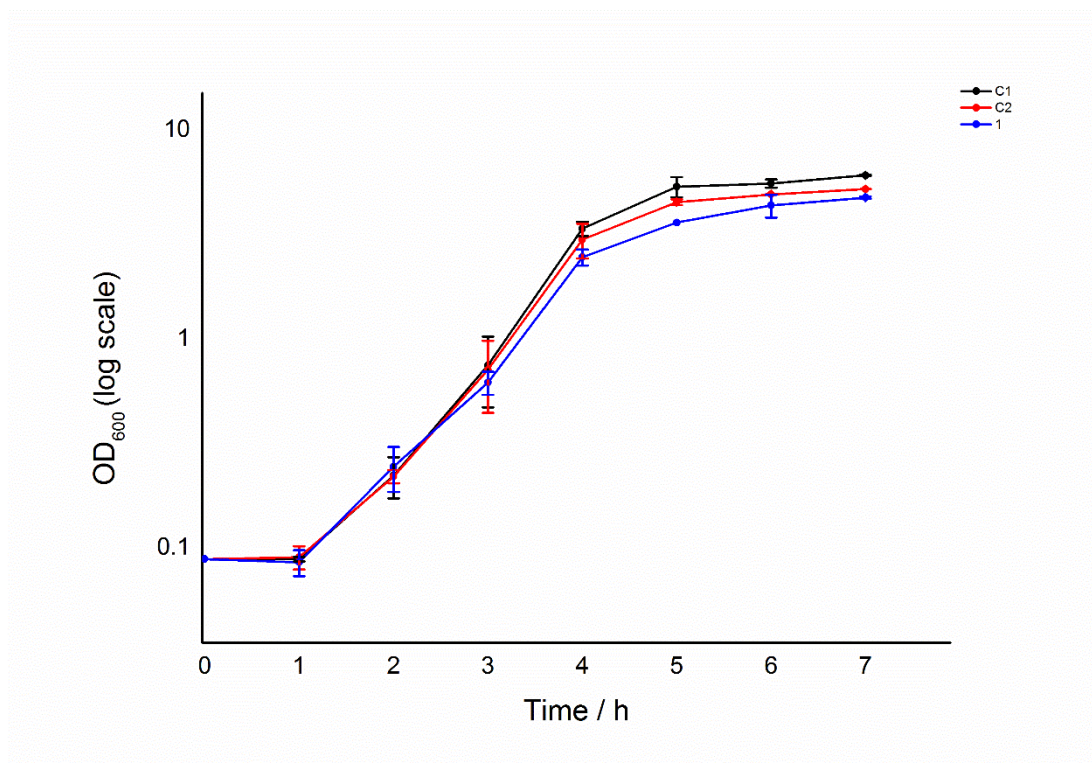


Figure A.7 Kinetics of growth of *E. coli* (bottom) at 37 °C in the presence of the platinum(II) complexes. C1) Untreated culture, C2) 0.1% DMSO control, 1) [Pt(CNC)(bpy-PPh₃)].

Appendix B

Table B.1. Photophysical data for **Py-Napht**

Solvent	$\lambda_{\text{abs}} / \text{nm}$ ($10^4 \epsilon [\text{M}^{-1}\text{cm}^{-1}]$)	λ_{em} [nm]	$\tau_{\text{aer}} (\%)$ [ns]	$\Phi_{\text{aer}}^{\text{a}}$ %
CH_2Cl_2	282 (3.61), 431 (2.90)	525	11	30
DMSO	286 (2.34), 445 (1.911)	540	11	7
$\text{H}_2\text{O}^{\text{b}}$	283 (0.83), 449 (0.83)	566	2.82 (81), 11 (19)	2

[a] Measured vs $[\text{Ru}(\text{bpy})_3]^{2+}$ in H_2O ($\phi_r = 0.028$). [b] 0.1% DMSO was added to favour the solubilisation of the complex.

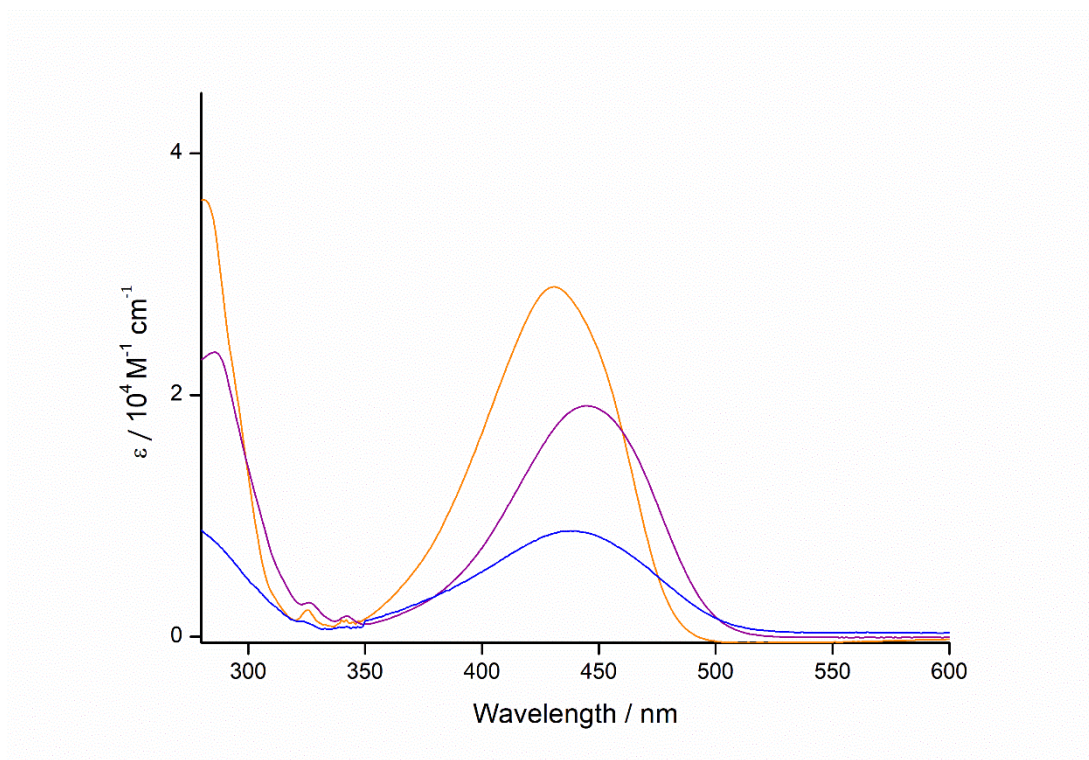


Figure B.1 Absorption profiles of **Py-Napht** from a diluted (10^{-5} M) dichloromethane (orange trace), DMSO (purple trace) and H_2O (0.1% DMSO, blue trace) solution.

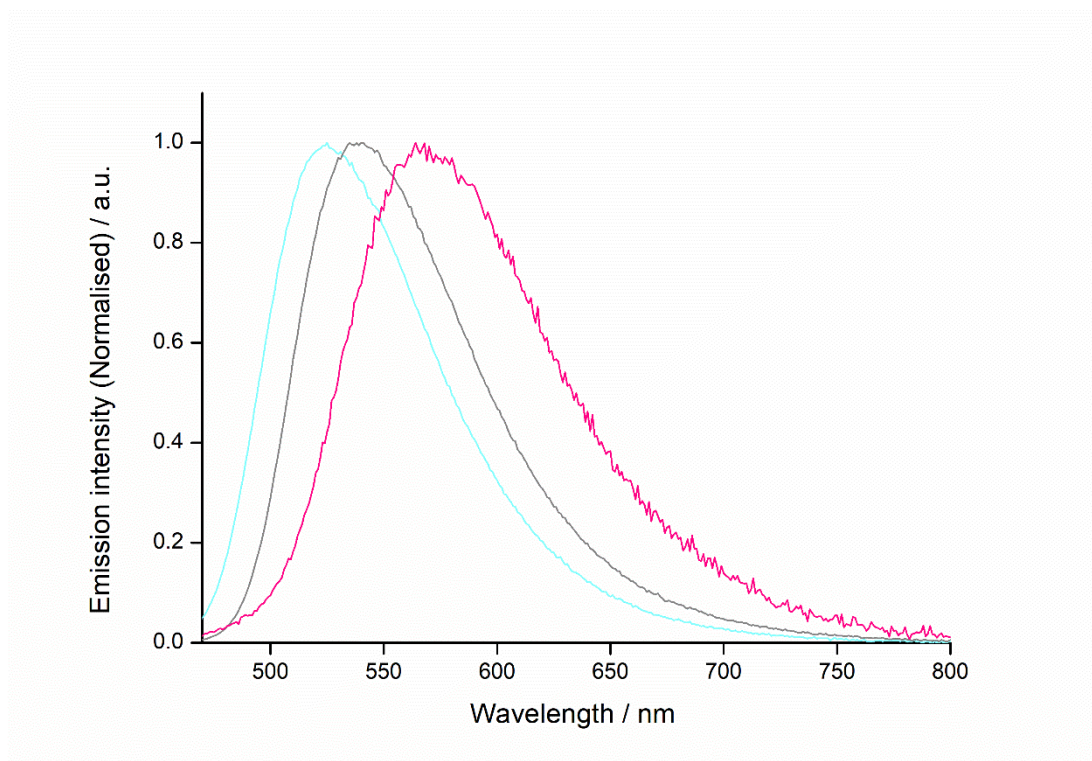


Figure B.2 Emission profiles of **Py-Napht** from a diluted (10^{-5} M) dichloromethane (light blue trace), DMSO (grey trace) and H₂O (0.1% DMSO, pink trace) solution.

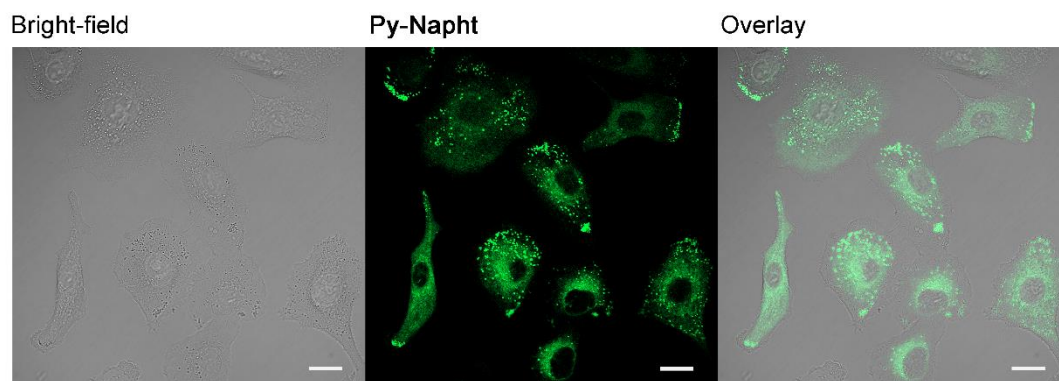


Figure B.3 Confocal microscopy images of A549 cells incubated with **Py-Napht**. Dose: 20 μ M, Scale bars 20 μ m.

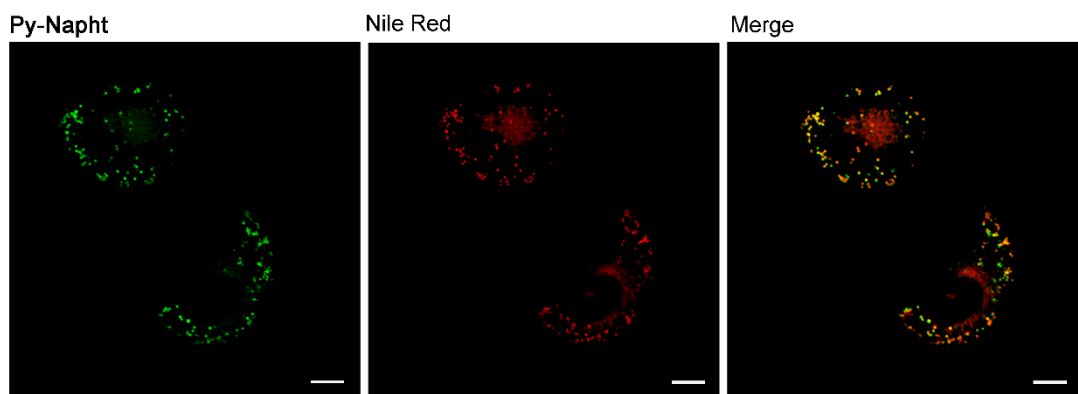


Figure B.4 Co-staining experiment. Micrographs of A549 cells stained with **Py-Napht** (green) and counter-stained with Nile Red (Red). Dose: 10 μ M, Scale bars 20 μ m.

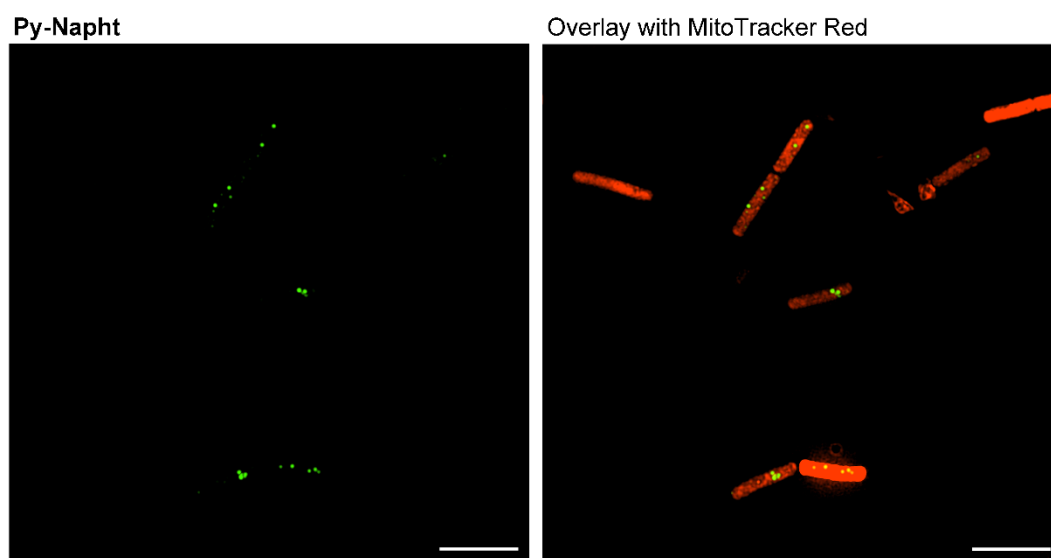


Figure B.5 SIM images of *B. cereus* incubated with **Py-Napht** (left) and co-stained with MitoTracker Red (Right). Scale bars: 5 μ m.

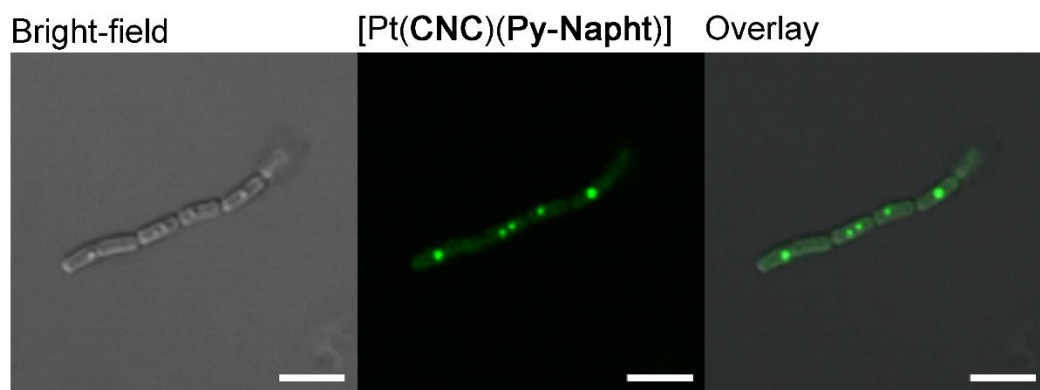


Figure B.6 Confocal images of fixed *B. cereus* incubated with [Pt(CNC)(Py-Napht)], showing how upon fixation the localisation of the dye is not limited to the lipid vacuoles but also spread along the cytoplasmic region.

Appendix C

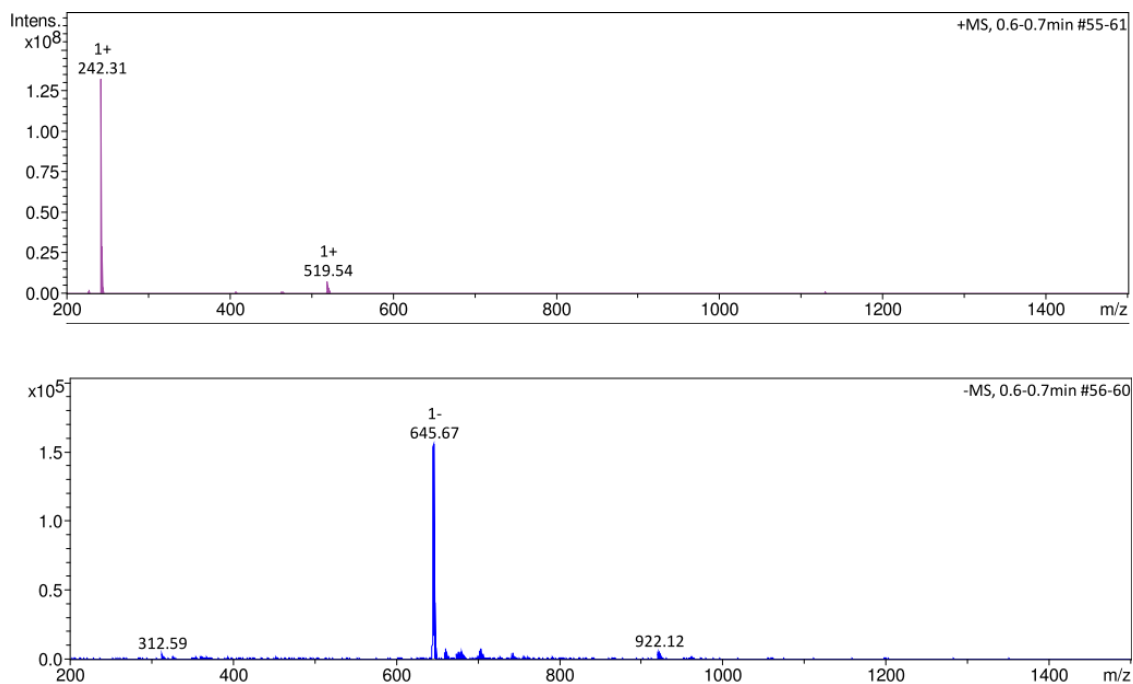


Figure C.1 ESI-MS spectrum of $[\text{Pt}(\text{CNC})(\text{TzH})][\text{TBA}]$. Top: positive ion region; bottom: negative ion region.

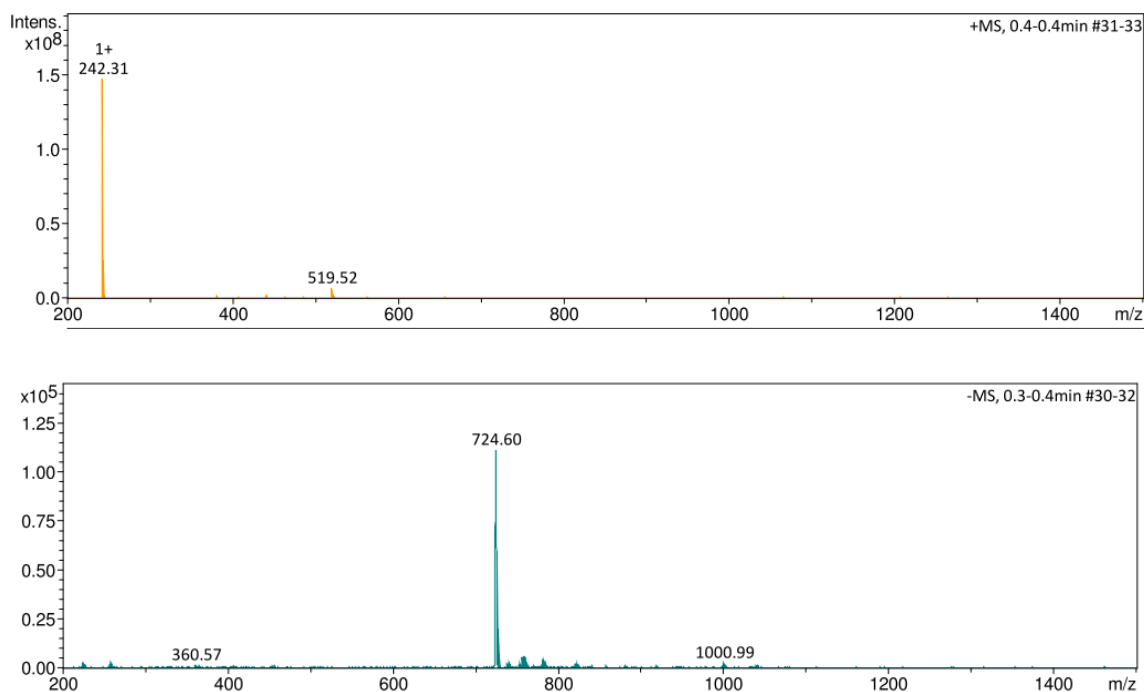


Figure C.2 ESI-MS spectrum of $[\text{Pt}(\text{CNC})(\text{TzBr})][\text{TBA}]$. Top: positive ion region; bottom: negative ion region.

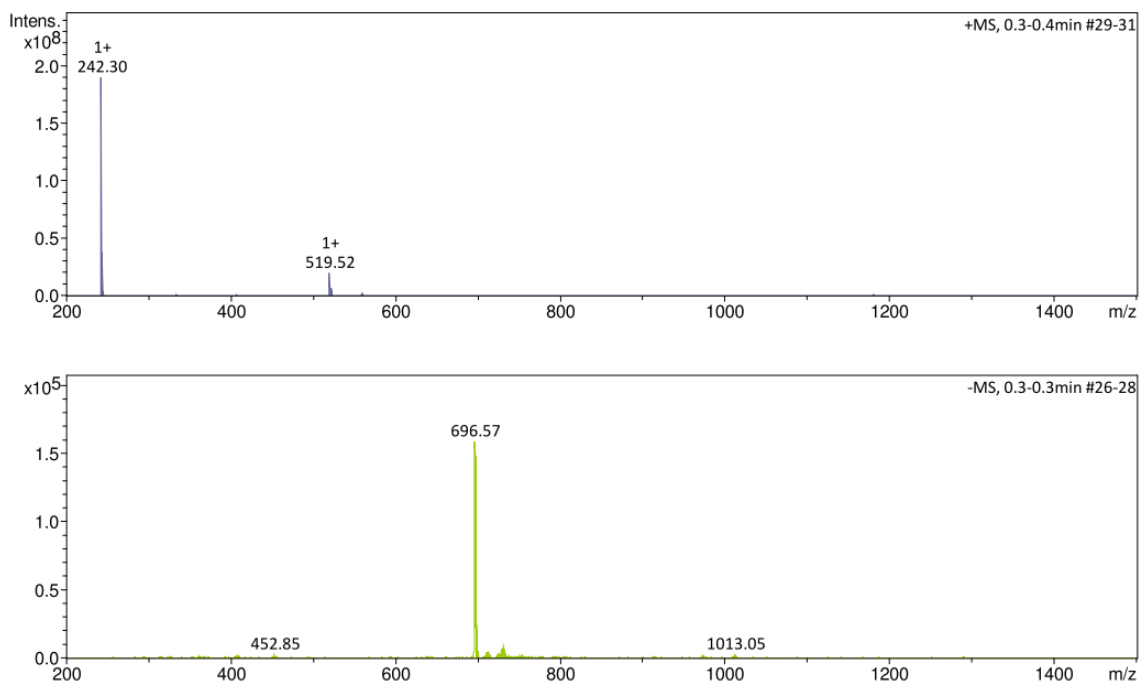


Figure C.3 ESI-MS spectrum of $[\text{Pt}(\text{CNC})(\text{TzQn})][\text{TBA}]$. Top: positive ion region; bottom: negative ion region.

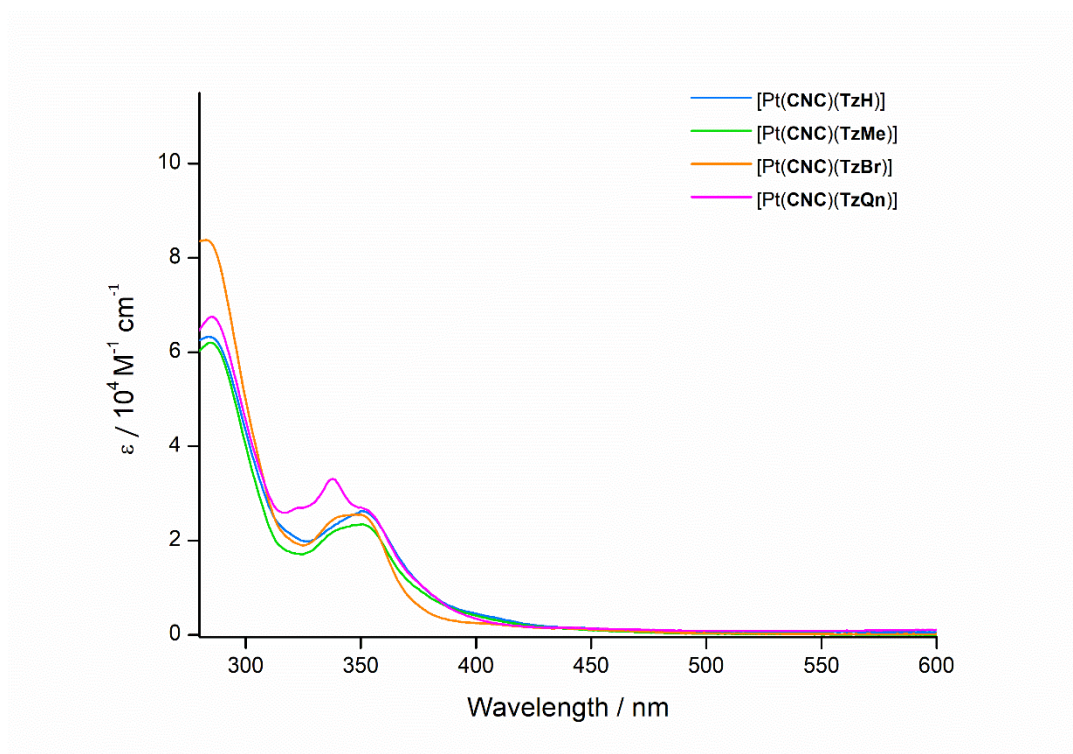


Figure C.4 Absorption spectra of the platinum complexes from 10^{-5} M solutions in DMSO.

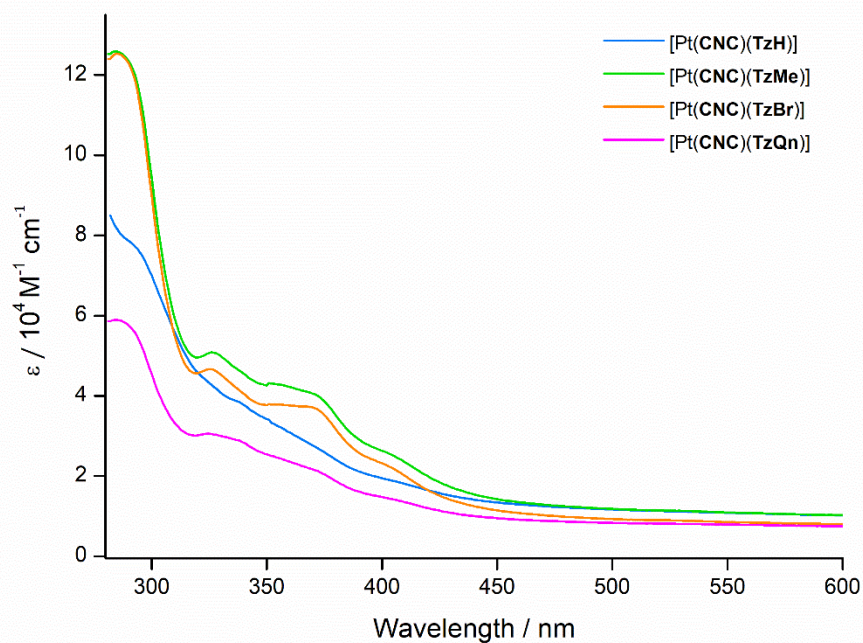


Figure C.5 Absorption spectra of the platinum complexes from 10^{-5} M solutions in H_2O (0.1% DMSO).

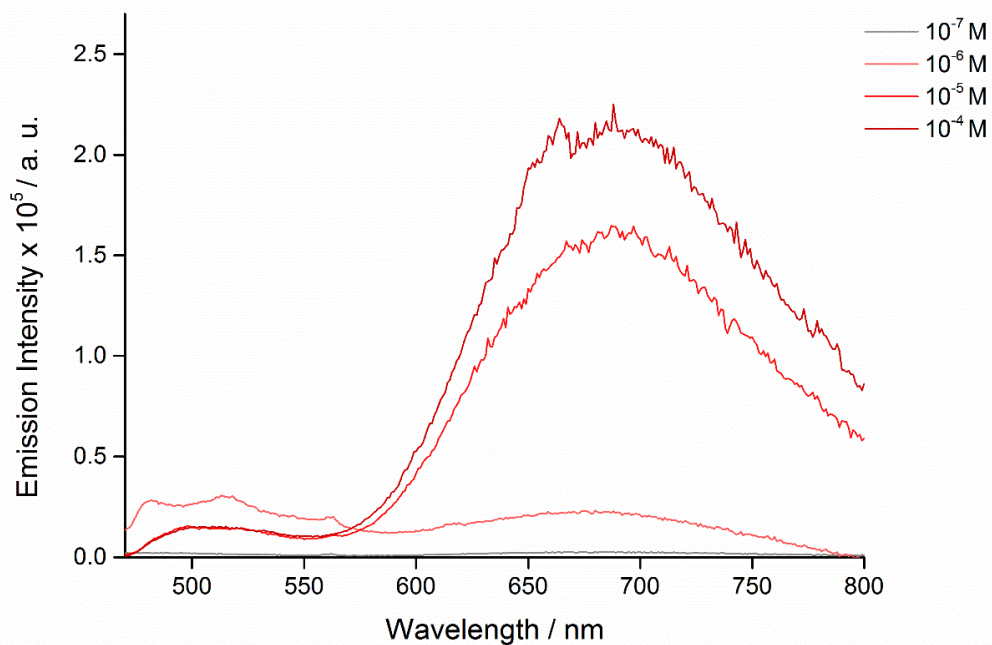


Figure C.6 Emission spectra of $[\text{Pt}(\text{CNC})(\text{TzH})]$ at different concentrations in a butyronitrile glass (77 K).

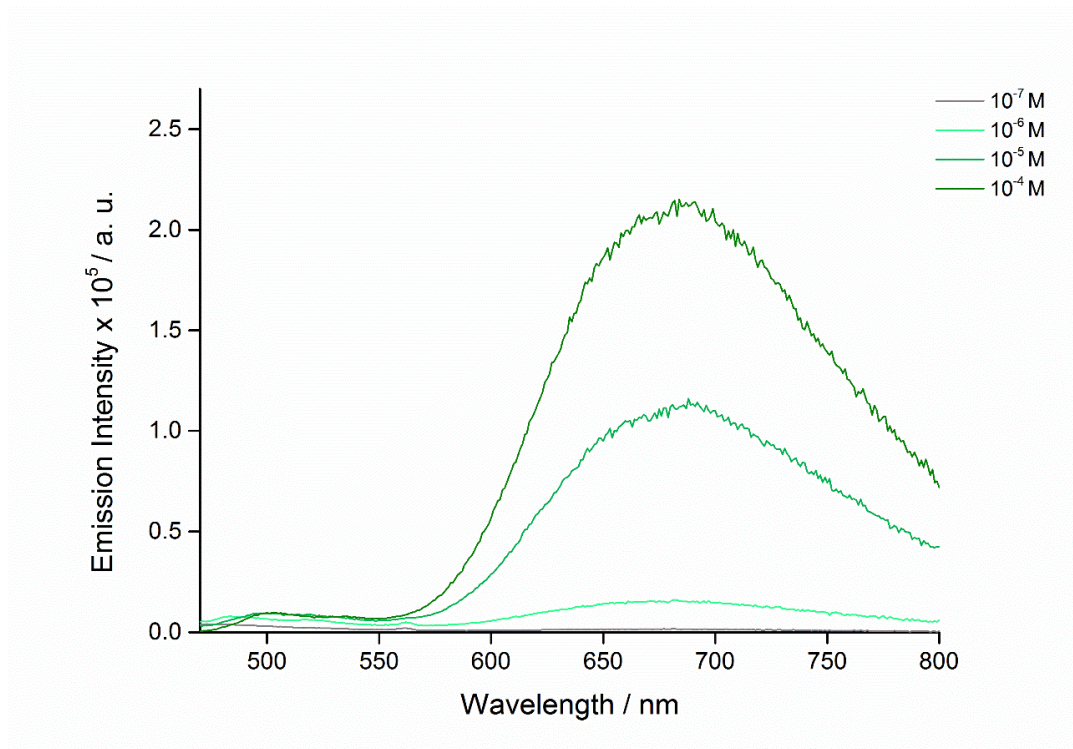


Figure C.7 Emission spectra of [Pt(CNC)(TzBr)] at different concentrations in a butyronitrile glass (77 K).

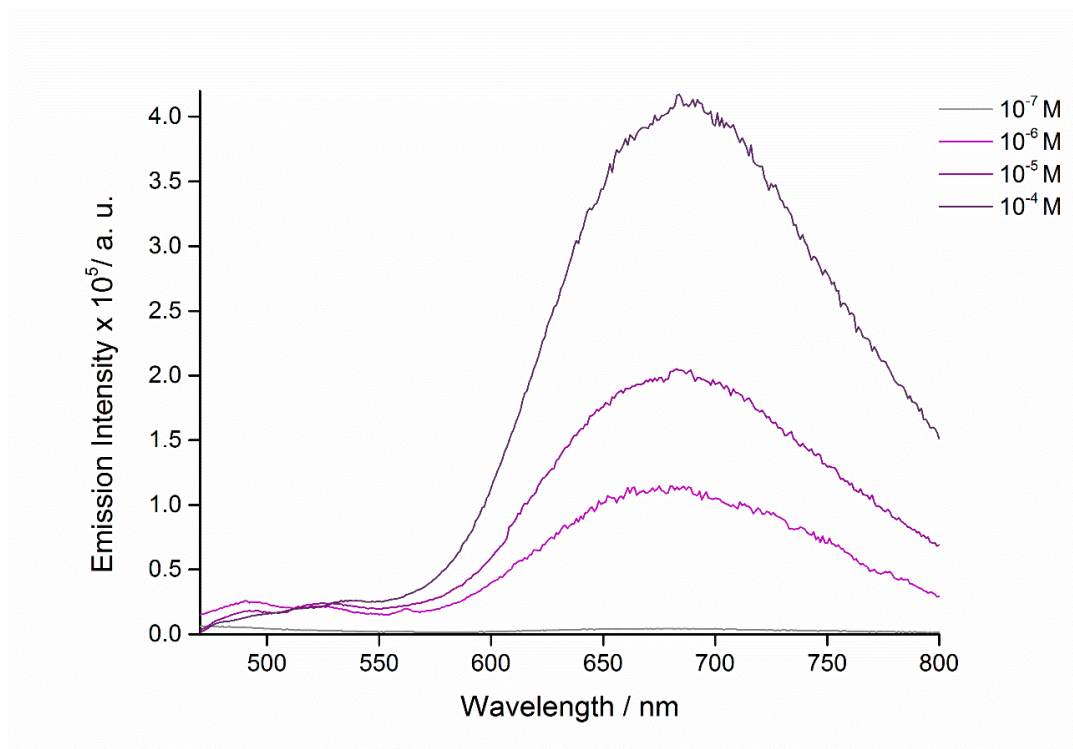


Figure C.8 Emission spectra of [Pt(CNC)(TzQn)] at different concentrations in a butyronitrile glass (77 K).

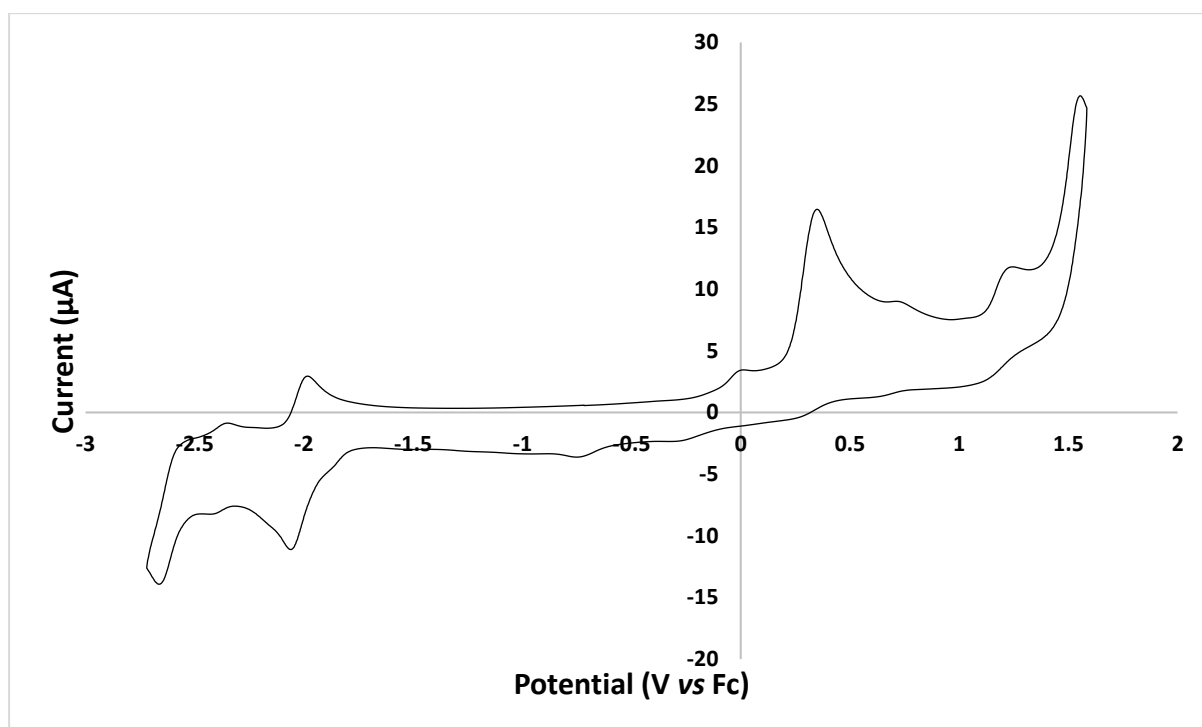


Figure C9. Cyclic voltammogram of [Pt(CNC)(DMSO)].

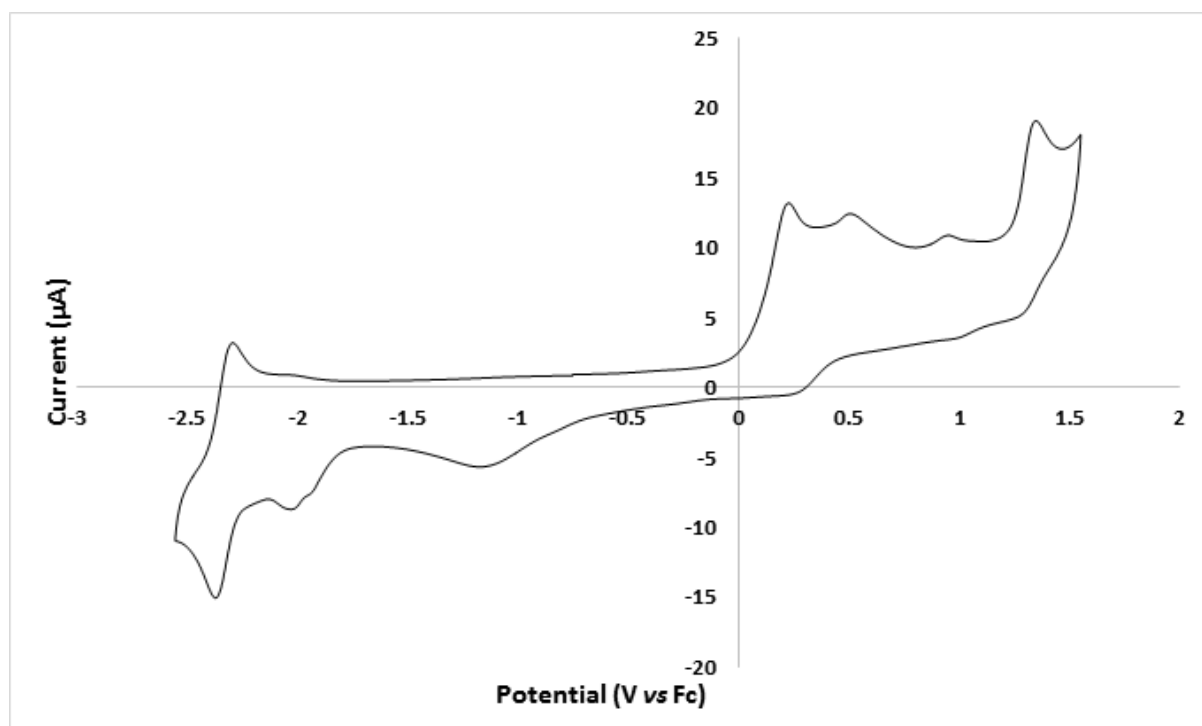


Figure C10: Cyclic voltammogram of [Pt(CNC)(TzH)]

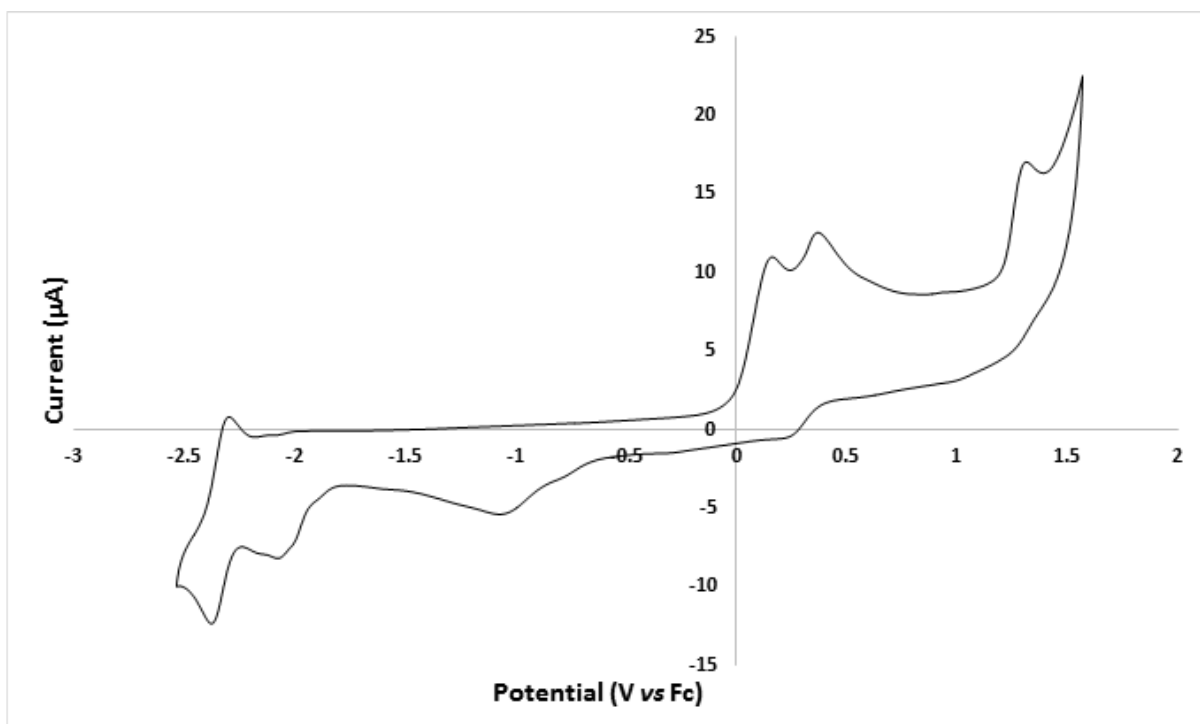


Figure C11: Cyclic voltammogram of [Pt(CNC)(TzMe)].

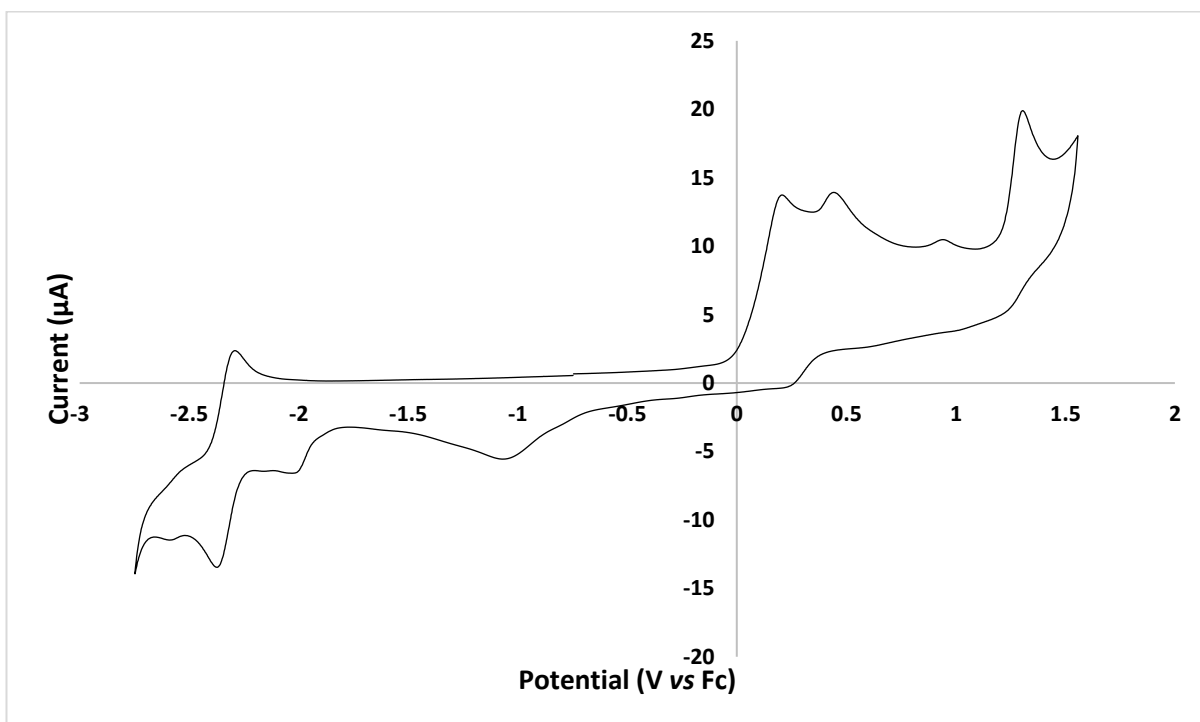


Figure C12: Cyclic voltammogram of [Pt(CNC)(TzBr)]

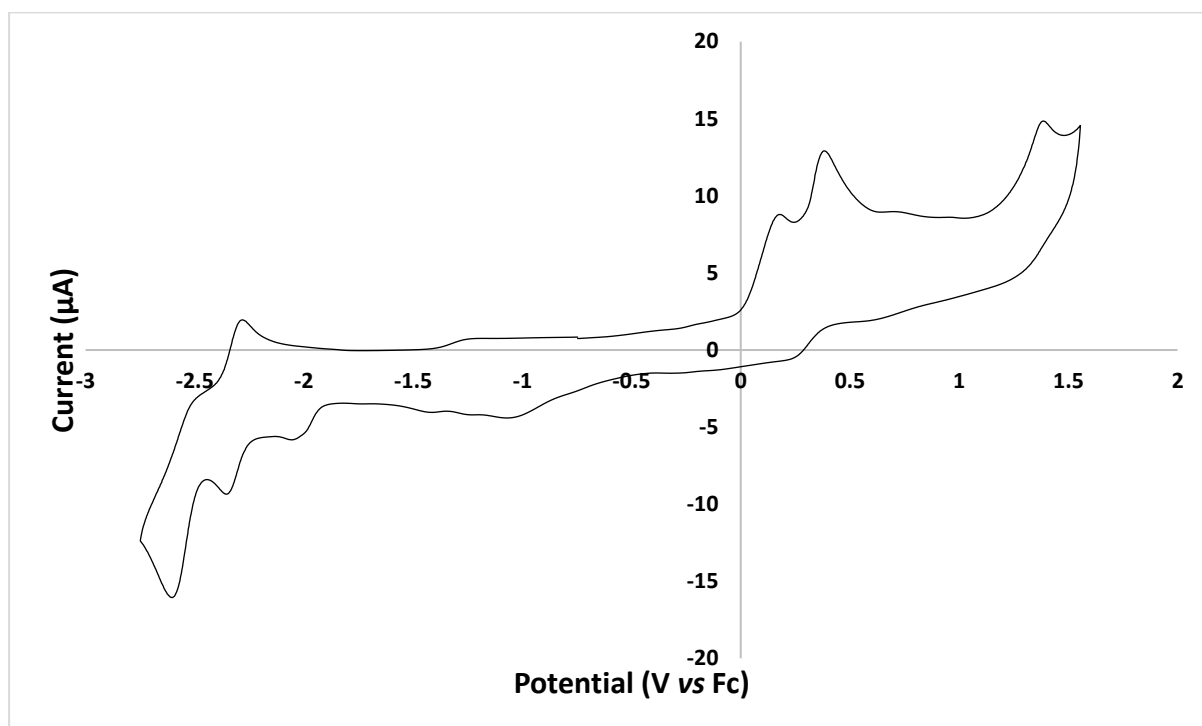


Figure C13: Cyclic voltammogram of [Pt(CNC)(TzQn)]

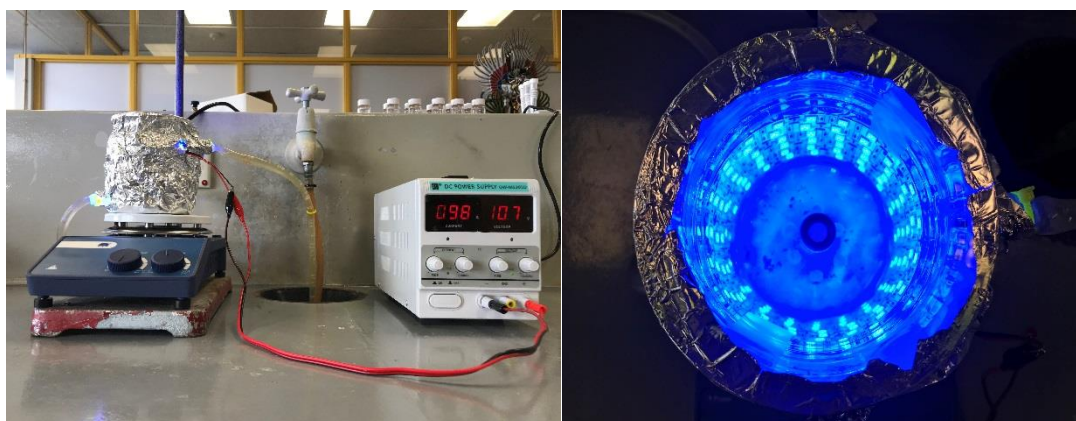


Figure C14. Photographs of blue LED photoreactor #1: **A)** side view; **B)** aerial view.

Custom blue LED (467 nm) photoreactor #2 was constructed using blue LEDs strips purchased from aliexpress.com (Figure S27). The 11-W blue LED photoreactor provides ~14,000 lux (measured at the center of the photoreactor). The plastic photoreactor features a condenser jacket that allows water cooling to maintain a constant temperature (24 °C) inside the reactor during irradiation. When the blue LED photoreactor was in use, it was completely covered in foil to block ambient light.

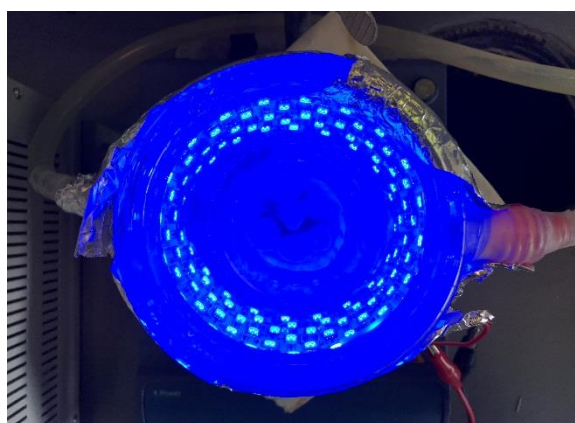
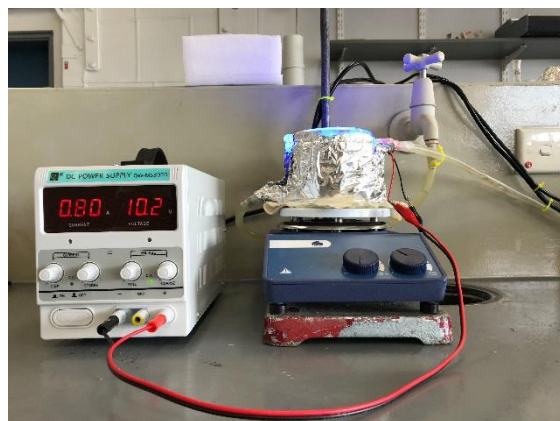


Figure C15. Photographs of blue LED photoreactor #2: **A)** side view; **B)** aerial view.

Appendix D

The supporting video can be found in:

<https://www.dropbox.com/sh/tbxdfbdjdh5nnz/AAAZx1Pyq6L9wEOUz-XKMF24a?dl=0>

SUPV1

The video shows the uptake of $[\text{Ir}(\text{F}_2\text{ppy})_2(\text{TzPyCN})]$ in *B. cereus*. The dosing of the complex (20 μM) was performed directly in the imaging dish. Scale bar: 5 μm . Interleave interval: 250 ms.

SUPV2

The video shows a view along the z plane of *B. cereus* incubated with $[\text{Ir}(\text{F}_2\text{ppy})_2(\text{TzPyCN})]$ (20 μM). Scale bar 5 μm .

SUPV3

Time-lapse experiment recording *B. cereus* incubated with $[\text{Ir}(\text{F}_2\text{ppy})_2(\text{TzPyCN})]$ (20 μM). The field of view has been scanned every 5 minutes for 1 hour. Scale bar: 5 μm . Interleave interval: 250 ms.

Appendix E

Table E.1 Emission profiles of SYTO 9 and the model complexes at pH 7.

Complex	λ_{em} [nm]	τ_{aer}^a [ns]	Φ_{aer}^b %
SYTO 9	570	14 (80), 1 (20)	1.2
[Pt(CNC)(Py-Napht)]	572	3	2
[Pt(CNC)(TzMe)] ⁻	700	28	0.4
[Ir(F ₂ ppy) ₂ (TzPyCN)]	552	189 (41), 628 (59)	5.7
[Ir(F ₂ ppy) ₂ (TzPyCN-Me)] ⁺	640	11 (76), 56 (24)	0.5
[Ir(F ₂ ppy) ₂ (TzPhCN) ₂] ⁻	520	45 (62), 8 (38)	3
[Ir(F ₂ ppy) ₂ (BTB)] ⁻	460, 487	340	0.8

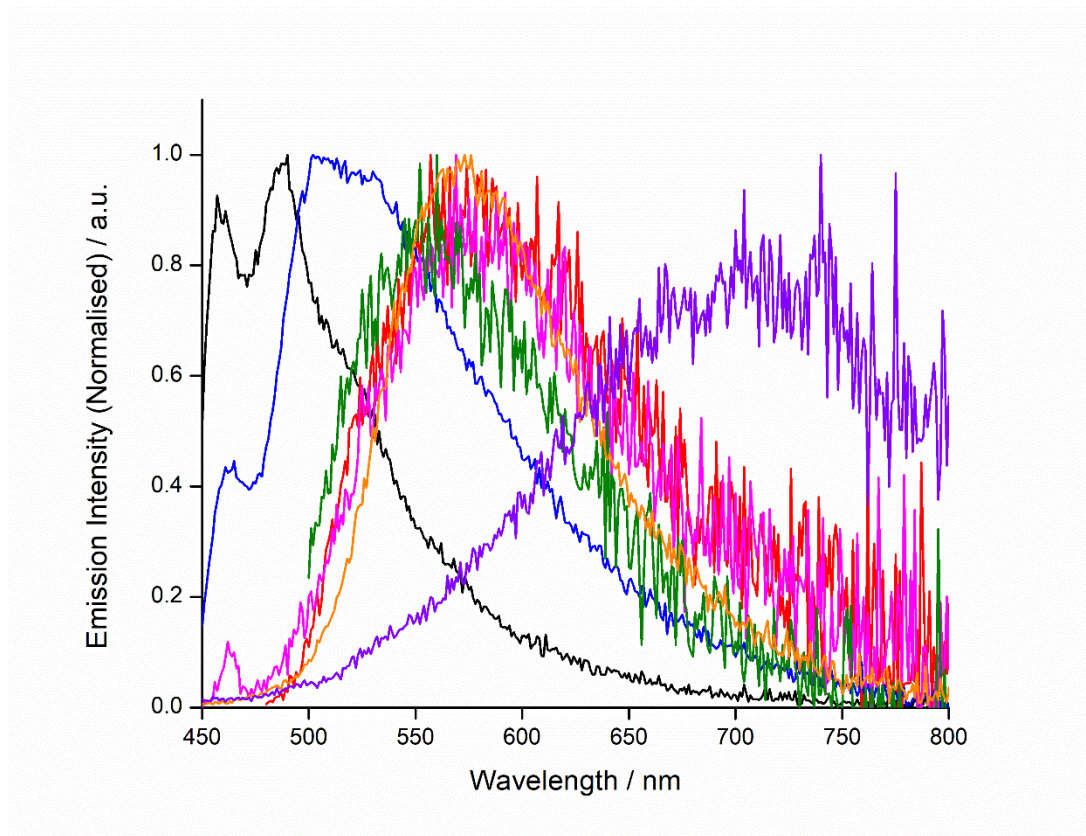


Figure E.1 Emission profiles of SYTO 9 (red line), $[\text{Ir}(\text{F}_2\text{ppy})_2(\text{TzPhCN})_2]^-$ (blue line) and $[\text{Ir}(\text{F}_2\text{ppy})_2(\text{BTB})]^-$ (black line) at pH 7. The emission at pH 7 of the other model complexes considered in this study is also reported. $[\text{Pt}(\text{CNC})(\text{Py-Napht})]$: orange line; $[\text{Pt}(\text{CNC})(\text{TzMe})]$: violet line; $[\text{Ir}(\text{F}_2\text{ppy})_2(\text{TzPyCN})]$: green line, $[\text{Ir}(\text{F}_2\text{ppy})_2(\text{TzPyCN-Me})]^+$: pink line.

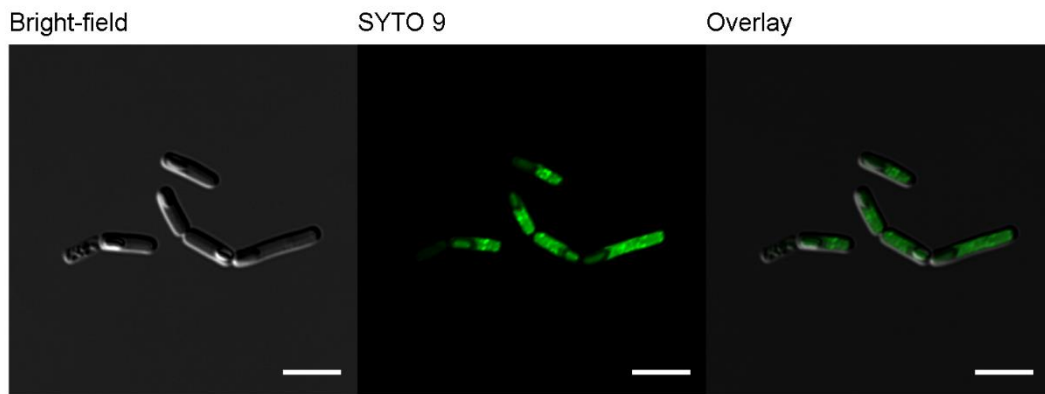


Figure E.2 Micrographs showing live *B. cereus* dosed with SYTO 9. Scalebars 5 μm .

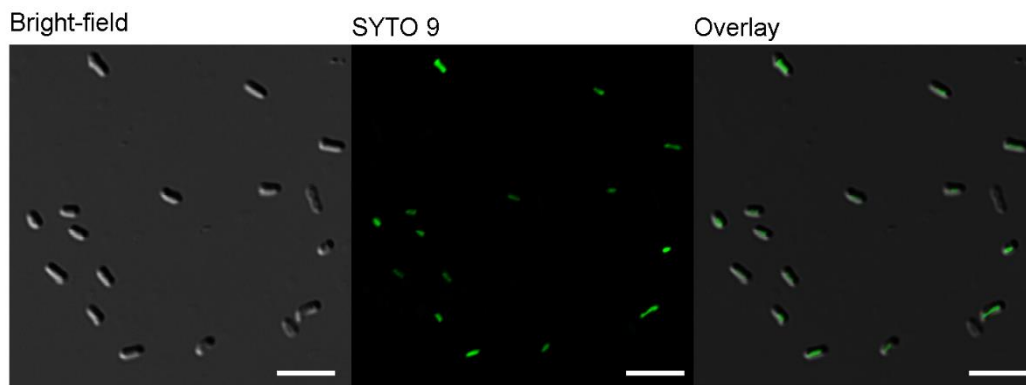


Figure E.3 Micrographs showing live *E. coli* dosed with SYTO 9. Scalebars 5 μm .

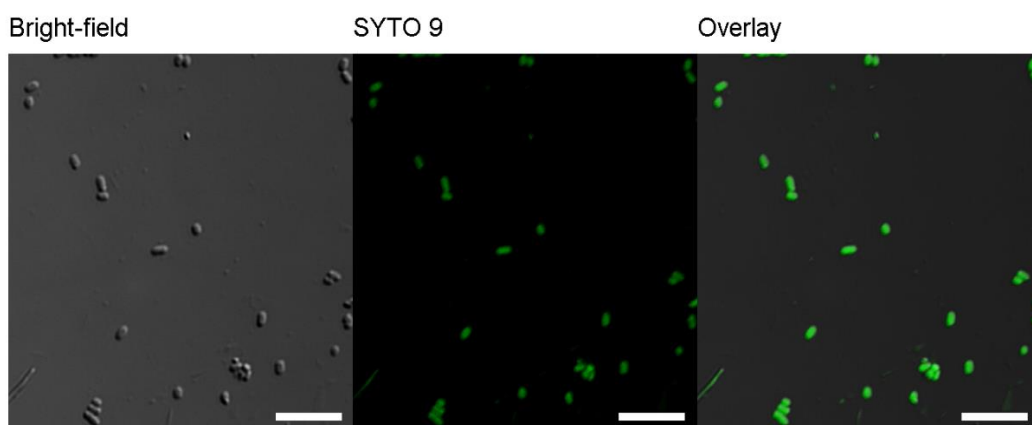


Figure E.4 Confocal images showing heat treated *At. ferrooxidans* dosed with 3 μM SYTO 9. Scalebars 5 μm .

Appendix F

This section includes the co-author statements for each publication included in this thesis or originated from results described in this thesis, but published or submitted after thesis submission (p. iv-viii).

To Whom It May Concern,

I, Anna Maria Ranieri, contributed to the microbiological testing of the Iridium Tetrazolato Complexes to the publication entitled

“Methylation of Ir(III)-tetrazolato complexes: an effective route to modulate the emission outputs and to switch to antimicrobial properties”

Reference details: V. Fiorini, I. Zanoni, S. Zacchini, A. L. Costa, A. Hochkoepler, V. Zanotti, A. M. Ranieri, M. Massi, A. Stefan and S. Stagni, *Dalton Trans.*, **2017**, *46*, 12328–12338.



Anna Maria Ranieri

I, as a Co-Author, endorse that this level of contribution by the candidate indicated above is appropriate.

Valentina Fiorini



To Whom It May Concern,

I, Anna Maria Ranieri, contributed to the microbiological testing of the Iridium Tetrazolato Complexes to the publication entitled

“Methylation of Ir(III)-tetrazolato complexes: an effective route to modulate the emission outputs and to switch to antimicrobial properties”

Reference details: V. Fiorini, I. Zanoni, S. Zacchini, A. L. Costa, A. Hochkoepler, V. Zanotti, A. M. Ranieri, M. Massi, A. Stefan and S. Stagni, *Dalton Trans.*, **2017**, *46*, 12328–12338.



Anna Maria Ranieri

I, as a Co-Author, endorse that this level of contribution by the candidate indicated above is appropriate.

Ilaria Zanoni



(Full Name of Co-Author)

Signature of Co-Author

To Whom It May Concern,

I, Anna Maria Ranieri, contributed to the microbiological testing of the Iridium Tetrazolato Complexes to the publication entitled

“Methylation of Ir(III)-tetrazolato complexes: an effective route to modulate the emission outputs and to switch to antimicrobial properties”

Reference details: V. Fiorini, I. Zandoni, S. Zacchini, A. L. Costa, A. Hochkoepler, V. Zanotti, A. M. Ranieri, M. Massi, A. Stefan and S. Stagni, *Dalton Trans.*, **2017**, *46*, 12328–12338.

Anna Maria Ranieri



I, as a Co-Author, endorse that this level of contribution by the candidate indicated above is appropriate.

Stefano Zacchini



To Whom It May Concern,

I, Anna Maria Ranieri, contributed to the microbiological testing of the Iridium Tetrazolato Complexes to the publication entitled

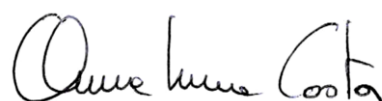
“Methylation of Ir(III)-tetrazolato complexes: an effective route to modulate the emission outputs and to switch to antimicrobial properties”

Reference details: V. Fiorini, I. Zanoni, S. Zacchini, A. L. Costa, A. Hochkoepler, V. Zanotti, A. M. Ranieri, M. Massi, A. Stefan and S. Stagni, *Dalton Trans.*, **2017**, *46*, 12328–12338.



Anna Maria Ranieri

I, as a Co-Author, endorse that this level of contribution by the candidate indicated above is appropriate.



Anna Luisa Costa

(Full Name of Co-Author)

Signature of Co-Author

To Whom It May Concern,

I, Anna Maria Ranieri, contributed to the microbiological testing of the Iridium Tetrazolato Complexes to the publication entitled

“Methylation of Ir(III)-tetrazolato complexes: an effective route to modulate the emission outputs and to switch to antimicrobial properties”

Reference details: V. Fiorini, I. Zanoni, S. Zacchini, A. L. Costa, A. Hochkoeppler, V. Zanotti, A. M. Ranieri, M. Massi, A. Stefan and S. Stagni, *Dalton Trans.*, **2017**, *46*, 12328–12338.



Anna Maria Ranieri

I, as a Co-Author, endorse that this level of contribution by the candidate indicated above is appropriate.

(Full Name of Co-Author)

Alejandro Hochkoeppler

Signature of Co-Author

Bologna, August 27th, 2019



To Whom It May Concern,

I, Anna Maria Ranieri, contributed to the microbiological testing of the Iridium Tetrazolato Complexes to the publication entitled

“Methylation of Ir(III)-tetrazolato complexes: an effective route to modulate the emission outputs and to switch to antimicrobial properties”

Reference details: V. Fiorini, I. Zanoni, S. Zacchini, A. L. Costa, A. Hochkoeppler, V. Zanotti, A. M. Ranieri, M. Massi, A. Stefan and S. Stagni, *Dalton Trans.*, **2017**, *46*, 12328–12338.



Anna Maria Ranieri

I, as a Co-Author, endorse that this level of contribution by the candidate indicated above is appropriate.

(Full Name of Co-Author)

Signature of Co-Author

Valerio Zanotti



To Whom It May Concern,

I, Anna Maria Ranieri, contributed to the microbiological testing of the Iridium Tetrazolato Complexes to the publication entitled

“Methylation of Ir(III)-tetrazolato complexes: an effective route to modulate the emission outputs and to switch to antimicrobial properties”

Reference details: V. Fiorini, I. Zanoni, S. Zacchini, A. L. Costa, A. Hochkoepler, V. Zanotti, A. M. Ranieri, M. Massi, A. Stefan and S. Stagni, *Dalton Trans.*, **2017**, *46*, 12328–12338.



Anna Maria Ranieri

I, as a Co-Author, endorse that this level of contribution by the candidate indicated above is appropriate.

(Full Name of Co-Author)

Massimiliano Massi

Signature of Co-Author



To Whom It May Concern,

I, Anna Maria Ranieri, contributed to the microbiological testing of the Iridium Tetrazolato Complexes to the publication entitled

“Methylation of Ir(III)-tetrazolato complexes: an effective route to modulate the emission outputs and to switch to antimicrobial properties”

Reference details: V. Fiorini, I. Zanoni, S. Zacchini, A. L. Costa, A. Hochkoepler, V. Zanotti, A. M. Ranieri, M. Massi, A. Stefan and S. Stagni, *Dalton Trans.*, **2017**, *46*, 12328–12338.



Anna Maria Ranieri

I, as a Co-Author, endorse that this level of contribution by the candidate indicated above is appropriate.

(Full Name of Co-Author)

ALESSANDRA STEFAN

Signature of Co-Author



To Whom It May Concern,

I, Anna Maria Ranieri, contributed to the microbiological testing of the Iridium Tetrazolato Complexes to the publication entitled

“Methylation of Ir(III)-tetrazolato complexes: an effective route to modulate the emission outputs and to switch to antimicrobial properties”

Reference details: V. Fiorini, I. Zanoni, S. Zacchini, A. L. Costa, A. Hochkoeppler, V. Zanotti, A. M. Ranieri, M. Massi, A. Stefan and S. Stagni, *Dalton Trans.*, **2017**, *46*, 12328–12338.



Anna Maria Ranieri

I, as a Co-Author, endorse that this level of contribution by the candidate indicated above is appropriate.

(Full Name of Co-Author)
STEFANO STAGNI

Signature of Co-Author



To Whom It May Concern,

I, Anna Maria Ranieri, synthesised the tetrazolato ligands, synthesised the platinum(II) complexes, characterised the complexes, performed the photophysical measurements and contributed to paper writing for the publication entitled

“Anionic Cyclometalated Platinum(II) Tetrazolato Complexes as Viable Photoredox Catalysts”

Reference details: A. M. Ranieri, L. K. Burt, S. Stagni, S. Zacchini, B. W. Skelton, M. I. Ogden, A. C. Bissember and M. Massi, *Organometallics*, **2019**, *38*, 1108–1117.



Anna Maria Ranieri

I, as a Co-Author, endorse that this level of contribution by the candidate indicated above is appropriate.



Liam Kevin Burt

To Whom It May Concern,

I, Anna Maria Ranieri, synthesised the tetrazolato ligands, synthesised the platinum(II) complexes, characterised the complexes, performed the photophysical measurements and contributed to paper writing for the publication entitled

“Anionic Cyclometalated Platinum(II) Tetrazolato Complexes as Viable Photoredox Catalysts”

Reference details: A. M. Ranieri, L. K. Burt, S. Stagni, S. Zacchini, B. W. Skelton, M. I. Ogden, A. C. Bissember and M. Massi, *Organometallics*, **2019**, 38, 1108–1117.



Anna Maria Ranieri

I, as a Co-Author, endorse that this level of contribution by the candidate indicated above is appropriate.

(Full Name of Co-Author)

Author STEFANO STAGNI

Signature of Co-



To Whom It May Concern,

I, Anna Maria Ranieri, synthesised the tetrazolato ligands, synthesised the platinum(II) complexes, characterised the complexes, performed the photophysical measurements and contributed to paper writing for the publication entitled

“Anionic Cyclometalated Platinum(II) Tetrazolato Complexes as Viable Photoredox Catalysts”

Reference details: A. M. Ranieri, L. K. Burt, S. Stagni, S. Zacchini, B. W. Skelton, M. I. Ogden, A. C. Bissember and M. Massi, *Organometallics*, **2019**, 38, 1108–1117.

Anna Maria Ranieri



I, as a Co-Author, endorse that this level of contribution by the candidate indicated above is appropriate.

Stefano Zacchini



To Whom It May Concern,

I, Anna Maria Ranieri, synthesised the tetrazolato ligands, synthesised the platinum(II) complexes, characterised the complexes, performed the photophysical measurements and contributed to paper writing for the publication entitled

“Anionic Cyclometalated Platinum(II) Tetrazolato Complexes as Viable Photoredox Catalysts”

Reference details: A. M. Ranieri, L. K. Burt, S. Stagni, S. Zacchini, B. W. Skelton, M. I. Ogden, A. C. Bissember and M. Massi, *Organometallics*, **2019**, 38, 1108–1117.



Anna Maria Ranieri

I, as a Co-Author, endorse that this level of contribution by the candidate indicated above is appropriate.

(Full Name of Co-Author)
Author

Signature of Co-

Brian Warwick Skelton



To Whom It May Concern,

I, Anna Maria Ranieri, synthesised the tetrazolato ligands, synthesised the platinum(II) complexes, characterised the complexes, performed the photophysical measurements and contributed to paper writing for the publication entitled

“Anionic Cyclometalated Platinum(II) Tetrazolato Complexes as Viable Photoredox Catalysts”

Reference details: A. M. Ranieri, L. K. Burt, S. Stagni, S. Zacchini, B. W. Skelton, M. I. Ogden, A. C. Bissember and M. Massi, *Organometallics*, **2019**, 38, 1108–1117.



Anna Maria Ranieri

I, as a Co-Author, endorse that this level of contribution by the candidate indicated above is appropriate.

Mark Ogden



To Whom It May Concern,

I, Anna Maria Ranieri, synthesised the tetrazolato ligands, synthesised the platinum(II) complexes, characterised the complexes, performed the photophysical measurements and contributed to paper writing for the publication entitled

“Anionic Cyclometalated Platinum(II) Tetrazolato Complexes as Viable Photoredox Catalysts”

Reference details: A. M. Ranieri, L. K. Burt, S. Stagni, S. Zacchini, B. W. Skelton, M. I. Ogden, A. C. Bissember and M. Massi, *Organometallics*, **2019**, 38, 1108–1117.



Anna Maria Ranieri

I, as a Co-Author, endorse that this level of contribution by the candidate indicated above is appropriate.

Alexander C. Bissember



(Full Name of Co-Author)

Signature of Co-Author

To Whom It May Concern,

I, Anna Maria Ranieri, synthesised the tetrazolato ligands, synthesised the platinum(II) complexes, characterised the complexes, performed the photophysical measurements and contributed to paper writing for the publication entitled

“Anionic Cyclometalated Platinum(II) Tetrazolato Complexes as Viable Photoredox Catalysts”

Reference details: A. M. Ranieri, L. K. Burt, S. Stagni, S. Zacchini, B. W. Skelton, M. I. Ogden, A. C. Bissember and M. Massi, *Organometallics*, **2019**, 38, 1108–1117.



Anna Maria Ranieri

I, as a Co-Author, endorse that this level of contribution by the candidate indicated above is appropriate.

(Full Name of Co-Author)
Author

Massimiliano Massi

Signature of Co-



To Whom It May Concern,

I, Anna Maria Ranieri, cultured the bacteria, performed the toxicity assays (growth curves), performed the confocal imaging experiments, contributed to the Raman spectroscopy experiments, contributed to paper writing for the publication entitled

“Complementary approaches to imaging sub-cellular lipid architectures in live bacteria using phosphorescent iridium complexes and Raman spectroscopy”

Reference details: A. M Ranieri, C. Caporale, V. Fiorini, A. Hubbard, P. Rigby, S. Stagni, E. Watkin, M. I. Ogden, M. J. Hackett, M. Massi, *Chem. Eur. J.*, **2019**, 25, 10566-10570.



Anna Maria Ranieri

I, as a Co-Author, endorse that this level of contribution by the candidate indicated above is appropriate.

Chiara Caporale



To Whom It May Concern,

I, Anna Maria Ranieri, cultured the bacteria, performed the toxicity assays (growth curves), performed the confocal imaging experiments, contributed to the Raman spectroscopy experiments, contributed to paper writing for the publication entitled

“Complementary approaches to imaging sub-cellular lipid architectures in live bacteria using phosphorescent iridium complexes and Raman spectroscopy”

Reference details: A. M Ranieri, C. Caporale, V. Fiorini, A. Hubbard, P. Rigby, S. Stagni, E. Watkin, M. I. Ogden, M. J. Hackett, M. Massi, *Chem. Eur. J.*, **2019**, 25, 10566-10570.



Anna Maria Ranieri

I, as a Co-Author, endorse that this level of contribution by the candidate indicated above is appropriate.

Valentina Fiorini



To Whom It May Concern,

I, Anna Maria Ranieri, cultured the bacteria, performed the toxicity assays (growth curves), performed the confocal imaging experiments, contributed to the Raman spectroscopy experiments, contributed to paper writing for the publication entitled

“Complementary approaches to imaging sub-cellular lipid architectures in live bacteria using phosphorescent iridium complexes and Raman spectroscopy”

Reference details: A. M Ranieri, C. Caporale, V. Fiorini, A. Hubbard, P. Rigby, S. Stagni, E. Watkin, M. I. Ogden, M. J. Hackett, M. Massi, *Chem. Eur. J.*, **2019**, 25, 10566-10570.



Anna Maria Ranieri

I, as a Co-Author, endorse that this level of contribution by the candidate indicated above is appropriate.

(Full Name of Co-Author)

Author STEFANO STAGNI

Signature of Co-

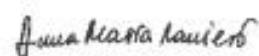


To Whom It May Concern,

I, Anna Maria Ranieri, cultured the bacteria, performed the toxicity assays (growth curves), performed the confocal imaging experiments, contributed to the Raman spectroscopy experiments, contributed to paper writing for the publication entitled

"Complementary approaches to imaging sub-cellular lipid architectures in live bacteria using phosphorescent iridium complexes and Raman spectroscopy"

Reference details: A. M Ranieri, C. Caporale, V. Fiorini, A. Hubbard, P. Rigby, S. Stagni, E. Watkin, M. I. Ogden, M. J. Hackett, M. Massi, *Chem. Eur. J.*, **2019**, *25*, 10566-10570.



Anna Maria Ranieri

I, as a Co-Author, endorse that this level of contribution by the candidate indicated above is appropriate.



(Full Name of Co-Author)



Signature of Co-Author

To Whom It May Concern,

I, Anna Maria Ranieri, cultured the bacteria, performed the toxicity assays (growth curves), performed the confocal imaging experiments, contributed to the Raman spectroscopy experiments, contributed to paper writing for the publication entitled

“Complementary approaches to imaging sub-cellular lipid architectures in live bacteria using phosphorescent iridium complexes and Raman spectroscopy”

Reference details: A. M Ranieri, C. Caporale, V. Fiorini, A. Hubbard, P. Rigby, S. Stagni, E. Watkin, M. I. Ogden, M. J. Hackett, M. Massi, *Chem. Eur. J.*, **2019**, 25, 10566-10570.



Anna Maria Ranieri

I, as a Co-Author, endorse that this level of contribution by the candidate indicated above is appropriate.

Mark Ogden



To Whom It May Concern,

I, Anna Maria Ranieri, cultured the bacteria, performed the toxicity assays (growth curves), performed the confocal imaging experiments, contributed to the Raman spectroscopy experiments, contributed to paper writing for the publication entitled

“Complementary approaches to imaging sub-cellular lipid architectures in live bacteria using phosphorescent iridium complexes and Raman spectroscopy”

Reference details: A. M Ranieri, C. Caporale, V. Fiorini, A. Hubbard, P. Rigby, S. Stagni, E. Watkin, M. I. Ogden, M. J. Hackett, M. Massi, *Chem. Eur. J.*, **2019**, *25*, 10566-10570.



Anna Maria Ranieri

I, as a Co-Author, endorse that this level of contribution by the candidate indicated above is appropriate.

Dr Mark John Hackett

(Full Name of Co-Author)



Signature of Co-Author

To Whom It May Concern,

I, Anna Maria Ranieri, cultured the bacteria, performed the toxicity assays (growth curves), performed the confocal imaging experiments, contributed to the Raman spectroscopy experiments, contributed to paper writing for the publication entitled

“Complementary approaches to imaging sub-cellular lipid architectures in live bacteria using phosphorescent iridium complexes and Raman spectroscopy”

Reference details: A. M Ranieri, C. Caporale, V. Fiorini, A. Hubbard, P. Rigby, S. Stagni, E. Watkin, M. I. Ogden, M. J. Hackett, M. Massi, *Chem. Eur. J.*, **2019**, 25, 10566-10570.



Anna Maria Ranieri

I, as a Co-Author, endorse that this level of contribution by the candidate indicated above is appropriate.

(Full Name of Co-Author)

Signature of Co-Author

Massimiliano Massi



To Whom It May Concern,

I, Anna Maria Ranieri, synthesised the platinum(II) complexes, characterised the complexes, performed the photophysical measurements, cultured the bacteria, performed the toxicity assays, performed the superresolution imaging experiments, contributed to paper writing for the publication entitled

“A platinum(II) based correlative probe for bacteria”

Reference details: Anna M. Ranieri, Kathryn G. Leslie, Song Huang, Stefano Stagni, Denis Jacquemin, Haibo Jiang, Alysia Hubbard, Elizabeth Watkin, Mark I. Ogden, Elizabeth J. New, Massimiliano Massi, *submitted for review, 2019*



Anna Maria Ranieri

I, as a Co-Author, endorse that this level of contribution by the candidate indicated above is appropriate.

(Full Name of Co-Author)

Signature of Co-Author

Kathryn Gwennyth Leslie



To Whom It May Concern,

I, Anna Maria Ranieri, synthesised the platinum(II) complexes, characterised the complexes, performed the photophysical measurements, cultured the bacteria, performed the toxicity assays, performed the superresolution imaging experiments, contributed to paper writing for the publication entitled

“A platinum(II) based correlative probe for bacteria”

Reference details: Anna M. Ranieri, Kathryn G. Leslie, Song Huang, Stefano Stagni, Denis Jacquemin, Haibo Jiang, Alysia Hubbard, Elizabeth Watkin, Mark I. Ogden, Elizabeth J. New, Massimiliano Massi, *submitted for review*, **2019**



Anna Maria Ranieri

I, as a Co-Author, endorse that this level of contribution by the candidate indicated above is appropriate.

(Full Name of Co-Author)
Author

Signature of Co-

STEFANO STAGNI



To Whom It May Concern,

I, Anna Maria Ranieri, synthesised the platinum(II) complexes, characterised the complexes, performed the photophysical measurements, cultured the bacteria, performed the toxicity assays, performed the superresolution imaging experiments, contributed to paper writing for the publication entitled

“A platinum(II) based correlative probe for bacteria”

Reference details: Anna M. Ranieri, Kathryn G. Leslie, Song Huang, Stefano Stagni, Denis Jacquemin, Haibo Jiang, Alysia Hubbard, Elizabeth Watkin, Mark I. Ogden, Elizabeth J. New, Massimiliano Massi, *submitted for review, 2019*



Anna Maria Ranieri

I, as a Co-Author, endorse that this level of contribution by the candidate indicated above is appropriate.

(Full Name of Co-Author) Prof. Denis. Jacquemin



Signature of Co-Author

To Whom It May Concern,

I, Anna Maria Ranieri, synthesised the platinum(II) complexes, characterised the complexes, performed the photophysical measurements, cultured the bacteria, performed the toxicity assays, performed the superresolution imaging experiments, contributed to paper writing for the publication entitled

“A platinum(II) based correlative probe for bacteria”

Reference details: Anna M. Ranieri, Kathryn G. Leslie, Song Huang, Stefano Stagni, Denis Jacquemin, Haibo Jiang, Alysia Hubbard, Elizabeth Watkin, Mark I. Ogden, Elizabeth J. New, Massimiliano Massi, *submitted for review, 2019*



Anna Maria Ranieri

I, as a Co-Author, endorse that this level of contribution by the candidate indicated above is appropriate.

Haibo Jiang

(Full Name of Co-Author)



Signature of Co-Author

To Whom It May Concern,

I, Anna Maria Ranieri, synthesised the platinum(II) complexes, characterised the complexes, performed the photophysical measurements, cultured the bacteria, performed the toxicity assays, performed the superresolution imaging experiments, contributed to paper writing for the publication entitled

“A platinum(II) based correlative probe for bacteria”

Reference details: Anna M. Ranieri, Kathryn G. Leslie, Song Huang, Stefano Stagni, Denis Jacquemin, Haibo Jiang, Alysia Hubbard, Elizabeth Watkin, Mark I. Ogden, Elizabeth J. New, Massimiliano Massi, *submitted for review, 2019*



Anna Maria Ranieri

I, as a Co-Author, endorse that this level of contribution by the candidate indicated above is appropriate.

Prof Elizabeth LJ Watkin
(Full Name of Co-Author)



Signature of Co-Author

To Whom It May Concern,

I, Anna Maria Ranieri, synthesised the platinum(II) complexes, characterised the complexes, performed the photophysical measurements, cultured the bacteria, performed the toxicity assays, performed the superresolution imaging experiments, contributed to paper writing for the publication entitled

“A platinum(II) based correlative probe for bacteria”

Reference details: Anna M. Ranieri, Kathryn G. Leslie, Song Huang, Stefano Stagni, Denis Jacquemin, Haibo Jiang, Alysia Hubbard, Elizabeth Watkin, Mark I. Ogden, Elizabeth J. New, Massimiliano Massi, *submitted for review*, **2019**



Anna Maria Ranieri

I, as a Co-Author, endorse that this level of contribution by the candidate indicated above is appropriate.

Mark Ogden



To Whom It May Concern,

I, Anna Maria Ranieri, synthesised the platinum(II) complexes, characterised the complexes, performed the photophysical measurements, cultured the bacteria, performed the toxicity assays, performed the superresolution imaging experiments, contributed to paper writing for the publication entitled

“A platinum(II) based correlative probe for bacteria”

Reference details: Anna M. Ranieri, Kathryn G. Leslie, Song Huang, Stefano Stagni, Denis Jacquemin, Haibo Jiang, Alysia Hubbard, Elizabeth Watkin, Mark I. Ogden, Elizabeth J. New, Massimiliano Massi, *submitted for review, 2019*



Anna Maria Ranieri

I, as a Co-Author, endorse that this level of contribution by the candidate indicated above is appropriate.

Elizabeth New

(Full Name of Co-Author)



Signature of Co-Author

To Whom It May Concern,

I, Anna Maria Ranieri, synthesised the platinum(II) complexes, characterised the complexes, performed the photophysical measurements, cultured the bacteria, performed the toxicity assays, performed the superresolution imaging experiments, contributed to paper writing for the publication entitled

“A platinum(II) based correlative probe for bacteria”

Reference details: Anna M. Ranieri, Kathryn G. Leslie, Song Huang, Stefano Stagni, Denis Jacquemin, Haibo Jiang, Alysia Hubbard, Elizabeth Watkin, Mark I. Ogden, Elizabeth J. New, Massimiliano Massi, *submitted for review*, **2019**



Anna Maria Ranieri

I, as a Co-Author, endorse that this level of contribution by the candidate indicated above is appropriate.

(Full Name of Co-Author)

Signature of Co-Author

Massimiliano Massi

